

Journal of Healthcare Engineering

# Medical Signal Processing in Biomedical and Clinical Applications

Lead Guest Editor: Kunal Pal

Guest Editors: Kunal Mitra, Arindam Bit, Saugat Bhattacharyya, and Anilesh Dey





---

# **Medical Signal Processing in Biomedical and Clinical Applications**

Journal of Healthcare Engineering

---

## **Medical Signal Processing in Biomedical and Clinical Applications**

Lead Guest Editor: Kunal Pal

Guest Editors: Kunal Mitra, Arindam Bit, Saugat Bhattacharyya,  
and Anilesh Dey



---

Copyright © 2018 Hindawi. All rights reserved.

This is a special issue published in “Journal of Healthcare Engineering.” All articles are open access articles distributed under the Creative Commons Attribution License, which permits unrestricted use, distribution, and reproduction in any medium, provided the original work is properly cited.

## Editorial Board

Saverio Affatato, Italy  
Hasan Ayaz, USA  
William Bertucci, France  
Olivier Beuf, France  
Hongwei Chen, USA  
Daniel H.K. Chow, Hong Kong  
Gianluca Ciardelli, Italy  
Elena De Momi, Italy  
Tiago H. Falk, Canada  
Mostafa Fatemi, USA  
Jesus Favela, Mexico  
Joseph Finkelstein, USA  
Jesus Fontecha, Spain  
Shahram M. Ghanaati, Germany  
Luca Giancardo, USA  
Antonio Gloria, Italy  
Kheng-Lim Goh, Singapore  
Pedro Gomes, Portugal  
Carlos Gómez, Spain  
Philippe Gorce, France  
Sophia Z. Gu, Australia  
Vincenzo Guarino, Italy  
Valentina Hartwig, Italy

Andreas H. Hielscher, USA  
Norio Iriguchi, Japan  
Zhongwei Jiang, Japan  
Rashed Karim, UK  
Pasi A. Karjalainen, Finland  
John S. Katsanis, Greece  
Terry K.K. Koo, USA  
Panagiotis Kosmas, UK  
Michel Labrosse, Canada  
Jui-Yang Lai, Taiwan  
Xiang Li, USA  
Feng-Huei Lin, Taiwan  
Yuan-Pin Lin, Taiwan  
Maria Lindén, Sweden  
Dongfei Liu, Finland  
Francisco Lopez-Valdes, Spain  
Zufu Lu, Australia  
Andreas Maier, Germany  
Mehran Moazen, UK  
Rafael Morales, Spain  
David Moratal, Spain  
Angkoon Phinyomark, Canada  
Vincenzo Positano, Italy

Alessandro Reali, Italy  
Lei Ren, UK  
Jose Joaquin Rieta, Spain  
Emanuele Rizzuto, Italy  
Sébastien Roth, France  
Hélder A. Santos, Finland  
Emiliano Schena, Italy  
Maurizio Schmid, Italy  
Jiann-Shing Shieh, Taiwan  
Tiago H. Silva, Portugal  
Jinshan Tang, USA  
Vinoy Thomas, USA  
Ioannis G. Tollis, Greece  
Uche Wejinya, USA  
Damon W.K. Wong, Singapore  
Ying Yang, UK  
Ping Yu, Australia  
Haihong Zhang, Singapore  
Hongbo Zhang, Finland  
Ping Zhou, USA  
Loredana Zollo, Italy

# Contents

## **Medical Signal Processing in Biomedical and Clinical Applications**

Kunal Pal , Kunal Mitra, Arindam Bit , Saugat Bhattacharyya, and Anilesh Dey  
Editorial (2 pages), Article ID 3932471, Volume 2018 (2018)

## **A Review on the Nonlinear Dynamical System Analysis of Electrocardiogram Signal**

Suraj K. Nayak , Arindam Bit , Anilesh Dey , Biswajit Mohapatra, and Kunal Pal   
Review Article (19 pages), Article ID 6920420, Volume 2018 (2018)

## **Detection of Heart Rate through a Wall Using UWB Impulse Radar**

Hui-Sup Cho  and Young-Jin Park  
Research Article (7 pages), Article ID 4832605, Volume 2018 (2018)

## **Identification of Cerebral Artery Stenosis Using Bilateral Photoplethysmography**

Hyun Goo Kang, Seogki Lee, Han Uk Ryu, and Youngsuk Shin   
Research Article (9 pages), Article ID 3253519, Volume 2018 (2018)

## **sEMG Signal Acquisition Strategy towards Hand FES Control**

Cinthyia Lourdes Toledo-Peral, Josefina Gutiérrez-Martínez , Jorge Airy Mercado-Gutiérrez,  
Ana Isabel Martín-Vignon-Whaley, Arturo Vera-Hernández , and Lorenzo Leija-Salas  
Research Article (11 pages), Article ID 2350834, Volume 2018 (2018)

## **Improved Multiscale Entropy Technique with Nearest-Neighbor Moving-Average Kernel for Nonlinear and Nonstationary Short-Time Biomedical Signal Analysis**

S. P. Arunachalam , S. Kapa, S. K. Mulpuru, P. A. Friedman, and E. G. Tolkacheva   
Research Article (13 pages), Article ID 8632436, Volume 2018 (2018)

## **Dynamic Analysis of the Abnormal Isometric Strength Movement Pattern between Shoulder and Elbow Joint in Patients with Hemiplegia**

Yali Liu , Yuezhen Hong , and Linhong Ji   
Research Article (7 pages), Article ID 1817485, Volume 2018 (2018)

## **Enhancement of the Comb Filtering Selectivity Using Iterative Moving Average for Periodic Waveform and Harmonic Elimination**

José L. Ferreira , Yan Wu, and Ronald M. Aarts  
Research Article (14 pages), Article ID 7901502, Volume 2018 (2018)

## **A Predictive Model to Classify Undifferentiated Fever Cases Based on Twenty-Four-Hour Continuous Tympanic Temperature Recording**

Pradeepa H. Dakappa, Keerthana Prasad, Sathish B. Rao, Ganaraja Bolumbu, Gopalkrishna K. Bhat,  
and Chakrapani Mahabala  
Research Article (6 pages), Article ID 5707162, Volume 2017 (2018)

## **Combination of Deep Recurrent Neural Networks and Conditional Random Fields for Extracting Adverse Drug Reactions from User Reviews**

Elena Tutubalina and Sergey Nikolenko  
Research Article (9 pages), Article ID 9451342, Volume 2017 (2018)



---

**A Method for Assessing the Retention of Trace Elements in Human Body Using Neural Network Technology**

Yulia Tunakova, Svetlana Novikova, Aligejdar Ragimov, Rashat Faizullin, and Vsevolod Valiev  
Research Article (7 pages), Article ID 3471616, Volume 2017 (2018)

## Editorial

# Medical Signal Processing in Biomedical and Clinical Applications

**Kunal Pal** <sup>1</sup>, **Kunal Mitra**,<sup>2</sup> **Arindam Bit** <sup>3</sup>, **Saugat Bhattacharyya**,<sup>4</sup> and **Anilesh Dey**<sup>5</sup>

<sup>1</sup>*Department of Biotechnology and Medical Engineering, National Institute of Technology, Rourkela, India*

<sup>2</sup>*Department of Biomedical Engineering, Florida Institute of Technology, Melbourne, FL, USA*

<sup>3</sup>*Department of Biomedical Engineering, National Institute of Technology, Raipur, India*

<sup>4</sup>*School of Computer Science and Electronic Engineering, University of Essex, Colchester, UK*

<sup>5</sup>*Department of Electronics and Communication Engineering, Kaziranga University, Jorhat, India*

Correspondence should be addressed to Kunal Pal; [kpal.nitrkl@gmail.com](mailto:kpal.nitrkl@gmail.com)

Received 18 March 2018; Accepted 18 March 2018; Published 12 June 2018

Copyright © 2018 Kunal Pal et al. This is an open access article distributed under the Creative Commons Attribution License, which permits unrestricted use, distribution, and reproduction in any medium, provided the original work is properly cited.

Biological signals are the reflection of accumulated action potentials of subdermal tissues of a living being. Its presence signifies the ionic and electrical activities of the muscular and the neural cells in a synchronized manner. Being a mosaic model of a living architecture, the resultant vectors of biological signals have temporal as well as spatial representation. These signals are stochastic in nature. Medical diagnostic tools are prevalent using the support of medical signals. In the course of time, a significant amount of progress has been achieved in the field of medical signal processing for the improvement of the signal-to-noise ratio, extraction of features from those filtered signals, and classification of the extracted signals for clinical applications. This special issue emphasized the recent development of medical signal processing, improvement of algorithms, and wider clinical applications. Entropy-based kernel extraction technique is being used for the analysis of the nonlinear and nonstationary epoch signals. This kind of approach shows robustness in noise reduction. Machine learning algorithms are also being used for real-time feature extraction (pattern extraction) from tympanic temperature profiles. Quadratic support vector machine algorithms were also found to enhance the accuracy of the detection mechanism.

Regulation of rehabilitation devices and protocols are also governed by the processing of medical signals. Reference techniques are often used for acquiring surface EMG signals for the activation of the rehabilitation actuators. Consecutive placement of stimulator-detector arrays influences the spatial acquisition of the functional electrical stimulus (FES) and

volitional sEMG which can be used for controlling EMG-driven FES neuroprosthesis. Dynamic models are also being used for analyzing and detecting features from sEMG of deltoid muscles, present in the upper arm. The analysis of the signals can be used for the evaluation of the differently abled persons to predict the treatment outcomes. Health monitoring can also be achieved by processing of time-domain biological signals of sub-nanosecond durations. It can even help in predicting the state of the human heart by correlating the activity of the heart muscles and the blood pumping process.

Deep recurrent neural networks are also found to be useful tools for predicting features related to the adverse effect of drugs on the human body. In addition to this technique, conditional random fields are also implemented by many researchers for identifying the biological signals from significantly highly correlated background noise due to the subsequent physiological modification after the introduction of the foreign particles within the body. Similarly, the assessment of the trace elements in the human body can also be achieved by extracting features of the biological signals and biomarkers, and subsequently analyzing the features. A neural network can play an important role towards the identification of the continuously adaptable trace elements within the physiological fluids.

Biomedical signaling has significant outreach in its clinical application domain. Cerebral arterial stenoses can also be predicted by a nonradioactive technique, namely, photoplethysmography. It involves the employment of an

optical detection technique, which is a wavelength-specific process. Corresponding photodetectors are being used to measure the wavelength of the reflected light. Cerebral disorder can also be detected from EEG-fMRI recordings. It involves a rigorous filtering process, which employs a comb filter, followed by a moving-averaged filter for the elimination of the random noises.

In this special issue, all the above topics are discussed with their recent state of the art and their corresponding clinical applications.

*Kunal Pal*  
*Kunal Mitra*  
*Arindam Bit*  
*Saugat Bhattacharyya*  
*Anilesh Dey*

## Review Article

# A Review on the Nonlinear Dynamical System Analysis of Electrocardiogram Signal

Suraj K. Nayak <sup>1</sup>, Arindam Bit <sup>2</sup>, Anilesh Dey <sup>3</sup>, Biswajit Mohapatra,<sup>4</sup> and Kunal Pal <sup>1</sup>

<sup>1</sup>Department of Biotechnology and Medical Engineering, National Institute of Technology, Rourkela, Odisha 769008, India

<sup>2</sup>Department of Biomedical Engineering, National Institute of Technology, Raipur, Chhattisgarh 492010, India

<sup>3</sup>Department of Electronics and Communication Engineering, Kaziranga University, Jorhat, Assam 785006, India

<sup>4</sup>Vesaj Patel Hospital, Rourkela, Odisha 769004, India

Correspondence should be addressed to Kunal Pal; [kpal.nitrkl@gmail.com](mailto:kpal.nitrkl@gmail.com)

Received 17 October 2017; Revised 13 January 2018; Accepted 27 February 2018; Published 2 May 2018

Academic Editor: Maria Lindén

Copyright © 2018 Suraj K. Nayak et al. This is an open access article distributed under the Creative Commons Attribution License, which permits unrestricted use, distribution, and reproduction in any medium, provided the original work is properly cited.

Electrocardiogram (ECG) signal analysis has received special attention of the researchers in the recent past because of its ability to divulge crucial information about the electrophysiology of the heart and the autonomic nervous system activity in a noninvasive manner. Analysis of the ECG signals has been explored using both linear and nonlinear methods. However, the nonlinear methods of ECG signal analysis are gaining popularity because of their robustness in feature extraction and classification. The current study presents a review of the nonlinear signal analysis methods, namely, reconstructed phase space analysis, Lyapunov exponents, correlation dimension, detrended fluctuation analysis (DFA), recurrence plot, Poincaré plot, approximate entropy, and sample entropy along with their recent applications in the ECG signal analysis.

## 1. Introduction

In the last few decades, the ECG signals have been widely analyzed for the diagnosis of the numerous cardiovascular diseases [1, 2]. Apart from this, the ECG signals are processed to extract the RR intervals, which have been reported to divulge information about the influence of the autonomic nervous system activity on the heart through heart rate variability (HRV) analysis [3, 4]. HRV refers to the study of the variation in the time interval between consecutive heart beats and the instantaneous heart rate [5]. An important step in the analysis of the ECG signals is the extraction of the clinically relevant features containing all the relevant information of the original ECG signal and, hence, can act as the representative of the signal for further analysis [6, 7]. Features can be extracted from the ECG signals using the time-domain, frequency-domain, and joint time-frequency domain analysis methods including the nonlinear methods [7–9]. The analysis of the ECG signals using the nonlinear signal analysis

methods has received special attention of the researchers in recent years [7–9]. The nonlinear methods of the ECG signal analysis derive their motivation from the concept of nonlinear dynamics [10, 11]. This may be attributed to the fact that the biomedical signals like ECG can be generated by the nonlinear dynamical systems [12]. A dynamical system is a system that changes over time [9]. However, a dynamical system may also be defined as an iterative physical system, which undergoes evolution over time in such a way that the future states of the system can be predicted using the preceding states [13]. Dynamical systems form the basis of the nonlinear methods of the signal analysis [14]. The highly explored nonlinear signal analysis methods include reconstructed phase space analysis, Lyapunov exponents, correlation dimension, detrended fluctuation analysis (DFA), recurrence plot, Poincaré plot, approximate entropy, and sample entropy. This study attempts to provide a theoretical background of the above-mentioned nonlinear methods and their recent applications (last 5 years) in the analysis of the

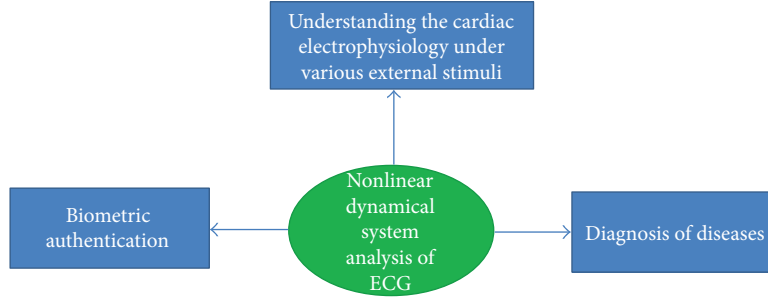


FIGURE 1: Various types of application of nonlinear dynamical system analysis of ECG.

ECG signal for the diagnosis of diseases, understanding the effect of external stimuli (e.g., low-frequency noise and music), and human biometric authentication (Figure 1).

## 2. Dynamical System

Dynamical systems form the basis of the nonlinear methods of signal analysis [15–17]. The study of the dynamical systems has found applications in a number of fields like physics [15–17], engineering [15], biology, and medicine [16]. A dynamical system can be defined as a system, whose state can be described by a set of time-varying (continuous or discrete) variables governed by the mathematical laws [17]. Such a system is said to be deterministic if the current values of time and the state variables can exactly describe the state of the system at the next instant of time. On the other hand, the dynamical system is regarded as stochastic, if the current values of time and the state variables describe only the probability of variation in the values of the state variables over time [18–20]. Dynamical systems can also be categorized either as linear or nonlinear systems. A system is regarded as linear when the change in one of its variable is proportional to the alteration in a related variable. Otherwise, it is regarded as nonlinear [18]. The main difference between the linear and the nonlinear systems is that the linear systems are easier to analyze. This can be attributed to the fact that the linear systems, unlike the nonlinear systems, facilitate the breaking down of the system into parts, performing analysis of the individual parts, and finally recombining the parts to obtain the solution of the system [21]. A set of coupled first-order autonomous differential equations ((1)) is used to mathematically describe the evolution of a continuous time dynamical system [22].

$$\frac{d\bar{\mathbf{x}}(\mathbf{t})}{dt} = \bar{\mathbf{F}}(\bar{\mathbf{x}}(\mathbf{t}), \bar{\boldsymbol{\mu}}), \quad (1)$$

where  $\bar{\mathbf{x}}(\mathbf{t})$  = vector representing the dynamical variables of the system,  $\bar{\boldsymbol{\mu}}$  = vector corresponding to the parameters, and  $\bar{\mathbf{F}}$  = vector field whose components are the dynamical rules governing the nature of the dynamical variables.

A system involving any nonautonomous differential equation in  $\mathbb{R}^n$  can be transformed into an autonomous differential equation in  $\mathbb{R}^{n+1}$  [23]. The forced Duffing-Van der Pol oscillator has been regarded as a well-known example

of a nonlinear dynamical system, which is described by a second-order nonautonomous differential equation [14, 23].

$$\frac{d^2y}{dt^2} - \mu(1 - y^2) \frac{dy}{dt} + y^3 = f \cos wt, \quad (2)$$

where  $\mu$ ,  $f$ , and  $w$  represent the parameters.

This nonautonomous differential equation can be converted into a set of coupled first-order autonomous differential equations (3), (4), and (5) by delineating 3 dynamical variables, that is,  $x_1 = y$ ,  $x_2 = dy/dt$ , and  $x_3 = wt$  [23].

$$\frac{dx_1}{dt} = x_2, \quad (3)$$

$$\frac{dx_2}{dt} = \mu(1 - x_1^2)x_2 - x_1^3 + f \cos x_3, \quad (4)$$

$$\frac{dx_3}{dt} = w. \quad (5)$$

The discrete time dynamical systems are described by a set of coupled first-order autonomous difference equations [14, 23, 24].

$$\bar{\mathbf{x}}(n+1)(n+1) = \bar{\mathbf{G}}(\bar{\mathbf{x}}(n), \bar{\boldsymbol{\mu}}), \quad (6)$$

where  $\bar{\mathbf{G}}$  = vector describing the dynamical rules and  $n$  = integer representing time.

It is possible to obtain a discrete dynamical system from a continuous dynamical system through the sampling of its solution at a regular time interval  $T$ , in which the dynamical rule representing the relationship between the consecutive sampled values of the dynamical variables is regarded as a *time T map*. The sampling of the solution of a continuous dynamical system in the  $\mathbb{R}^n$  dimensional space at the consecutive transverse intersections with a  $\mathbb{R}^{n-1}$  dimensional surface of the section also results in the formation of a discrete dynamical system. In this case, the dynamical rule representing the relationship between the consecutive sampled values of the dynamical variables is regarded as a *Poincaré map* or a *first return map*. For the forced Duffing-Van der Pol oscillator, the *Poincaré map* is equivalent to the *time T map* with  $T = 2\pi/w$  when a surface of section is defined by  $x_3 = \theta_0$  with  $\theta_0 \in (0, 2\pi)$  [14, 22, 23].

Generally, randomness is considered to be associated with noise (unwanted external disturbances like power line interference). However, it has been well reported in the last

few decades that most of the dynamical systems are deterministic nonlinear in nature and their solutions can be statistically random as that of the outcomes of tossing an unbiased coin (i.e., head or tail) [23]. This statistical randomness is regarded as deterministic chaos, and it allows the development of models for characterizing the systems producing the random signals.

As per the reported literature, the random signals produced by noise fundamentally differ from the random signals produced from the deterministic dynamical systems with a small number of dynamical variables [25]. The differences between them cannot be analyzed using the statistical methods. Phase space reconstruction-based dynamical system analysis has been recommended by the researchers for this purpose [12].

### 3. Nonlinear Dynamical System Analysis Techniques

**3.1. Reconstructed Phase Space Analysis of a Dynamical System.** The phase space is an abstract multidimensional space, which is used to graphically represent all the possible states of a dynamical system [23]. The dimension of the phase space is the number of variables required to completely describe the state of the system [19, 26]. Its axes depict the values of the dynamical variables of the system [26]. If the actual number of variables governing the behaviour of the dynamical system is unknown, then the phase space plots are reconstructed by time-delayed embedding, which is based on the concept of Taken's theorem [19]. The theorem states that if the dynamics of a system is governed by a number of interdependent variables (i.e., its dynamics is multidimensional), and only one variable of the system, say,  $x$ , is accessible (i.e., only one dimension can be measured), then it is possible to reconstruct the complete dynamics of the system from the single observed variable  $x$  by plotting its values against itself for a certain number of times at a predefined time delay [27]. Fang et al. [28] have reported that the reconstructed phase spaces can be regarded as topologically equivalent to the original system and, hence, can recover the nonlinear dynamics of the system.

Let us consider that all the values of the observed variable  $x$  is represented by the vector  $\bar{x}$ .

$$\bar{x} = (x_1, x_2, x_3, \dots, x_n), \quad (7)$$

where  $n$  = number of points in the time series.

If  $d$  is the true/estimated embedding dimension of the system (i.e., number of variables governing the dynamics of the system), then each state of the system can be represented in the phase space by the  $d$ -dimensional vectors of the form  $\bar{v}_i$  given as follows:

$$\bar{v}_i = (x_1, x_{1+\tau}, x_{1+2\tau}, \dots, x_{1+(d-1)\tau}), \quad (8)$$

where  $\tau$  = time lag, and  $1 \leq i \leq n - (d - 1)\tau$ .

A total of  $n - (d - 1)\tau$  number of such vectors are obtained, which can be arranged in a matrix  $\mathbf{V}$  (9) [26, 27].

In matrix  $\mathbf{V}$ , the row indices signify time, and the column indices refer to a dimension of the phase space.

This set of vectors forms the entire reconstructed phase space [12, 26].

$$\mathbf{V} = \begin{bmatrix} \bar{v}_1 \\ \bar{v}_2 \\ \vdots \\ \bar{v}_{n-(d-1)\tau} \end{bmatrix} = \begin{bmatrix} x_1 & x_{1+\tau} & \cdots & x_{1+(d-1)\tau} \\ x_2 & x_{2+\tau} & \cdots & x_{2+(d-1)\tau} \\ \vdots & \vdots & \ddots & \vdots \\ x_{n-(d-1)\tau} & x_{n-(d-2)\tau} & \cdots & x_n \end{bmatrix}, \quad (9)$$

where the rows correspond to the  $d$ -dimensional phase space vectors and the columns represent the time-delayed versions of the initial  $n - (d - 1)\tau$  points of the vector  $\bar{x}$ .

The two factors, namely, embedding dimension ( $d$ ) and time delay ( $\tau$ ) play an important role during the reconstruction of the phase space of a dynamical system [29, 30]. The embedding dimension is determined using either the method of false nearest neighbours [12] or Cao's method [29] or empirically [30]. The false nearest neighbour method has been regarded as the most popular method for the determination of the optimal embedding dimension [31]. This method is based on the principle that the pair of points which are located very near to each other at the optimal embedding dimension  $m$  will remain close to each other as the dimension  $m$  increases further. Nevertheless, if  $m$  is small, then the points located far apart may appear to be neighbours due to projecting into a lower dimensional space. In this method, the neighbours are checked at increasing embedding dimensions until a negligible number of false neighbours are found while moving from dimension  $m$  to  $m + 1$ . This resulting dimension  $m$  is considered as the optimal embedding dimension.

The time delay is usually determined using either the first minimum of the average mutual information function (AMIF) [32] or first zero crossing of the autocorrelation function (ACF) [33] or empirically. The implementation of ACF is computationally convenient and does not require a large data set. However, it has been reported that the use of ACF is not appropriate for nonlinear systems, and hence AMIF should be used for the computation of the optimal time delay [34, 35]. For the discrete time signals, the AMIF can be defined as follows [36]:

$$\text{AMI}(X, Y) = \sum_{i=1}^M \sum_{j=1}^N P_{XY}(x_i, y_j) \log \frac{P_{XY}(x_i, y_j)}{P_X(x_i)P_Y(y_j)}, \quad (10)$$

where  $X = \{x_i\}$  and  $Y = \{y_j\}$  are discrete time variables,  $P_X(x_i)$  is the probability of occurrence of  $X$ ,  $P_Y(y_j)$  is the probability of occurrence of  $Y$ , and  $P_{XY}(x_i, y_j)$  is the probability of occurrence of both  $X$  and  $Y$ .

Let us consider an RR interval (RRI) time series extracted from the 5 min ECG recording of a person (Indian male volunteer of 27 years old) consuming cannabis (Figure 2). The ECG signal was acquired using the commercially available single lead ECG sensor (Vernier Software & Technology,

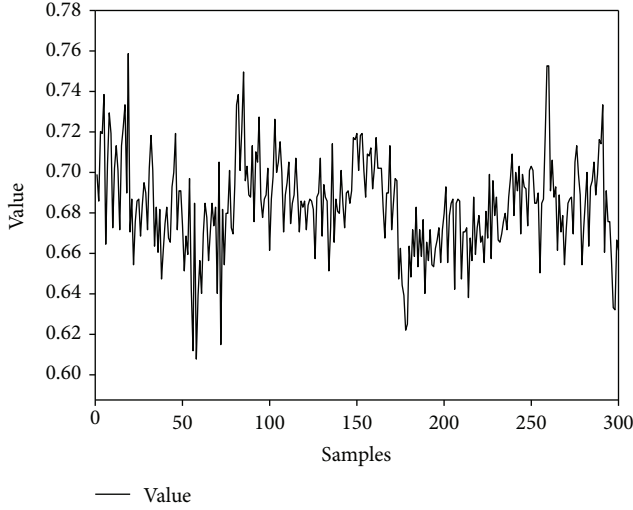


FIGURE 2: A representative RRI time series obtained from a 5 min ECG signal.

USA) and stored into a laptop using a data acquisition device (NI USB 6009, National Instruments, USA). The sampling rate of the device was set at 1000 Hz. The RRI time series was extracted from the acquired ECG signal using Biomedical Workbench toolkit of LabVIEW (National Instruments, USA). The determination of the optimal value of the embedding dimension for this RRI time series by the method of false nearest neighbours is shown in Figure 3. The determination of the proper value of the time delay (by the first minimum of the AMIF) for the above-mentioned RRI time series has been shown in Figure 4.

Each point in the reconstructed phase space of a system describes a potential state of the system. The system starts evolving from any point in the phase space (regarded as the initial state/condition of the system), following the dynamic trajectory determined by the equations of the system [19]. A dynamic trajectory describes the rate of change of the system's state with time. All the possible trajectories, for a given initial condition, form the flow of the system. Each trajectory occupies a subregion of the phase space, called as an attractor. An attractor can also be defined as a set of points (indicating the steady states) in the phase space, through which the system migrates over time [38]. The 3D attractor of the RRI time series (represented in Figure 2) has been shown in Figure 5.

Each attractor is associated with a basin of attraction, which represents all the initial states/conditions of the system that can go to that particular attractor [38]. Attractors can be points, curves, manifolds, or complicated objects, known as strange attractors. A strange attractor is an attractor having a noninteger dimension.

**3.2. Lyapunov Exponents.** The nonlinear dynamical systems are highly sensitive to the initial conditions, that is, a small change in the state variables at an instant will cause a large change in the behaviour of the system at a future instant of time. This is visualized in the reconstructed phase space as the adjacent trajectories that diverge widely from the initial close positions or converge. Lyapunov exponents are a

quantitative measure of the average rate of this divergence or convergence [40]. They provide an estimation of the duration for which the behaviour of a system is predictable before chaotic behaviour prevails [9]. Positive Lyapunov exponent values indicate that the phase space trajectories are diverging (i.e., the closely located points in the initial state are rapidly separating from each other in the  $i$ th direction) and the system is losing its predictability, exhibiting chaotic behaviour [41, 42]. On the other hand, the negative Lyapunov exponent values are representatives of the average rate of the convergence of the phase space trajectories. For example, in a three-dimensional system, the three Lyapunov exponents provide information about the evolution of the volume of a cube and their sum specifies how a hypercube evolves in a multidimensional attractor. The sum of the positive Lyapunov exponents represents the rate of spreading of the hypercube, which in turn, indicates the increase in unpredictability per unit time. The largest positive (dominant) Lyapunov exponent mainly governs its dynamics [43].

If  $\|\delta x_i(0)\|$  and  $\|\delta x_i(t)\|$  represent the Euclidean distance between two neighbouring points of the phase space in the  $i$ th direction at the time instances of 0 and  $t$ , respectively, then, the Lyapunov exponent can be defined as the average growth  $\lambda_i$  of the initial distance  $\|\delta x_i(0)\|$  [23, 44].

$$\frac{\|\delta x_i(t)\|}{\|\delta x_i(0)\|} = e^{\lambda_i t} (t \rightarrow \infty), \quad (11)$$

$$\text{or } \lambda_i = \lim_{t \rightarrow \infty} \frac{1}{t} \log \frac{\|\delta x_i(t)\|}{\|\delta x_i(0)\|},$$

where  $\lambda_i$  is the average growth of the initial distance  $\|\delta x_i(0)\|$ .

The dimensionality of the dynamical system decides the number of Lyapunov exponents, that is, if the system is defined in  $R^m$ , then it possesses  $m$  Lyapunov exponents ( $\lambda_1 \geq \lambda_2 \geq \dots, \lambda_m$ ). The complete set of Lyapunov exponents can be described by considering an extremely small sphere of initial conditions having  $m$  dimensions, which is fastened to a reference phase space trajectory. If  $P_i(t)$  represents the length of the  $i$ th axis, and the axes are arranged in the order of the fastest to the slowest growing axes, then 12 denotes the complete set of Lyapunov exponents arranged in the order of the largest to the smallest exponent [23].

$$\lambda_i = \lim_{t \rightarrow \infty} \frac{1}{t} \log \left( \frac{P_i(t)}{P_i(0)} \right), \quad (12)$$

where  $i = 1, 2, \dots, m$ .

The divergence of the vector field of a dynamical system is identical to the sum of all its Lyapunov exponents (13). Hence, the sum of all the Lyapunov exponents is negative in case of the dissipative systems. Also, one of the Lyapunov exponents is zero for the bounded trajectories, which do not approach a fixed point.

$$\sum_{i=1}^m \lambda = \bar{\nabla} \cdot \bar{F}, \quad (13)$$

where  $\bar{F}$  represents the vector field of a dynamical system.

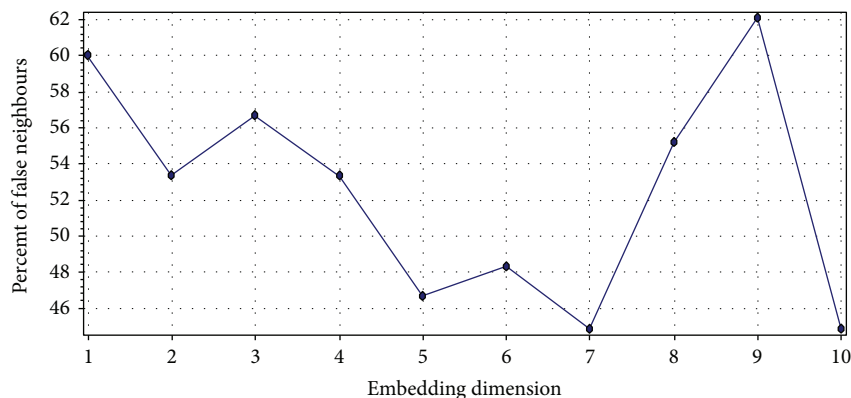


FIGURE 3: Computation of the optimal embedding dimension by the method of false nearest neighbours. The optimal embedding dimension was 7, and the corresponding percent false neighbour was 44.83%. The method of false nearest neighbour was implemented using Visual Recurrence Analysis freeware (V4.9, USA), developed by Kononov [37].

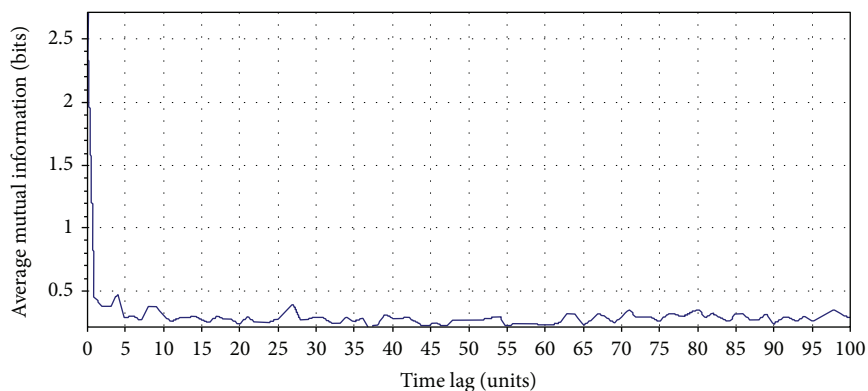


FIGURE 4: Optimal time delay computation by the first minimum of the AMIF. The first minimum of the AMIF was 2. The AMIF was calculated using Visual Recurrence Analysis freeware (V4.9, USA), developed by Kononov [37].

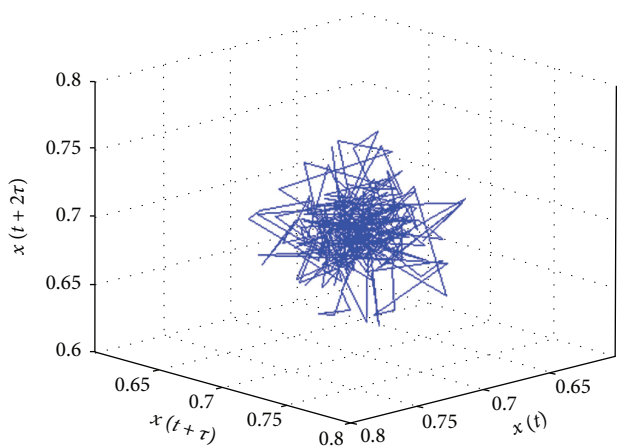


FIGURE 5: 3D phase space attractor of an RRI time series. The attractor was plotted using the MATLAB Toolbox developed by Yang [39].

Lyapunov exponents can be calculated from either the mathematical equations describing the dynamical systems (if known) or the observed time series [45]. Usually, two different types of methods are used for obtaining the Lyapunov

exponents from the observed signals. The first method is based on the concept of the time-evolution of nearby points in the phase space [46]. However, this method enables the evaluation of the largest Lyapunov exponent only. The other method is dependent on the computation of the local Jacobi matrices and estimates all the Lyapunov exponents [47]. All the Lyapunov exponents (in vector form) of a particular system constitute the Lyapunov spectra [45].

**3.3. Correlation Dimensions.** The geometrical objects possess a definite dimension. For example, a point, a line, and a surface have dimensions of 0, 1, and 2, respectively [9]. This notion has led to the development of the concept of fractal dimension. A fractal dimension refers to any noninteger dimension possessed by the set of points (representing a dynamical system) in a Euclidean space. The determination of the fractal dimension plays a significant role in the nonlinear dynamic analysis. This may be attributed to the fact that the strange attractors are fractal in nature and their fractal dimension indicates the minimum number of dynamical variables required to describe the dynamics of the strange attractors. It also quantitatively portrays the complexity of a nonlinear system. The higher is the dimension of the system; the more is the complexity. The commonly employed

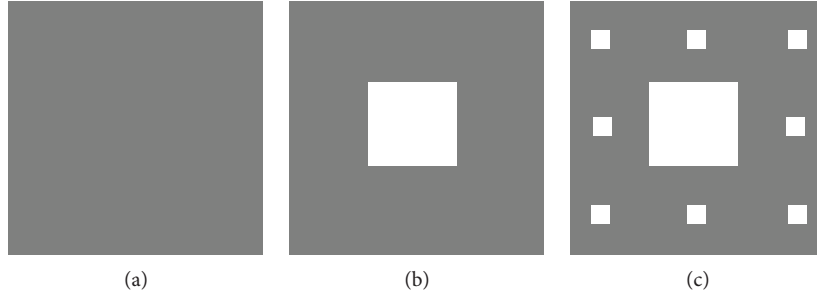


FIGURE 6: Illustration of the first 3 stages during the construction of a Cantor set in 2D: (a)  $n = 0$ , (b)  $n = 1$ , and (c)  $n = 2$  [48].

method for the determination of the dimension of a set is the measurement of the *Kolmogorov capacity* (i.e., box-counting dimension). This method covers the set with tiny cells/boxes (squares for sets embedded in 2D and cubes for sets embedded in 3D space) having size  $\epsilon$ . The dimension  $D$  can be defined as follows [23]:

$$D = \lim_{\epsilon \rightarrow 0} \frac{\log(M(\epsilon))}{\log(1/\epsilon)}, \quad (14)$$

where  $M(\epsilon)$  is the number of the tiny boxes containing a part of the set.

The mathematical example of a set possessing noninteger fractal dimension is a Cantor set. A Cantor set can be defined as the limiting set in a sequence of sets [48]. Let us consider a Cantor set in 2D, characterized by the below mentioned sequence of sets. At stage  $n = 0$  (Figure 6(a)), let  $S_0$  designate a square having sides of length  $l$ . The square  $S_0$  is divided into 9 uniform squares of size  $l/3$ , and the middle square is removed at stage  $n = 1$  (Figure 6(b)). This set of squares is regarded as  $S_1$ . At stage  $n = 2$ , each square of set  $S_1$  is further divided into 9 squares of size  $l/9$  and the middle squares are removed, which constitute the set  $S_2$  (Figure 6(c)). When this process of subdivision and removal of squares is continued to get the sequence of sets  $S_0, S_1$ , and  $S_2$ , then the Cantor set is the limiting set defined by  $S = \lim_{n \rightarrow \infty} S_n$ . The *Kolmogorov capacity*-based dimension of this Cantor set can be calculated easily using the principle of mathematical induction as described below. When  $n = 0$ ,  $S_0$  consists of a square of size  $l$ , and hence,  $\epsilon = l$  and  $M(\epsilon) = 1$ . When  $n = 1$ ,  $S_1$  comprises of 8 squares of size  $l/3$ . Therefore,  $\epsilon = l/3$  and  $M(\epsilon) = 8$ . At  $n = 2$ ,  $S_2$  is made of 64 squares of size  $l/9$ . Therefore,  $\epsilon = (l/3)^2$  and  $M(\epsilon) = 8^2$ . Thus, the fractal dimension of the Cantor set is given as follows:

$$D = \lim_{\epsilon \rightarrow 0} \frac{\log(M(\epsilon))}{\log(1/\epsilon)} = \lim_{n \rightarrow \infty} \frac{\log(8^n)}{\log(l/3^n)} = 1.892, \quad (15)$$

where the fractal dimension  $< 2$  suggests that the Cantor set does not completely fill an area in the 2D space.

However, the *Kolmogorov capacity*-based dimension measurement does not describe whether a box contains many points or few points of the set. To describe the inhomogeneities or correlations in the set, Hentschel and Procaccia defined the dimension spectrum [49].

$$D_q = \lim_{r \rightarrow 0} \frac{1}{q-1} \frac{\log \sum_{i=1}^{M(r)} P_i^q}{\log r}, \quad q = 0, 1, 2, \dots, \quad (16)$$

where  $M(r)$  = number of  $m$ -dimensional boxes of size  $r$  required to cover the set,  $p_i = N_i/N$  is the probability that the  $i$ th box contains a point of the set,  $N$  is the total number of points in the set, and  $N_i$  is the number of points of the set contained by the  $i$ th box.

It can be readily inferred that the *Kolmogorov capacity* is equivalent to  $D_0$ . The dimension  $D_1$  defined by taking the limit  $q \rightarrow 1$  in 16 is regarded as the information dimension.

$$D_1 = \lim_{q \rightarrow 1} D_q = \lim_{r \rightarrow 0} \frac{\sum_{i=1}^{M(r)} P_i \log P_i}{\log r}, \quad (17)$$

where the dimension  $D_2$  is the known as the correlation dimension.

The correlation dimension can be expressed as follows:

$$D_2 = \lim_{r \rightarrow 0} \frac{\log C(r)}{\log r}, \quad (18)$$

where  $C(r) = \sum_{i=1}^{M(r)} p_i^2$  is the correlation sum. It represents the probability of occurrence of two points of the set in a single box.

The correlation dimension signifies the number of the independent variables required to describe the dynamical system [50]. A widely used algorithm for the computation of the correlation dimension ( $D_2$ ) from a finite, discrete time series was introduced by Grassberger and Procaccia [51]. It was based on the assumption that the probability of occurrence of two points of the set in a box of size  $r$  is approximately same as the probability that the two points of the set are located at a distance  $\rho \leq r$ . Using this assumption, the correlation sum can be computed as given as follows:

$$C(r) \approx \frac{\sum_{i=1, j > i}^N \Theta(r - \rho(x_i, y_i))}{1/2N(N-1)}, \quad (19)$$

where  $\Theta$  is the Heaviside function and can be defined as

$$\Theta(u) = \begin{cases} 0, & \text{if } u \leq 0, \\ 1, & \text{if } u \geq 0. \end{cases} \quad (20)$$

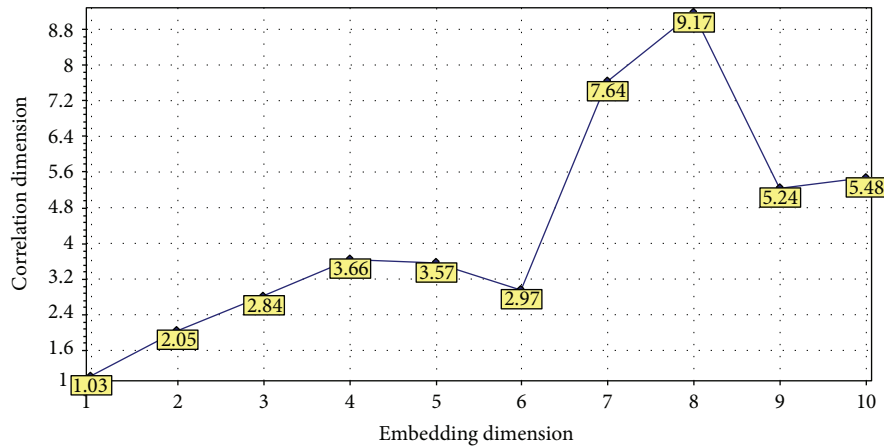


FIGURE 7: Correlation dimensions of the reconstructed phase space plot of RRI time series at different embedding dimensions. The correlation dimensions were calculated using Visual Recurrence Analysis freeware (V4.9, USA), developed by Kononov [37].

Practically, it is not possible to achieve the limit  $r \rightarrow 0$  that is used in the definition of the correlation dimension (18). Hence, Grassberger and Procaccia [51] proposed the approximate calculation of the correlation sum  $C(r)$  (19) for a number of values of  $r$  and then deducing the correlation dimension from the slope of the linear fitting in the linear region of the plot of  $\log(C(r))$  versus  $\log(r)$ . The correlation dimension of the reconstructed phase space plot of a dynamical system varies with its embedding dimension. The correlation dimensions of the reconstructed phase space plot of the aforementioned RRI time series at different embedding dimensions have been shown in Figure 7.

**3.4. Detrended Fluctuation Analysis (DFA).** The detection of long-range correlation of a nonstationary time series data requires the distinction between the trends and long-range fluctuations innate to the data. Trends are resulted due to external effects, for example, the seasonal alteration in the environmental temperature values, which exhibits a smooth and monotonous or gradually oscillating behaviour. Strong trends in the time series can cause the false discovery of long-range correlations in the time series if only one nondetrending technique is used for its analysis or if the outcomes of a method are misinterpreted. In recent years, DFA is explored for identifying long-range correlations (autocorrelations) of the nonstationary time series data (or the corresponding dynamical systems) [52]. This may be attributed to the ability of DFA to systematically eliminate the trends of different orders embedded into the data [52]. It provides an insight into the natural fluctuation of the data as well as into the trends in the data. DFA estimates the inherent fractal-type correlation characteristics of the dynamical systems, where the fractal behaviour corresponds to the scale invariance (or self-similarity) among the various scales [9]. The method of DFA was first proposed by Peng et al. [53] for the identification and the quantification of long-range correlations in DNA sequences. It was developed for detrending the variability in a sequence of events, which in turn, can divulge information about the long-term variations in the dataset. Since its inception, DFA has found

applications in the study of HRV [54], gait analysis [55, 56], stock market prediction [57, 58], meteorology [59], and geology [60–62]. DFA method has also been given alternative terminologies [61] by various researchers like “linear regression detrended scaled windowed variance” [63] and “residuals of regression” [64].

In order to implement DFA, the bounded time series  $x_t$  ( $t \in N$ ) is converted into an unbounded series  $X_t$  [65].

$$X_t = \sum_{i=1}^t (x_i - \langle x_i \rangle), \quad (21)$$

where  $X_t$  = cumulative sum and  $\langle x_i \rangle$  = mean of the time series  $x_t$  in the window  $t$ .

The unbounded time series  $X_t$  is then split into a number of portions of equal length  $n$ , and a straight line fitting is performed to the data using the method of least square fitting. The fluctuation (i.e., the root-mean-square variation) for every portion from the trend is calculated using [9]

$$F(n) = \sqrt{\frac{1}{n} \sum_{i=1}^n (X_i - a_i - b)^2}, \quad (22)$$

where  $a_i$  and  $b$  indicate the slope and intercept of the straight line fitting, respectively, and  $n$  is the split-unbounded time series portion length.

Finally, the log-log graph of  $F(n)$  versus  $n$  is drawn (Figure 8), where the statistical self-similarity of the signal is represented by the straight line on this graph, and the scaling exponent  $\alpha$  is obtained from the slope of the line. The self-similarity is indicated as  $F(n) \propto n^\alpha$ . The fluctuation exponent  $\alpha$  has different values for different types of data (e.g.,  $\alpha \sim 1/2$  for the uncorrelated white noise and  $\alpha > 1/2$  for the correlated processes) [66, 67].

**3.5. Recurrence Plot and Recurrence Quantification Analysis.** The dynamical features (e.g., entropy, information dimension, dimension spectrum, and Lyapunov exponents) of a time series can be computed using various methods [68]. However, most of these methods assume that the time series

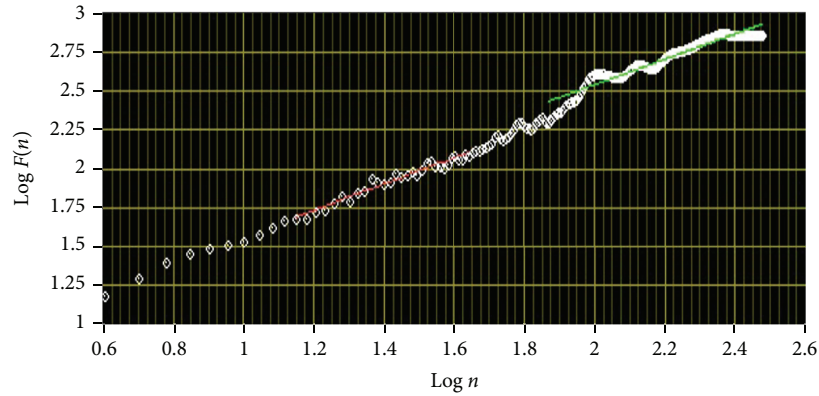


FIGURE 8: Log-log graph of  $F(n)$  versus  $n$  for RRI time series. The graph was plotted using Biomedical Workbench toolkit of LabVIEW (National Instruments, USA).

data is obtained from an autonomous dynamical system. In other words, the evolution equation of the time series data does not involve the time explicitly. Further, the time series data should be longer than the characteristic time of the underlying dynamical system. In this regard, the recurrence plot reported by Eckmann et al. [68] has emerged as an important method for the analysis of the dynamical systems and provides useful information even when the aforementioned assumptions are not satisfied. If  $\{\bar{x}_i\}_{i=1}^N$  represents the phase-space trajectory of a dynamical system in a  $d$ -dimensional space, then the recurrence plot can be defined as an array of points positioned at the places  $(i, j)$  in a  $N \times N$  square matrix (23) such that  $\bar{x}_j$  is approximately equal to  $\bar{x}_i$  as described by 24 [68–70].

$$\mathbf{R}_{i,j}(\varepsilon) = \begin{cases} 1, & x_i \approx x_j, \\ 0, & x_i \neq x_j, \end{cases} \quad (23)$$

$$i, j = 1, 2, \dots, N,$$

$$|\bar{x}_j - \bar{x}_i| \leq \varepsilon, \quad (24)$$

where  $\varepsilon$  = acceptable distance (error) between  $\bar{x}_i$  and  $\bar{x}_j$ . This  $\varepsilon$  is required because many systems often do not recur exactly to a previous state but just approximately.

Recurrence plot divulges natural time correlation information at times  $i$  and  $j$ . In other words, it evaluates the states of a system at times  $i$  and  $j$  and indicates the existence of similarity by placing a dot (corresponding to  $\mathbf{R}_{i,j} = 1$ ) in the recurrence plot. The recurrence plot of the RRI time series present in Figure 2 has been shown in Figure 9.

The main advantage of the recurrence plot is that it does not require any mathematical transformation or assumption [69]. But the drawback of this method lies in the fact that the information provided is qualitative. To overcome this limitation, several measures of complexity that quantify the small-scale structures in the recurrence plot have been proposed by many researchers, regarded as recurrence quantification analysis (RQA) [71]. These measures are derived from the recurrence point density as well as the diagonal and the vertical line structures of the recurrence plot. The calculation of

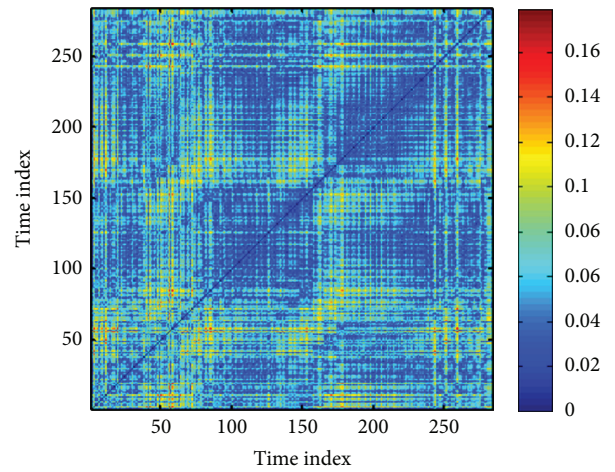


FIGURE 9: Recurrence plot of an RRI time series. The recurrence plot was generated using the MATLAB Toolbox developed by Yang [39].

these measures in small windows, passing along the line of identity (LOI) of the recurrence plot, provides information about the time-dependent behaviour of these variables. Several studies have reported that the RQA variables can detect the bifurcation points like the chaos-order transitions [72]. The vertical structures in the recurrence plot have been reported to represent the intermittency and the laminar states. The RQA variables, corresponding to the vertical structures, enable the detection of the chaos-chaos transition [71]. The following discussion introduces the RQA parameters along with their potentials in the identification of the changes in the recurrence plot.

- (i) Recurrence rate (RR) or percent recurrences: RR is the simplest variable of the RQA. It is a measure of the density of the recurrence points in the recurrence plot. Mathematically, it can be defined as 25, which is related to the correlation sum (19) except LOI, which is not included.

$$\text{RR}(\varepsilon) = \frac{1}{N^2} \sum_{i,j=1}^N \mathbf{R}_{i,j}(\varepsilon), \quad (25)$$

where  $\mathbf{R}_{ij}(\varepsilon)$  is the recurrence matrix and  $N$  is the length of the data series.

- (ii) Average number of neighbours: It is defined by 26 and represents the average number of neighbours possessed by each point of the trajectory in its  $\varepsilon$ -neighbourhood.

$$N_n(\varepsilon) = \frac{1}{N} \sum_{i,j=1}^N R_{ij}(\varepsilon), \quad (26)$$

where  $N_n$  is the number of (nearest) neighbours.

- (iii) Determinism: The recurrence plot comprises of diagonal lines. The uncorrelated, stochastic, or chaotic processes exhibit either no diagonal lines or very short diagonal lines. On the other hand, the deterministic processes are associated with longer diagonals and less number of isolated recurrence points. The ratio of the number of recurrence points forming diagonal structures (having length  $\geq l_{\min}$ ) to the total number of recurrence points is regarded as determinism (DET) or predictability of the system (27). The threshold  $l_{\min}$  is used to exclude the diagonal lines which are produced by the tangential motion of the phase space trajectory.

$$\text{DET} = \frac{\sum_{l=l_{\min}}^N lP(l)}{\sum_{l=1}^N lP(l)}, \quad (27)$$

where  $P(l) = \sum_{i,j=1}^N (1 - \mathbf{R}_{i-1,j-1}(\varepsilon))(1 - \mathbf{R}_{i+l,j+l}(\varepsilon)) \prod_{k=0}^{l-1} \mathbf{R}_{i+k,j+k}(\varepsilon)$  represents the histogram of diagonal lines of length  $l$ .

- (iv) Divergence: Divergence (DIV) is the inverse of the longest diagonal line appearing in the recurrence plot (28). It corresponds to the exponential divergence of the phase space trajectory, that is, when the divergence is more, the diagonal lines are shorter, and the trajectory diverges faster.

$$\text{DIV} = \frac{1}{L_{\max}} = \frac{1}{\max(\{l_i\}_{i=1}^{N_i})}, \quad (28)$$

where  $L_{\max}$  is the length of the longest diagonal line.

- (v) Entropy: Entropy (ENTR) is the Shannon entropy of the probability  $p(l)$  of finding a diagonal line of length  $l$  in the recurrence plot (29). It indicates the complexity of the recurrence plot in respect of the diagonal lines. For example, the uncorrelated noise possesses a small value of entropy, which suggests its low complexity.

$$\text{ENTR} = - \sum_{l=l_{\min}}^N p(l) \ln(p(l)), \quad (29)$$

where  $p(l)$  is the probability of finding a diagonal line of length  $l$ .

- (vi) RATIO: It is the ratio of the determinism and the recurrence rate (30). It has been reported to be useful for identifying the transitions in the dynamics of the system.

$$\text{RATIO} = N^2 \frac{\sum_{l=l_{\min}}^N lP(l)}{\left(\sum_{l=1}^N lP(l)\right)^2}, \quad (30)$$

where  $P(l)$  = number of diagonal lines of length  $l$ .

- (vii) Laminarity: Laminarity (LAM) is the ratio of the number of recurrence points forming vertical lines to the total number of recurrence points in the recurrence plot (31). LAM has been reported to provide information about the occurrence of the laminar states in the system. However, it does not describe the length of the laminar states. The value of LAM decreases if more number of single recurrence points are present in the recurrence plot than the vertical structures.

$$\text{LAM} = \frac{\sum_{v=v_{\min}}^N vP(v)}{\sum_{v=1}^N vP(v)}, \quad (31)$$

where  $P(v) = \sum_{i,j=1}^N (1 - \mathbf{R}_{i,j})(1 - \mathbf{R}_{i+j,v}) \prod_{k=0}^{v-1} \mathbf{R}_{i+j+k}$  is number of vertical lines of length  $v$ .

- (viii) Trapping time: Trapping time (TT) is an estimate of the average length of the vertical structures, defined by 32. It indicates the average time for which the system will abide by a specific state. The computation of TT requires the consideration of a minimum length  $v_{\min}$ .

$$\text{TT} = \frac{\sum_{v=v_{\min}}^N vP(v)}{\sum_{v=v_{\min}}^N P(v)}, \quad (32)$$

where  $v_{\min}$  is the predefined minimum length of a vertical length.

- (ix) Maximum length of the vertical lines: The maximum length of the vertical lines ( $V_{\max}$ ) in the recurrence plot can be defined as follows:

$$V_{\max} = \max(\{v_l\}_{l=1}^{N_v}), \quad (33)$$

where  $N_v$  is the absolute number of vertical lines.

**3.6. Poincaré Plot.** A Poincaré plot is a plot that enables the visualization of the evolution of a dynamical system in the phase space and is useful for the identification of the hidden patterns. It facilitates the reduction of dimensionality of the phase space and simultaneously converts the continuous time flow into a discrete time map [9]. The Poincaré plot varies from the recurrence plot in the sense that Poincaré

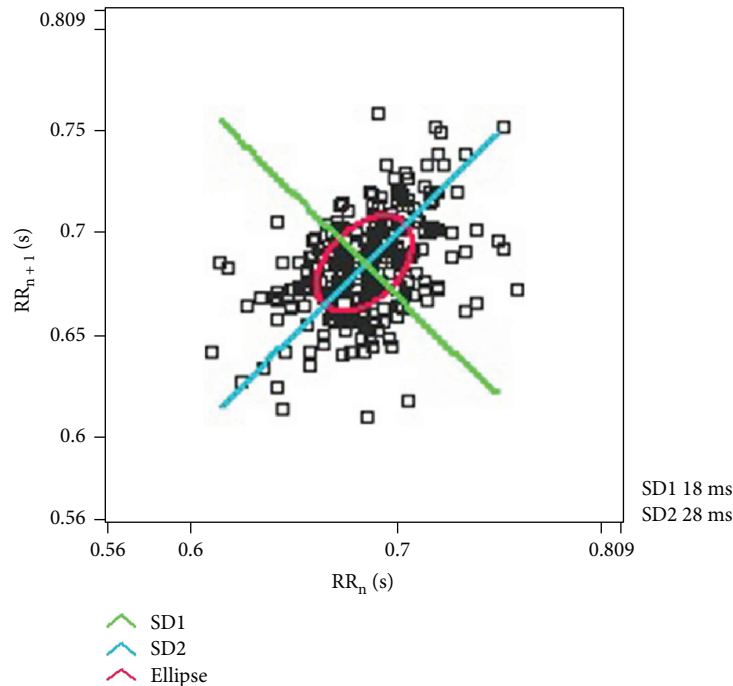


FIGURE 10: The Poincaré plot of the RRI time series represented in Figure 2. The plot was generated using Biomedical Workbench toolkit of LabVIEW (National Instruments, USA).

plot is defined in a phase space, whereas, the recurrence plot is created in the time space. In the recurrence plot, the points represent the instances when the dynamical system traverses approximately the same section of the phase space [9]. On the other hand, the Poincaré plot is generated by plotting the current value of the RR interval ( $RR_n$ ) against the RR interval value preceding it ( $RR_{n+1}$ ) [73, 74]. Hence, the Poincaré plot takes into account only the length of the RR intervals but not the amount of the RR intervals that occur [75]. The Poincaré plot is also named as scatter plot or scattergram, return map, and Lorentz plot [76]. The Poincaré plot of the aforementioned RRI time series has been shown in Figure 10.

Two important descriptors of the Poincaré plot are SD1 and SD2. SD1 refers to the standard deviation of the projection of the Poincaré plot on the line normal to the line of identity (i.e.,  $y = -x$ ), whereas, the projection on the line of identity (i.e.,  $y = x$ ) is regarded as SD2 [77]. The ratio of SD1 and SD2 is named as SD12. The Poincaré plot has been reported to divulge information about the cardiac autonomic activity [78, 79]. This can be attributed to the fact that SD1 provide information on the parasympathetic activity, whereas, SD2 is inversely related to sympathetic activity [80].

Apart from the above-mentioned dynamical system analysis methods, entropy-based measures such as approximate entropy (ApEn) and sample entropy (SaEn) have also been studied for the analysis of nonstationary signals [9]. These measures have been proposed to reduce the number of points required to obtain the dimension or entropy of low-dimensional chaotic systems and to quantify the changes in the process entropy. However, the methodological drawbacks of ApEn have been pointed out by Richman

and Moorman and Costa et al. [9, 81, 82]. SaEn has also suffered from criticism for not completely characterizing the complexity of the signal [9, 83].

#### 4. Applications of Nonlinear Dynamical System Analysis Methods in ECG Signal Analysis

*4.1. Applications of Phase Space Reconstruction in ECG Signal Analysis.* The phase space reconstruction has found a wide range of applications in the field of research, such as wind speed forecasting for wind farms [84], analyzing molecular dynamics of polymers [85], river flow prediction in urban area [86], and biosignal (such as ECG and EEG) analysis [28]. Among the applications related to biosignal analysis, many extensive studies have been performed for the analysis of ECG signals [87].

The different types of cardiac arrhythmias include ventricular tachycardia, atrial fibrillation, and ventricular fibrillation. Al-Fahoum and Qasaimieh [12] have reported the development of a simple ECG signal processing algorithm which employs reconstructed phase space for the classification of the different types of arrhythmia. The regions occupied by the ECG signals (belonging to the different types of arrhythmias) in the reconstructed phase space were used to extract the features for the classification of the arrhythmias. The authors reported the occurrence of 3 regions in the reconstructed phase space, which were representative of the concerned arrhythmias. Hence, 3 simple features were computed for the purpose of arrhythmia classification. The performance of the proposed algorithm was verified by classifying the datasets from the MIT database. The algorithm was able to achieve a sensitivity of 85.7–100%, a

TABLE 1: Recent studies performed for arrhythmia detection using phase space analysis of ECG.

| Types of arrhythmia   | Classification method  | Performance   | Ref. |
|---|--|---|------|
| Atrial fibrillation, ventricular tachycardia, and ventricular fibrillation  | Distribution of the attractor in the reconstructed phase space | 85.7–100% sensitivity, 86.7–100% specificity, and 95.55% overall efficiency | [12] |
| Ventricular tachycardia, ventricular fibrillation, and ventricular tachycardia followed by ventricular fibrillation                           | Box-counting in phase space diagrams                           | 96.88% sensitivity, 100% specificity, and 98.44% accuracy                   | [89] |
| Ventricular fibrillation and normal sinus rhythm  | Neural network with weighted fuzzy membership functions        | 79.12% sensitivity, 89.58% specificity, and 87.51% accuracy                 | [90] |
| Atrial premature contraction, premature ventricular contraction, normal sinus rhythm, left bundle branch block, and right bundle branch block | K-nearest neighbour  | 99.42% sensitivity, 98.19% specificity, and 98.7% accuracy                  | [88] |
| Soon-terminating atrial fibrillation and immediately terminating atrial fibrillation  | A genetic algorithm in combination with SVM                    | 100% sensitivity, 100% specificity, and 100% accuracy                       | [91] |

specificity of 86.7–100%, and an overall efficiency of 95.55%. Sayed et al. [88] have proposed the use of a novel distance series transform domain, which can be derived from the reconstructed phase space of the ECG signals, for the classification of the five types of arrhythmias. The transform space represents the manner in which the successive points of the original reconstructed phase space travel nearer or farther from the origin of the phase space. A combination of the raw distance series values and the parameters of the autoregressive (AR) model, the amplitude of the discrete Fourier transform (DFT), and the coefficients of the wavelet transform was used as the features for classification using K-nearest neighbour (K-NN) classifier. The authors have reported that the proposed method outperformed the state-of-the-art methods of classification with an extraordinary accuracy of 98.7%. The sensitivity and the specificity of the classifier were 99.42% and 98.19%, respectively. Based on the results, the authors suggested that their proposed method can be used for the classification of the ECG signals. The recent studies performed in the last 5 years for arrhythmia detection using phase space analysis of the ECG signals have been tabulated in Table 1.

Sleep apnoea is a kind of sleep disorder, where a distinct short-term cessation of breathing for >10sec is observed when the person is sleeping [92]. It can be categorized into 3 categories, namely, obstructive sleep apnoea, central sleep apnoea, and mixed sleep apnoea. Sleep apnoea results in symptoms like daytime sleeping, irritation, and poor concentration [93]. Jafari reported the extraction of the features from the reconstructed phase space of the ECG signals and the frequency components of the heart rate variability (HRV) (i.e., very low-frequency (VLF), low-frequency (LF), and high-frequency (HF) components) for the detection of the sleep apnoea [93]. The extracted features were subjected to SVM-based classification. For the sleep apnoea dataset provided by Physionet database, the proposed feature set exhibited a classification accuracy of 94.8%. Based on the results, the author concluded that the proposed method can help in improving the efficiency of sleep apnoea detection systems.

Syncope, also known as fainting, refers to the unanticipated and the temporary loss of consciousness [94]. This is due to the malfunctioning of the autonomic nervous system (ANS), which is responsible for the regulation of the heart rate and blood pressure [95]. Syncope is characterized by a reduction in blood pressure and bradycardia [95]. It is diagnosed using a medical procedure known as head-up tilt test (HUTT) that varies from 45 to 60 min [96]. Since the test has to be carried out for a long time, it is unsuitable for the physically weak patients as they cannot complete the test. Thus, methods have been proposed to reduce the duration of the test through the prediction of the HUTT results by analyzing cardiovascular signals (e.g., ECG and blood pressure) acquired during HUTT. Khodor et al. [96] proposed a novel phase space analysis algorithm for the detection of syncope. HUTT was carried out for 12 min, and the ECG signals were acquired simultaneously. RR intervals were extracted from the ECG signals, and the phase space plots were reconstructed. Features were extracted from the phase space plot (such as phase space density) and recurrence quantification analysis. Statistically significant parameters were determined using Mann–Whitney test, which were further used for the SVM-based classification. Sensitivity and specificity of 95% and 47% were achieved. In 2015, the same group further reported the acquisition of arterial blood pressure signal along with the ECG signal during the HUTT for the detection of syncope [95]. Features were derived from the phase space analysis of the acquired signals, and important predictors were identified using the relief method [97]. The K-NN-based classification was performed, and a sensitivity of 95% and a specificity of 87% were achieved. Based on the results, the authors suggested that a bivariate analysis may be performed instead of univariate analysis to predict the outcome of HUTT with improved performance.

In recent years, ECG is being widely explored as a biometric to secure body sensor networks, human identification, and verification [98]. As compared to the other biometrics, it provides the advantage that it has to be acquired from a living body. In many previous studies related to the ECG-based biometric, features extracted from the ECG signals were

amplitudes, durations, and areas of P, Q, R, S, and T waves [99–101]. However, the extraction of these features becomes difficult when the ECG gets contaminated by noise [102]. Wavelet analysis of the ECG signals was also attempted for the extraction of the ECG features for the identification of persons [103]. But, it required shifting of one ECG waveform with respect to the other for obtaining the best fit [104]. Recently, Fang and Chan proposed the development of an ECG biometric using the phase space analysis of the ECG signals [102]. The phase space plots were reconstructed from the 5 sec ECG signals, and the trajectories were condensed, single *course-grained* structure. The distinction between the *course-grained* structures was performed using the normalized spatial correlation (nSC), the mutual nearest point match (MNPM), and the mutual nearest point distance (MNPD) methods. The proposed strategy was tested on 100 volunteers using both single-lead and 3-lead ECG signals. The use of single-lead ECG signals resulted in the person identification accuracies of 96%, 95%, and 96% for MNPD, nSC, and MNPD methods, respectively, whereas, the accuracies increased up to 99%, 98%, and 98% for 3-lead ECG signals. Earlier, the same group had proposed the ECG biometric-based identification of humans by measuring the similarity or dissimilarity among the phase space portraits of the ECG signals [105]. In the experiment involving 100 volunteers, the person identification accuracies of 93% and 99% were achieved for single-lead and 3-lead ECG, respectively.

**4.2. Applications of Lyapunov Exponents in ECG Signal Analysis.** The concept of Lyapunov exponents has been employed to describe the dynamical characteristics of many biological nonlinear systems including cardiovascular systems. The versatility of the dominant Lyapunov exponents (DLEs) of the ECG signals was effectively applied by Valenza et al. [43] to characterize the nonlinear complexity of HRV in stipulated time intervals. The aforementioned study evaluated the HRV signal during emotional visual elicitation by using approximate entropy (ApEn) and dominant Lyapunov exponents (DLEs). A two-dimensional (valence and arousal) conceptualization of emotional mechanisms derived from the circumplex model of affects (CMAs) was adopted in this study. A distinguished switching mechanism was correlated between regular and chaotic dynamics when switching from neutral to arousal elicitation states [43]. Valenza et al. [106] reported the use of Lyapunov exponents to understand the instantaneous complex dynamics of the heart from the RR interval signals. The proposed method employed a high-order point-process nonlinear model for the analysis. The Volterra kernels (linear, quadratic, and cubic) were expanded using the orthonormal Laguerre basis functions. The instantaneous dominant Lyapunov exponents (IDLE) were estimated and tracked for the RRI time series. The results suggested that the proposed method was able to track the nonlinear dynamics of the autonomic nervous system-(ANS-) based control of the heart. Du et al. [107] reported the development of a novel Lyapunov exponent-based diagnostic method for the classification of premature ventricular contraction from other types of ECG beats.

HRV has been reported to be sensitive to both physiological and psychological disorders [108]. In recent years, HRV has been used as a tool in the diagnosis of the cardiac diseases. HRV is estimated by analyzing the RR intervals extracted from the ECG signals. The HRV analysis requires a sensitive tool, as the nature of the RR interval signal is chaotic and stochastic, and it remains very much controversial [108]. Researchers have proposed Lyapunov exponents as a means for improving the sensitivity of the HRV analysis. In earlier studies, Wolf et al. and Tayel and AlSaba had developed two algorithms for the estimation of the Lyapunov exponents [46, 108]. However, those methods were found to diverge while determining the HRV sensitivity. Recently, Tayel and AlSaba [108] proposed an algorithm known as Mazhar-Eslam algorithm that increases the sensitivity of the HRV analysis with improved accuracy. The accuracy was increased up to 14.34% as compared to Wolf's method. Ye and Huang [109] reported the estimation of Lyapunov exponents of the ECG signals for the development of an image encryption algorithm, which can provide security to images from all sorts of differential attacks. In the same year, Silva et al. [110] proposed the largest Lyapunov exponent-based analysis of the RR interval time series extracted from ECG signals for predicting the outcomes of HUTT.

**4.3. Applications of Correlation Dimension in ECG Signal Analysis.** The correlation dimension provides a measure of the amount of correlation contained in a signal. It has been used by a number of researchers for analyzing the ECG and the derived RRI time series in order to detect various pathological conditions [111, 112]. Bolea et al. proposed a methodological framework for the robust computation of correlation dimension of the RRI time series [113]. Chen et al. [114] used correlation dimension and Lyapunov exponents for the extraction of the features from the ECG signals for developing ECG-based biometric applications. The extracted ECG features could be classified with an accuracy of 97% using multilayer perceptron (MLP) neural networks [114]. Rawal et al. [115] proposed the analysis of the HRV during menstrual cycle using an adaptive correlation dimension method. In the conventional correlation dimension method, the time delay is calculated using the autocorrelation function, which does not provide the optimum time delay value. In the proposed method, the authors calculated the time delay using the information content of the RR interval signal. The proposed adaptive correlation dimension method was able to detect the HRV variations in 74 young women during the different stages of the menstrual cycle in the lying and the standing positions with a better accuracy than the conventional correlation dimension and the detrended fluctuation analysis methods. Lerma et al. [50] investigated the relationship between the abnormal ECG and the less complex HRV using correlation dimension. ECG signals (24 h Holter ECG signals as well as standard ECG signals) were acquired from 100 volunteers (university workers), among which 10 recordings were excluded due to the detection of >5% of false RR intervals. Examination of the rest 90 standard ECG signals by two cardiologists suggested 29 standard ECG signals to

be abnormal. Estimation of the correlation dimensions suggested that the abnormal ECG signals were associated with reduced HRV complexity. Moeynoi and Kitjaidure analyzed the dimensional reduction of sleep apnea features by using the canonical correlation analysis (CCA). The sleep apnea features were extracted from the single-lead ECG signals. The linear and nonlinear techniques to estimate the variance of heart rhythm and HRV from electrocardiography signal were applied to extract the corresponding features. This study reported a noninvasive way to evaluate sleep apnea and used CCA method to establish a relationship among the pair data sets. The classification of the extracted features derived from apnea annotation was comparatively better than the classical techniques [116].

**4.4. Applications of DFA in ECG Signal Analysis.** It is a well-reported fact that the exposure to the environmental noise can result in annoyance, anxiety, depression, and various psychiatric diseases [117, 118]. However, noise exposure has also been reported to cause cardiovascular problems [118]. Chen et al. [114] proposed the DFA of the RR intervals during exposure to low-frequency noise for 5 min to detect the changes in the cardiovascular activity [119]. From the results, it could be summarized that an exposure to the low-frequency noise might alter the temporal correlation of HRV, though there was no significant change in the mean blood pressure and the mean RR interval variability. Kamath et al. reported the implementation of DFA for the classification of congestive heart failure (CHF) disease [120]. Short-term ECG signals of 20 sec duration, from normal persons and CHF patients, were subjected analysis using DFA. The receiver operating characteristics (ROC) curve suggested the suitability of the proposed method with an average efficiency of 98.2%. Ghasemi et al. reported the DFA of RR interval time series to predict the mortality of the patients in intensive care units (ICUs) suffering from sepsis [121]. In the proposed study, DFA was performed on the RR interval time series of the last 25 h duration of the survived and non-survived patients, who were admitted to the ICUs. The results suggested that the scaling exponent ( $\alpha$ ) was significantly different for the survived and the nonsurvived patients from 9 h before the demise and can be used to predict the mortality. Chiang et al. tested the hypothesis that cardiac autonomic dysfunction estimated by DFA can also be a potential prognostic factor in patients affected by end-stage renal disease and undertaking peritoneal dialysis. Total mortality and increased cardiac varied significantly with a decrease in the corresponding prognostic predictor DFA $\alpha$ 1. DFA $\alpha$ 1 ( $\geq 95\%$ ) was related to lower cardiac mortality (hazard ratio (HR) 0.062, 95% CI=0.007–0.571,  $P = 0.014$ ) and total mortality [122].

**4.5. Applications of RQA in ECG Signal Analysis.** RQA has found many applications in ECG signal analysis [123–125]. Chen et al. investigated the effect of the exposure to low-frequency noise of different intensities (for 5 min) on the cardiovascular activities using recurrence plot analysis [126]. The RR intervals were extracted from the ECG signals acquired during the noise exposure of intensities 70 dBC,

80 dBC, and 90 dBC. The change in the cardiovascular activity was estimated using RQA of the RR intervals. Based on the results, the authors concluded that RQA-based parameters can be used as an effective tool for analyzing the effect of the low-frequency noise even with a short-term RR interval time series.

Acharya et al. reported the use of RQA and Kolmogorov complexity analysis of RRI time series for the automated prediction of sudden cardiac death (SCD) risk [127]. In this study, the authors designed a sudden cardiac death index (SCDI) using the RQA and the Kolmogorov complexity parameters for the prediction of SCD. The statistically important parameters were identified using  $t$ -test. These statistically important parameters were used as inputs for classification using K-NN, SVM, decision tree, and probabilistic neural network. The K-NN classifier was able to classify the normal and the SCD classes with 86.8% accuracy, 80% sensitivity, and 94.4% specificity. The probabilistic neural network also provided 86.8% accuracy, 85% sensitivity, and 88.8% specificity. Based on the results, the authors proposed that RQA and Kolmogorov complexity analysis can be performed for the efficient detection of SCD. Apart from these studies, the RQA of the ECG signals has been widely studied for the detection of different types of diseases. A few RQA-based studies performed in the last 5 years for the diagnosis of different clinical conditions have been summarized in Table 2.

**4.6. Applications of Poincaré Plot in ECG Signal Analysis.** Ventricular fibrillation has been reported to be the most severe type of cardiac arrhythmia [131]. It results from the cardiac impulses that have gone berserk within the ventricular muscle mass and is indicated by complex ECG patterns [131]. Electrical defibrillation is used as an effective technique to treat ventricular fibrillation. Gong et al. reported the application of Poincaré plot for the prediction of occurrence of successful defibrillation in the patients suffering from ventricular fibrillation [132]. The Euclidean distance of the successive points in Poincaré plot was used to calculate the stepping median increment of the defibrillation, which in turn, was used to estimate the possibility of successful defibrillation. The testing of the proposed method was analyzed using the ROC curve, and the results suggested that the performance was comparable to the established methods for successfully estimating defibrillation.

Polycystic ovary syndrome (PCOS) is a common endocrine disease found in 5–10% of the reproductive women [133]. PCOS has been reported to be associated with cardiovascular risks due to its connection with obesity [134]. Saranya et al. performed the Poincaré plot-based nonlinear dynamical analysis of the HRV signals acquired from the PCOS patients to predict the associated cardiovascular risk [135]. The authors found that the PCOS patients had reduced HRV and autonomic dysfunction (in terms of increased sympathetic activity and reduced vagal activity), which might herald cardiovascular risks. Based on the results, the authors suggested that the Poincaré plot analysis may be used independently to measure the extent of autonomic dysfunction in PCOS patients. Some Poincaré plot-based studies

TABLE 2: Recent studies performed for the diagnosis of clinical conditions using RQA-based ECG analysis.

| Clinical conditions   | Classification method  | Performance   | Ref.  |
|---|--|---|-------|
| Atrial fibrillation, atrial flutter, ventricular fibrillation, and normal sinus rhythm                  | Decision tree, random forest, and rotation forest            | 98.37%, 96.29%, and 94.14% accuracy for rotation forest, random forest, and decision tree, respectively   | [123] |
| Effect of the exposure to low-frequency noise of different intensities on the cardiovascular activities | Statistical analysis of RQA-based measures                   | Statistically significant parameters obtained with $p$ value $\leq 0.05$  | [126] |
| Obstructive sleep apnea   | A soft decision fusion rule combining SVM and neural network | 86.37% sensitivity, 83.47% specificity, and 85.26% accuracy   | [128] |
| Arrhythmia  | Joint probability density classifier                         | 94.83 $\pm$ 0.37% accuracy  | [129] |
| Sudden cardiac death  | K-NN, SVM, decision tree, and probabilistic neural network   | 86.8% accuracy, 80% sensitivity, and 94.4% specificity with K-NN classifier and 86.8% accuracy, 85% sensitivity, and 88.8% specificity with PNN | [127] |
| Atrial fibrillation   | Unthresholded recurrence plots                               | 72% accuracy  | [130] |

TABLE 3: Recent studies performed for the diagnosis of clinical conditions using Poincaré plot analysis.

| Clinical conditions       | Classification method                                | Performance  | Ref.  |
|---------------------------|--|--|-------|
| Dilated cardiomyopathy    | Multivariate discriminant analysis                   | 92.9% sensitivity, 85.7% specificity, and 92.1% AUC                      | [136] |
| Preeclampsia              | Multivariate discriminant analysis                   | 91.2% accuracy   | [137] |
| Polycystic ovary syndrome | Statistical analysis of Poincaré plot-based measures | Statistically significant parameters obtained with $p$ value $\leq 0.05$ | [135] |
| Atrial fibrillation       | SVM optimized with particle swarm optimization       | 92.9% accuracy   | [138] |

performed in the last 5 years for the diagnosis of different clinical conditions have been given in Table 3.

**4.7. Applications of Multiple Nonlinear Dynamical System Analysis Methods in ECG Signal Analysis.** In the last few years, some researchers have also implemented multiple nonlinear methods simultaneously for the analysis of the ECG signals [42]. In some cases, the nonlinear methods have been used in combination with the linear methods [139]. Acharya et al. performed analysis of ECG signals using time domain, frequency domain, and nonlinear (i.e., Poincaré plot, RQA, DFA, Shannon entropy, ApEn, SaEn, higher-order spectrum (HOS) methods, empirical mode decomposition (EMD), cumulants, and correlation dimension) techniques for the diagnosis of coronary artery disease [140]. Goshvarpour et al. studied the effect of the pictorial stimulus on the emotional autonomic response by analyzing the nonlinear methods, that is, DFA, ApEn, and Lyapunov exponent-based parameters along with statistical measures of ECG, pulse rate, and galvanic skin response signals [141]. Karegar et al. extracted the nonlinear ECG features using the methods, namely, rescaled range analysis, Higuchi's fractal dimension, DFA, generalized Hurst exponent (GHE), and RQA for ECG-based biometric authentication [142]. The combination of different nonlinear methods for obtaining better performance was observed in the previously reported literature, but the studies prescribing superiority

of one method in comparison to the other methods could not be found.

## 5. Conclusion

Most of the biosignals are nonstationary in nature, which often makes their analysis cumbersome using the conventional linear methods of signal analysis. This led to the development of nonlinear methods, which can perform a robust analysis of the biosignals [9]. Among the biosignals, the analysis of the ECG signals using nonlinear methods has been highly explored. The nonlinear analysis of the ECG signals has been investigated by many researchers for early diagnosis of diseases, human identification, and understanding the effect of different stimuli on the heart and the ANS. The current review dealt with the relevant theory, potential, and recent applications of the nonlinear ECG signal analysis methods. Although the nonlinear methods of ECG signal analysis have shown promising results, it is envisaged that the existing methods may be extended and new methods can be proposed to improve the performance and handle large and complex datasets.

## Conflicts of Interest

The authors declare that they have no conflicts of interest.

## Acknowledgments

The authors thank the National Institute of Technology Rourkela, India, for the facilities provided for the successful completion of the manuscript.

## References

- [1] Y. Birnbaum, J. M. Wilson, M. Fiol, A. B. de Luna, M. Eskola, and K. Nikus, "ECG diagnosis and classification of acute coronary syndromes," *Annals of Noninvasive Electrocardiology*, vol. 19, no. 1, pp. 4–14, 2014.
- [2] C. Stengaard, J. T. Sørensen, M. B. Rasmussen, M. T. Bøtker, C. K. Pedersen, and C. J. Terkelsen, "Prehospital diagnosis of patients with acute myocardial infarction," *Diagnosis*, vol. 3, no. 4, 2016.
- [3] J. Koenig, M. N. Jarczok, M. Warth et al., "Body mass index is related to autonomic nervous system activity as measured by heart rate variability — a replication using short term measurements," *The Journal of Nutrition, Health & Aging*, vol. 18, no. 3, pp. 300–302, 2014.
- [4] D. Petković, Ž. Čojbašić, and S. Lukić, "Adaptive neuro fuzzy selection of heart rate variability parameters affected by autonomic nervous system," *Expert Systems with Applications*, vol. 40, no. 11, pp. 4490–4495, 2013.
- [5] Task Force of the European Society of Cardiology the North American Society of Pacing Electrophysiology, "Heart rate variability: standards of measurement, physiological interpretation, and clinical use," *Circulation*, vol. 93, no. 5, pp. 1043–1065, 1996.
- [6] I. Guyon and A. Elisseeff, "An introduction to feature extraction," *Feature Extraction*, vol. 207, pp. 1–25, 2006.
- [7] T. Li and M. Zhou, "ECG classification using wavelet packet entropy and random forests," *Entropy*, vol. 18, no. 12, p. 285, 2016.
- [8] S. Poli, V. Barbaro, P. Bartolini, G. Calcagnini, and F. Censi, "Prediction of atrial fibrillation from surface ECG: review of methods and algorithms," *Annali dell'Istituto Superiore di Sanità*, vol. 39, no. 2, pp. 195–203, 2003.
- [9] K. J. Blinowska and J. Zygierewicz, *Practical Biomedical Signal Analysis Using MATLAB®*, CRC Press, Boca Raton, FL, USA, 2011.
- [10] A. Schumacher, "Linear and nonlinear approaches to the analysis of R-R interval variability," *Biological Research for Nursing*, vol. 5, no. 3, pp. 211–221, 2004.
- [11] U. R. Acharya, E. C. P. Chua, O. Faust, T. C. Lim, and L. F. B. Lim, "Automated detection of sleep apnea from electrocardiogram signals using nonlinear parameters," *Physiological Measurement*, vol. 32, no. 3, pp. 287–303, 2011.
- [12] A. S. Al-Fahoum and A. M. Qasaimeh, "A practical reconstructed phase space approach for ECG arrhythmias classification," *Journal of Medical Engineering & Technology*, vol. 37, no. 7, pp. 401–408, 2013.
- [13] E. Thelen and L. B. Smith, "Dynamic systems theories," in *Handbook of Child Psychology*, pp. 258–312, John Wiley & Sons, Inc., Hoboken, NJ, USA, 1998.
- [14] A. A. Toor, R. T. Sabo, C. H. Roberts et al., "Dynamical system modeling of immune reconstitution after allogeneic stem cell transplantation identifies patients at risk for adverse outcomes," *Biology of Blood and Marrow Transplantation*, vol. 21, no. 7, pp. 1237–1245, 2015.
- [15] V. Gintautas, G. Foster, and A. W. Hübler, "Resonant forcing of chaotic dynamics," *Journal of Statistical Physics*, vol. 130, no. 3, pp. 617–629, 2008.
- [16] E. Kreyszig, *Advanced Engineering Mathematics*, John Wiley & Sons, Inc., Hoboken, NJ, USA, 2010.
- [17] T. Jackson and A. Radunskaya, *Applications of Dynamical Systems in Biology and Medicine*, vol. 158, John Wiley & Sons, Inc., Hoboken, NJ, USA, 2015.
- [18] Q. Din, "Stability analysis of a biological network," *Network Biology*, vol. 4, no. 3, pp. 123–129, 2014.
- [19] J. Jaeger and N. Monk, "Bioattractors: dynamical systems theory and the evolution of regulatory processes," *The Journal of Physiology*, vol. 592, no. 11, pp. 2267–2281, 2014.
- [20] I. Stewart, *In Pursuit of the Unknown: 17 Equations That Changed the World*, pp. 283–294, John Wiley & Sons, Inc., New York, NY, USA, 2012.
- [21] T. D. Pham, "Possibilistic nonlinear dynamical analysis for pattern recognition," *Pattern Recognition*, vol. 46, no. 3, pp. 808–816, 2013.
- [22] S. H. Strogatz, *Nonlinear Dynamics and Chaos: With Applications to Physics, Biology, Chemistry, and Engineering*, Harper-Collins Publishers, New York, NY, USA, 2014.
- [23] B. Henry, N. Lovell, and F. Camacho, "Nonlinear dynamics time series analysis," *Nonlinear Biomedical Signal Processing, Dynamic Analysis and Modeling*, vol. 2, pp. 1–39, 2012.
- [24] W. Szemplińska-Stupnicka and J. Rudowski, "Neimark bifurcation, almost-periodicity and chaos in the forced van der Pol-Duffing system in the neighbourhood of the principal resonance," *Physics Letters A*, vol. 192, no. 2-4, pp. 201–206, 1994.
- [25] J. Ford, "How random is a coin toss?," *Physics Today*, vol. 36, no. 4, pp. 40–47, 1983.
- [26] S. Wallot, A. Roepstorff, and D. Mønster, "Multidimensional recurrence quantification analysis (MdrQA) for the analysis of multidimensional time-series: a software implementation in MATLAB and its application to group-level data in joint action," *Frontiers in Psychology*, vol. 7, 2016.
- [27] F. Takens, "Detecting strange attractors in turbulence," *Lecture Notes in Mathematics*, vol. 898, pp. 366–381, 1981.
- [28] Y. Fang, M. Chen, and X. Zheng, "Extracting features from phase space of EEG signals in brain-computer interfaces," *Neurocomputing*, vol. 151, pp. 1477–1485, 2015.
- [29] A. Krakovská, K. Mezeiová, and H. Budáčová, "Use of false nearest neighbours for selecting variables and embedding parameters for state space reconstruction," *Journal of Complex Systems*, vol. 2015, Article ID 932750, 12 pages, 2015.
- [30] S. H. Chai and J. S. Lim, "Forecasting business cycle with chaotic time series based on neural network with weighted fuzzy membership functions," *Chaos, Solitons & Fractals*, vol. 90, pp. 118–126, 2016.
- [31] H. Ye, E. R. Deyle, L. J. Gilarranz, and G. Sugihara, "Distinguishing time-delayed causal interactions using convergent cross mapping," *Scientific Reports*, vol. 5, no. 1, article 14750, 2015.
- [32] A. V. Glushkov, O. Y. Khetselius, S. V. Brusentseva, P. A. Zaichko, and V. B. Ternovsky, "Studying interaction dynamics of chaotic systems within a non-linear prediction method: application to neurophysiology," *Advances in Neural*

- Networks, Fuzzy Systems and Artificial Intelligence*, vol. 21, pp. 69–75, 2014.
- [33] B. Paul, R. C. George, and S. K. Mishra, “Phase space interrogation of the empirical response modes for seismically excited structures,” *Mechanical Systems and Signal Processing*, vol. 91, pp. 250–265, 2017.
- [34] A. M. Fraser and H. L. Swinney, “Independent coordinates for strange attractors from mutual information,” *Physical Review A*, vol. 33, no. 2, pp. 1134–1140, 1986.
- [35] H. S. Kim, R. Eykholt, and J. D. Salas, “Nonlinear dynamics, delay times, and embedding windows,” *Physica D: Nonlinear Phenomena*, vol. 127, no. 1-2, pp. 48–60, 1999.
- [36] N. Mars and G. Van Arragon, “Time delay estimation in nonlinear systems,” *IEEE Transactions on Acoustics, Speech, and Signal Processing*, vol. 29, no. 3, pp. 619–621, 1981.
- [37] E. Kononov, “Visual recurrence analysis,” 2006, <http://visual-recurrence-analysis.software.informer.com/download/>.
- [38] A. Colombelli and N. von Tunzelmann, “The persistence of innovation and path dependence,” *Handbook on the Economic Complexity of Technological Change*, pp. 105–119, Edward Elgar Publishing Limited, Cheltenham, UK, 2011.
- [39] H. Yang, “Tool box of recurrence plot and recurrence quantification analysis,” <http://visual-recurrence-analysis.software.informer.com/download/>.
- [40] E. D. Übeyli, “Adaptive neuro-fuzzy inference system for classification of ECG signals using Lyapunov exponents,” *Computer Methods and Programs in Biomedicine*, vol. 93, no. 3, pp. 313–321, 2009.
- [41] S. Haykin and X. B. Li, “Detection of signals in chaos,” *Proceedings of the IEEE*, vol. 83, no. 1, pp. 95–122, 1995.
- [42] M. I. Owis, A. H. Abou-Zied, A. B. M. Youssef, and Y. M. Kadam, “Study of features based on nonlinear dynamical modeling in ECG arrhythmia detection and classification,” *IEEE Transactions on Biomedical Engineering*, vol. 49, no. 7, pp. 733–736, 2002.
- [43] G. Valenza, P. Allegrini, A. Lanatà, and E. P. Scilingo, “Dominant Lyapunov exponent and approximate entropy in heart rate variability during emotional visual elicitation,” *Frontiers in Neuroengineering*, vol. 5, 2012.
- [44] E. D. Übeyli, “Recurrent neural networks employing Lyapunov exponents for analysis of ECG signals,” *Expert Systems with Applications*, vol. 37, no. 2, pp. 1192–1199, 2010.
- [45] N. F. Güler, E. D. Übeyli, and I. Güler, “Recurrent neural networks employing Lyapunov exponents for EEG signals classification,” *Expert Systems with Applications*, vol. 29, no. 3, pp. 506–514, 2005.
- [46] A. Wolf, J. B. Swift, H. L. Swinney, and J. A. Vastano, “Determining Lyapunov exponents from a time series,” *Physica D: Nonlinear Phenomena*, vol. 16, no. 3, pp. 285–317, 1985.
- [47] M. Sano and Y. Sawada, “Measurement of the Lyapunov spectrum from a chaotic time series,” *Physical Review Letters*, vol. 55, no. 10, pp. 1082–1085, 1985.
- [48] B. Henry, N. Lovell, and F. Camacho, “Nonlinear dynamics time series analysis,” *Nonlinear Biomedical Signal Processing, Dynamic Analysis and Modeling*, vol. 2, pp. 1–39.
- [49] H. G. E. Hentschel and I. Procaccia, “The infinite number of generalized dimensions of fractals and strange attractors,” *Physica D: Nonlinear Phenomena*, vol. 8, no. 3, pp. 435–444, 1983.
- [50] C. Lerma, M. A. Reyna, and R. Carvajal, “Association between abnormal electrocardiogram and less complex heart rate variability estimated by the correlation dimension,” *Revista Mexicana de Ingeniería Biomédica*, vol. 36, pp. 55–64, 2015.
- [51] P. Grassberger and I. Procaccia, “Measuring the strangeness of strange attractors,” *Physica D: Nonlinear Phenomena*, vol. 9, no. 1-2, pp. 189–208, 1983.
- [52] J. W. Kantelhardt, E. Koscielny-Bunde, H. H. A. Rego, S. Havlin, and A. Bunde, “Detecting long-range correlations with detrended fluctuation analysis,” *Physica A: Statistical Mechanics and its Applications*, vol. 295, no. 3-4, pp. 441–454, 2001.
- [53] C.-K. Peng, S. V. Buldyrev, S. Havlin, M. Simons, H. E. Stanley, and A. L. Goldberger, “Mosaic organization of DNA nucleotides,” *Physical Review E*, vol. 49, no. 2, pp. 1685–1689, 1994.
- [54] S. E. Perkins, H. F. Jelinek, H. A. al-Aubaidy, and B. de Jong, “Immediate and long term effects of endurance and high intensity interval exercise on linear and nonlinear heart rate variability,” *Journal of Science and Medicine in Sport*, vol. 20, no. 3, pp. 312–316, 2017.
- [55] J. M. Hausdorff, S. L. Mitchell, R. Firtion et al., “Altered fractal dynamics of gait: reduced stride-interval correlations with aging and Huntington’s disease,” *Journal of Applied Physiology*, vol. 82, no. 1, pp. 262–269, 1997.
- [56] R. D. Stout, M. W. Wittstein, C. T. LoJacono, and C. K. Rhea, “Gait dynamics when wearing a treadmill safety harness,” *Gait & Posture*, vol. 44, pp. 100–102, 2016.
- [57] R. Gu, W. Xiong, and X. Li, “Does the singular value decomposition entropy have predictive power for stock market?—evidence from the Shenzhen stock market,” *Physica A: Statistical Mechanics and its Applications*, vol. 439, pp. 103–113, 2015.
- [58] B. R. Auer, “Are standard asset pricing factors long-range dependent?,” *Journal of Economics and Finance*, vol. 42, no. 1, pp. 66–88, 2018.
- [59] K. Ivanova and M. Ausloos, “Application of the detrended fluctuation analysis (DFA) method for describing cloud breaking,” *Physica A: Statistical Mechanics and its Applications*, vol. 274, no. 1-2, pp. 349–354, 1999.
- [60] B. D. Malamud and D. L. Turcotte, “Self-affine time series: measures of weak and strong persistence,” *Journal of Statistical Planning and Inference*, vol. 80, no. 1-2, pp. 173–196, 1999.
- [61] C. Heneghan and G. McDarby, “Establishing the relation between detrended fluctuation analysis and power spectral density analysis for stochastic processes,” *Physical Review E*, vol. 62, no. 5, pp. 6103–6110, 2000.
- [62] S. Ménard, M. Darveau, and L. Imbeau, “The importance of geology, climate and anthropogenic disturbances in shaping boreal wetland and aquatic landscape types,” *Écoscience*, vol. 20, no. 4, pp. 399–410, 2013.
- [63] M. J. Cannon, D. B. Percival, D. C. Caccia, G. M. Raymond, and J. B. Bassingthwaite, “Evaluating scaled windowed variance methods for estimating the Hurst coefficient of time series,” *Physica A: Statistical Mechanics and its Applications*, vol. 241, no. 3-4, pp. 606–626, 1997.
- [64] M. S. Taqqu, V. Teverovsky, and W. Willinger, “Estimators for long-range dependence: an empirical study,” *Fractals*, vol. 3, no. 4, pp. 785–798, 1995.
- [65] A. A. Pranata, J. M. Lee, and D. S. Kim, “Detecting smoking effects with detrended fluctuation analysis on ECG device,” in *한국통신학회 학술대회논문집*, pp. 425–426, Korea, 2017.

- [66] J. W. Kantelhardt, S. A. Zschiegner, E. Koscielny-Bunde, S. Havlin, A. Bunde, and H. E. Stanley, "Multifractal detrended fluctuation analysis of nonstationary time series," *Physica A: Statistical Mechanics and its Applications*, vol. 316, no. 1-4, pp. 87-114, 2002.
- [67] T. Penzel, J. W. Kantelhardt, L. Grote, J. Peter, and A. Bunde, "Comparison of detrended fluctuation analysis and spectral analysis for heart rate variability in sleep and sleep apnea," *IEEE Transactions on Biomedical Engineering*, vol. 50, no. 10, pp. 1143-1151, 2003.
- [68] J.-P. Eckmann, S. Oliffson Kamphorst, and D. Ruelle, "Recurrence plots of dynamical systems," *Europhysics Letters (EPL)*, vol. 4, no. 9, pp. 973-977, 1987.
- [69] J. P. Zbilut, N. Thomasson, and C. L. Webber, "Recurrence quantification analysis as a tool for nonlinear exploration of nonstationary cardiac signals," *Medical Engineering & Physics*, vol. 24, no. 1, pp. 53-60, 2002.
- [70] S. G. Firooz, F. Almasganj, and Y. Shekofteh, "Improvement of automatic speech recognition systems via nonlinear dynamical features evaluated from the recurrence plot of speech signals," *Computers & Electrical Engineering*, vol. 58, pp. 215-226, 2017.
- [71] N. Marwan, N. Wessel, U. Meyerfeldt, A. Schirdewan, and J. Kurths, "Recurrence-plot-based measures of complexity and their application to heart-rate-variability data," *Physical Review E*, vol. 66, no. 2, 2002.
- [72] L. L. Trulla, A. Giuliani, J. P. Zbilut, and C. L. Webber Jr, "Recurrence quantification analysis of the logistic equation with transients," *Physics Letters A*, vol. 223, no. 4, pp. 255-260, 1996.
- [73] S. Chandra, A. K. Jaiswal, R. Singh, D. Jha, and A. P. Mittal, "Mental stress: neurophysiology and its regulation by Sudarshan Kriya yoga," *International Journal of Yoga*, vol. 10, no. 2, pp. 67-72, 2017.
- [74] M. Nardelli, A. Greco, J. Bolea, G. Valenza, E. P. Scilingo, and R. Bailon, "Reliability of lagged Poincaré plot parameters in ultra-short heart rate variability series: application on affective sounds," *IEEE Journal of Biomedical and Health Informatics*, p. 1, 2017.
- [75] M. Das, T. Jana, P. Dutta et al., "Study the effect of music on HRV signal using 3D Poincare plot in spherical co-ordinates - a signal processing approach," in *2015 International Conference on Communications and Signal Processing (ICCSP)*, pp. 1011-1015, Melmaruvathur, India, April 2015.
- [76] K. Muralikrishnan, K. Balasubramanian, S. M. Ali, and B. V. Rao, "Poincare plot of heart rate variability: an approach towards explaining the cardiovascular autonomic function in obesity," *Indian Journal of Physiology and Pharmacology*, vol. 57, no. 1, pp. 31-37, 2013.
- [77] B. Roy, R. Choudhuri, A. Pandey, S. Bandopadhyay, S. Sarangi, and S. Kumar Ghatak, "Effect of rotating acoustic stimulus on heart rate variability in healthy adults," *The Open Neurology Journal*, vol. 6, no. 1, pp. 71-77, 2012.
- [78] P. W. Kamen, H. Krum, and A. M. Tonkin, "Poincaré plot of heart rate variability allows quantitative display of parasympathetic nervous activity in humans," *Clinical Science*, vol. 91, no. 2, pp. 201-208, 1996.
- [79] M. Toichi, T. Sugiura, T. Murai, and A. Sengoku, "A new method of assessing cardiac autonomic function and its comparison with spectral analysis and coefficient of variation of R-R interval," *Journal of the Autonomic Nervous System*, vol. 62, no. 1-2, pp. 79-84, 1997.
- [80] M. M. Corrales, B. . . C. Torres, A. G. Esquivel, M. A. G. Salazar, and J. Naranjo Orellana, "Normal values of heart rate variability at rest in a young, healthy and active Mexican population," *Health*, vol. 4, no. 07, pp. 377-385, 2012.
- [81] J. S. Richman and J. R. Moorman, "Physiological time-series analysis using approximate entropy and sample entropy," *American Journal of Physiology-Heart and Circulatory Physiology*, vol. 278, no. 6, pp. H2039-H2049, 2000.
- [82] M. Costa, A. L. Goldberger, and C.-K. Peng, "Multiscale entropy analysis of complex physiologic time series," *Physical Review Letters*, vol. 89, no. 6, 2002.
- [83] R. B. Govindan, J. D. Wilson, H. Eswaran, C. L. Lowery, and H. Preißl, "Revisiting sample entropy analysis," *Physica A: Statistical Mechanics and its Applications*, vol. 376, pp. 158-164, 2007.
- [84] Y. Wang, J. Wang, and X. Wei, "A hybrid wind speed forecasting model based on phase space reconstruction theory and Markov model: a case study of wind farms in northwest China," *Energy*, vol. 91, pp. 556-572, 2015.
- [85] S. Habershon, D. E. Manolopoulos, T. E. Markland, and T. F. Miller III, "Ring-polymer molecular dynamics: quantum effects in chemical dynamics from classical trajectories in an extended phase space," *Annual Review of Physical Chemistry*, vol. 64, no. 1, pp. 387-413, 2013.
- [86] N. H. Adenan, N. Z. A. Hamid, Z. Mohamed, and M. S. M. Noorani, "A pilot study of river flow prediction in urban area based on phase space reconstruction," *AIP Conference Proceedings, 040011*, 2017, pp. 1-4, Malaysia, 2017.
- [87] G. Koulaouzidis, S. Das, G. Cappiello, E. B. Mazomenos, K. Maharatna, and J. Morgan, "A novel approach for the diagnosis of ventricular tachycardia based on phase space reconstruction of ECG," *International Journal of Cardiology*, vol. 172, no. 1, pp. e31-e33, 2014.
- [88] K. S. Sayed, A. F. Khalaf, and Y. M. Kadah, "Arrhythmia classification based on novel distance series transform of phase space trajectories," in *2015 37th Annual International Conference of the IEEE Engineering in Medicine and Biology Society (EMBC)*, pp. 5195-5198, Milan, Italy, August 2015.
- [89] G. Cappiello, S. Das, E. B. Mazomenos et al., "A statistical index for early diagnosis of ventricular arrhythmia from the trend analysis of ECG phase-portraits," *Physiological Measurement*, vol. 36, no. 1, pp. 107-131, 2014.
- [90] S.-H. Lee, K. Y. Chung, and J. S. Lim, "Detection of ventricular fibrillation using Hilbert transforms, phase-space reconstruction, and time-domain analysis," *Personal and Ubiquitous Computing*, vol. 18, no. 6, pp. 1315-1324, 2014.
- [91] S. Parvaneh, M. R. H. Golpaygani, M. Firoozabadi, and M. Haghjoo, "Analysis of Ecg in phase space for the prediction of spontaneous atrial fibrillation termination," *Journal of Electrocardiology*, vol. 49, no. 6, pp. 936-937, 2016.
- [92] A. Malhotra and D. P. White, "Obstructive sleep apnoea," *The Lancet*, vol. 360, no. 9328, pp. 237-245, 2002.
- [93] A. Jafari, "Sleep apnoea detection from ECG using features extracted from reconstructed phase space and frequency domain," *Biomedical Signal Processing and Control*, vol. 8, no. 6, pp. 551-558, 2013.
- [94] Developed in collaboration with, A. Moya, R. Sutton et al., "Guidelines for the diagnosis and management of syncope (version 2009): the task force for the diagnosis and management of syncope of the European Society of Cardiology

- (ESC),” *European Heart Journal*, vol. 30, no. 21, pp. 2631–2671, 2009.
- [95] N. Khodor, G. Carrault, D. Matelot, N. Ville, F. Carre, and A. Hernandez, “A comparison study between fainter and non-fainter subjects during head-up tilt test using reconstructed phase space,” in *2015 Computing in Cardiology Conference (CinC)*, pp. 1117–1120, Nice, France, September 2015.
- [96] N. Khodor, G. Carrault, D. Matelot et al., “A new phase space analysis algorithm for the early detection of syncope during head-up tilt tests,” in *Computing in Cardiology 2014*, pp. 141–144, Cambridge, MA, USA, September 2014.
- [97] K. Kira and L. A. Rendell, “The feature selection problem: traditional methods and a new algorithm,” *Aaai*, pp. 129–134, AAAI Press, San Jose, CA, USA, 1992.
- [98] F. M. Bui, F. Agrafioti, and D. Hatzinakos, “Chapter 16. Electrocardiogram (ECG) biometric for robust identification and secure communication,” in *Biometrics: Theory, Methods, and Applications*, vol. 2, pp. 383–427, AAAI Press, Hoboken, NJ, USA, 2009.
- [99] L. Biel, O. Pettersson, L. Philipson, and P. Wide, “ECG analysis: a new approach in human identification,” *IEEE Transactions on Instrumentation and Measurement*, vol. 50, no. 3, pp. 808–812, 2001.
- [100] M. Kyoso and A. Uchiyama, “Development of an ECG identification system,” in *2001 Conference Proceedings of the 23rd Annual International Conference of the IEEE Engineering in Medicine and Biology Society*, vol. 4, pp. 3721–3723, Istanbul, Turkey, October 2001.
- [101] Y. Gahi, M. Lamrani, A. Zoglat, M. Guennoun, B. Kapralos, and K. El-Khatib, “Biometric identification system based on electrocardiogram data,” in *2008 New Technologies, Mobility and Security*, pp. 1–5, Tangier, Morocco, November 2008.
- [102] S.-C. Fang and H.-L. Chan, “QRS detection-free electrocardiogram biometrics in the reconstructed phase space,” *Pattern Recognition Letters*, vol. 34, no. 5, pp. 595–602, 2013.
- [103] A. D. C. Chan, M. M. Hamdy, A. Badre, and V. Badee, “Wavelet distance measure for person identification using electrocardiograms,” *IEEE Transactions on Instrumentation and Measurement*, vol. 57, no. 2, pp. 248–253, 2008.
- [104] G. Wübbeler, M. Stavridis, D. Kreiseler, R. D. Bousseljot, and C. Elster, “Verification of humans using the electrocardiogram,” *Pattern Recognition Letters*, vol. 28, no. 10, pp. 1172–1175, 2007.
- [105] S.-C. Fang and H.-L. Chan, “Human identification by quantifying similarity and dissimilarity in electrocardiogram phase space,” *Pattern Recognition*, vol. 42, no. 9, pp. 1824–1831, 2009.
- [106] G. Valenza, L. Citi, and R. Barbieri, “Estimation of instantaneous complex dynamics through lyapunov exponents: a study on heartbeat dynamics,” *PLoS ONE*, vol. 9, no. 8, article e105622, 2014.
- [107] H. Du, Y. Bai, S. Zhou, H. Wang, and X. Liu, “A novel method for diagnosing premature ventricular contraction beat based on chaos theory,” in *2014 11th International Conference on Fuzzy Systems and Knowledge Discovery (FSKD)*, pp. 497–501, Xiamen, China, August 2014.
- [108] M. B. Tayel and E. I. ALSaba, “Robust and sensitive method of lyapunov exponent for heart rate variability,” pp. 1–19, 2015, <https://arxiv.org/abs/1508.00996>.
- [109] G. Ye and X. Huang, “An image encryption algorithm based on autoblocking and electrocardiography,” *IEEE Multimedia*, vol. 23, no. 2, pp. 64–71, 2016.
- [110] F. M. H. S. P. Silva, M. A. Leite, J. C. Crescencio, A. C. S. Filho, and L. Gallo, “Looking for changes in the heart rate of patients with neurocardiogenic syncope,” in *2016 Computing in Cardiology Conference (CinC)*, pp. 1005–1008, Vancouver, BC, Canada, September 2016.
- [111] C. Bogaert, F. Beckers, D. Ramaekers, and A. E. Aubert, “Analysis of heart rate variability with correlation dimension method in a normal population and in heart transplant patients,” *Autonomic Neuroscience*, vol. 90, no. 1–2, pp. 142–147, 2001.
- [112] R. Carvajal, N. Wessel, M. Vallverdú, P. Caminal, and A. Voss, “Correlation dimension analysis of heart rate variability in patients with dilated cardiomyopathy,” *Computer Methods and Programs in Biomedicine*, vol. 78, no. 2, pp. 133–140, 2005.
- [113] J. Bolea, P. Laguna, J. M. Remartínez, E. Rovira, A. Navarro, and R. Bailón, “Methodological framework for estimating the correlation dimension in HRV signals,” *Computational and Mathematical Methods in Medicine*, vol. 2014, Article ID 129248, 11 pages, 2014.
- [114] C.-K. Chen, C.-L. Lin, S.-L. Lin, Y.-M. Chiu, and C.-T. Chiang, “A chaotic theoretical approach to ECG-based identity recognition [application notes],” *IEEE Computational Intelligence Magazine*, vol. 9, no. 1, pp. 53–63, 2014.
- [115] K. Rawal, B. S. Saini, and I. Saini, “Adaptive correlation dimension method for analysing heart rate variability during the menstrual cycle,” *Australasian Physical & Engineering Sciences in Medicine*, vol. 38, no. 3, pp. 509–523, 2015.
- [116] P. Moeynoi and Y. Kitjaidure, “Canonical correlation analysis for dimensionality reduction of sleep apnea features based on ECG single lead,” in *2016 9th Biomedical Engineering International Conference (BMEiCON)*, pp. 1–5, Laung Prabang, Laos, December 2016.
- [117] W. Passchier-Vermeer and W. F. Passchier, “Noise exposure and public health,” *Environmental Health Perspectives*, vol. 108, Supplement 1, pp. 123–131, 2000.
- [118] G. Leventhall, P. Pelmar, and S. Benton, *A Review of Published Research on Low Frequency Noise and Its Effects*, pp. 38–42, Defra Publications, London, UK, 2003.
- [119] S. T. Chen, L. H. Tseng, Y. P. Lee, H. Z. Wu, and C. Y. Chou, “Detrended fluctuation analysis of heart rate variability in noise exposure,” *Advanced Materials Research*, vol. 1044–1045, pp. 1129–1134, 2014.
- [120] C. Kamath, “A new approach to detect congestive heart failure using detrended fluctuation analysis of electrocardiogram signals,” *Journal of Engineering Science and Technology*, vol. 10, no. 2, pp. 145–159, 2015.
- [121] P. Ghasemi and M. R. Raoufy, “Prediction of mortality in patients with sepsis using detrended fluctuation analysis of heart rate variability,” in *2016 23rd Iranian Conference on Biomedical Engineering and 2016 1st International Iranian Conference on Biomedical Engineering (ICBME)*, pp. 150–154, Tehran, Iran, November 2016.
- [122] J.-Y. Chiang, J. W. Huang, L. Y. Lin et al., “Detrended fluctuation analysis of heart rate dynamics is an important prognostic factor in patients with end-stage renal disease receiving peritoneal dialysis,” *PloS one*, vol. 11, no. 2, article e0147282, 2016.
- [123] U. Desai, R. J. Martis, U. R. Acharya, C. G. Nayak, G. Seshikala, and S. K. Ranjan, “Diagnosis of multiclass tachycardia beats using recurrence quantification analysis

- and ensemble classifiers,” *Journal of Mechanics in Medicine and Biology*, vol. 16, no. 01, article 1640005, 2016.
- [124] J. Rolink, M. Kutz, P. Fonseca, X. Long, B. Misgeld, and S. Leonhardt, “Recurrence quantification analysis across sleep stages,” *Biomedical Signal Processing and Control*, vol. 20, pp. 107–116, 2015.
- [125] L. Y. Di Marco, D. Raine, J. P. Bourke, and P. Langley, “Recurring patterns of atrial fibrillation in surface ECG predict restoration of sinus rhythm by catheter ablation,” *Computers in Biology and Medicine*, vol. 54, pp. 172–179, 2014.
- [126] S.-T. Chen, C. Y. Chou, and L. H. Tseng, “Recurrence plot analysis of HRV for exposure to low-frequency noise,” *Advanced Materials Research*, vol. 1044-1045, pp. 1251–1257, 2014.
- [127] U. Rajendra Acharya, H. Fujita, V. K. Sudarshan, D. N. Ghista, W. J. E. Lim, and J. E. W. Koh, “Automated prediction of sudden cardiac death risk using Kolmogorov complexity and recurrence quantification analysis features extracted from HRV signals,” in *2015 IEEE International Conference on Systems, Man, and Cybernetics*, pp. 1110–1115, Kowloon, China, October 2015.
- [128] H. D. Nguyen, B. A. Wilkins, Q. Cheng, and B. A. Benjamin, “An online sleep apnea detection method based on recurrence quantification analysis,” *IEEE Journal of Biomedical and Health Informatics*, vol. 18, no. 4, pp. 1285–1293, 2014.
- [129] Q.-Z. Liang, X. M. Guo, W. Y. Zhang, W. D. Dai, and X. H. Zhu, “Identification of heart sounds with arrhythmia based on recurrence quantification analysis and Kolmogorov entropy,” *Journal of Medical and Biological Engineering*, vol. 35, no. 2, pp. 209–217, 2015.
- [130] O. Meste, S. Zeemering, J. Karel et al., “Noninvasive recurrence quantification analysis predicts atrial fibrillation recurrence in persistent patients undergoing electrical cardioversion,” in *2016 Computing in Cardiology Conference (CinC)*, pp. 677–680, Vancouver, BC, Canada, September 2016.
- [131] M. D. Vaz, T. D. Raj, and K. D. Anura, *Guyton & Hall Textbook of Medical Physiology-E-Book: A South Asian Edition*, Reed Elsevier India Private Limited, Gurgaon, Haryana, India, 2014.
- [132] Y. Gong, Y. Lu, L. Zhang, H. Zhang, and Y. Li, “Predict defibrillation outcome using stepping increment of Poincaré plot for out-of-hospital ventricular fibrillation cardiac arrest,” *BioMed Research International*, Article ID 493472, 2017 pages, 2015.
- [133] H. A. Zacur, “Epidemiology, clinical manifestations and pathophysiology of polycystic ovary syndrome,” *Advanced Studies in Medicine*, vol. 3, pp. 733–739, 2003.
- [134] A. J. Cussons, B. G. A. Stuckey, and G. F. Watts, “Cardiovascular disease in the polycystic ovary syndrome: new insights and perspectives,” *Atherosclerosis*, vol. 185, no. 2, pp. 227–239, 2006.
- [135] K. Saranya, G. K. Pal, S. Habeebullah, and P. Pal, “Analysis of Poincaré plot of heart rate variability in the assessment of autonomic dysfunction in patients with polycystic ovary syndrome,” *International Journal of Clinical and Experimental Physiology*, vol. 2, no. 1, pp. 34–39, 2015.
- [136] A. Voss, C. Fischer, R. Schroeder, H. R. Figulla, and M. Goernig, “Lagged segmented Poincaré plot analysis for risk stratification in patients with dilated cardiomyopathy,” *Medical & Biological Engineering & Computing*, vol. 50, no. 7, pp. 727–736, 2012.
- [137] C. Fischer and A. Voss, “Three-dimensional segmented Poincaré plot analyses SPPA3 investigates cardiovascular and cardiorespiratory couplings in hypertensive pregnancy disorders,” *Frontiers in Bioengineering and Biotechnology*, vol. 2, p. 51, 2014.
- [138] J. P. Sepulveda-Suescun, J. Murillo-Escobar, R. D. Urda-Benitez, D. A. Orrego-Metaute, and A. Orozco-Duque, “Atrial fibrillation detection through heart rate variability using a machine learning approach and Poincaré plot features,” in *VII Latin American Congress on Biomedical Engineering CLAIB 2016, Bucaramanga, Santander, Colombia, October 26th -28th, 2016*, pp. 565–568, Springer Nature Singapore Pte Ltd., Springer, Singapore, 2017.
- [139] F. A. Elhaj, N. Salim, A. R. Harris, T. T. Swee, and T. Ahmed, “Arrhythmia recognition and classification using combined linear and nonlinear features of ECG signals,” *Computer Methods and Programs in Biomedicine*, vol. 127, pp. 52–63, 2016.
- [140] U. R. Acharya, O. Faust, V. Sree et al., “Linear and nonlinear analysis of normal and CAD-affected heart rate signals,” *Computer Methods and Programs in Biomedicine*, vol. 113, no. 1, pp. 55–68, 2014.
- [141] A. Goshvarpour, A. Abbasi, and A. Goshvarpour, “Affective visual stimuli: characterization of the picture sequences impacts by means of nonlinear approaches,” *Basic and Clinical Neuroscience*, vol. 6, no. 4, pp. 209–222, 2015.
- [142] F. P. Karegar, A. Fallah, and S. Rashidi, “Using recurrence quantification analysis and generalized Hurst exponents of ECG for human authentication,” in *2017 2nd Conference on Swarm Intelligence and Evolutionary Computation (CSIEC)*, pp. 66–71, Kerman, Iran, March 2017.

## Research Article

# Detection of Heart Rate through a Wall Using UWB Impulse Radar

Hui-Sup Cho  and Young-Jin Park

*Intelligent Devices and Systems Research Group, DGIST, Daegu, Republic of Korea*

Correspondence should be addressed to Hui-Sup Cho; [mozart73@dgist.ac.kr](mailto:mozart73@dgist.ac.kr)

Received 16 May 2017; Revised 1 January 2018; Accepted 1 February 2018; Published 1 April 2018

Academic Editor: Kunal Pal

Copyright © 2018 Hui-Sup Cho and Young-Jin Park. This is an open access article distributed under the Creative Commons Attribution License, which permits unrestricted use, distribution, and reproduction in any medium, provided the original work is properly cited.

Measuring the physiological functions of the human body in a noncontact manner through walls is useful for healthcare, security, and surveillance. And radar technology can be used for this purpose. In this paper, a new method for detecting the human heartbeat using ultra wideband (UWB) impulse radar, which has advantages of low power consumption and harmlessness to human body, is proposed. The heart rate is extracted by processing the radar signal in the time domain and then using a principal component analysis of the time series data to indicate the phase variations that are caused by heartbeats. The experimental results show that a highly accurate detection of heart rate is possible with this method.

## 1. Introduction

The demand for noninvasive and contactless measurement of physiological functions is constantly on the rise, and such technology is useful for monitoring the conditions of hospitalized patients [1] as well as detecting individuals for security, surveillance, and military purposes. Research has been carried out to utilize the radar technology, which is mainly used in aeronautical navigation and military applications, to acquire physiological information from the human body [2, 3]. Ultra wideband (UWB) impulse radar has low exposure risk for the human body as well as low power consumption and high compatibility with peripheral equipment [4]. Thus, UWB impulse radar has been considered as a useful tool for measuring biological information. The signal processing method for extracting biometric information from the radar signal reflected from the human body is dependent on the radar pulse shape. This method can be regarded as a process of searching for critical factors that can describe the characteristics of the physiological functions effectively. Moreover, the radar signal is processed for extracting the physiological information in various domains such as time domain and frequency domain [5, 6]. There are previous works on detecting the heartbeats of a human body through a wall with UWB impulse radar [7–9], but these studies deal

with radar signals in the frequency domain, so these methods can only express the dominant frequency component during a particular time interval and cannot provide time domain characteristics. In this paper, to overcome these limitations, a new method that can both detect human heartbeats and extract their transient characteristics through walls by utilizing a UWB impulse radar is proposed. In order to accomplish this, the radar signals are accumulated at specific time intervals, and the set of accumulated signals is sent through a bandpass filter designed to remove the components reflected by the wall. The heartbeat information is extracted through a principal component analysis (PCA) of the filtered data set. An experiment for verifying the performance of the proposed method is also carried out, and it is confirmed that the heart rate can be accurately extracted with this method.

## 2. UWB Impulse Radar Signal

A radar transceiver, NVA6201 [10], which emits pulses via an antenna and digitizes the pulses coming back from the target using a strobed sampling method, is employed in the experiment. Each pulse is in the form of a sine wave with a Gaussian envelope and a width of less than 0.4 ns, and the pulse has a center frequency of 6.8 GHz and a bandwidth of 2.3 GHz. The shape of an output pulse is shown in Figure 1.

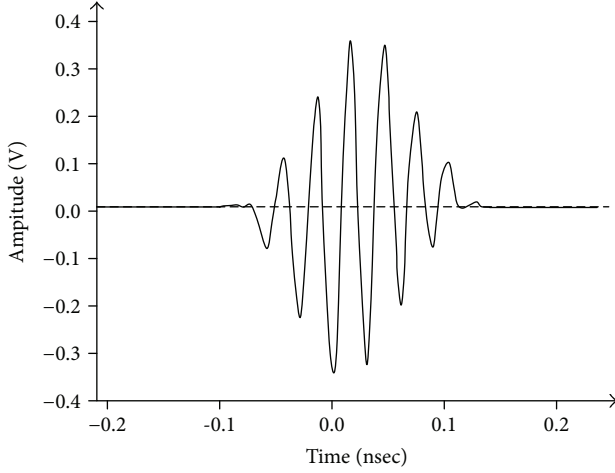


FIGURE 1: The shape of a radar output pulse.

A clay brick wall is used in the present experiment, and the pulses reflected from the body return to the radar antenna through the wall. As the pulse reaching the human body loses energy due to the wall, the amplitude of the component acquired by the transceiver is reduced. The attenuation of the signal corresponding to the frequency differs according to the wall material [11]. Pulses that pass through the body's surface interact with tissues. Most of the energy of the pulses that travel into body tissues is absorbed by the tissues, and the components that are reflected at the interface of each tissue and released into the air are negligible. Therefore, it can be assumed that the pulses arriving at the antenna are mainly reflected from the interfaces of either the wall or the body surface. In the present study, the radar pulse reflected by the wall is assumed as a stationary signal with time-invariant characteristics, and the component reflected from the human body is a nonstationary signal that has phase variations caused by the respiration and heartbeats. Hence, considering these properties, it is necessary to separate these two components. The conceptual images used to describe the shapes of the radar pulses captured at the receiving antenna mathematically are shown in Figure 2. The range sampled at the sampling rate of the receiver that samples the pulse is referred to as the pulse sampling time, and the cross-range sampled at the pulse repetition frequency, which is the frequency at which the pulse is emitted, is referred to as the pulse acquisition time in this paper. According to Ren et al. [12], the radar pulse emitted by the antenna is expressed as

$$x_{tx}(t, mT_{tx}) = g(t, mT_{tx})\sin(2\pi f_c t), \quad (1)$$

where  $g(t)$  and  $f_c$  denote the Gaussian function and the center frequency of the sine wave, respectively, and  $t$  denotes the time variable in pulse sampling time.  $T_{tx}$  represents the period for emitting pulses to the target, and  $mT_{tx}$  represents the time at which the  $m$ th pulse is emitted. In addition, the expression for the pulses received by the radar system after

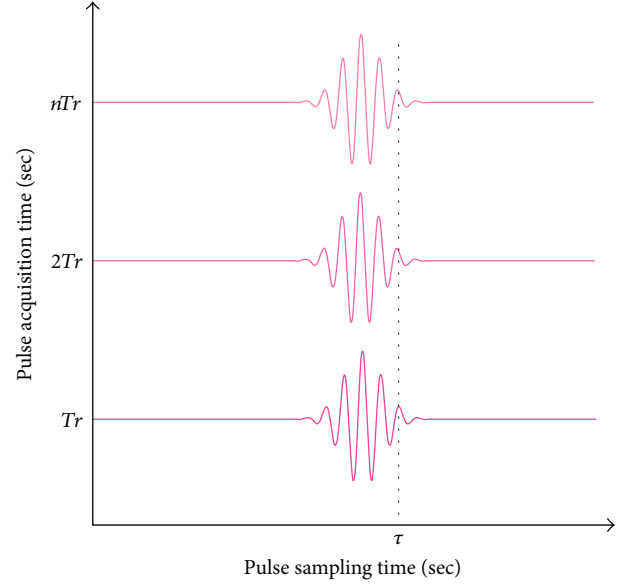


FIGURE 2: Conceptual shape of radar pulses used in mathematical expression.

being reflected from the human body can be found in [12] and is

$$x_{rx}(t, nT_{rx}) = g(t - T_d, nT_{rx})\sin(2\pi f_c(t - T_d)), \quad (2)$$

$$T_d = 2 \frac{[R + A_r \sin(2\pi f_r nT_{rx}) + A_h \sin(2\pi f_h nT_{rx})]}{c}, \quad (3)$$

where  $T_{rx}$  represents the period for collecting pulses reflected from the target, and  $nT_{rx}$  represents the time at which the  $n$ th pulse is collected. In addition,  $T_d$  represents the time delay that occurs on the path along which the pulse is reflected off the target and back to the radar system and includes  $A_r$ ,  $A_h$ ,  $f_r$ ,  $f_h$ , and  $c$  that represent the respiration amplitude, heartbeat amplitude, respiration frequency, heartbeat frequency, and speed of light, respectively. Assuming that the antenna is in close contact with body surface and the subject holds breathing in order to make the equation simpler,  $A_r = 0$  and  $R = 0$ . Under this condition, as shown in Figure 2, at the moment when  $t$  is a specific time  $\tau$ , (2) is expressed as

$$x_{rx}(\tau, nT_{rx}) = g(\tau - T_d, nT_{rx})\sin(2\pi f_c(\tau - T_d)), \quad (4)$$

$$T_d = 2 \frac{[A_h \sin(2\pi f_h nT_{rx})]}{c}. \quad (5)$$

It can be seen that the  $g(\tau - T_d, nT_{rx})$  is independent of  $nT_{rx}$ , so  $T_d$  determines the shape of the received radar pulse as a function of  $nT_{rx}$  in (4). As a result, the phase changes of the radar signals due to the heartbeats can be observed along the pulse acquisition time axis in the accumulated received signals.

### 3. Previous Work

A study was carried out to extract the heartbeat frequency accurately as well as to observe the change of the heartbeat patterns by processing the radar signals in the time domain [5]. A method using SFCW (stepped frequency continuous wave) radar for approximating the frequencies of the heart rates and the position of persons behind a wall was proposed by Shirodkar et al. [7], but they made no mention of the method's quantitative accuracy. Chia et al. [8] introduced a UWB radar prototype that meets FCC emission limits and can measure the heartbeat and breathing rate of persons behind a wall, but they did not indicate how accurately the prototype could measure heart and breathing rates. Singh et al. [9] applied the short-term Fourier transform (STFT) and singular value decomposition (SVD) methods to radar signals reflected from gypsum walls, wooden doors, and persons behind walls. However, heartbeats could not be discriminated.

### 4. Methodology

**4.1. Setup for Radar Signal Measurement.** The setup for measuring radar signals is shown in Figure 3. Pulses were emitted from the transmitter antenna (Tx), and the pulses coming back from the target were received by the receiver antenna (Rx). The radar pulse emitted from the transceiver has an average power of  $-12.6$  dBm and the antenna amplifies this by 6 dBi. The UWB impulse radar system converted the received radar signals into digital data and transmitted them to the host PC that executed the proposed algorithm. The ECG sensor system was synchronized with the UWB impulse radar system using the same time base, and the ECG heartbeats were compared with those extracted by the radar system as reference points. The power of the received signal is inversely proportional to the fourth power of distance in the radar equation. If the distance to the target is more than 1 m, then signal amplification is needed in the radar pulse transmitter/receiver stage in order to detect the heartbeats. In the present study, it was not appropriate to use signal amplification, because this might have led to excessive human exposure to electromagnetic waves. Therefore, the experimental radar data was measured from human bodies located no further than 1 m from the radar device.

**4.2. Preprocessing of the Radar Signal.** A received pulse was a superposition of all the reflected waves that exhibited changes in both amplitude and phase at a particular moment. Furthermore, considering the movement of the ribcage by breathing and heartbeat, the shape of the pulse became more complicated. The accumulation, using specific time intervals, of the reflected received signals has a phase component. This phase is a function of the time delay that occurs on the path through which the pulse is reflected from the target and back to the radar system. Because both respiration and heartbeat change the time delay, an observation of the accumulated signals along the pulse acquisition time axis reveals phase changes due to these factors as well. The received pulse was output as digital data after being sampled in the transceiver.

A set of outputs of each sampler representing the amplitudes of the received pulse is called a "frame." For detecting the heartbeat, a "frame set," which was obtained by accumulating 512 frames, was used. The frameset can be viewed as a two-dimensional array consisting of 256 sampler indices and 512 time units. The shape of a frame and a frame set are shown in Figure 4. As mentioned earlier, the time series of each sampler of the frame set contains the phase changes of the radar pulses caused by both the respiration and the heartbeat. The peaks with constant amplitudes near the 120th sampler index in Figure 4(b) are the components reflected by the wall, and some of the ripples near the 170th index in Figure 4(b) are the components reflected by the human body. Specifically, the small and large ripples were due to phase changes caused by heartbeat and breathing, respectively.

**4.3. Heartbeat Extraction Method.** The algorithm described below was used in order to extract heartbeat information in the time domain.

**4.3.1. Bandpass Filtering.** As the frequency range of a heartbeat is between 1 and 3 Hz [13], the time series of each sampler was passed through a bandpass filter (BPF) that selectively passes the frequency components between 1 and 3 Hz. With this filter, high-frequency noise and low-frequency components originating from stationary targets, such as walls or human respiration, were effectively removed. The function of the bandpass filter can be observed clearly by comparing the frame sets before and after passing through the filter. To accomplish this, two frame sets are shown together in a top view in Figures 5(a) and 5(b), respectively. The peaks observed in the time series of the samplers between the 100th and 125th indices are caused by the peaks of the pulses reflected from the wall, and the peaks observed in the time series of the samplers between the 150th and 180th indices are caused by the peaks of the pulses reflected from the human body. It is clear in Figure 5(b) that the component reflected from the wall was effectively removed near the 120th sampler. It is also apparent that a certain pattern appears in the region between the 150th and 200th samplers, which was a combination of a pattern of heartbeats in the time axis direction and the peak of a frame whose amplitude had been changed by the BPF in the sampler axis direction. To implement the bandpass filter, a fourth order Butterworth filter with cutoff frequencies of 1 Hz and 3 Hz was designed.

**4.3.2. Extracting Principal Pattern via Dimensional Reduction of Time Series.** The frames in the frame set at 2.34 and at 2.66 s that were passed through the bandpass filter, shown in Figure 5(b), are extracted and shown in Figure 6(a), and the two frames seem to be mirror images of one another. In fact, the frame at 2.34 s corresponds to a case in which the chest cavity was swollen by a heartbeat, and the frame at 2.66 s corresponds to a case in which the chest cavity was reduced, so the phases of the frames are extremely different. It is clear that the phase of the pulse changes as the propagation path of the radar pulse changes. In addition, the phase change of the radar pulse appears in the time series data of each sampler. To visualize this, the time series data of four

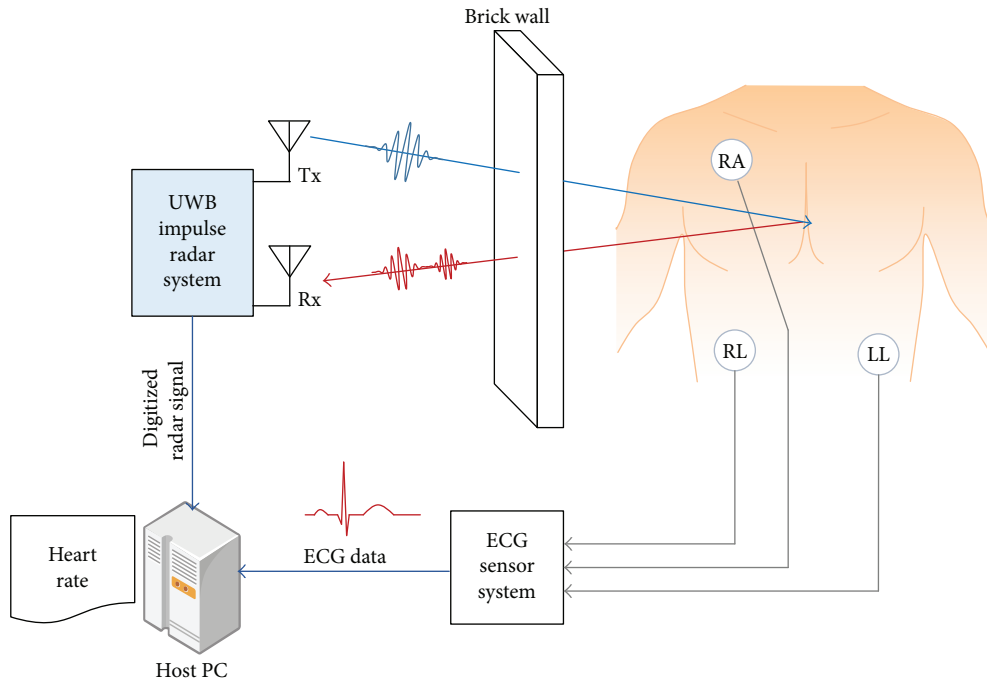


FIGURE 3: Experimental setup.

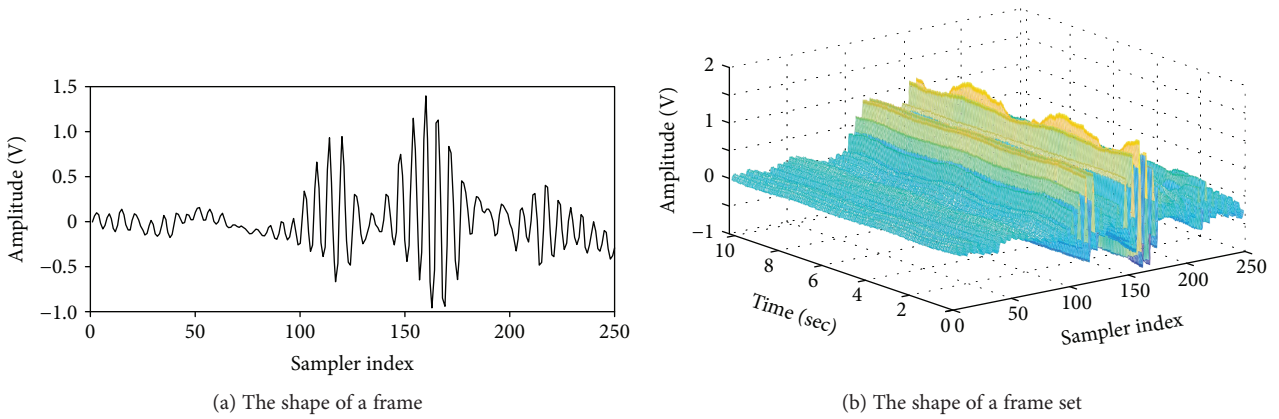


FIGURE 4: Received radar pulses.

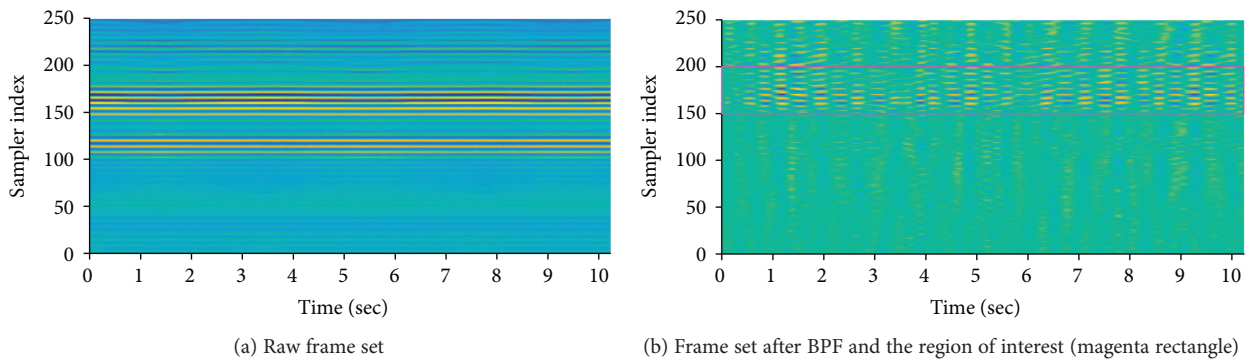


FIGURE 5: Shape of the frame set before and after BPF (top view).

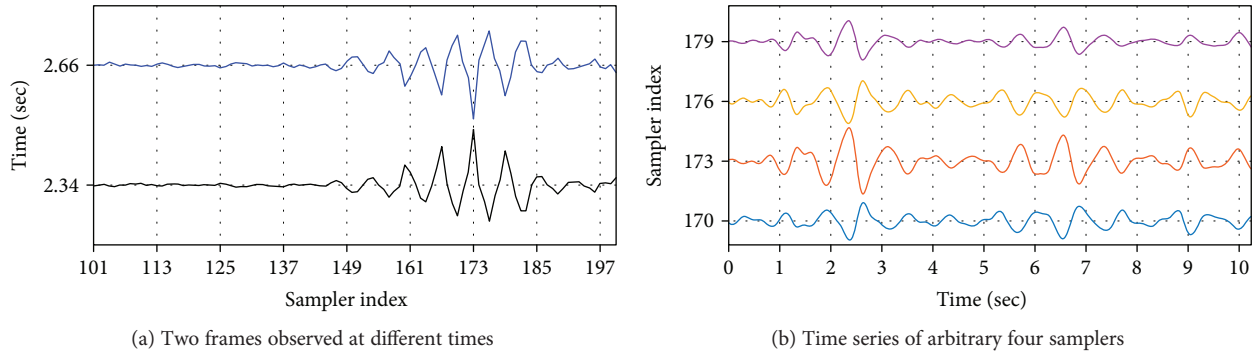


FIGURE 6: Shape of the frames and the time series after BPF.

samplers are shown in Figure 6(b). Since these four samplers correspond to the positive and negative peaks in the frame shown in Figure 6(a), each waveform synchronized with the actual heartbeat of each sampler is inverted vertically. Because there are waveforms synchronized with the actual heartbeats in the time series of the samplers in the region of interest, designated in Figure 5(b) as a magenta rectangle, if a pattern that can represent the multiple time series is found, it is regarded as the heartbeat waveform. In other words, heartbeat waveforms can be found by reducing the dimensions of the time series data. The following procedure is performed for this purpose.

- (a) Construct a matrix with the time series data in the region of interest and call it the “original data set.” From a different perspective, each matrix frame corresponds to an observation of a particular event, and each matrix sampler corresponds to a variable.
- (b) Create a covariance matrix of the original data set.
- (c) Perform eigenvalue decomposition on the covariance matrix in order to find eigenvectors.
- (d) Select the eigenvector with the highest eigenvalue and name it the “principal component.”
- (e) Convert the original data set into one-dimensional data by projecting it onto the principal component vector.

This process is known as PCA [14], and in this paper, the heartbeat waveform is found from the data restored by the PCA. Specifically, the PCA for the time series of 50 samplers (i.e., the  $50 \times 512$  matrix represented by the magenta rectangle in Figure 5(b)) was performed. The shape of the restored signal revealing the phase change due to heartbeat is shown by the black line in Figure 7. It is preferable to detect the heartbeat using patterns found with the PCA of multiple time series data rather than using only one specific time series in the region of interest. Although the time series in the region of interest has a larger signal amplitude than the other samplers do and the waveform synchronized to the heartbeat is evident, each individual time series is susceptible to both quantization errors occurring in the transceiver and noise caused by movement of the subject.

Therefore, it is reasonable to use PCA, which can overcome the vulnerabilities of individual time series by considering multiple time series.

**4.3.3. Calculating the Heartbeat Intervals.** As part of the process of extracting the heartbeat components by removing high-frequency glitches from the restored signal obtained by PCA, the signal was passed through a low-pass filter with an adaptive cutoff frequency, which is a value obtained by adding 0.3 Hz to the dominant frequency of the restored signal. The dominant frequency is obtained by the fast Fourier transform (FFT) of the restored signal. The shape of the signal passing through the LPF is shown by the blue line in Figure 7. Because this signal was synchronized with the heartbeat, the interval of each peak corresponded to the interval of the heartbeat. The temporal position of the extracted heartbeat is indicated by the dotted magenta line. The mean value of every peak interval was estimated as the heart rate.

**4.4. ECG Data Processing.** It is necessary to quantify how accurately the heartbeats detected by the UWB impulse radar follow the actual heartbeats. Therefore, the time at which the R peak occurred in the ECG was compared with the temporal position of the heartbeats extracted by the radar. The accuracy of the proposed method was quantified by calculating the error between these values. For this purpose, the UWB radar system and the ECG sensor system were synchronized at the same time base. The QRS complexes that consisted of successive Q, R, and S waves and were the most obvious parts of the ECG were extracted utilizing the Pan and Tompkins algorithm [15]. The time at which the R peak occurred and the time interval between the R peaks were then used as the reference values. Because a detailed description of the QRS detection algorithm was beyond the scope of this paper, it has been omitted.

## 5. Experiment and Discussion

The setup for the experiment was the one shown in Figure 3, where the clay brick wall was located 50 cm from the antenna of the radar system, and the subject was located 15 cm away from the wall. The subject was breathing normally without sudden movements while sitting in a chair, and electrodes

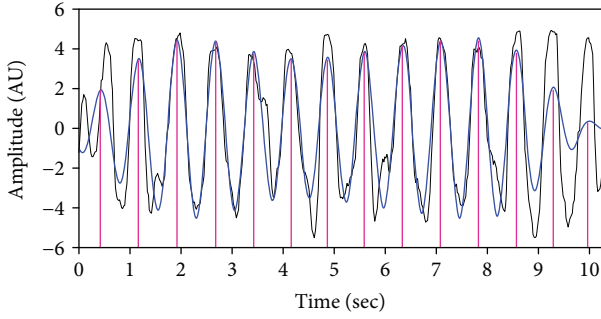


FIGURE 7: Heartbeats restored from the PCA.

were attached to his or her right arm (RA), left leg (LL), and right leg (RL) to obtain a LEAD II ECG. After emitting radar pulses to each subject, the signals reflected from the body were collected, and the heart rate was extracted using the proposed method for the radar signals. Five subjects with different physical conditions participated in the experiment. During the collection of the radar signal, the ECG was measured and used as a reference point for determining the accuracy of the estimation method. The error rate of beats per minute (BPM) is used as an index of the accuracy of the proposed method. The BPM is obtained by multiplying the heartbeat frequency by 60. The error rate was expressed as

$$\text{Error rate} = \frac{|\text{BPM}_{\text{Estimate}} - \text{BPM}_{\text{Ref}}|}{\text{BPM}_{\text{Ref}}} \times 100(\%), \quad (6)$$

where  $\text{BPM}_{\text{Estimate}}$  and  $\text{BPM}_{\text{Ref}}$  represented the BPM extracted from the radar signals and the BPM from the ECG, respectively.

Sixteen frame sets were taken from each subject in the experiment. The average error rate for 80 frame sets was approximately 1.05%. Despite the fact that the heartbeat frequency of each subject had different values, the heart rate could be detected accurately with the proposed method. When a person participates in the experiment as a target, the area of the body surface, where the radar pulses are reflected from, is considered as a factor affecting the power of the received radar signals [5]. However, the results from the experiment showed that a difference in the area had an insignificant effect on the power of the received radar pulse. Therefore, the physical factor can be considered as not affecting the accuracy of the proposed method, which is due to the fact that the subjects are relatively close to the antenna and the opening angles of the antenna are narrow.

Because comparable studies utilizing UWB impulse radar to measure human heart rate through a wall did not quantify the accuracy of their heart rates, it is difficult to compare the results obtained in this paper directly with those of the other studies. However, some studies using UWB impulse radar to extract a heartbeat without wall penetration [16, 17] found a minimum error rate of 4.0–5.4%, and even in comparison to these studies, the experimental result of this study demonstrated higher accuracy. The researchers of all comparable studies extracted heart rate in the frequency domain. Frequency domain processing carries the limitation that it

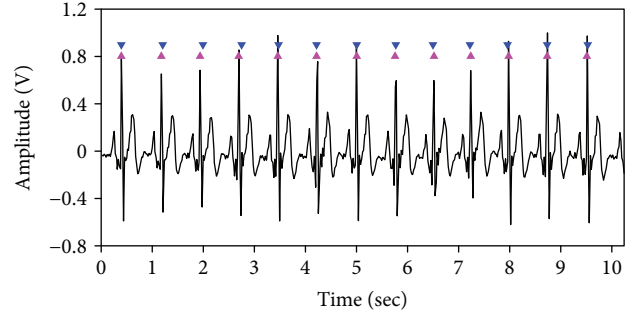


FIGURE 8: Comparison of heartbeat positions indicated by ECG (magenta upward-pointing triangles) and the positions estimated by the proposed algorithm (blue downward-pointing triangles).

cannot ensure high frequency and time resolution simultaneously. In contrast, the proposed method has the ability to satisfy two requirements: to provide sufficiently high-frequency resolution and to observe heartbeat changes in the time domain. This was confirmed by placing the positions of the heartbeats detected by the proposed method at the same time intervals as those of the measured ECG. The ECG and the detected heartbeats, where the first beat position was aligned with the first QRS peak of the ECG, are shown in Figure 8. There appear to be slight errors in the third and fourth positions, but the extracted heartbeats follow the actual ECG readings closely.

Heart rate was extracted with high accuracy in experiments with walls such as a clay brick wall, a wooden wall, and a concrete wall with uniform internal structure. However, since the power of the received radar signal was significantly attenuated due to reflection and scattering of the radar pulse in a wall composed of materials with different properties, a wall containing conductive materials, and a wall with cavities, an accurate detection of heartbeat was not possible in experiments using these kinds of wall.

## 6. Conclusion

In this paper, a new method to extract the human heart rate through a wall using UWB impulse radar is proposed. Unlike conventional methods that process the radar signal in the frequency domain for extracting the heartbeat information from the radar signal reflected from the human body, for this method, the radar signal was processed in the time domain. To accomplish this, a frame set was made by accumulating radar pulses at regular time intervals. The frame set was then converted to binary form, and the heartbeat information was extracted from the PCA of the time series data that indicated the presence of the heartbeats. Experiments were conducted to verify the performance of the proposed method for various subjects. In the experiments, the frequencies of the heart rates of subjects located within 1 m from the antenna were extracted, with an average error rate of 1.05%, and it was confirmed that instantaneous changes in the heartbeats could be detected with the proposed method.

In conclusion, the proposed method, which has a performance differentiated from other methods discussed above,

can be used to extract heart rates through walls using radar signals.

### Conflicts of Interest

The authors declare no conflict of interests.

### Acknowledgments

This work was supported by the DGIST R&D Program of the Ministry of Science, ICT, and Technology of Korea (18-NT-01).

### References

- [1] C. G. Bilich, "Bio-medical sensing using ultra wideband communications and radar technology: a feasibility study," in *2006 Pervasive Health Conference and Workshops*, pp. 1–9, Innsbruck, Austria, 2006.
- [2] V. Michell, D. J. Rosenorn, S. R. Culliver, and W. Currie, *Handbook of Research on Patient Safety and Quality Care through Health Informatics*, IGI Global, Hershey, PA, USA, 2013.
- [3] K. F. Wu and Y. T. Zhang, "Contactless and continuous monitoring of heart electric activities through clothes on a sleeping bed," in *2008 International Conference on Technology and Applications in Biomedicine*, pp. 282–285, Shenzhen, China, 2008.
- [4] B. Gupta, E. Cianca, M. Ruggieri, and R. Prasad, "A novel FM-UWB system for vital sign monitoring and its comparison with IR-UWB," in *2009 2nd International Symposium on Applied Sciences in Biomedical and Communication Technologies*, pp. 1–4, Bratislava, Slovakia, 2009.
- [5] H.-S. Cho, Y.-J. Park, H.-K. Lyu, and J.-H. Cho, "Novel heart rate detection method using UWB impulse radar," *Journal of Signal Processing Systems*, vol. 87, no. 2, pp. 229–239, 2017.
- [6] H.-S. Cho, Y.-J. Park, and H.-K. Lyu, "Robust heart rate detection method using UWB impulse radar," in *2016 International Conference on Information and Communication Technology Convergence (ICTC)*, pp. 1138–1142, Jeju, Republic Korea, 2016.
- [7] S. Shirodkar, P. Barua, D. Anuradha, and R. Kuloor, "Heart-beat detection and ranging through a wall using ultra wide band radar," in *2011 International Conference on Communications and Signal Processing*, pp. 579–583, Calicut, India, 2011.
- [8] M. Y. W. Chia, S. W. Leong, C. K. Sim, and K. M. Chan, "Through-wall UWB radar operating within FCC's mask for sensing heart beat and breathing rate," in *European Radar Conference, 2005. EURAD 2005*, pp. 267–270, Paris, France, 2005.
- [9] S. Singh, Q. Liang, D. Chen, and L. Sheng, "Sense through wall human detection using UWB radar," *EURASIP Journal on Wireless Communications and Networking*, vol. 2011, no. 1, 2011.
- [10] Novelda, *NVA620x Preliminary Datasheet*, Novelda AS, Oslo, Norway, 2013.
- [11] L. E. Miller, *Why UWB? A Review of Ultra Wideband Technology*, Gaithersburg, MD, USA, Wireless Communication Technologies Group National Institute of Standards and Technology, 2003.
- [12] L. Ren, Y. S. Koo, Y. Wang, and A. E. Fathy, "Noncontact heartbeat detection using UWB impulse Doppler radar," in *2015 IEEE Topical Conference on Biomedical Wireless Technologies, Networks, and Sensing Systems (BioWireless)*, pp. 14–16, San Diego, CA, USA, 2015.
- [13] F. Mohammad-Zahed, F. Taghibakhsh, and B. Kaminska, "Contactless heart monitoring (CHM)," in *2007 Canadian Conference on Electrical and Computer Engineering*, pp. 583–585, Vancouver, BC, Canada, 2007.
- [14] I. T. Jolliffe, *Principal Component Analysis*, Springer, New York, NY, USA, 2nd edition, 1986.
- [15] J. Pan and W. J. Tompkins, "A real-time QRS detection algorithm," *IEEE Transactions on Biomedical Engineering*, vol. BME-32, no. 3, pp. 230–236, 1985.
- [16] T. Sakamoto, R. Imasaka, H. Taki et al., "Accurate heartbeat monitoring using ultra-wideband radar," *IEICE Electronics Express*, vol. 12, no. 3, article 20141197, 2015.
- [17] V. Nguyen, A. Q. Javaid, and M. A. Weitnauer, "Spectrum-averaged harmonic path (SHAPA) algorithm for non-contact vital sign monitoring with ultra-wideband (UWB) radar," in *2014 36th Annual International Conference of the IEEE Engineering in Medicine and Biology Society*, pp. 2241–2244, Chicago, IL, USA, 2014.

## Research Article

# Identification of Cerebral Artery Stenosis Using Bilateral Photoplethysmography

Hyun Goo Kang,<sup>1</sup> Seogki Lee,<sup>2</sup> Han Uk Ryu,<sup>3</sup> and Youngsuk Shin <sup>4</sup>

<sup>1</sup>Department of Neurology, Chosun University School of Medicine and Hospital, No. 375 Seosuk-dong, Dong-gu, Gwangju 501-759, Republic of Korea

<sup>2</sup>Department of Thoracic Surgery, Chosun University School of Medicine and Hospital, No. 375 Seosuk-dong, Dong-gu, Gwangju 501-759, Republic of Korea

<sup>3</sup>Department of Neurology, Chunbuk National University School of Medicine and Hospital, San 2-20, Geumam-dong, Deokjin-gu, Jeonbuk 561-180, Republic of Korea

<sup>4</sup>School of Information and Communication Engineering, Chosun University, No. 309 Pilmun-daero, Dong-gu, Gwangju 61452, Republic of Korea

Correspondence should be addressed to Youngsuk Shin; [ysshin@chosun.ac.kr](mailto:ysshin@chosun.ac.kr)

Received 29 July 2017; Accepted 24 January 2018; Published 19 March 2018

Academic Editor: Anilesh Dey

Copyright © 2018 Hyun Goo Kang et al. This is an open access article distributed under the Creative Commons Attribution License, which permits unrestricted use, distribution, and reproduction in any medium, provided the original work is properly cited.

Cerebral artery stenosis is currently diagnosed by transcranial Doppler (TCD), computed tomographic angiography (CTA), or magnetic resonance angiography (MRA). CTA exposes a patient to radiation, while CTA and MRA are invasive and side effects were related to contrast medium use. This study aims to provide a technique that can simply discriminate between people with normal blood vessels and those with cerebral artery stenosis using photoplethysmography (PPG), which is noninvasive and inexpensive. Moreover, the measurement takes only 120 seconds and is conducted on the fingers. The technique projects the light of a specific wavelength and analyzes the pulse waves which are generated when the blood passes through the blood vessels according to one's heartbeat using the transmitted light. Normalization was performed after dividing the extracted pulse waveform into windows, and maximum positive and negative amplitudes (MPA, MNA) were extracted from the detected pulse waves as features. The extracted features were used to identify normal subjects and those with cerebral artery stenosis using a linear discriminant analysis. The study results showed that the recognition rate using MPA was 92.2%, MNA was 90.6%, and combined MPA + MNA was 90.6%. The technique proposed is expected to detect early stage asymptomatic cerebral artery stenosis and help prevent ischemic stroke.

## 1. Introduction

Photoplethysmography (PPG) is a technology that presents the pulse wave generated by the blood passing through the blood vessels along with the heartbeat and is measured by extracting the transmitted light after projecting the light of a specific wavelength. The measurement of a biosignal using PPG is noninvasive, and it is possible to measure various signals including respiration, heart rate, vasomotor activity, and saturation by pulse oximetry (SPO<sub>2</sub>) using just one probe [1–4]. PPG can be used to evaluate atherosclerosis [5, 6], arterial stenosis [7–10], arterial properties [2, 11–13], hypertension [10, 12], diabetes mellitus [14],

and cardiovascular risk factors [15]. PPG has been widely used to study cardiovascular function. PPG is a very effective method measuring the blood volume of each heartbeat in the body using the characteristics of the light. It enables the measurement of the subtle changes in blood volume of the arterioles and capillary vessels in the tissue along the systole-diastole cycle of the heart by using the changes in the transmittance of light even when the absorbance of a material is unknown.

Cardiovascular function is closely related to the brain, the top-level organ regulating all the body's functions. The brain requires high energy to maintain its vigorous metabolism, and energy is delivered to the brain by the blood. The blood

is then delivered to every area of the body through the blood vessels. Ischemic stroke (cerebral infarction) indicates a cerebrovascular disease induced by energy depletion in the brain due to the insufficient blood supply to the brain caused by the abnormal blood vessel to the brain that damages the brain tissues and causes abnormal brain function. Cerebral artery stenosis may induce hemodynamic disturbance in the flow of the blood to the brain that can create blood clots in the narrowed blood vessel. Therefore, it is an important risk factor causing ischemic stroke.

The cerebral artery is divided into large arteries (e.g., cerebral artery) and small perforating arteries that diverge from the large artery. The carotid and vertebral arteries are important large arteries that supply blood to the brain from the aorta. Since stenosis slowly progresses in the large arteries, the cerebral artery does not show any symptoms until the blood vessel is occluded. When the blood vessel is completely occluded due to stenosis, blood is not supplied to brain parenchyma. Consequently, cell death occurs due to ischemia and symptoms associated with the necrosis of these cells and tissues occur. Ischemic stroke indicates these phenomena. Since necrotic brain cells do not regenerate, most people who experience ischemic stroke suffer permanent disability. Therefore, it is very important to prevent ischemic stroke and identify its curable risk factors such as cerebral artery stenosis.

Magnetic resonance angiography (MRA), computed tomographic angiography (CTA), carotid ultrasonography (CUS), and transcranial Doppler (TCD) are representative methods used to confirm cerebral artery stenosis. However, the majority of cases of cerebral artery stenosis are asymptomatic, as stated above, so it is recommended that preventative measures should be taken via periodic examinations. Most of the stated tests are expensive and have a risk of side effects due to the use of contrast medium. In addition, CUS can detect carotid artery stenosis at the neck and TCD has a poor temporal window because it cannot visualize the area when the temporal bone is too thick.

The objective of this cardiovascular function study was to evaluate the correlation between cerebral artery stenosis and the PPG signal reflecting the characteristics of microvessels in the tissues according to the cardiac contraction and relaxation cycle. If there is a correlation between the PPG signal and cerebral artery stenosis, it is expected that we can periodically screen for the presence of cerebral artery stenosis using a noninvasive, side-effect-free, and inexpensive technology instead of the known invasive and expensive methods. In addition, the advantage of PPG screening is that it can simultaneously check for stenosis of the intracranial artery and the carotid artery rather than that of limited blood vessels. People can easily notice that a more thorough blood vessel test is necessary when abnormalities are observed in the screening test. Moreover, if the location and degree of cerebral artery stenosis are found on a thorough medical examination, the stenosis can be treated by using drug therapy in the early stage and managed systematically by exercise. The results of this study will help clinicians control the occurrence of ischemic stroke, which burdens society.

## 2. Material and Methods

The PPG waveform amplitude was used to extract the characteristics of cerebral artery stenosis between the neck and the brain. Previous results showed that the PPG pulse wave amplitude was proportionate to the vessel distensibility under highly variable heartbeat conditions [16]. Data collection and preprocessing were conducted as a preparation step to extract the PPG waveform amplitude's characteristics. After preprocessing, the amplitude was transformed as a normalized pulse wave to compare the subjects' amplitudes. The characteristics of the amplitudes were extracted from the normalized pulse waves. The extracted features were analyzed using a linear discriminant analysis method and used to differentiate normal people from patients with cerebral artery stenosis. A schematic diagram of the proposed technique is shown in Figure 1.

*2.1. Data Collection.* In recent years, MRA has been increasingly used as a noninvasive imaging method for evaluating intracranial cerebral artery atherosclerosis [17], intracranial cerebral artery stenosis [18], internal carotid artery (ICA) stenosis, or middle cerebral artery (MCA) stenosis [19–21]. Stenosis of the cerebral artery on MRA is frequently observed in the ICA and MCA [18–21]. Therefore, the detection of cerebral artery stenosis within ICA or MCA appears greatly accomplished via a noninvasive method such as MRA.

Our study subjects were divided into a treatment group and a control group. The treatment group included outpatients with cerebral artery stenosis or ischemic stroke detected on brain MRA who consented to participate in the study. The control group included patients without cerebral artery stenosis who consented to participate in the study. The medical records and brain MRA scans were reviewed and determined by H.G.K (a neurologist). A total of 64 research subjects were included: 32 in the treatment group and 32 in the control group. The study subjects received an explanation of the PPG test method, provided written consent, and underwent PPG measuring. This study was conducted after receiving approval from the Chosun University Hospital Medical Ethics Review Committee (CHOSUN 2016-06-017).

Blood oxygen saturation measurement sensors were connected to an INNO-MEDU 100, a biological signal measurement system development kit based on medical grade sensors (INNOTEMS Co. Ltd., Korea). PPG probes were mounted on the index fingers of a study subject in a seated position. The pulse wave was measured for 2 minutes, and data were stored in a PC wirelessly. The PPG measures the pulse wave using the differences in light attenuation in the blood using the photodetector detecting the decay of transmitted light irradiated from a light-emitting diode light to the capillary vessel in an index finger. Figures 2(a) and 2(b) show screenshots of the measurement instrument and the PPG measurement software used in this study.

*2.2. Preprocessing.* It is necessary to resample a certain number of waveform data within a set timeframe to compare the magnitude of the subjects' waveform amplitudes measured

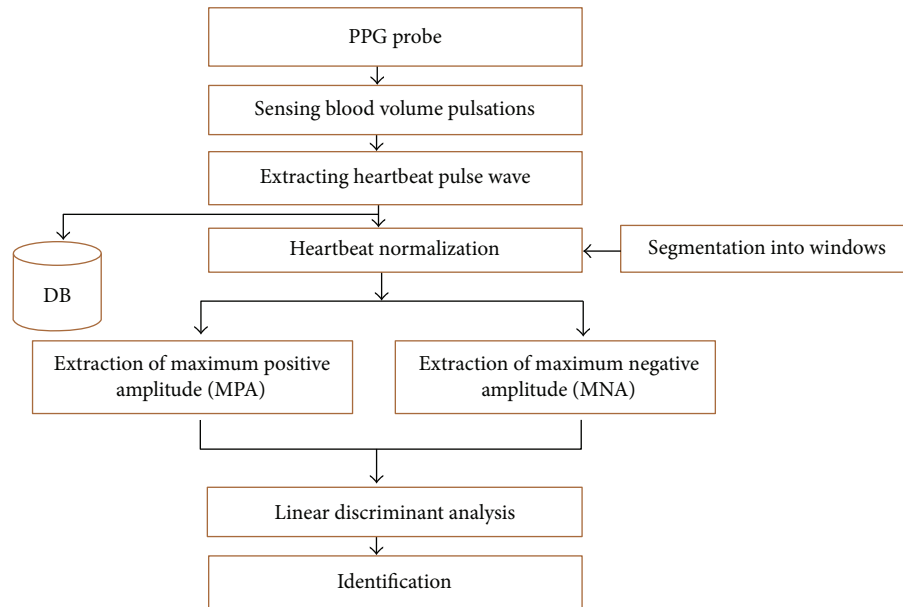


FIGURE 1: Flow diagram of the proposed screening method.

by the PPG pulse wave. The resampling of this study was conducted by extracting 66,000 data points during 1 minute (60 seconds) from the initial waveform data points (1,200,000) extracted at a 1 KHz sampling rate during 2 minutes (Figure 3(a)). After resampling in 66,000 data points, the resampled data size reduced to 449 KB from the initial waveform data size 10.3 MB. The reduced data size provides great advantages for fast processing time and a small memory size. The resampling data were designed to facilitate the extraction of the heart rate within the waveform. The extracted resampling data have an overlapped wave pattern in a single heartbeat (Figure 3(b)).

Therefore, the second step of the resampling procedure should be conducted to remove it and produce the optimized sample pulse wave (Figure 3(c)). The optimization sampling was used to design the sampling interval to make the pulse wave include mean heart rate per minute. In this study, sampling was conducted at 23 intervals. Figure 4 shows the pulse waves extracted from the control and treatment groups after the optimization sampling. The results revealed that the amplitude of the normal subject (Figure 4(a)) was larger than that of the patient with cerebral artery stenosis (Figure 4(b)).

**2.3. Feature Extraction.** Multiple optimally sampled pulse waves were normalized to reduce the changes in the pulse wave signals that showed variations. Pulse wave normalization was conducted as follows:

$$w = \sqrt{\sum_{j=1}^N (Y_{ij})^2}, \quad (1)$$

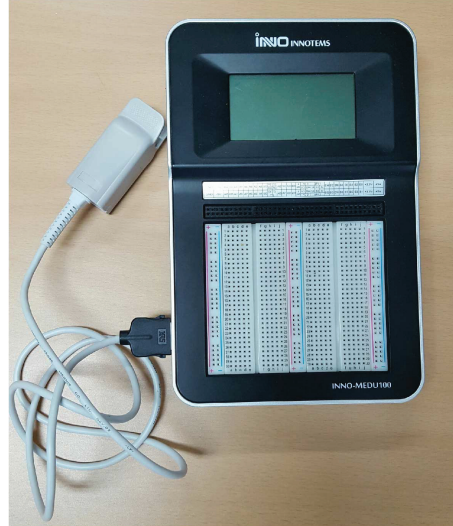
$$Y_i^* = \frac{Y_i}{w}.$$

$Y = \{Y_i\}_{i=1}^N$  can be calculated where  $Y$  is the total number of measurements obtained from the subject and  $N$  is the

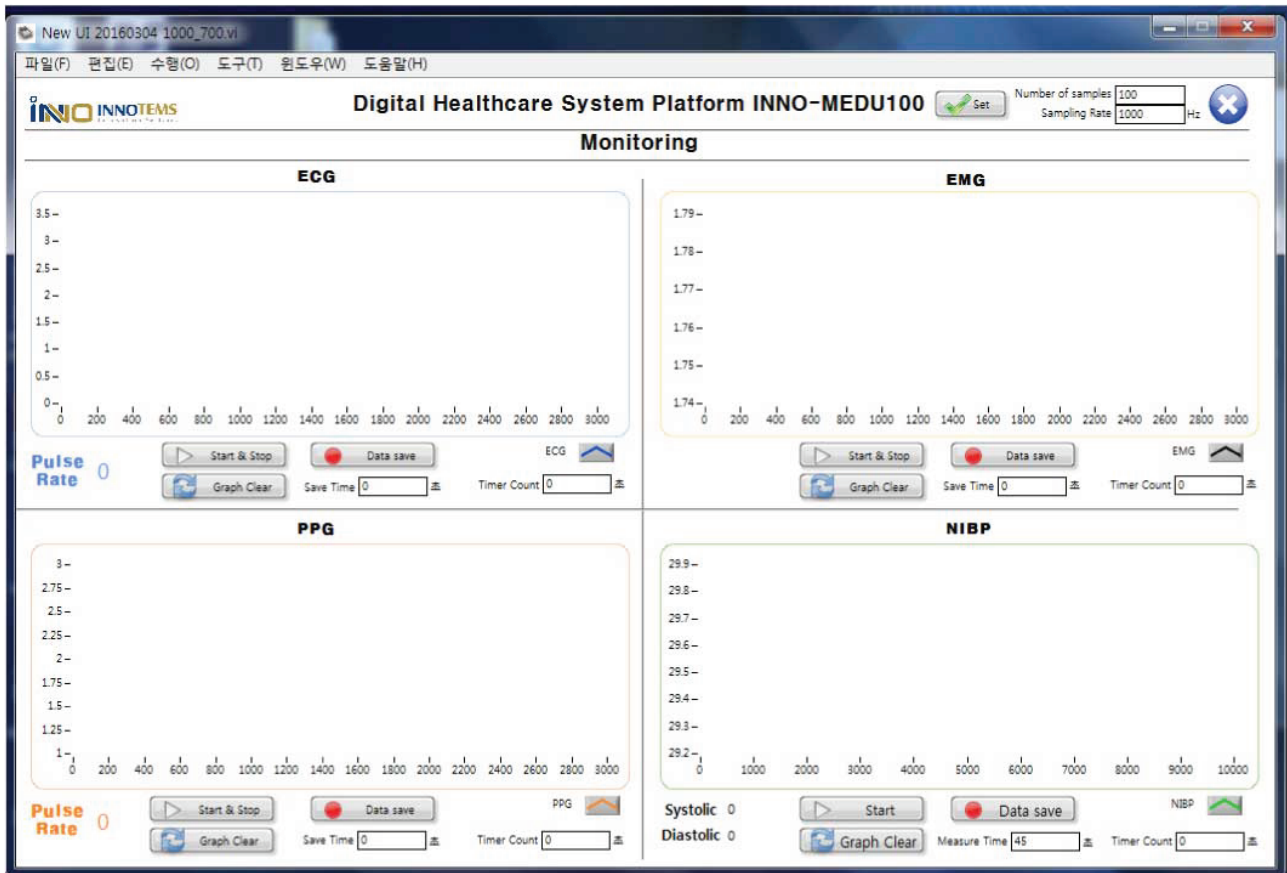
number of subjects. Moreover, the pulse waves obtained from the same subject can be expressed as  $Y_i = \{Y_{ij}\}_{j=1}^{N_i}$ . Pulse wave ( $Y_{ij}$ ) indicates the  $j$ th pulse wave of the  $i$ th subject.

The normalized pulse wave of each subject was divided into multiple windows, and a representative pulse wave amplitude was calculated for the pulse wave of each window. The advantage of dividing the whole section into windows is the possible extraction of representative feature values from each similar pulse wave section in a continuous time scale. Moreover, it makes it possible to easily compare the magnitudes of the amplitudes between subjects in the same window. Two feature values were extracted for each window (i.e., maximum positive amplitude [MPA] and maximum negative amplitude [MNA]). MPA indicated the largest positive amplitude, and MNA indicated the largest negative amplitude in each window. Consequently, 120 features were extracted from 60 windows for each subject.

**2.4. Identification.** Normal subjects and those with cerebral artery stenosis were classified using a linear discriminant analysis (LDA) algorithm [22] based on the extracted MPA and MNA feature values. LDA is a method that uses a linear classifier and dimensionality reduction by mapping data along the main axis to maximize the class separation in a specific space. It can be used as a classifier when it is applied to previously extracted features. The basic principle of the LDA algorithm is to reduce the dimension of a feature vector for data by maximizing the ratio of inter- and intraclass scatter. Electrocardiography and oscillometric arterial blood pressure measurements were used to identify individuals using features of the heartbeats [23, 24]. These studies reported that the LDA technique is a successful classifier for the amplitude features of the heart rate. It was believed that the amplitude



(a)



(b)

FIGURE 2: (a) Measurement device. (b) Screenshot of the photoplethysmography (PPG) measurement software.

features extracted from the capillary blood vessels from the proposed PPG would be similar to the amplitude features of previous studies. Consequently, this study used the LDA algorithm to optimally classify normal subjects and those with cerebral artery stenosis using the MPA and MNA features extracted from each window.

When  $N = \sum_{i=1}^C C_i$  of the study subjects exists,  $C$  represents the classes to be classified and  $N$  is the number of PPG samples extracted from all subjects. This study classified the PPG samples of the 64 subjects into two groups. When a learning group is considered  $Y = \{Y_i^*\}_{i=1}^C$ , each class is composed of  $Y_i^* = \{Y_{ij}^*\}_{j=1}^{C_i}$  in the  $C$  class, where  $Y_{ij}^*$  indicates the

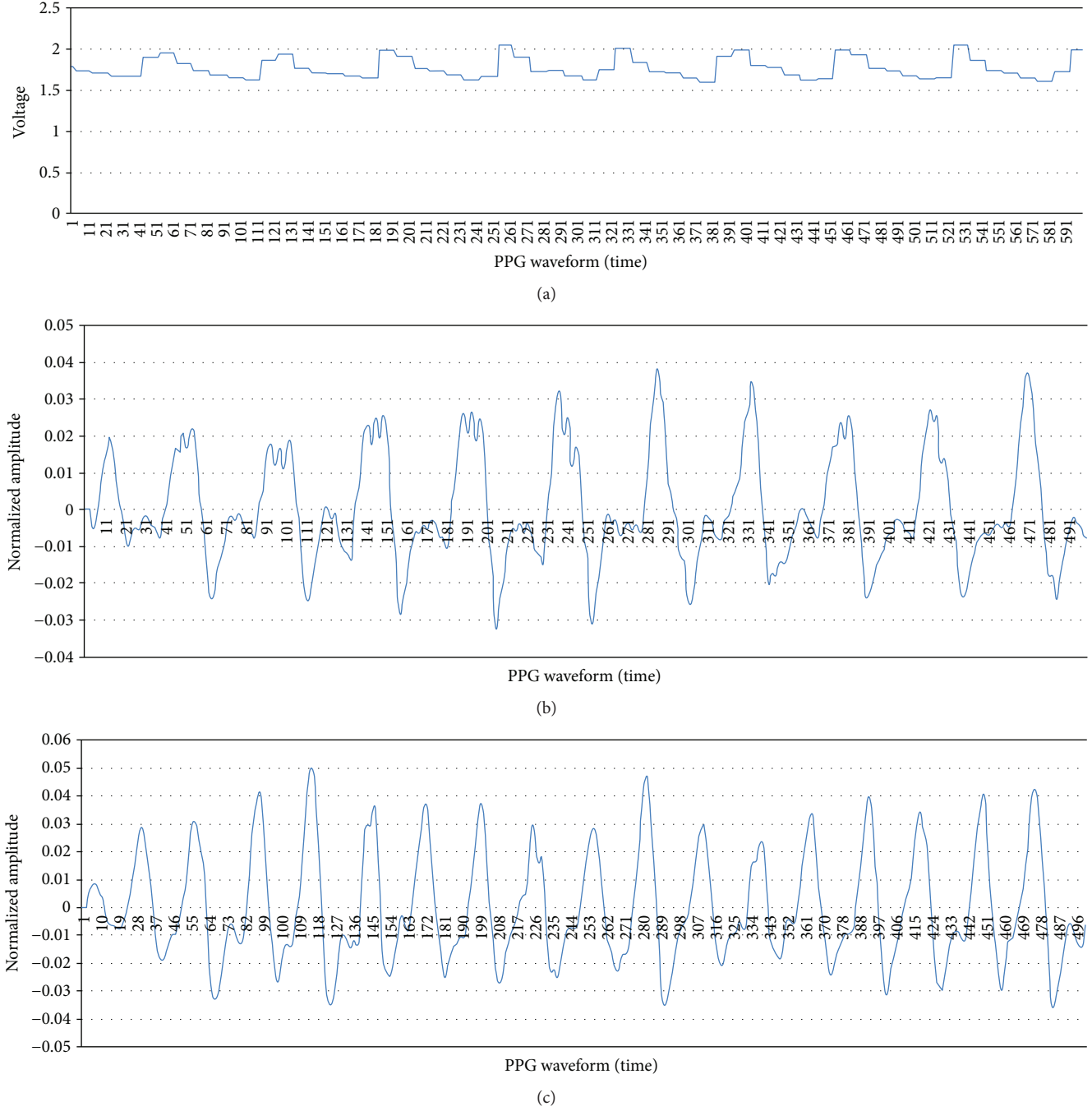


FIGURE 3: (a) Original PPG signal acquired from the measurement device. (b) Resampled PPG signal. (c) Optimized PPG signal.

features extracted from the PPG.  $S_{WT}$  and  $S_{BT}$  represent intra- and interclass scatter, respectively, as follows:

$$S_{WT} = \frac{1}{N} \sum_{i=1}^c \sum_{j=1}^{c_i} (Y_{ij}^* - \mu_i) (Y_{ij}^* - \mu_i)^T, \quad (2)$$

$$S_{BT} = \frac{1}{N} \sum_{i=1}^c (\mu_i - \mu) (\mu_i - \mu)^T.$$

$C$  represents the number of classes, and  $c_i$  indicates the feature values in class  $i$ . The symbols  $\mu_i$ ,  $\mu$ , and  $Y_{ij}^*$  represent

the mean of class  $i$ , the mean of all classes, and the  $j$ th feature value of class  $i$ , respectively. LDA finds a set of feature basis vectors described by  $\psi$  that maximizes the ratio between  $S_{WT}$  and  $S_{BT}$  of the training sample set [22] as follows:

$$\psi = \arg \max \frac{|\psi^T S_{BT} \psi|}{|\psi^T S_{WT} \psi|}. \quad (3)$$

When  $S_{WT}$  is nonsingular, the basis vectors  $\psi$  in (3) correspond to the first  $M(\leq N)$  eigenvectors with the largest eigenvalues of  $S_{WT}^{-1} S_{BT}$ . The feature representation based on

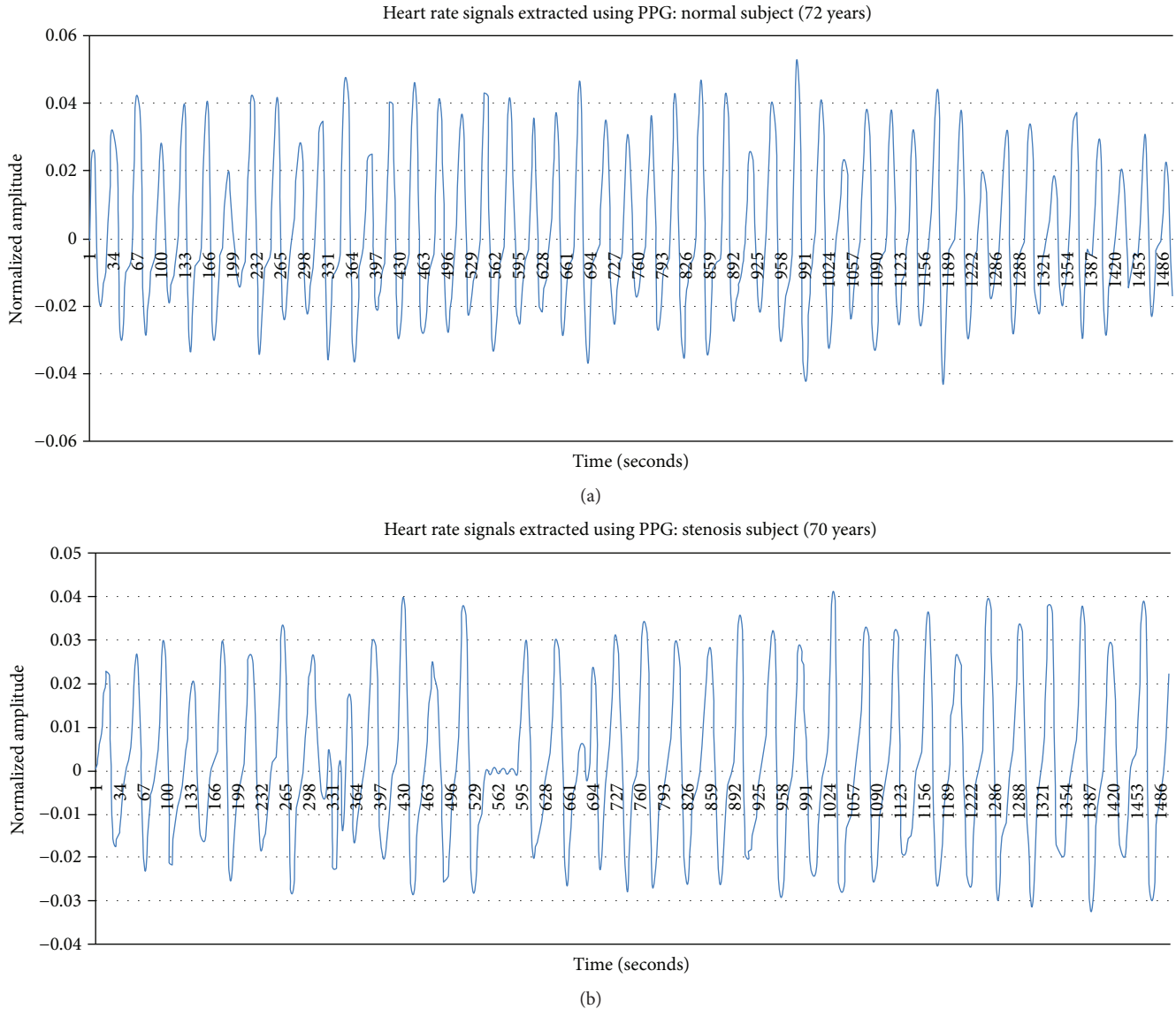


FIGURE 4: Pulse wave signals extracted from a normal subject and from a subject with cerebral artery stenosis after optimization sampling: (a) normal subject and (b) cerebral artery stenosis subject.

the LDA is produced by projecting input features  $Y^*$  onto the subspace spanned by the  $M$  eigenvectors  $X = \psi^T Y^*$ .

### 3. Results

The classification results of the control group and treatment group were determined using the first eigenvector of the LDA algorithm and the MPA and MNA feature values. The MPA and MNA data extracted from both index fingers of the 64 study subjects were studied: 32 subjects in the control group (mean age,  $59.8 \pm 14.6$  years) and 32 subjects in the treatment group (mean age,  $62.7 \pm 11.2$  years). The feature values of MPA and MNA were composed of 60 data points each. Figure 5 shows the classification results of the control and treatment groups using the first eigenvector and the second eigenvector in the LDA algorithm after applying each MPA and MNA feature. Figure 5(a) reveals the results after

application of the MPA features, while Figure 5(b) indicates the results after application of the MNA features. Regarding the decision boundary of the control and treatment groups, a patient was classified into the cerebral artery stenosis group when the first eigenvector from the LDA results was larger than 0 or into the normal group when it was smaller than 0.

The results showed that the recognition rate was higher when the features of both index fingers were used than when those of only one index finger were used. When the features of both index fingers were used, the recognition rate using MPA was 92.2%, while that using MNA was 90.6%. Table 1 compares the recognition rate results when the features of the right index finger, left index finger, and both index fingers were used. When the combination of MPA and MNA was used for the classification, the recognition rate was 90.6%, which was not better than the results derived from the independent use of the MPA and MNA features. Table 2 shows

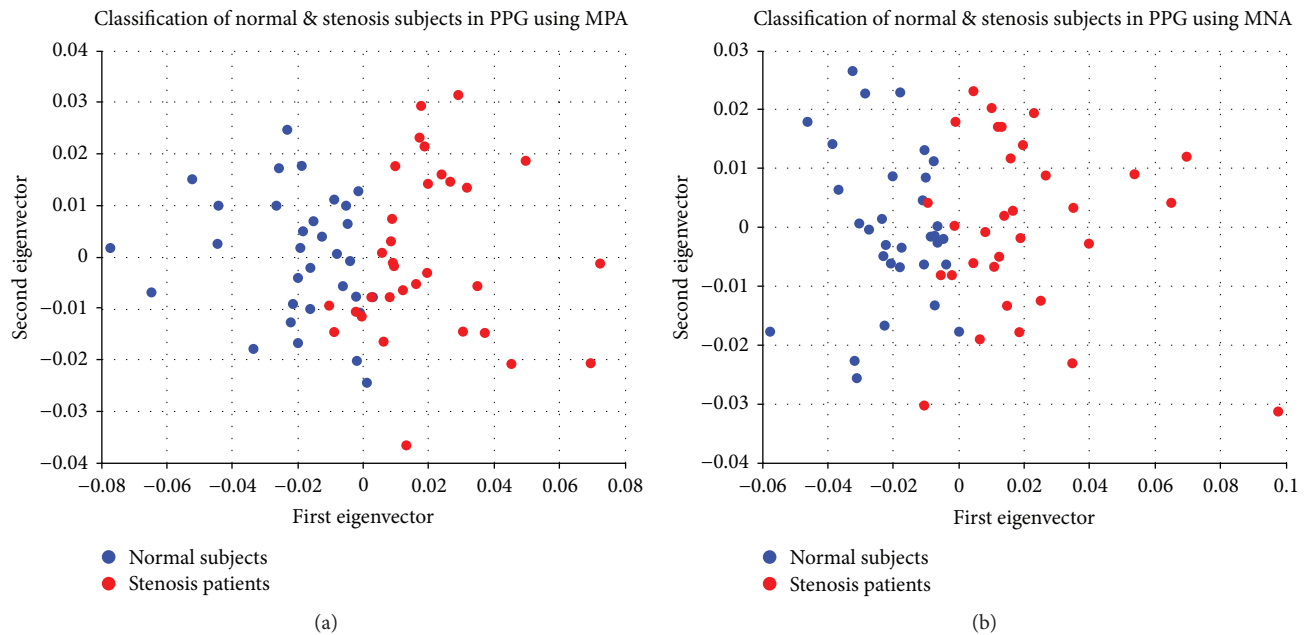


FIGURE 5: Classification results of normal subjects and those with cerebral artery stenosis using a linear discriminant analysis algorithm after applying the maximum positive amplitude (MPA) and maximum negative amplitude (MNA): (a) MPA features and (b) MNA features.

TABLE 1: Experimental results based on the linear discriminant analysis (LDA).

| Feature type               | Experiment                | Recognition rate (%) |
|----------------------------|---------------------------|----------------------|
| Maximum positive amplitude | Left + right index finger | 92.2                 |
|                            | Left index finger         | 78.1                 |
|                            | Right index finger        | 81.1                 |
| Maximum negative amplitude | Left + right index finger | 90.6                 |
|                            | Left index finger         | 76.6                 |
|                            | Right index finger        | 79.7                 |

TABLE 2: Sensitivity and specificity for the proposed technique in the best recognition rate.

| Proposed technique | Feature type | Performance parameters      |                             |
|--------------------|--------------|-----------------------------|-----------------------------|
|                    |              | Sensitivity (true positive) | Specificity (true negative) |
| Proposed technique | MPA          | 90.6%                       | 93.8%                       |
|                    | MNA          | 80%                         | 100%                        |

MPA: maximum positive amplitude; MNA: maximum negative amplitude.

the sensitivity and specificity of the normal subjects and those with cerebral artery stenosis within the highest recognition rate. Sensitivity and specificity using the MPA features were 90.6% and 93.8%, respectively, while those using MNA features were 80% and 100%, respectively.

#### 4. Discussion

Precision instruments such as MRA, CTA, CUS, and TCD are used to diagnose cerebral artery stenosis and have many advantages. However, diagnosing cerebral artery stenosis using PPG signals is advantageous because it is noninvasive, simple to use, and inexpensive. During the study period, 98

patients were asked to participate in this study. Of them, 31 patients refused to participate (control group: 19, stenosis group: 12) and 3 patients excluded due to poor image quality. Finally, 64 patients were enrolled and analyzed. The results of this study confirm the possibility of screening for cerebral artery stenosis using the PPG signal characteristics. The results of this study can be summarized as follows.

First, the results of the study indicated that the MPA and MNA features of the PPG signal may contribute to screening for early stage cerebral artery stenosis. In particular, MPA features are expected to show high classification accuracy, specifically 92.2%, for normal people and patients with cerebral artery stenosis. In contrast, MNA features revealed a

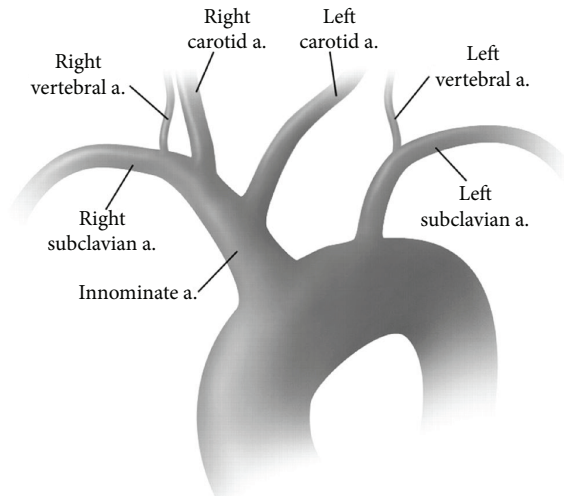


FIGURE 6: Anatomy of the common aortic arch branching patterns of the innominate, left carotid, and left subclavian arteries [26].

90.6% accuracy. Sensitivity and specificity analyses, a statistical method for evaluating performance, indicated that MPA features had a sensitivity of 90.6% and a specificity of 93.8%, while MNA features had a sensitivity of 80% and a specificity of 100%. A test's sensitivity represents its ability to correctly identify patients with a certain condition [25]. Regarding a medical diagnostic test's ability to diagnose a disease, sensitivity means the percentage of people with the disease. On the other hand, specificity refers to a test's ability to correctly identify patients without a specific condition. Regarding medical diagnostic tests, sensitivity means the ratio of correctly diagnosed healthy people without the disease. The results of this study showed that the classification using MPA features showed >90% accuracy sensitivity and specificity, suggesting that MPA features have high accuracy for differentiating subjects with cerebral artery stenosis from normal subjects. The MNA features were less effective at identifying patients with cerebral artery stenosis (80%) but very effective at detecting normal people (100%).

Second, using both index fingers showed the highest discrimination power for screening for early stage cerebral artery stenosis using the MPA and MNA features of PPG signals. In particular, the recognition rate of the right index finger was higher than that of the left index finger using both MPA and MNA features. This could be because of the anatomical characteristics that the left subclavian artery, delivering the blood from the heart to left arm, and common carotid artery, delivering the blood from the heart to the brain, emerge separately from the aortic arch on the left side of the body while the right subclavian artery, delivering the blood from the heart to the right arm, and right common carotid artery, delivering the blood from the heart to the brain, split from the innominate artery at the neck (Figure 6). In other words, we believe that the recognition rate was higher because the presence of cerebral artery stenosis could affect the ability of the right subclavian artery to move blood through the innominate artery to the right arm.

Third, discrimination between the normal group and the cerebral artery stenosis group could be successfully achieved using the first eigenvector of the LDA classification algorithm using the PPG signal. The decision boundary distinguishing normal people from people with cerebral artery stenosis was first eigenvector = 0; a positive first eigenvector indicated patients with cerebral artery stenosis, while a negative first eigenvector indicated normal people. The majority of errors generated in the recognition rate using the MPA and MNA features occurred in data near the decision boundary of a 0 value.

Fourth, the MPA and MNA features from PPG signals were determined as the important detector parameters for distinguishing normal people from those with cerebral artery stenosis. In particular, MPA features were considered the most important parameter with the best discriminatory power to detect the possibility of cerebral artery stenosis.

## 5. Conclusions

The objective of the study was to evaluate the correlation between cerebral artery stenosis and the PPG signal characteristics that could reflect the characteristics of the microvessels in the tissues according to the contraction and relaxation period of the heart. The study results showed that the MPA and MNA features of the PPG signals measured on the index fingers of both hands were important parameters for discriminating cerebral artery stenosis. MPA had particularly high discrimination power. Moreover, the right index finger better identified cerebral artery stenosis than the left index finger. One limitation of the study was its sample size. The study was conducted after patients provided informed consent, so it was challenging to secure a large number of study subjects. Therefore, the generalization of the study results should be made carefully. We plan to conduct a systematic study including more patients to identify a powerful and accurate marker for identifying patients with cerebral artery stenosis. To secure a large number of study subjects, we are designing multicenter linking neighboring hospitals and hospitals of overpopulation zone in the metropolitan area. The study results confirmed that PPG was a successful tool for screening for early stage cerebral artery stenosis. When a patient with cerebral artery stenosis is identified on the screening, the patient may receive clinical or drug treatment after a thorough examination. It is expected that the method presented here will play an important role in preventing cerebrovascular disease, which places a great burden on advanced society.

## Disclosure

An earlier version of this work was presented as a poster at Korean Stroke Society, September 2017.

## Conflicts of Interest

The authors declare that they have no conflicts of interest.

## Acknowledgments

This study was supported by research funds from Chosun University in 2016.

## References

- [1] J. Allen, "Photoplethysmography and its application in clinical physiological measurement," *Physiological Measurement*, vol. 28, no. 3, pp. R1–R39, 2007.
- [2] S. C. Millasseau, J. M. Ritter, K. Takazawa, and P. J. Chowienczyk, "Contour analysis of the photoplethysmographic pulse measured at the finger," *Journal of Hypertension*, vol. 24, no. 8, pp. 1449–1456, 2006.
- [3] P.-H. Lai and I. Kim, "Lightweight wrist photoplethysmography for heavy exercise: motion robust heart rate monitoring algorithm," *Healthcare Technology Letters*, vol. 2, no. 1, pp. 6–11, 2015.
- [4] H. H. Asada, P. Shaltis, A. Reisner, S. Rhee, and R. C. Hutchinson, "Mobile monitoring with wearable photoplethysmographic biosensors," *IEEE Engineering in Medicine and Biology Magazine*, vol. 22, pp. 28–40, 2013.
- [5] I. Imanaga, H. Hara, S. Koyanagi, and K. Tanaka, "Correlation between wave components of the second derivative of plethysmogram and arterial distensibility," *Japanese Heart Journal*, vol. 39, no. 6, pp. 775–784, 1998.
- [6] B. Jönsson, C. Laurent, T. Skau, and L. -G. Nindberg, "A new probe for ankle systolic pressure measurement using photoplethysmography (PPG)," *Annals of Biomedical Engineering*, vol. 33, no. 2, pp. 232–239, 2005.
- [7] R. Erts, J. Spigulis, I. Kukulis, and M. Ozols, "Bilateral photoplethysmography studies of the leg arterial stenosis," *Physiological Measurement*, vol. 26, no. 5, pp. 865–874, 2005.
- [8] J.-X. Wu, B. Y. Lim, C. M. Li, M. J. Wu, C. H. Lin, and Y. C. du, "Bilateral photoplethysmography analysis for arteriovenous fistula dysfunction screening with fractional-order feature and cooperative game-based embedded detector," *Healthcare Technology Letters*, vol. 2, no. 3, pp. 64–69, 2015.
- [9] J.-X. Wu, C.-M. Li, Y.-R. Ho, M.-J. Wu, P.-T. Huang, and C.-H. Lin, "Bilateral photoplethysmography analysis for peripheral arterial stenosis screening with a fractional-order integrator and info-gap decision-making," *IEEE Sensors Journal*, vol. 16, no. 8, pp. 2691–2700, 2016.
- [10] Y.-C. Du and A. Stephanus, "A novel classification technique of arteriovenous fistula stenosis evaluation using bilateral PPG analysis," *Micromachines*, vol. 7, no. 12, p. 147, 2016.
- [11] J. Simek, D. Wichterle, V. Melenovský, J. Malík, S. Svacina, and J. Widimský, "Second derivative of the finger arterial pressure waveform: an insight into dynamics of the peripheral arterial pressure pulse," *Physiological Research*, vol. 54, no. 5, pp. 505–513, 2005.
- [12] E. Zahedi, K. Chellappan, M. A. M. Ali, and H. Singh, "Analysis of the effect of ageing on rising edge characteristics of the photoplethysmogram using a modified Windkessel model," *Cardiovascular Engineering*, vol. 7, no. 4, pp. 172–181, 2007.
- [13] P. Uangpaioj and M. Shibata, "Evaluation of vascular wall elasticity of human digital arteries using alternating current-signal photoplethysmography," *Vascular Health and Risk Management*, vol. 9, pp. 283–295, 2013.
- [14] A. Buchs, Y. Slovik, M. Rapoport, C. Rosenfeld, B. Khanokh, and M. Nitzan, "Right-left correlation of the sympathetically induced fluctuations of photoplethysmographic signal in diabetic and non-diabetic subjects," *Medical & Biological Engineering & Computing*, vol. 43, no. 2, pp. 252–257, 2005.
- [15] L. A. Bortolotto, J. Blacher, T. Kondo, K. Takazawa, and M. E. Safar, "Assessment of vascular aging and atherosclerosis in hypertensive subjects: second derivative of photoplethysmogram versus pulse wave velocity," *American Journal of Hypertension*, vol. 13, no. 2, pp. 165–171, 2000.
- [16] J. C. Dorlas and J. A. Nijboer, "Photo-electric plethysmography as a monitoring device in anaesthesia. Application and interpretation," *British Journal of Anaesthesia*, vol. 57, no. 5, pp. 524–530, 1985.
- [17] T. Gao, W. Yu, and C. Liu, "Mechanisms of ischemic stroke in patients with intracranial atherosclerosis: a high-resolution magnetic resonance imaging study," *Experimental and Therapeutic Medicine*, vol. 7, no. 5, pp. 1415–1419, 2014.
- [18] W.-H. Xu, J. Liu, M.-L. Li, Z.-Y. Sun, J. Chen, and J.-H. Wu, "3D printing of intracranial artery stenosis based on the source images of magnetic resonance angiograph," *Annals of Translational Medicine*, vol. 2, no. 8, p. 74, 2014.
- [19] H.-J. Seo, J. R. Pagsisihan, J.-C. Paeng et al., "Hemodynamic significance of internal carotid or middle cerebral artery stenosis detected on magnetic resonance angiography," *Yonsei Medical Journal*, vol. 56, no. 6, pp. 1686–1693, 2015.
- [20] J.-M. Kim, K. H. Jung, C. H. Sohn, J. Moon, M. H. Han, and J. K. Roh, "Middle cerebral artery plaque and prediction of the infarction pattern," *Archives of Neurology*, vol. 69, no. 11, pp. 1470–1475, 2012.
- [21] A. J. Degnan, G. Gallagher, Z. Teng, J. Lu, Q. Liu, and J. H. Gillard, "MR angiography and imaging for the evaluation of middle cerebral artery atherosclerotic disease," *American Journal of Neuroradiology*, vol. 33, no. 8, pp. 1427–1435, 2012.
- [22] R. O. Duda, P. E. Hart, and D. G. Stork, *Pattern Classification*, Wiley Press, New York, NY, USA, 2nd edition, 2001.
- [23] Y. Wang, F. Agrafioti, D. Hatzinakos, and K. N. Plataniotis, "Analysis of human electrocardiogram for biometric recognition," *EURASIP Journal on Advances in Signal Processing*, vol. 2008, no. 1, article 148658, 2007.
- [24] Y.-S. Shin, "Monitoring personalized trait using oscillometric arterial blood pressure measurements," *Journal of Applied Mathematics*, vol. 2012, Article ID 591252, 12 pages, 2012.
- [25] D. G. Altman and J. M. Bland, "Statistics notes: diagnostic tests 1: sensitivity and specificity," *BMJ*, vol. 308, no. 6943, p. 1552, 1994.
- [26] K. F. Layton, D. F. Kallmes, H. J. Cloft, E. P. Lindell, and V. S. Cox, "Bovine aortic arch variant in humans: clarification of a common misnomer," *American Journal of Neuroradiology*, vol. 27, no. 7, pp. 1541–1542, 2006.

## Research Article

# sEMG Signal Acquisition Strategy towards Hand FES Control

**Cinthya Lourdes Toledo-Peral,<sup>1</sup> Josefina Gutiérrez-Martínez<sup>1</sup>,  
Jorge Airy Mercado-Gutiérrez,<sup>1</sup> Ana Isabel Martín-Vignon-Whaley,<sup>2</sup>  
Arturo Vera-Hernández<sup>3</sup>, and Lorenzo Leija-Salas<sup>3</sup>**

<sup>1</sup>*División de Investigación en Ingeniería Médica, Instituto Nacional de Rehabilitación “Luis Guillermo Ibarra Ibarra”, Calz. México-Xochimilco No. 289, Col. Arenal de Guadalupe, Tlalpan, 14389 Ciudad de México, Mexico*

<sup>2</sup>*Facultad de Ingeniería, Universidad La Salle, Benjamín Franklin 45, Col. Condesa, Cuauhtémoc, 06140 Ciudad de México, Mexico*

<sup>3</sup>*LAREMUS, Sección Bioelectrónica, Departamento de Ingeniería Eléctrica, Centro de Investigación y de Estudios Avanzados del Instituto Politécnico Nacional, Av. Instituto Politécnico Nacional 2508, Col. San Pedro Zacatenco, Gustavo A. Madero, 07360 Ciudad de México, Mexico*

Correspondence should be addressed to Josefina Gutiérrez-Martínez; [josefina\\_gutierrez@hotmail.com](mailto:josefina_gutierrez@hotmail.com)

Received 11 August 2017; Revised 1 December 2017; Accepted 27 December 2017; Published 14 March 2018

Academic Editor: Kunal Mitra

Copyright © 2018 Cinthya Lourdes Toledo-Peral et al. This is an open access article distributed under the Creative Commons Attribution License, which permits unrestricted use, distribution, and reproduction in any medium, provided the original work is properly cited.

Due to damage of the nervous system, patients experience impediments in their daily life: severe fatigue, tremor or impaired hand dexterity, hemiparesis, or hemiplegia. Surface electromyography (sEMG) signal analysis is used to identify motion; however, standardization of electrode placement and classification of sEMG patterns are major challenges. This paper describes a technique used to acquire sEMG signals for five hand motion patterns from six able-bodied subjects using an array of recording and stimulation electrodes placed on the forearm and its effects over functional electrical stimulation (FES) and volitional sEMG combinations, in order to eventually control a sEMG-driven FES neuroprosthesis for upper limb rehabilitation. A two-part protocol was performed. First, personalized templates to place eight sEMG bipolar channels were designed; with these data, a universal template, called forearm electrode set (FELT), was built. Second, volitional and evoked movements were recorded during FES application. 95% classification accuracy was achieved using two sessions per movement. With the FELT, it was possible to perform FES and sEMG recordings simultaneously. Also, it was possible to extract the volitional and evoked sEMG from the raw signal, which is highly important for closed-loop FES control.

## 1. Introduction

Neurological disabilities are caused by damage of the nervous system (which includes the brain and spinal cord); this damage results in the loss of capacity to move and manipulate things, especially if fine movements are required [1]. The effects of many neurological conditions can vary greatly from person to person, as well as from time to time for the same person. People with neurological conditions, such as a stroke, may present hand motor impairment and deficit in motor execution, severe fatigue and/or weakness, impaired hand dexterity, tremors, spasticity, abnormal muscle synergies, and deficit in motor planning and motor learning [2]. Stroke survivors may have great difficulty to modulate

muscle activation, and their ability to span region is curtailed [3].

Biomedical signals, such as surface electromyography (sEMG), play a significant role in the measurement of the electrical muscle contraction. Plus, its analysis is one of the standard procedures used to identify muscle actions in normal and pathologic conditions. sEMG signals can be used for various applications, which include identifying neuromuscular diseases, controlling signals for orthotic or prosthetic devices [4], anticipating movements of the muscles [5], controlling machines or robots, or detecting hand gestures to improve the quality of life [6].

sEMG patterns during movements exhibit a great deal of intersubject, intermuscle, and context-dependent variability.

Understanding the sEMG interactions in hand movements is a challenge [7]. Several researches have been directed to determine the extent to which each muscle participates in each synchronous and time-varying synergies for an individualized human hand motor pattern [8] or to predict the sEMG patterns associated with static hand postures [9]. These studies show the importance of considering different intensities and durations of sEMG bursts, temporal patterns, strength of the muscle contraction [10], and muscle synergy as a framework for sEMG patterns of hand postures.

sEMG patterns are used for neuromuscular biofeedback [11], robot-aided [12] training, and neurorehabilitation, as well as to control devices such as neuroprosthesis based on functional electrical stimulation (FES), to mimic a neuromuscular function for both upper and lower extremities [13], or to enhance hand motor recovery when physical therapy alone is ineffective in stroke patients [14] or with spinal cord injury [15].

Several techniques have been employed for addressing human hand movement patterns from sEMG signal. Techniques, such as an adaptive neuro-fuzzy inference system integrated with a real-time learning scheme and time-frequency features, have been used to identify hand motion commands suitable for hand prosthesis control [16]. Ordinal pattern analysis is used to describe corrections of sEMG recordings during hand open and hand close states. The results suggest that the mutual information analysis has potential in identifying different hand movements [17]. Usually, wavelet transformations and artificial neural network classifiers are used for hand movement analysis [10]. The Hilbert-Huang transform is another technique used to detect, measure, filter, and decompose sEMG signals in order to identify patterns in time, frequency, or space or the combination of flexion/extension arm movements. However, the sEMG patterns can present abnormal muscle synergies and be indistinguishable [18]. This fact could make the classification in some stroke patients more difficult; for example, a solution proposed in [3] is to use voice recognition as an auxiliary in a sEMG-driven actuated glove for clinical therapy purposes.

Recognizing sEMG signals with the aim of controlling assisting devices is not only concerned about feature extraction and classification of signals but the acquisition site is also of major importance.

M-wave is an electrophysiological response evoked by electrostimulation detected in standard sEMG. It has been studied widely in order to verify the functionality of the stimulation site measurement over the target muscle, which closely relates to muscle fiber recruitment. This electrophysiologically driven approach is expected to lead to the identification of selective electrode configurations of an array for functional movements [19]. However, finding the best electrode configuration for sEMG recording to get the right sequence for movement activation still represents a challenge.

This paper is related to the acquisition and analysis of sEMG signals for active movements and to obtaining usable hand patterns with simultaneous placing of recording and stimulation electrodes on the forearm, for the eventual

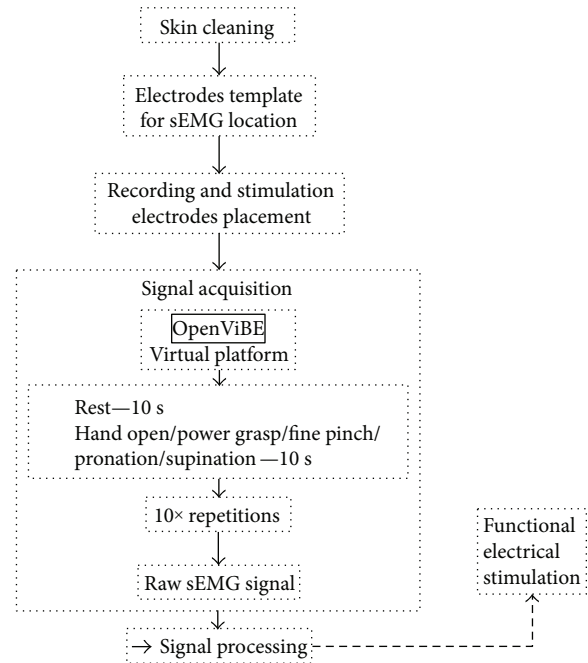


FIGURE 1: Electrode placement using a personalized template to find sEMG signal for acquisition task and stimulation location. After cleaning the skin and placing the electrodes, the isometric contraction (hand open, power grasp, fine pinch, pronation, and supination) was performed by the subject during 10 seconds, with 10 seconds for rest. The task was repeated 10 times. A session included a task for each movement.

control of a neuroprosthesis to aid in motor neurorehabilitation of patients suffering from a stroke aftermath.

The presented technique is based on an array of recording and stimulation electrodes on the forearm, used to acquire sEMG signals from five hand motion patterns from six able-bodied subjects, and the effects of this technique over functional electrical stimulation (FES) and volitional sEMG combinations.

## 2. Methodology

*2.1. Identification of sEMG Locations.* The first step was to find the best electrode positioning for sEMG recording. This position was found at the belly of the muscle, on the upper part of the forearm, which is formed by the following muscles: brachioradialis, palmaris longus, flexor carpi radialis, flexor carpi ulnaris, extensor carpi radialis longus, and extensor carpi ulnaris. Stimulation is performed at the ends of the same muscles.

In order to make sure that the electrodes were placed on the same positions for the different trials for each subject, a personalized template was made. This template was created as follows: for bipolar channel placement, eight spots, where the electrodes would be placed, were allocated and marked on a piece of acetate paper. Then, the unique physical characteristics of the individual and the positions of five stimulation bipolar electrodes were marked on the same paper. Once the places were allocated and the personalized template was designed, sEMG acquisition was carried out.

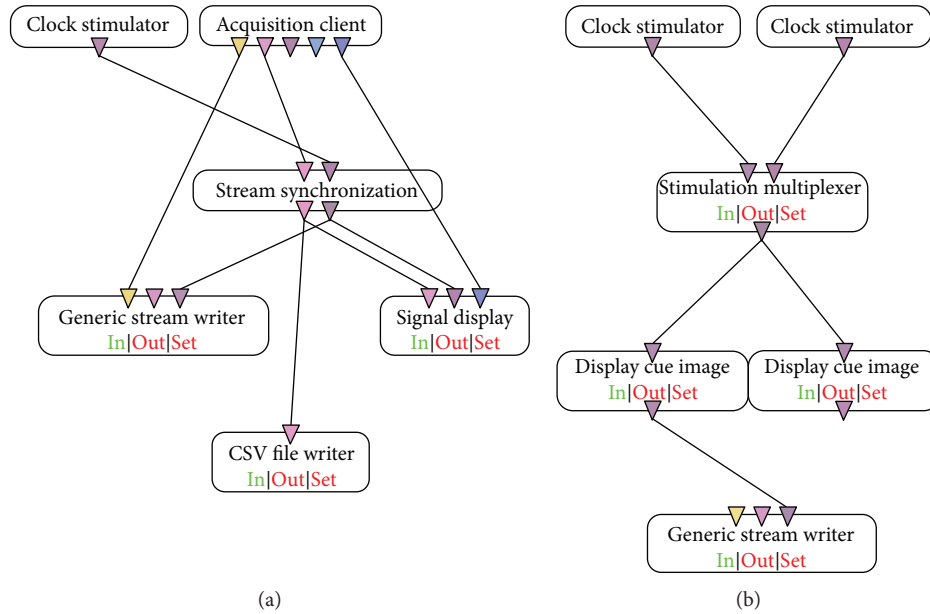


FIGURE 2: OpenViBE flow diagram used to acquire raw sEMG signal (a); image cue synchronization control (b). This algorithm completes a movement task.

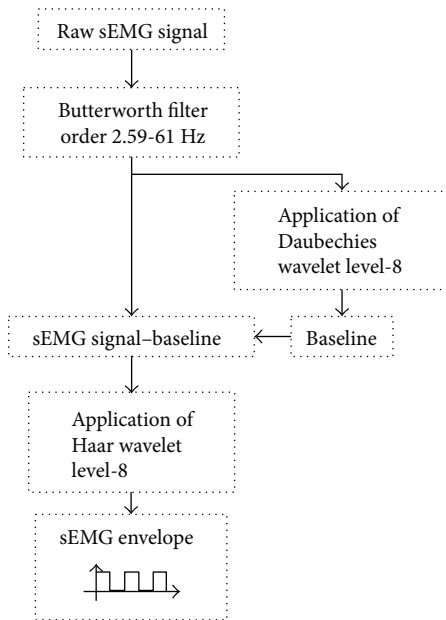


FIGURE 3: sEMG signal processing algorithm. The signal was filtered for 60 Hz, baseline was subtracted through DWT, and the envelope signal that selected the active pattern was obtained.

**2.2. sEMG Signals Acquisition.** Six able-bodied subjects were included for the acquisition of sEMG signals, their age ranged from 21 to 33 years old, three males and three females. The subject was sitting in a comfortable position with his/her right arm supinated and leaning on the table. The subject was asked to perform an isometric contraction for five movements: hand open, power grasp, fine pinch, pronation, and supination. While contraction was active, the forearm muscles that participate in the motion were palpated and located.

TABLE 1: Stimulation electrode positions for each of the five target movements.

| Target movement | Electrode position   |
|-----------------|--|
| Power grasp     | Finger and wrist flexors. Flexor carpi radialis, flexor carpi ulnaris, flexor digitorum superficialis. |
| Lumbrical grip  | Ulnar nerve. Flexor pollicis longus, flexor digitorum superficialis.                                   |
| Hand open       | Finger and wrist extensors. Extensor carpi radialis. Extensor digitorum.                               |
| Pronation       | Pronator teres.  |
| Supination      | Supinator.   |

The subject's skin was cleaned using an alcohol swab in order to reduce impedance and have a better coupling for the skin-electrode interface. Afterwards, the template was placed on the subject's forearm and marked; these were the spots where the electrodes should be placed. Figure 1 shows this procedure. The electrodes were kept in contact with the skin with a tubular mesh; this also reduced artifacts due to cable movements.

Electrodes were connected to an open-source platform called OpenViBE. This acquired the sEMG signal through a compatible open hardware acquisition device (OpenBCI) which was connected to a designer space, where an algorithm was designed for trial tasks (Figure 2).

OpenViBE configuration was 24 for gain, 250 Hz for sampling rate, and eight channels for sEMG. The subject was asked to perform the movement shown in a cue image while it was on the screen. The task started with a rest of 10 seconds, and it continued with a ten-second isometric contraction of hand open, power grasp, fine pinch, pronation, or supination, depending on the trial. Cue images were shown alternatively until the subject completed ten

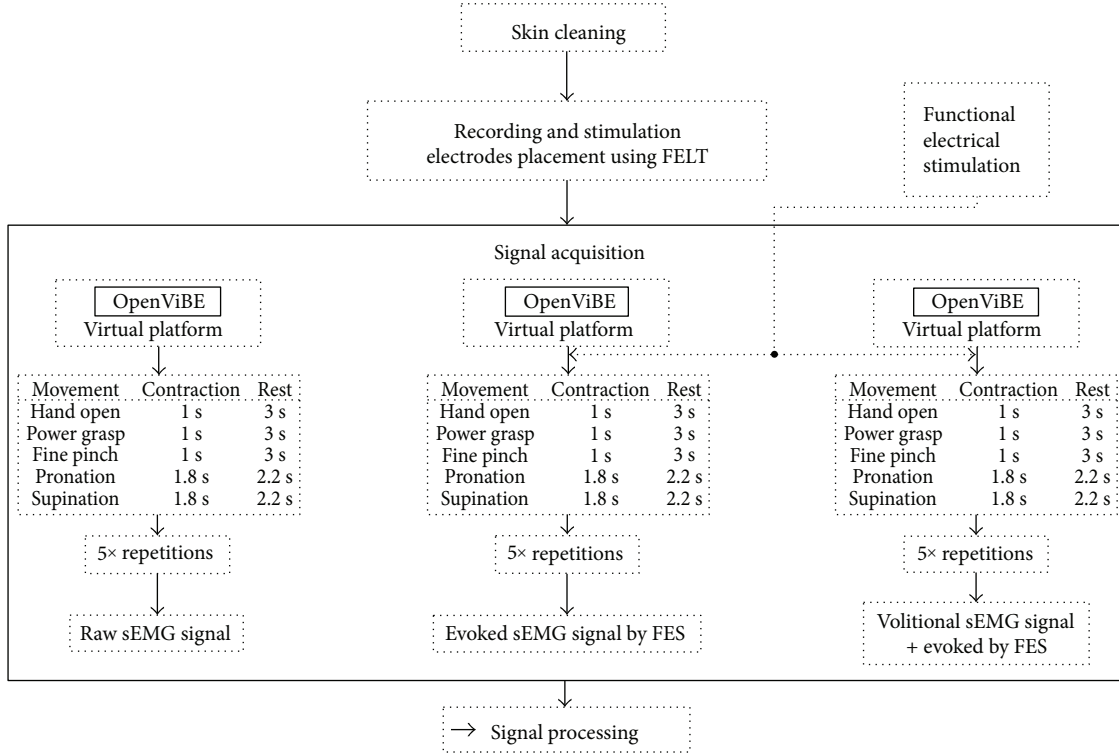


FIGURE 4: sEMG signal acquisition for tasks (hand open, power grasp, fine pinch, pronation, and supination) with FES stimulation. An isometric contraction was performed by the subject for each part of the trial. The motion was repeated 5 times per part. A session included 5 repetitions of volitional contraction, followed by 5 repetitions of sEMG evoked by FES, and finally, 5 repetitions of volitional contraction plus the evoked sEMG by the FES stimulation.

repetitions of the motion. A session was considered completed when two movement tasks were finished (Figure 1). All subjects completed two sessions for each of the mentioned motions. The tasks of sEMG recordings were saved as .csv files that included the information of eight channels and a time vector.

From all the personalized positions, which were based on common regions found for each subject, a universal template that kept the array for recording and stimulation electrodes was designed. It was called forearm electrode set (FELT).

**2.3. Preprocessing, Selection, and Feature Extraction.** Each sEMG record was imported into MATLAB® environment for processing. From the .csv files, information of eight channels and a time vector was extracted. As seen in Figure 3, the signal was cleaned from line interference at 60 Hz by using a Butterworth filter, order 2, with a 59 to 61 Hz bandwidth.

After acquisition, data were conditioned using discrete wavelet transforms (DWT). An eight-level decomposition using mother wavelet Daubechies-4 was applied, and the reconstructed signal was subtracted in order to eliminate baseline drift [20]; this was equivalent to filter a 0.7 Hz signal.

Then, the DWT was applied, again, to an eight-level decomposition, but this time a mother wavelet Haar was used in order to find the envelope of the signal, which was obtained from its reconstruction. This envelope was used to find the parts of the sEMG signal that represented a movement, in this case open hand or power grasp; then it was converted to a logic signal (Figure 3).

TABLE 2: Stimulation parameters for each subject and target movement.

| Subject | Movement | Pulse amplitude (mA <sub>p</sub> ) | Pulse width (μs) | Pulse frequency (Hz) | On/Off time (s) |
|---------|----------|------------------------------------|------------------|----------------------|-----------------|
| 1       | PG       | 10                                 | 300              | 30                   | 1/3             |
|         | LG       | 10                                 | 300              | 30                   | 1/3             |
|         | HO       | 10                                 | 500              | 30                   | 1/3             |
|         | SU       | 10                                 | 500              | 50                   | 1.8/2.2         |
|         | PR       | 10                                 | 500              | 30                   | 1.8/2.2         |
| 2       | PG       | 10                                 | 300              | 30                   | 1/3             |
|         | LG       | 12                                 | 300              | 30                   | 1/3             |
|         | HO       | 10                                 | 300              | 30                   | 1/3             |
|         | SU       | 10                                 | 300              | 50                   | 1.8/2.2         |
|         | PR       | 10                                 | 300              | 30                   | 1.8/2.2         |
| 3       | PG       | 10                                 | 300              | 30                   | 1/3             |
|         | LG       | 8                                  | 400              | 30                   | 1/3             |
|         | HO       | 12                                 | 300              | 30                   | 1/3             |
|         | SU       | 10                                 | 500              | 50                   | 1.8/2.2         |
|         | PR       | 10                                 | 500              | 30                   | 1.8/2.2         |

PG: power grasp; HO: hand open; SU: forearm supination; PR: forearm pronation; LG: lumbrical grip, applied through the RehaStim 2 electrical stimulator.

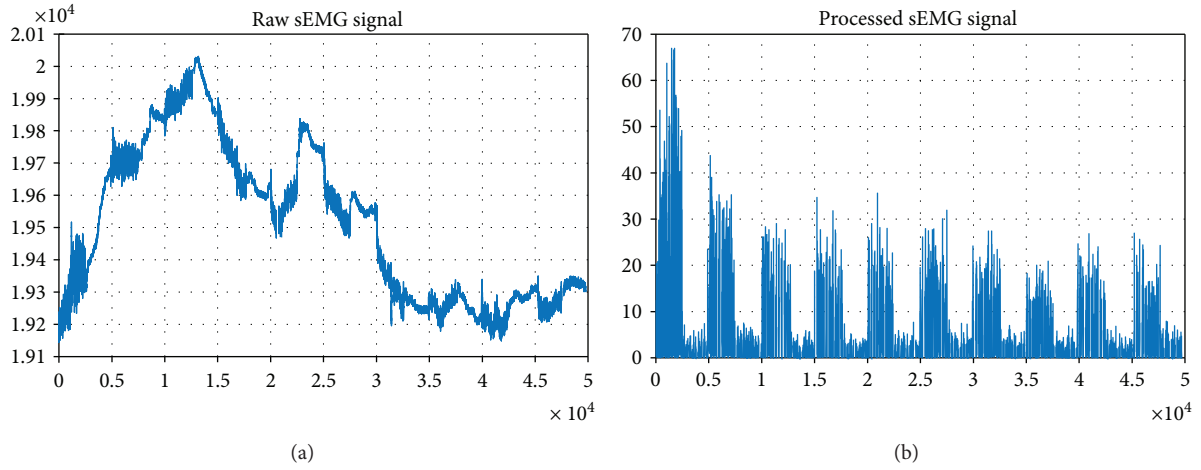


FIGURE 5: Subject 1, open hand/rest. Comparison of sEMG signal before and after processing using DWT. (a) Raw sEMG signal containing baseline drift and 60 Hz noise. (b) Processed sEMG signal drift-free and visible active and rest patterns.

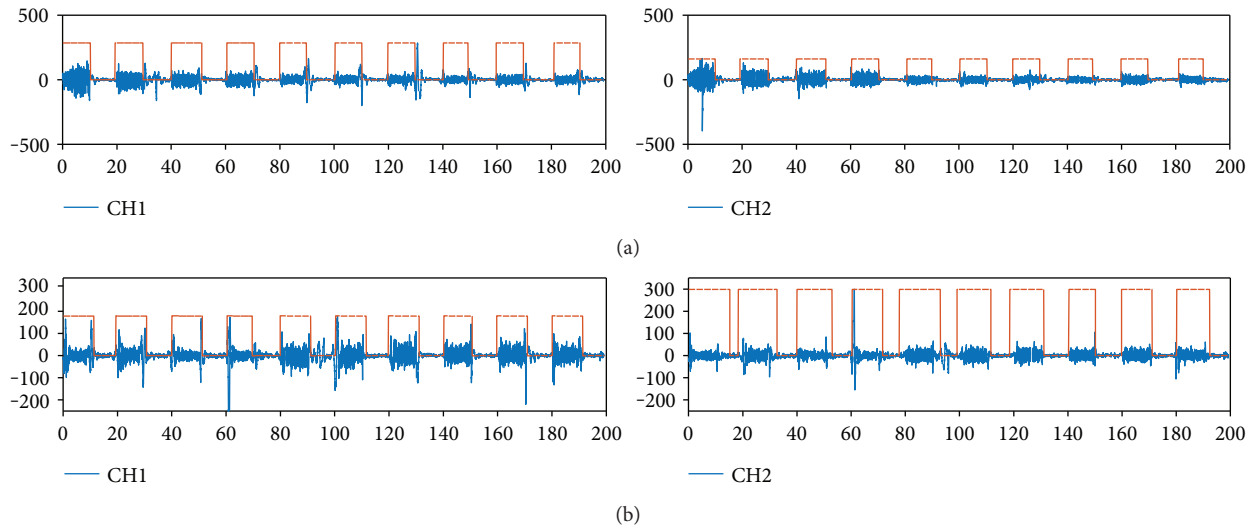


FIGURE 6: For subject 1, (a) open hand and (b) power grasp, sEMG processed and envelope signal obtained for active pattern selection. Example for channels 1 and 2 of 8.

In order to find the characteristic features of the five target movements, the following parameters were calculated: mean absolute value—MAV (1), wave length—WL (2), zero crossing—ZC (3), standard deviation—SD (4), integral of absolute value—IAV (5), variance—V (6), and slope sign change—SSC (7).

$$\text{MAV} = \frac{1}{n} \sum_{i=1}^n |x_i|, \quad (1)$$

$$\text{WL} = \sum_{i=1}^n |x_i - x_{i-1}|, \quad (2)$$

$$\text{ZC} = \sum_{i=1}^{n-1} \begin{cases} 1, & x_{i+1} < 0, x_i > 0, \\ 1, & x_{i+1} > 0, x_i < 0, \\ 0, & \text{else.} \end{cases} \quad (3)$$

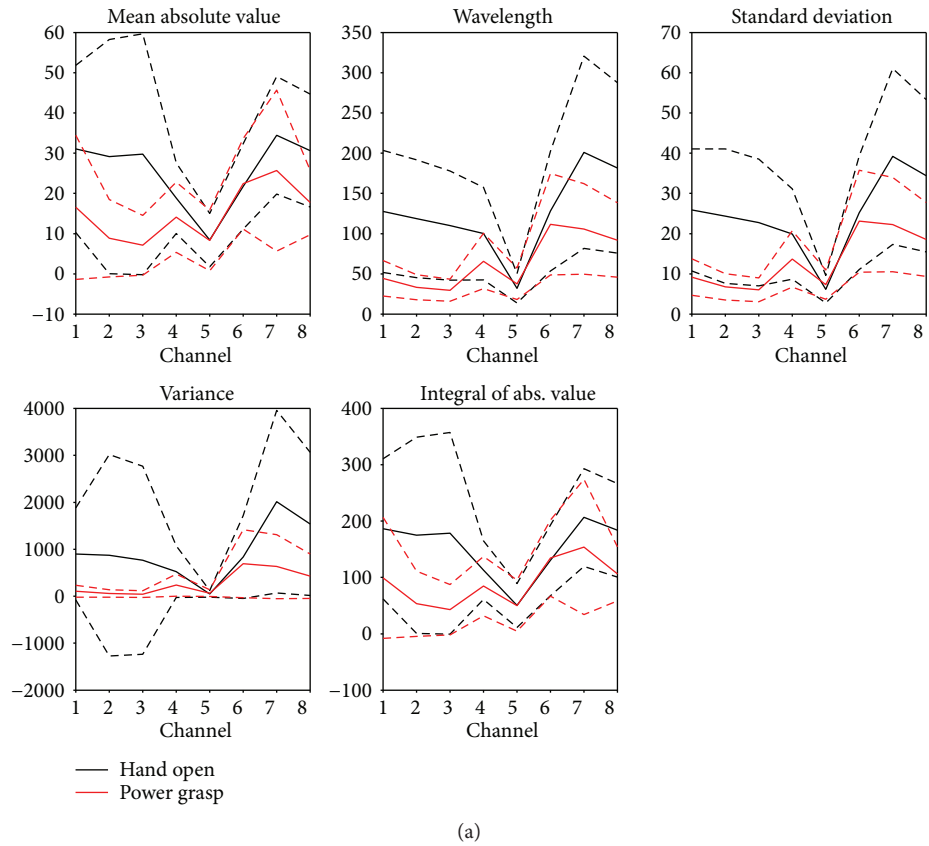
$$\text{SD} = \sqrt{\frac{1}{n-1} \sum_{i=1}^n (x_i - \bar{x})^2}, \quad (4)$$

$$\text{IAV} = \sum_{i=1}^n x_i, \quad (5)$$

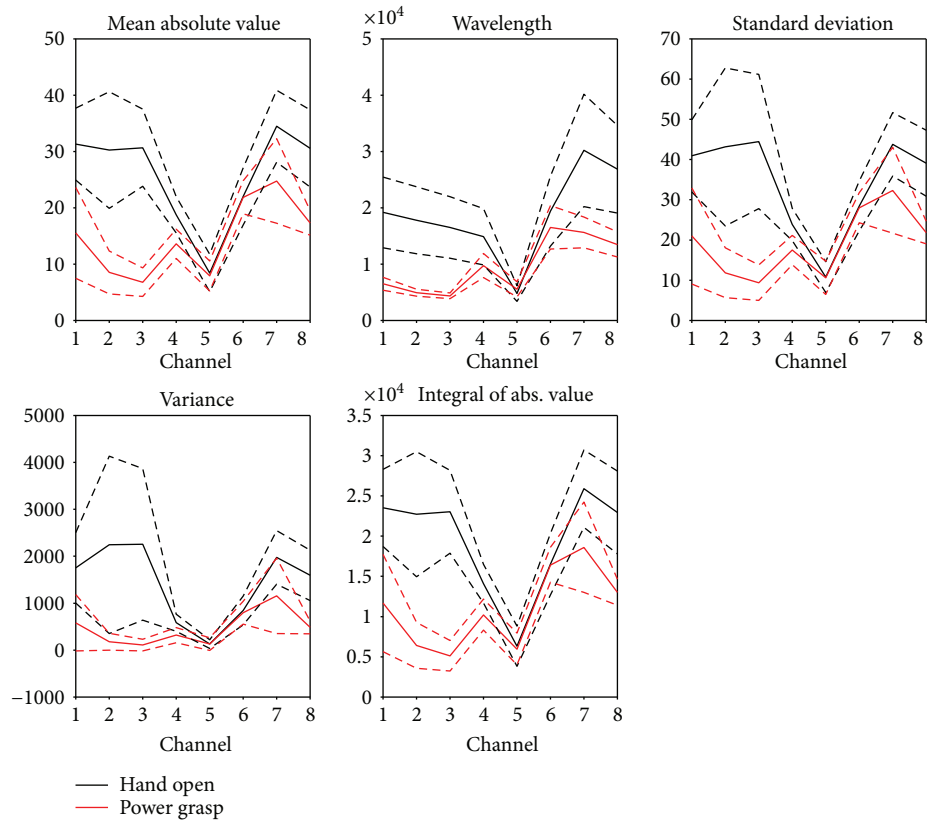
$$\text{V} = \frac{1}{n-1} \sum_{i=1}^n (x_i - \bar{x})^2, \quad (6)$$

$$\text{SSC} = \begin{cases} 1, & x_i > x_{i+1}, x_i > x_{i-1}, \\ 1, & x_i < x_{i+1}, x_i > x_{i-1}, \\ 0, & \text{else.} \end{cases} \quad (7)$$

From these parameters, a subset was selected for classification based on separability between movements and



(a)



(b)

FIGURE 7: Analysis of window length for (a) 20 ms and (b) 3 s for all features (MAV, WL, SD, IAV, and V) and 8 channels, using data from the 6 subjects.

classification accuracy. The new set of parameters were used for classification.

**2.4. Classification.** For the classification of sEMG signals, feature and window length analysis were performed for the eight channels. The sEMG envelope signal was used for selection of active patterns at the processing stage. From this ~10 s of sEMG activity, windows of 20 ms, 50 ms, 100 ms, 300 ms, and 500 ms and 1 s and 3 s length, with a 25% overlap, were used to calculate the seven features described in (1), (2), (3), (4), (5), (6), and (7).

A linear discriminant analysis (LDA) was executed for sets of two movements following the process described ahead, in this case for hand open and power grasp:

- (1) For each subject and each analysis window value, the seven features were extracted for the eight channels; for hand open task and power grasp task.
- (2) The resulting 56 features obtained from each window were considered as a single trial for each movement.
- (3) All available trials from the first session (one task per movement) of all subjects were concatenated movement-wise and randomized afterwards.
- (4) Label classes for each trial were set as 1 for hand open and 2 for power grasp.
- (5) For each window length value, the analysis was performed ten times.
- (6) All trials were divided in 70% for a training set and 30% for a testing set.
- (7) A LDA classifier was trained with the training set.
- (8) The trials on the testing set were classified with the LDA classifier, and its classification accuracy was calculated as the ratio of correctly classified trials versus the total number of trials.

All subjects' data from the first session (combinations of features, channels and window lengths) that obtained a classification accuracy higher than 90% were chosen as the subset of features used to train the final LDA classifier. Data from the second session, which consisted of hand open and power grasp for each subject, was processed in the same way and was used to test the LDA classifier.

**2.5. sEMG Recording and FES Application: Acquisition and Processing.** For the trials of sEMG signal acquisition during FES application, the acquisition was performed using the OpenViBE platform and OpenBCI device with the same configuration mentioned above. For FES application, a RehaStim 2 electrical stimulator (Hasomed GmbH, Germany) was used and programmed in an interface developed in Simulink®/MATLAB Environment.

Three able-bodied subjects out of the six that performed the previous trials without FES, age range from 22 to 34 years old, two males and one female, were included for sEMG acquisition. Their skin was cleaned with alcohol and

TABLE 3: Analysis of the combinations of selected channels and features with best performance during training, for each window length.

| Window length (s) | Channels        | Features                | Classifier accuracy (%) |
|-------------------|-----------------|-------------------------|-------------------------|
| 0.02              | 1-3             | WL, SD                  | 80.69                   |
| 0.05              | 1-3             | WL, SD                  | 88.23                   |
| 0.10              | 1-3             | WL, SD, V               | 91.56                   |
| 0.30              | 1-3, 7-8        | MAV, WL, SD, V          | 93.86                   |
| <b>0.50</b>       | <b>1-3, 7</b>   | <b>MAV, WL, SD</b>      | <b>95.83</b>            |
| 1.00              | 1-4, 7-8        | MAV, WL, SD, V, IAV     | 94.68                   |
| <b>3.00</b>       | <b>1-3, 7-8</b> | <b>MAV, WL, SD, IAV</b> | <b>95.14</b>            |

The bold rows correspond to classification accuracies above 95%.

the FELT was placed accordingly. For each target motion, there was a pair of self-adhesive stimulation electrodes (Axxelgard, USA) placed within the FELT, positioned as presented in Table 1.

The subject was asked to perform an isometric contraction for five movements: hand open, power grasp, fine pinch, pronation, and supination, but this time the trial consisted of three parts (Figure 4):

- (1) Five isometric contractions of the selected movement, each lasting one second with three seconds rest (except pronation and supination: 1.8 active to 2.2 second rest)
- (2) Five FES stimulations of the selected movement, each lasting one second with three seconds rest
- (3) Five isometric contractions during FES stimulations of the selected movement, each lasting one second with three seconds rest

The algorithm in Figure 4 was performed once for each movement and subject. The stimulation parameters changed for each movement according to Table 2.

The new records were analyzed for processing the sEMG data because these signals included evoked and/or volitional sEMG as well as the FES stimulus. In order to extract the sEMG evoked/volitional sEMG from the stimulus artifact, a comb-type filter was applied to eliminate the 30 or 50 Hz signal of the stimulus, by means of a Butterworth filter, order two, with a 29 to 31 Hz or 49 to 51 Hz bandwidths, accordingly. All data processing is designed and performed in MATLAB environment. The parameters calculated for these signals are MAV (1) and root mean square (RMS) (8) to compare sEMG of evoked and volitional and evoked signals.

$$\text{RMS} = \sqrt{\frac{1}{n} \sum_{i=1}^n (x_i)^2}. \quad (8)$$

### 3. Results and Discussion

A personalized template was designed for each subject. These templates were used to successfully locate muscle sites and place electrodes for the second trial, with the

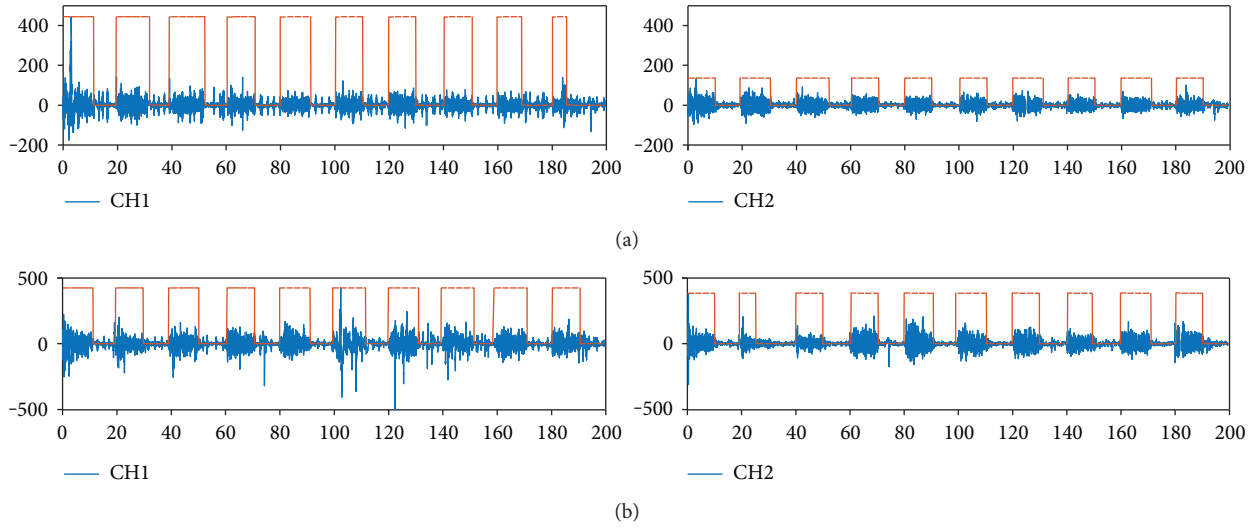


FIGURE 8: Subject 1 using FELT: (a) channels 1 and 2 for open hand and (b) channels 1 and 2 for power grasp.

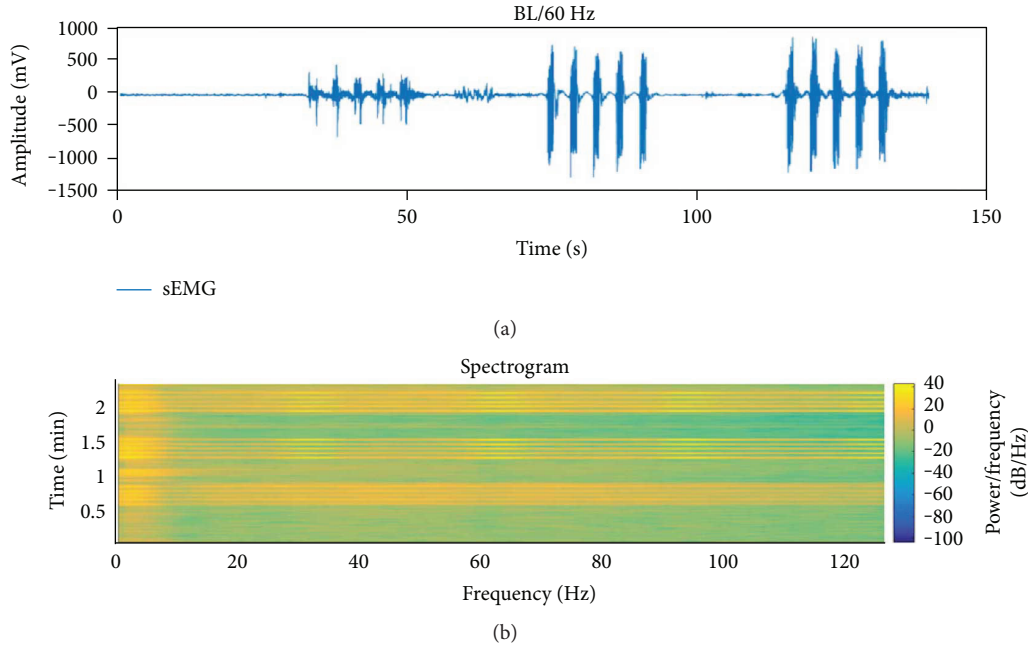


FIGURE 9: (a) Power grasp sEMG signal recorded from trial (algorithm Figure 4), channel 1. Baseline has been eliminated using algorithm of Figure 2. (b) Spectrogram of sEMG signal, where activity in the 30 Hz band for the 2nd and 3rd sets of motions and their harmonics can be observed.

advantage of a tenfold reduction in location time, approximately. Then, the FELT was designed as a universal array from all the individual templates.

The main purpose of the FELT was to simplify recording and stimulation electrode placing, for a future FES-based neuroprosthesis clinical application for stroke aftermath rehabilitation at upper limb and hand. There are not standardized designs for sEMG recording and FES application. The sEMG signals acquired for open hand and power grasp were used to evaluate the right position of the recording electrodes at the FELT.

One of the objectives of this work was to allocate all electrodes keeping the balance between having available

positions to acquire eight sEMG channels and enough place for five bipolar stimulation channels. It is important to mention that since the forearm is a small area, it was difficult to find the right allocation for all the electrodes (stimulation electrodes are 5×5 cm and recording electrodes are 1 cm in diameter) and still have useful signals that could be processed and classified.

Due to this critical disposition, the electrode locations from the personalized templates were assessed through the sEMG signals obtained by means of signal processing and classification of movements.

A baseline drift-free signal was obtained from the raw sEMG signal during the preprocessing stage (Figure 5). All

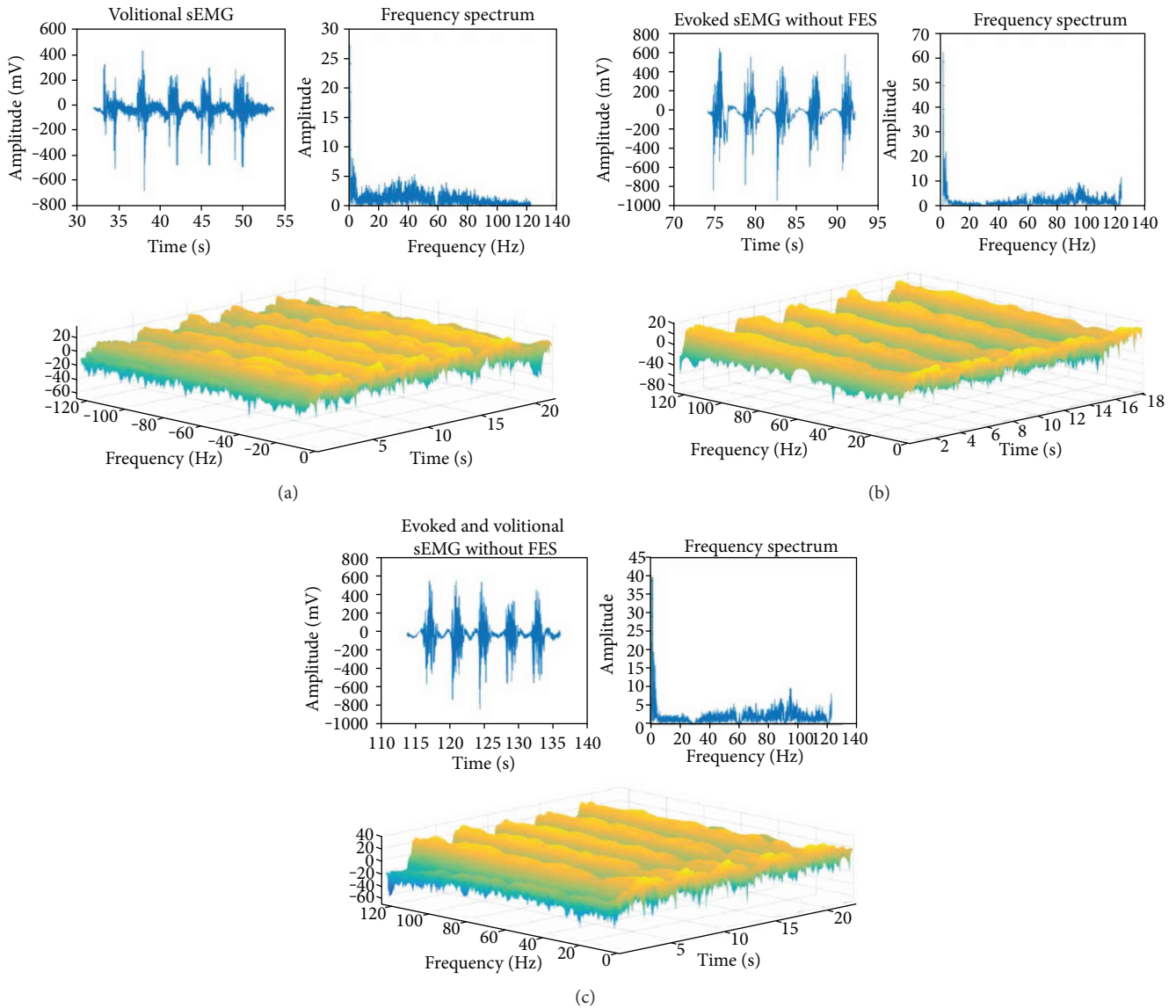


FIGURE 10: Power grasp, subject 1, channel 1, sEMG signals of the 3 parts of the trial. (a) Set of 5 isometric contractions of the selected movement, each lasting 1 second with 3 seconds rest. (b) 5 FES stimulations of the selected movement, each lasting 1 second with 3 seconds rest. (c) 5 isometric contractions during FES stimulations of the selected movement, each lasting 1 second with 3 seconds rest.

sessions from the six subjects were put through this processing. sEMG signal in Figure 5(a) has a large baseline, while Figure 5(b) shows a cleaner sEMG signal despite original baseline drifting; also, the differences between each contraction repetition are clearer.

The preprocessing analysis and processing method showed that no matter the 60 Hz noise and drifting baseline, the signal could be isolated for feature extraction and classification. It is important to mention that if the acquisition signal was less contaminated, this process could be faster and closer to real time for control applications, which emphasizes the need to design and build a specialized acquisition stage in order to start with the best version of a raw sEMG signal (which can also consider a configuration that allows the simultaneous application of FES, for volitional sEMG extraction).

Figure 6 shows an example of two of the eight sEMG channels processed and the envelope signal obtained, which shows the active sEMG sections selected. These correspond to open hand and power grasp movements.

From the analysis of the combinations of features, channel, and window length for all subjects, it was found that only 5 features (MAV, WL, SD, IAV, and V) yield enough information for classification, above 90% accuracy (Figure 7). In Figure 7(b), it can be observed that when the length of the window was larger, for features like MAV or SD, it was easier to find a clear separation of the value of the parameters. Even the smaller windows, i.e., 20 ms, (Figure 7(a)) performed with an accuracy of 80.69%. Then, it is important to find a compromise between window length and classifier performance.

From this analysis, using 9 out of 10 repetitions of each movement per session and considering session 1 for training

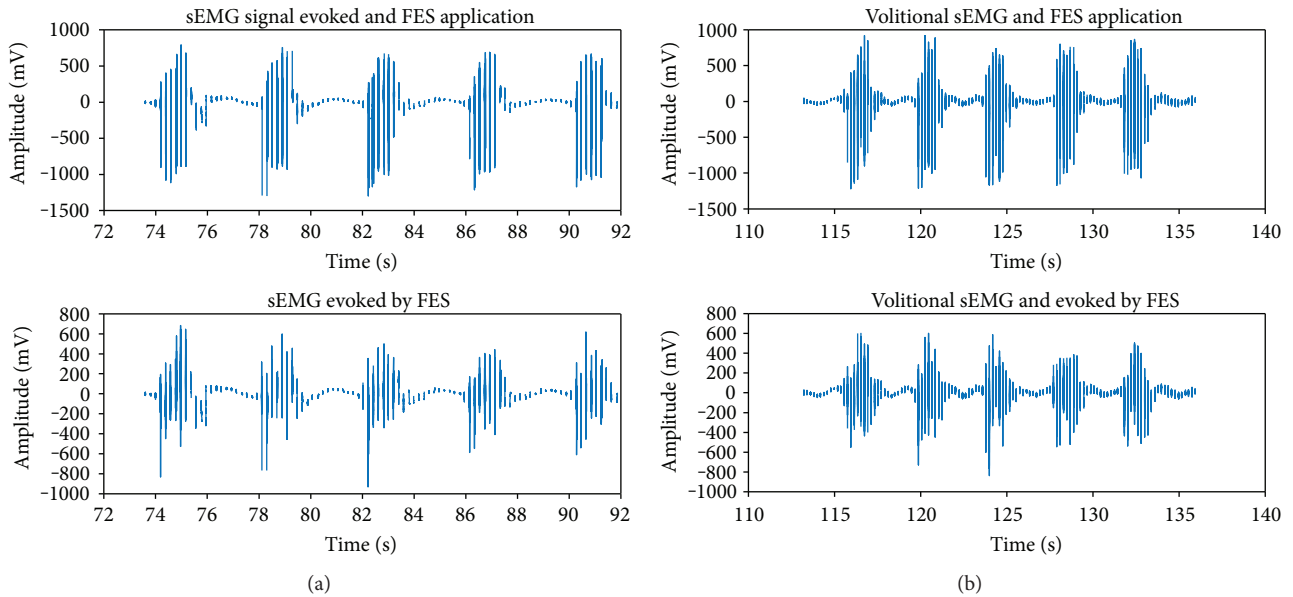


FIGURE 11: Comparison of sEMG signals between 2 parts of the trial involving FES application. (a) Raw signal including FES (top) and sEMG signal evoked by FES free of the stimulus (bottom). (b) Raw signal including volitional sEMG and FES (top) and volitional sEMG signal and evoked by FES free of the stimulus (bottom).

and session 2 for testing, it was found that MAV, WL, and SD features and a 0.50 seconds' window length were the best combinations for the classifier to perform with only 4 channels (CH1, CH2, CH3, and CH7) at a 95.83% classification accuracy. The results from all combinations can be seen in Table 3.

This study and analysis was performed to minimize inputs for the classifier, with the aim of getting a closer approach to a real-time application. This analysis is a classification method for multisubjects, used to generate a sEMG-driven control for a FES neuroprosthesis application.

An example of the sEMG signals obtained for subject 1 using FELT, for channels 1 and 2, is shown in Figure 8. It can be observed that even though the signal was noisier for this session, the processing algorithm was still able to find the active sEMG sections.

Figure 9 shows the signal resulting from the sEMG (evoked/volitional) and FES stimulus signal acquisition using the FELT.

Figure 10 shows each set of repetitions of the 3 parts of the trial. The frequency spectrum and a 3D spectrogram are presented.

Figure 11 shows the sets of contractions for sEMG evoked by FES and those from a volitional sEMG contribution used in order to compare the effects of both conditions.

The RMS and MAV values for each repetition were calculated; Table 4 shows an example of these values.

#### 4. Conclusions

The design of a personalized template presented in this paper replicates the sEMG signal between sessions. Also, the forearm electrode set (FELT) resulted from the need to find the correct place for eight sEMG bipolar channels

TABLE 4: RMS and MAV values obtained for 3 able-bodied subjects, comparison between sEMG evoked by FES and the combination of volitional and evoked by FES signals. Values obtained from motion of power grasp, channel 1.

| Subject | Gender | sEMG evoked by FES |          | Volitional sEMG + sEMG evoked by FES |          |
|---------|--------|--------------------|----------|--------------------------------------|----------|
|         |        | RMS (mV)           | MAV (mV) | RMS (mV)                             | MAV (mV) |
| 1       | Male   | 147.5061           | 105.6109 | 147.4792                             | 104.6412 |
| 2       | Male   | 159.2150           | 109.0613 | 169.7005                             | 126.7346 |
| 3       | Female | 306.5072           | 200.5491 | 215.4075                             | 138.3950 |

and five bipolar stimulation channels (larger electrodes, 5×5 cm) in the forearm, which is a small area for so many electrodes (a total of 27).

Signal processing yielded a very clean signal that preserved sEMG components by using DWT and allowed to differentiate between movements through feature extraction and classification.

We found an optimal combination between window length and number of channels and features, at 0.5 seconds, with four channels and three features (MAV, WL, and SD), which allowed a more efficient classification in terms of time and channels.

The stimulation parameters were selected in order to generate a complete movement without subject discomfort; however, range of movement is yet to be evaluated. As for signal processing, knowing the stimulus frequency beforehand allows the use of a filtering technique feasible for offline and online application. From Figure 10, it is evident that a natural sEMG contraction activates the slow fibers of the muscle, but in the cases of FES application (Figures 10(b) and 10(c)), the fast twitch fibers have a larger contribution

to the sEMG record. Additionally, the evoked and volitional sEMG with FES were similar; however, it should be considered that the sample was small and that all subjects were able-bodied. Therefore, a protocol with a bigger sample is needed and it still remains to be seen if these results hold for patients.

Using the FELT, it was possible to perform sEMG recording and FES simultaneously. Moreover, it was possible to extract the volitional and evoked sEMG from the raw signal, which was accomplished without blanking the signal allowing better control techniques to be implemented. This is highly important for closed-loop FES control.

In the evoked/volitional sEMG and FES trials, the FES stimulus was successfully eliminated from the recorded signal leaving a usable sEMG signal for FES control and other applications as orthosis, prosthetics, neuroprosthesis, and other rehabilitation and assistive devices.

## Conflicts of Interest

The authors declare that they have no conflicts of interest.

## Acknowledgments

The authors would like to thank the National Council for Science and Technology (Consejo Nacional de Ciencia y Tecnología—CONACyT) for supporting the Project CONACyT-SALUD-2016-1-272983 as well as Gabriel Vega Martínez, M.Sc., for his contributions.

## References

- [1] S. W. Lee, K. M. Wilson, B. A. Lock, and D. G. Kamper, "Subject-specific myoelectric pattern classification of functional hand movements for stroke survivors," *IEEE Transactions on Neural Systems and Rehabilitation Engineering*, vol. 19, no. 5, pp. 558–566, 2011.
- [2] P. Raghavan, "The nature of hand motor impairment after stroke and its treatment," *Current Treatment Options in Cardiovascular Medicine*, vol. 9, no. 3, pp. 221–228, 2007.
- [3] D. G. Kamper, "Restoration of hand function in stroke and spinal cord injury," in *Neurorehabilitation Technology*, D. Reinkensmeyer and V. Dietz, Eds., pp. 311–324, Springer, Cham, 2nd edition, 2016.
- [4] A. Altamirano, A. Vera, R. Muñoz, L. Leija, and D. Wolf, "Multichannel sEMG signal analysis using Hilbert-Huang transform to identify time-frequency features," in *36th Annual International Conference of the IEEE Engineering in Medicine and Biology Society*, Chicago, IL, USA, August 2014.
- [5] Y. Hou, J. Zurada, and W. Karwowski, "Prediction of EMG signals of trunk muscles in manual lifting using a neural network model," in *2004. Proceedings. 2004 IEEE International Joint Conference on Neural Networks*, pp. 1935–1940, Budapest, Hungary, January 2004.
- [6] E. H. Shroffe and P. Manimegalai, "Hand gesture recognition based on EMG signals using ANN," *International Journal of Computer Application*, vol. 3, no. 2, pp. 31–39, 2013.
- [7] Y. P. Ivanenko, R. E. Poppele, and F. Lacquaniti, "Five basic muscle activation patterns account for muscle activity during human locomotion," *The Journal of Physiology*, vol. 556, no. 1, pp. 267–282, 2004.
- [8] M. D. Klein Breteler, K. J. Simura, and M. Flanders, "Timing of muscle activation in a hand movement sequence," *Cerebral Cortex*, vol. 17, no. 4, pp. 803–815, 2007.
- [9] A. B. Ajibove and R. F. Weir, "Muscle synergies as a predictive framework for the EMG patterns of new hand postures," *Journal of Neural Engineering*, vol. 6, no. 3, article 036004, 2009.
- [10] S. M. Mane, R. A. Kambli, F. S. Kazi, and N. M. Singh, "Hand motion recognition from single channel surface EMG using wavelet & artificial neural network," *Procedia Computer Science*, vol. 49, pp. 58–65, 2015.
- [11] O. M. Giggins, U. M. Persson, and B. Caulfield, "Biofeedback in rehabilitation," *Journal of Neuroengineering and Rehabilitation*, vol. 10, no. 1, p. 60, 2013.
- [12] B. Cesqui, P. Tropea, S. Micera, and H. Krebs, "EMG-based pattern recognition approach in post stroke robot-aided rehabilitation: a feasibility study," *Journal of Neuroengineering and Rehabilitation*, vol. 10, no. 1, p. 75, 2013.
- [13] D. B. Popović, T. Sinkaer, and M. B. Popović, "Electrical stimulation as a means for achieving recovery of function in stroke patients," *NeuroRehabilitation*, vol. 25, no. 1, pp. 45–58, 2009.
- [14] F. Quandt and F. C. Hummel, "The influence of functional electrical stimulation on hand motor recovery in stroke patients: a review," *Experimental & Translational Stroke Medicine*, vol. 6, no. 1, p. 9, 2014.
- [15] C. H. Ho, R. J. Triolo, A. L. Elias et al., "Functional electrical stimulation and spinal cord injury," *Physical Medicine and Rehabilitation Clinics of North America*, vol. 25, no. 3, pp. 631–654, 2014.
- [16] M. Khezri and M. Jahed, "A novel approach to recognize hand movements via sEMG patterns," in *2007 29th Annual International Conference of the IEEE Engineering in Medicine and Biology Society*, pp. 4907–4910, Lyon, France, August 2007.
- [17] G. Ouyang, Z. Ju, and H. Liu, "Mutual information analysis with ordinal pattern for EMG based hand motion recognition," in *ICIRA, Intelligent Robotics and Applications*, vol. 7506 of Lecture Notes in Computer Science, pp. 499–506, Springer, Berlin, Heidelberg, 2012.
- [18] Y. Lan, J. Yao, and J. Dewald, "The impact of shoulder abduction loading on EMG-based intention detection of hand opening and closing after stroke," in *2011 Annual International Conference of the IEEE Engineering in Medicine and Biology Society*, pp. 4136–4139, Boston, MA, USA, September 2011.
- [19] C. De Marchis, T. S. Monteiro, C. Simon-Martinez, S. Conforto, and A. Gharabaghi, "Multi-contact functional electrical stimulation for hand opening: electrophysiologically driven identification of the optimal stimulation site," *Journal of Neuroengineering and Rehabilitation*, vol. 13, no. 1, p. 22, 2016.
- [20] G. Vega-Martinez, C. Alvarado-Serrano, and L. Leija, "ECG baseline drift removal using discrete wavelet transform," in *2011 8th International Conference on Electrical Engineering Computing Science and Automatic Control (CCE)*, Merida City, Mexico, October 2011.

## Research Article

# Improved Multiscale Entropy Technique with Nearest-Neighbor Moving-Average Kernel for Nonlinear and Nonstationary Short-Time Biomedical Signal Analysis

S. P. Arunachalam <sup>1</sup>, S. Kapa,<sup>2</sup> S. K. Mulpuru,<sup>3</sup> P. A. Friedman,<sup>2</sup> and E. G. Tolkacheva <sup>1</sup>

<sup>1</sup>Department of Biomedical Engineering, University of Minnesota, Minneapolis, MN, USA

<sup>2</sup>Department of Cardiovascular Medicine, Mayo Clinic, Rochester, MN, USA

<sup>3</sup>Department of Cardiovascular Medicine, Mayo Clinic, Phoenix, AZ, USA

Correspondence should be addressed to S. P. Arunachalam; [poigaiarunachalam.shivaram@mayo.edu](mailto:poigaiarunachalam.shivaram@mayo.edu)

Received 7 April 2017; Revised 8 December 2017; Accepted 21 December 2017; Published 5 March 2018

Academic Editor: Arindam Bit

Copyright © 2018 S. P. Arunachalam et al. This is an open access article distributed under the Creative Commons Attribution License, which permits unrestricted use, distribution, and reproduction in any medium, provided the original work is properly cited.

Analysis of biomedical signals can yield invaluable information for prognosis, diagnosis, therapy evaluation, risk assessment, and disease prevention which is often recorded as short time series data that challenges existing complexity classification algorithms such as Shannon entropy (SE) and other techniques. The purpose of this study was to improve previously developed multiscale entropy (MSE) technique by incorporating nearest-neighbor moving-average kernel, which can be used for analysis of nonlinear and non-stationary short time series physiological data. The approach was tested for robustness with respect to noise analysis using simulated sinusoidal and ECG waveforms. Feasibility of MSE to discriminate between normal sinus rhythm (NSR) and atrial fibrillation (AF) was tested on a single-lead ECG. In addition, the MSE algorithm was applied to identify pivot points of rotors that were induced in *ex vivo* isolated rabbit hearts. The improved MSE technique robustly estimated the complexity of the signal compared to that of SE with various noises, discriminated NSR and AF on single-lead ECG, and precisely identified the pivot points of *ex vivo* rotors by providing better contrast between the rotor core and the peripheral region. The improved MSE technique can provide efficient complexity analysis of variety of nonlinear and nonstationary short-time biomedical signals.

## 1. Introduction

Biomedical signals are characteristic of their corresponding physiological events and carry specific signatures [1]. Consequently, deciphering signal characteristics provides information regarding underlying processes that can be useful to inform or guide therapy. Most physiological processes are characterized by specific signals that reflect the nature and activities of such processes, which can contain biochemical, electrical, or physical information coming from molecular, cellular, organ, or systemic level sources [2]. Hence in a disease state, alterations to these physiological processes yield signal signatures that are different in some aspects from the normal

state [1]. Electrocardiogram (ECG), electroencephalogram (EEG), electromyogram (EMG), electroretinogram, and so on are some examples of electrical signals that are commonly acquired for risk assessment, prognosis, diagnosis, therapy evaluation, and prevention of various diseases [3].

Biomedical signal analysis requires accurate quantification of the system state to distinguish between normal and pathological function or to predict the future state of the system using only short time series data that may only last a few seconds. Signal analysis is typically complicated by contamination with electromagnetic interference, power line interference, zero mean white noise, pink noise, brown noise from electrode movement, and other random noise [2].

Many biomedical signals are captured only for 3–8 s and therefore are short nonstationary and/or nonlinear time series data, which prevent ordinary biomedical analysis algorithms from completely capturing their intrinsic complexity. For instance, Shannon entropy (SE) is commonly used for biomedical complexity analysis of EEG and ECG recordings [3–5]. However, one of the major limitations of the SE approach is related to the specific characteristics of the nonstationary and/or nonlinear time series data that work well for long but is not robust for short data segments. Several other symbolic dynamic approaches that use various entropy-based measures, such as Kolmogorov entropy, spectral entropy, wavelet entropy, permutation entropy, approximate entropy, and sample entropy, have been proposed to capture the intrinsic dynamics of nonstationary time series data to quantify their complexity [6–12]. However, it has been shown that these various entropy-based methods are efficient only for long time series and do not completely capture the complexities of shorter nonstationary time series data [13].

Recently, a multiscale entropy (MSE) technique was proposed for coarse-grained time-scaling procedures to offer more robust determination of the complexity of time series data [14]. Such coarse-graining procedures may result in invalid entropy value estimation for shorter time series; and this limitation was addressed by implementing a moving-average time series estimate [15]. However, the moving average in prior work was only performed in the forward direction, which can lead to significant underestimation of the complexity information that is present in the time series data [15]. Several variants of MSE have thus been proposed [16], but all of them provide only slight modifications from the original technique [15] and specifically depend on a one-sided moving average, which yields biased entropy estimates over different time scales. Several variants of MSE have been applied to test synthetic biomedical datasets without a rigorous demonstration of their feasibility for a biomedical application [17–19]. Therefore, using entropy-based techniques for rigorous complexity analysis of a biomedical signal in normal and diseased states has been very limited. Several researchers have used MSE technique for a variety of analysis using cardiac signal analysis [20–25] showing some promise for complexity assessment to aid diagnosis. However, the authors identify a major limitation of these MSE variants with the systematic bias in the one-sided average which may have affected the results. The introduced bias becomes extremely important to consider for improvement because most biological signals embed only subtle changes in short time series data which may have significant diagnostic potential that could be lost with such bias.

The challenge with short time series data analysis comes from the fact that the complexity of the data may not embed in the raw signal. Previously developed MSE techniques were introduced with time-averaged time series over multiple time scales for short time series analysis [15]. However, forward averaging introduces a systematic bias in the complexity estimation. To overcome this limitation, we proposed a nearest-neighbor moving-average kernel to better capture

the complexity of nonlinear, nonstationary short time series data. We introduce the concept of “memory” by taking into account the past and future time series value while computing the nearest-neighbor moving average for time series data. Therefore, we introduce the time-scale factor “ $\tau$ ”, which represents time scaling in both forward and reverse directions with respect to a particular time point. Once this new time series is derived, the MSE estimate can be obtained by calculating the entropy of the new time series sample over multiple time scales to fully capture the intrinsic complexity of nonlinear and nonstationary time series data.

In this work, we propose an improved MSE technique, which includes significant and robust modification of the previously described MSE techniques. Specifically, we propose computation of the new time series with a nearest-neighbor moving-average kernel that uses information from the “past” and “future” values to accurately capture the intrinsic dynamics of the short time series. Our modification will allow a robust analysis of nonlinear and nonstationary time series.

The efficacy and robustness of the improved MSE technique will be validated by performing noise analysis with respect to white, pink, and brown noise, which are commonly present in cardiac signals such as the ECG. Since SE has been used widely for biomedical signal complexity analysis so far, we will use it as a “gold standard”, and we will compare the performance of the novel MSE technique with SE. We further hypothesized that the improved MSE technique will robustly quantify the complexity of nonlinear and nonstationary short time series data. We tested this hypothesis by applying the improved MSE technique for the analysis of the two physiological applications: (i) discrimination between normal sinus rhythm (NSR) and atrial fibrillation (AF) using a single-lead ECG and (ii) the accurate identification of the pivot point of rotors, which are potential ablation targets for AF and other arrhythmias.

## 2. An Improved MSE Technique with Nearest-Neighbor Moving-Average Kernel

The improved MSE algorithm consists of several steps as described below. Let  $x = \{x_1, x_2, x_3, \dots, x_N\}$  represent the electrogram time series of length  $N$ .

- (1) Nearest-neighbor moving-averaged time series  $z^\tau$  is computed for the chosen time-scale factor “ $\tau$ ” as illustrated in Figure 1 using the following equation:

$$z_j^\tau = \frac{1}{(2\tau + 1)} \sum_{i=j}^{2\tau+1} x_i, \quad (1)$$

where  $1 \leq j \leq N - \tau$  and  $i = 1, 2, 3, \dots, N$ ; Figure 1 shows the schematic to obtain the nearest-neighbor moving-window-averaging approach to obtain the new time series.

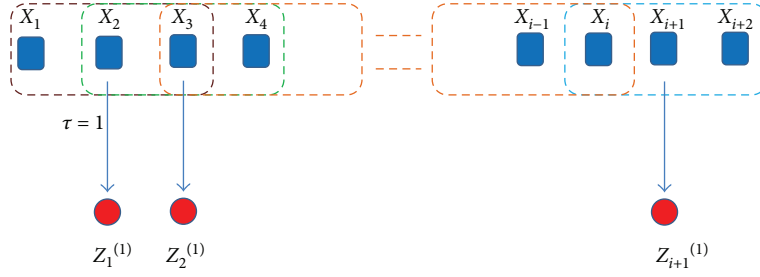


FIGURE 1: Schematic illustration to produce nearest neighbor moving-average time series with scale factor  $\tau = 1$  for the MSE algorithm. Blue squares represent raw time series data, and red dots represent the nearest-neighbor moving-averaged time series from which MSE is obtained. Brown squares represent the moving-window-averaging kernel for the raw second time point ( $X_2$ ) that averages one neighbor on both sides with  $\tau = 1$  to produce the first new time series point  $Z_1^{(1)}$ . Similarly, green square produces  $Z_2^{(1)}$  and so on (orange square) with the blue square producing the last time series point  $Z_{i+1}^{(1)}$ .

- (2) Template vectors  $\mathbf{y}_k^m(\delta)$  with dimension  $m$  and delay  $\delta$  are constructed from  $z^\tau$  (see Figure 1) at each specific  $\tau$  as the following:

$$\mathbf{y}_k^m(\delta) = \{z_k z_k + \delta \cdots z_k + (m-1)\delta\}, \quad (2)$$

where  $1 \leq k \leq N - m\delta$ .

- (3) The Euclidean distance  $d_{ij}^m$  for each pair of template vectors  $\{\mathbf{y}_i^m, \mathbf{y}_j^m\}$  is calculated using the infinity norm as below:

$$d_{ij}^m(\delta) = \left\| \mathbf{y}_i^m(\delta) - \mathbf{y}_j^m(\delta) \right\|_\infty, \quad (3)$$

where  $1 \leq i, j \leq N - m\delta$  and  $j > i + \delta$ .

- (4) Matched template vector pairs  $\{\mathbf{y}_i^m, \mathbf{y}_j^m\}$  are computed based on a predefined tolerance threshold  $r$  as

$$d_{ij}^m(\delta) \leq r. \quad (4)$$

In this manuscript, the value for  $r$  is chosen to be 0.2 times the standard deviation of the raw time series  $x$ . The delay factor  $\delta$  is chosen to be 1. The total number of matched template vectors is computed and denoted by  $n(m, \delta, r)$ .

Steps 2–4 are then repeated for  $m+1$  dimension, and the total number of matched template vectors being computed is denoted by  $n(m+1, \delta, r)$ .

Finally, the improved MSE is calculated as the following:

$$\text{MSE}(x, m, \delta, r) = -\ln \frac{n(m+1, \delta, r)}{n(m, \delta, r)}. \quad (5)$$

### 3. Materials and Methods

**3.1. Noise Analysis.** We evaluated the performance of the improved MSE technique and compared it with the performance of SE approach with respect to the most common sources of noise: (i) zero mean white noise, (ii) pink noise which has the inverse frequency response ( $1/f$ ), and (iii) brown noise which has the inverse frequency squared response ( $1/f^2$ ) [26, 27].

White, pink, and brown noises were simulated in MATLAB™, with 10,000 sample points. Ten short time series (TS) versions of these data were created with 250, 500, 750, 1000, 2000, 4000, 5000, 6000, 8000, and 10,000 samples. MSE was calculated via (5) for each noise using different time-scale factors “ $\tau$ ” from 1 to 20 over varying time series lengths. Normalized MSE (for  $\tau = 1, 2, 3, 5$ ) and SE were calculated by dividing the MSE (and SE) values by the maximum value of MSE (and SE) across varying time series. MSE and SE results for  $\tau > 5$  are quantitatively similar to that of  $\tau = 5$  and therefore are not shown.

**3.2. Description of Datasets for Noise Analysis.** To test the robustness of an improved MSE technique in the presence of various noises, we used (1) simplified non-physiological sinusoidal wave and (2) physiological ECG signal, which is the most commonly used time series signal for the diagnostic of various diseases of the heart.

- (1) A sinusoidal wave with single frequency of 10 Hz and a multifrequency sinusoidal wave with superposition of 2, 5, 10, 15, and 20 Hz frequencies were used. Ten short time series versions of the data were simulated in MATLAB.
- (2) Noise-free flat baseline ECG was obtained using an electronic ECG simulator with 10,000 sample points at 250 Hz sampling rate. Ten short time series versions of these data were created.

White, pink, and brown noises were added to the noise-free signals and the analysis was performed as described in sub-Section A to compare the performance of MSE and SE techniques.

**3.3. NSR and AF ECG Discrimination Analysis.** Publically available ECG datasets were obtained from the MIT-BIH Physionet database during NSR and AF [28]. Ten NSR and AF datasets of 10-second duration and 250 Hz sampling rate were used for analysis. The signals were not preprocessed for noise removal and  $\tau = 3$  for MSE calculation. NSR and AF datasets were compared using custom MATLAB software. Mann–Whitney test with  $p$  value of

0.01 was used for testing statistical significance and was performed using OriginPro software (OriginLab Corporation, Northampton, Massachusetts).

**3.4. Optical Mapping Data from Isolated Rabbit Hearts.** Optical mapping movies during a single rotor or figure-of-8 reentry were obtained from an isolated rabbit heart by inducing ventricular tachycardia via burst pacing as described previously [29, 30]. The movies were 3-second long, acquired at 600 frames per second temporal and  $64 \times 64$ -pixel spatial resolution. Two-dimensional (2D) MSE maps were generated for both single rotor and figure-of-8 reentry using the MSE values with the scale factors  $\tau = 1, 2, \text{ and } 3$  at each pixel location across all the frames. For comparison purposes, the 2D SE map was computed. A custom MATLAB (MathWorks Inc., Natick, MA) program was developed for all processing. Supplemental videos SV1 and SV2 are provided for reference that shows the phase movie of single and double rotor, respectively.

## 4. Results

**4.1. Noise Analysis.** Figure 2 shows the robustness of MSE and SE techniques with respect to different types of noise: white (a), pink (b), and brown (c). The middle row of Figures 2(a)–2(c) shows the MSE values as a function of  $\tau$  for varying TS lengths. As expected, for white noise, MSE monotonically decreases as  $\tau$  increases, and changing TS length does not affect the data. For pink noise, MSE increases with the increase of the TS length, and for long TS (1000 samples), MSE does not depend on  $\tau$ . For brown noise, MSE decreases with the increase in the TS length and does not depend on  $\tau$  for long TS. These results demonstrate the robustness of MSE since the expected behavior is observed for each noise. The bottom row of Figures 2(a)–2(c) shows the normalized values of MSE (for different  $\tau$ ) and SE as a function of the TS length. As seen from these data, the values of SE decrease as TS decreases for all types of noises, while MSE values do not depend on the TS length. These results demonstrate that the performance of MSE is better than SE, especially for short time series.

The MSE of white noise is expected to show a monotonically decreasing response with higher scale factors [14–16] which was seen in Figure 2(a) middle panel with increasing scale factor due to the nearest neighbor averaging that leads to lower MSE for white noise is shown. For pink noise which has a  $1/f$  response, higher MSE than white noise is expected but with a constant value across multiple time scales [14]. As expected, MSE levels out at higher time series lengths above 1000 sample points across the different time scales seen in Figure 2(b) middle panel. This means that for a sampling rate of 250 Hz, MSE can capture the complexity with just 4 s of data. Similarly, for brown noise, MSE is expected to be constant and as seen from Figure 2(c) middle panel after a TS length of 750 sample points, MSE is more or less the same across multiple time scales. Figures 2(a)–2(c) bottom panel demonstrates the fact that SE estimates lower values for short time series and gradually increases with increasing time series length for all three types of noise. MSE has higher

values even for the shortest time series, thereby capturing the complexity better than SE. Overall, the results indicate that if at least 1000 sample points are available, MSE can capture the complexity robustly compared to SE. For most physiological monitoring, 250 Hz sampling frequency is common, which indicates that 4 s short time series data should be sufficient for robust analysis using MSE.

Figure 3 demonstrates the robustness of MSE compared with SE technique for single-frequency sinusoidal wave in the absence and presence of different noises. Figure 3(a) shows the single-frequency sinusoidal wave at 10 Hz for 500 sample points (left panel), the MSE values as a function of  $\tau$  for varying TS (middle panel), and the normalized values of MSE (for different  $\tau$ ) and SE as a function of TS length (right panel) in the absence of noise. These data demonstrate higher efficacy of the MSE technique in capturing the complexity of the sine wave than that of SE, which only works well for larger TS lengths. The robustness of the MSE and SE techniques in identifying the complexity of a single-frequency sinusoidal wave in the presence of noise is shown in Figure 3 for the white (b), pink (c), and brown (d) noises. The top row of Figures 3(b)–3(d) shows the amplitude of sinusoidal wave with noise, while the bottom row shows the normalized values of MSE (for different  $\tau$ ) and SE as a function of TS length. Our results suggest that MSE captures the complexity of sinusoidal waves better than SE in the presence of these noises.

Figures 4 and 5 show the results for the multifrequency sinusoidal wave and the noise-free flat ECG, respectively. Similar to the response seen in Figure 2 for raw noise, (b)–(d) of Figures 4 and 5 demonstrate that SE is very small for short TS and gradually increases with increasing TS length, while MSE has high values even for the shortest TS, thereby capturing the complexity better than SE. The results demonstrate the efficacy of the novel MSE technique in quantifying the complexity of complex time series data in the presence of noise better than that of the commonly used SE approach.

**4.2. ECG Analysis.** Figure 6 shows the raw ECG with NSR (a) and AF (b). Note that visual inspection of these traces cannot be used to correctly discriminate between NSR and AF. Figure 6(c) shows the boxplot of MSE values for 10 AF and NSR datasets demonstrating statistically significant differences ( $p < 0.01$ ) and therefore accurate discrimination between NSR and AF. As observed in Figures 6(a) and 6(b) visually, it is difficult to interpret the difference between NSR and AF on the ECG as the chaotic nature of AF manifests itself into small morphological disturbances which need robust algorithms to effectively capture the complexity. MSE robustly discriminates NSR and AF.

**4.3. Identification of Pivot Point of the Rotor.** A snapshot of a phase movie of a single rotor in isolated rabbit heart is shown in Figure 7(a). In this movie, different colors represent different phases of the action potential, and the pivot point of the rotor can be easily identified as the point where different phases converge. Corresponding voltage traces from the core (pixel “1”) and periphery of the rotor (pixel “2”) are also shown. At the core of the rotor, broader distribution of

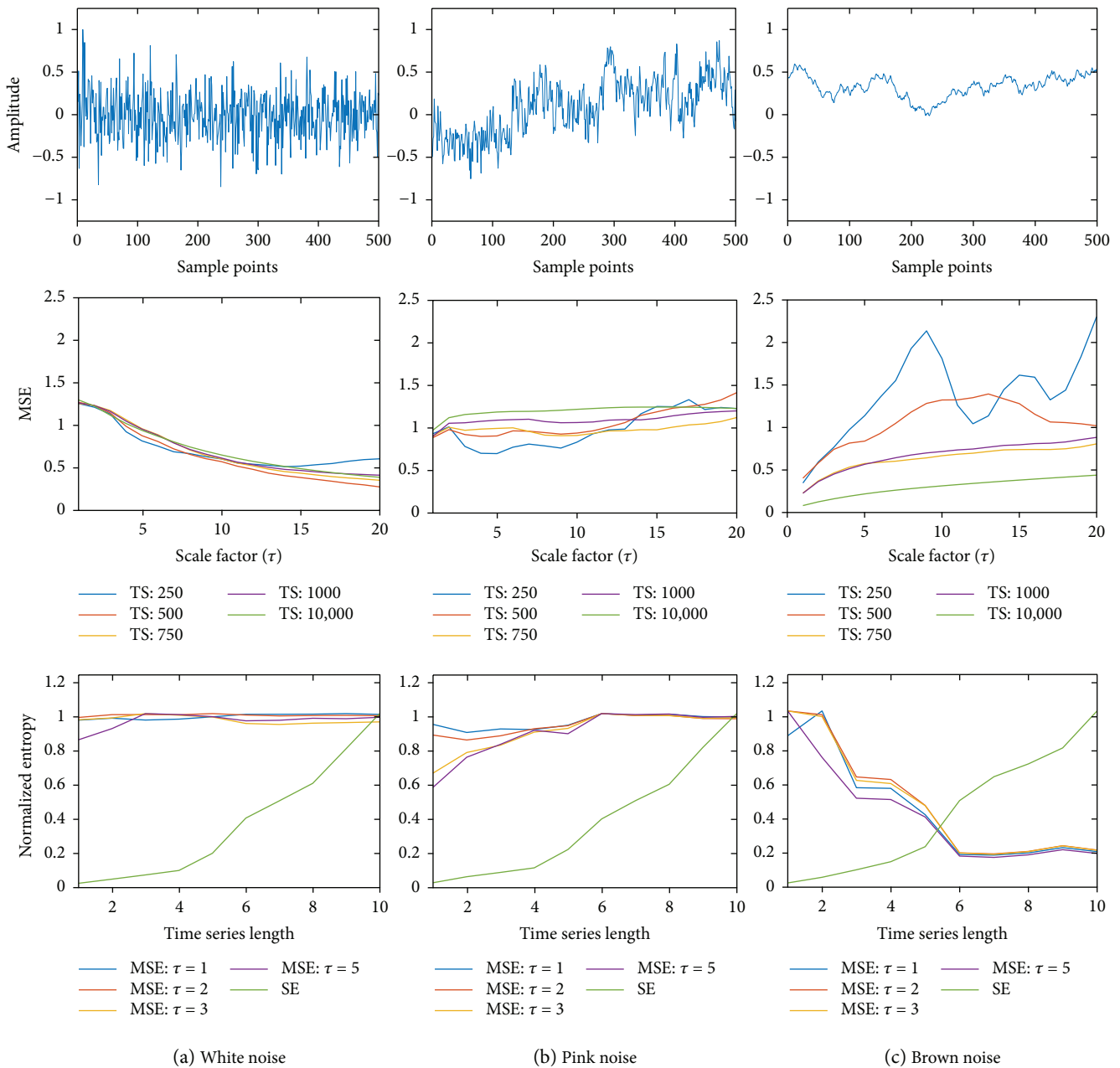


FIGURE 2: (a) Top panel shows white noise with 500 sample points; Middle panel shows the MSE for various time series (TS) lengths; bottom panel shows normalized MSE (for scale factors  $\tau = 1, 2, 3$ , and 5) and SE; (b) top panel shows pink noise with 500 sample points; middle panel shows the MSE for various time series (TS) lengths; bottom panel shows normalized MSE (for scale factors  $\tau = 1, 2, 3$ , and 5) and SE; (c) top panel shows brown noise with 500 sample points; middle panel shows the MSE for various time series (TS) lengths; bottom panel shows normalized MSE (for scale factors  $\tau = 1, 2, 3$ , and 5) and SE.

voltage amplitude occurs due to the chaotic nature at the rotor pivot point and therefore, a higher MSE value was expected. At the periphery of the rotor, more uniform electrical activity is observed and hence, a lower MSE value was expected. Figure 7(b) shows the 2D MSE maps for three time-scale factor  $\tau = 1, 2$ , and 3. Note the MSE technique can accurately identify the location of the pivot point of the rotor for each  $\tau$ . As seen from (b), the pivot point has higher MSE values than the periphery thereby enabling its precise localization, and higher values of “ $\tau$ ” results in better

contrast between the rotor core and periphery. Figure 7(c) shows the normalized 2D SE map of the same single rotor. It is important to note that although SE can correctly identify the pivot point of the rotor, the contrast between SE values at the core and the periphery is low, which challenges accurate identification.

Figure 8(a) shows a snapshot of a phase movie for an example of figure-of-8 reentry in an isolated rabbit heart. Similar to Figure 7, one can see that the MSE technique can correctly identify the location of the pivot points of the rotors

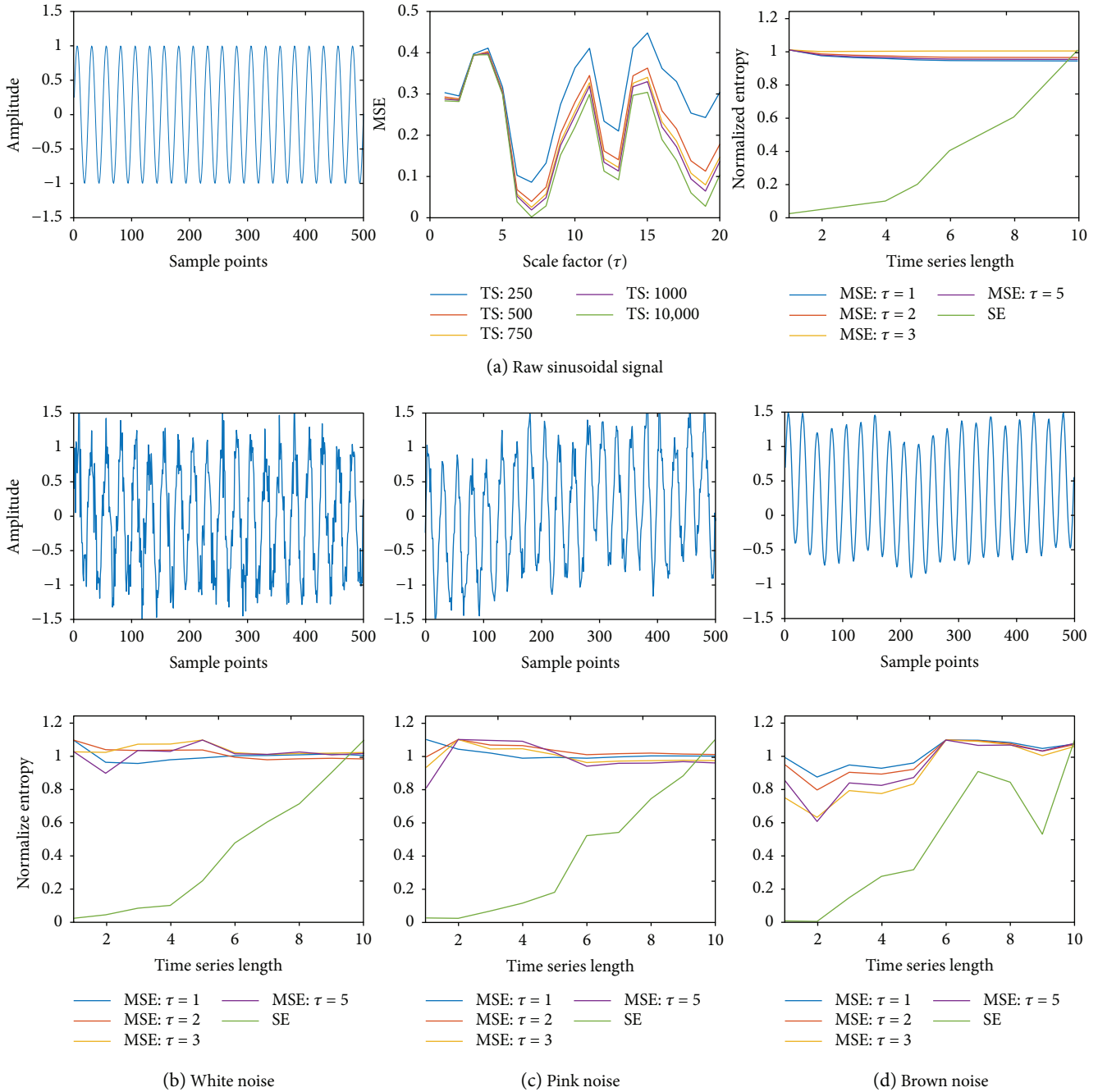


FIGURE 3: (a) Left panel shows single-frequency (10 Hz) sinusoidal wave with 500 sample points; middle panel shows the MSE for various length time series across several scaling factors; right panel shows normalized MSE (for scale factors  $\tau = 1-10$ ) and SE; (b) top row shows sinusoidal wave with white noise, (c) pink noise, and (d) brown noise; (b) bottom row shows normalized MSE (for scale factors  $\tau = 1-10$ ) and SE for sine wave with white noise, (c) pink noise, and (d) brown noise, respectively.

for each  $\tau$  and that the performance of the MSE technique is much better than SE observed in Figures 8(b)–8(c).

As seen in Figure 7(b), it is seen that a scale factor of  $\tau = 1$  was sufficient enough to provide the necessary contrast to identify the rotor pivot points with higher MSE values at the rotor pivot point than that in the periphery. Higher scale factor values provided improved contrast as seen when comparing 2D MSE maps in Figure 7(b). Similar results are observed for figure-of-8 reentry data seen in Figure 8. It is

interesting to note that at pixel location “1,” the rotor meanders to some extent which is also captured robustly by MSE compared to SE.

### 5. Discussion

In this study, we developed an improved MSE technique with nearest-neighbor moving-average kernel and demonstrated that it can be successfully used for the analysis of nonlinear

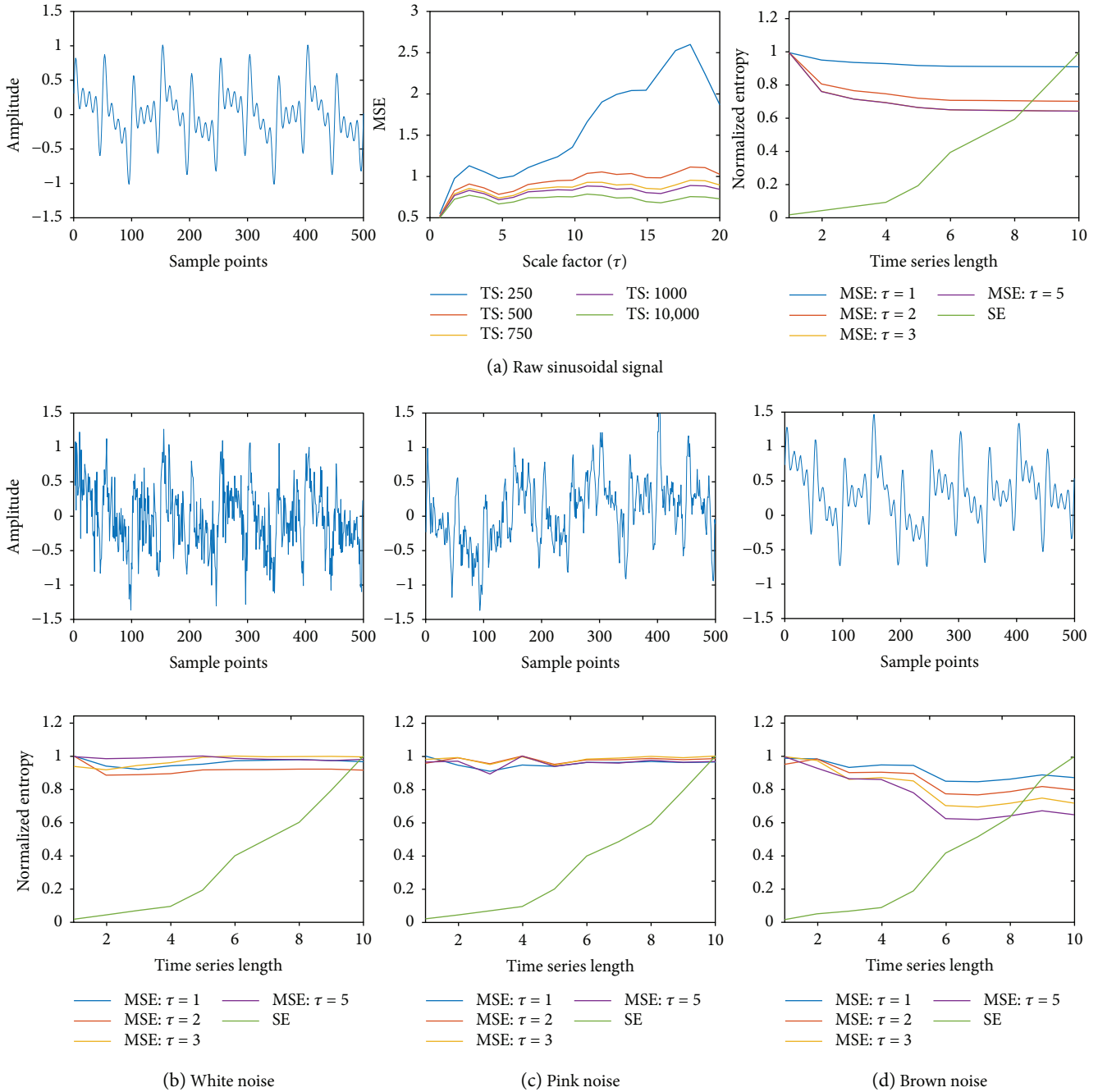


FIGURE 4: (a) Left panel shows multifrequency sinusoidal wave with 500 sample points; middle panel shows the MSE for various length time series across several scaling factors; right panel shows normalized MSE (for scale factors  $\tau = 1-10$ ) and SE; (b) top row shows sinusoidal wave with white noise, (c) pink noise, and (d) brown noise; (b) bottom row shows normalized MSE (for scale factors  $\tau = 1-10$ ) and SE for sinusoidal wave with white noise, (c) pink noise, and (d) brown noise, respectively.

and nonstationary short time series physiological data. The MSE robustly estimated the complexity of short time series data compared to SE with various noises such as white, pink, and brown noises. Major findings of this manuscript are the following: (1) MSE discriminated NSR and AF on single-lead ECG of 10 s recordings without any preprocessing steps and (2) MSE precisely identified the pivot point of the rotor (single and figure-of-8 reentry) with 3 s optical mapping data from isolated rabbit hearts by providing

better contrast between the rotor core and the periphery region when compared to the SE approach. The efficacy of MSE technique was clearly demonstrated with short time series analysis which can be used in a variety of other physiological applications.

**5.1. Sinusoidal Wave Analysis.** Sinusoidal wave analysis is the most elegant approach to demonstrate the efficacy of the improved MSE technique over the conventionally used SE

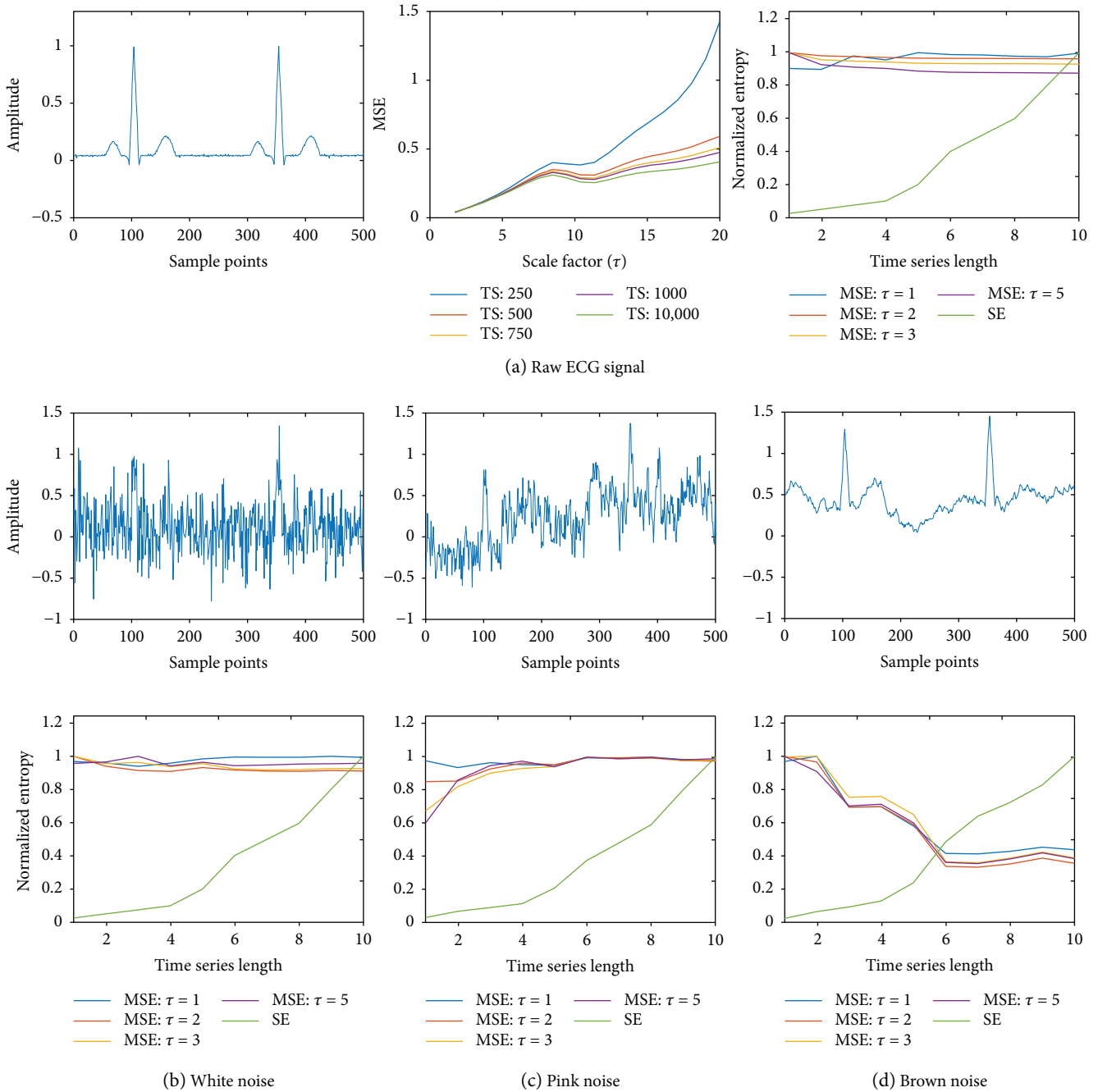


FIGURE 5: (a) Left panel shows sample ECG trace with 500 sample points; middle panel shows the MSE for various length time series across several scaling factors; right panel shows normalized MSE (for scale factors  $\tau = 1-10$ ) and SE; (b) top row shows sinusoidal wave with white noise, (c) pink noise, and (d) brown noise; (b) bottom row shows normalized MSE (for scale factors  $\tau = 1-10$ ) and SE for sinusoidal wave with white noise, (c) pink noise, and (d) brown noise, respectively.

approach for short time series analysis of biomedical signals. We demonstrated that both for single-frequency and multi-frequency sinusoidal waves with added noise, SE underestimated the complexity at short time series for all three noise cases and performed better at longer time series lengths. However, MSE was robust even at shorter time series with 1000 sample points in the presence of the three types of noise. The results suggest the value of MSE technique in analyzing complex short time series physiological signals that can be

contaminated with these noises and its use for the prognosis and diagnosis of various disease states.

5.2. *Noise-Free ECG Analysis.* ECG analysis is very commonly used for a wide variety of cardiac conditions to yield information regarding the state of the heart. Since most remote and ambulatory real-time ECG monitoring present at most 3–5 seconds of ECG data, conventional complexity analysis methods such as SE are limited. However, we

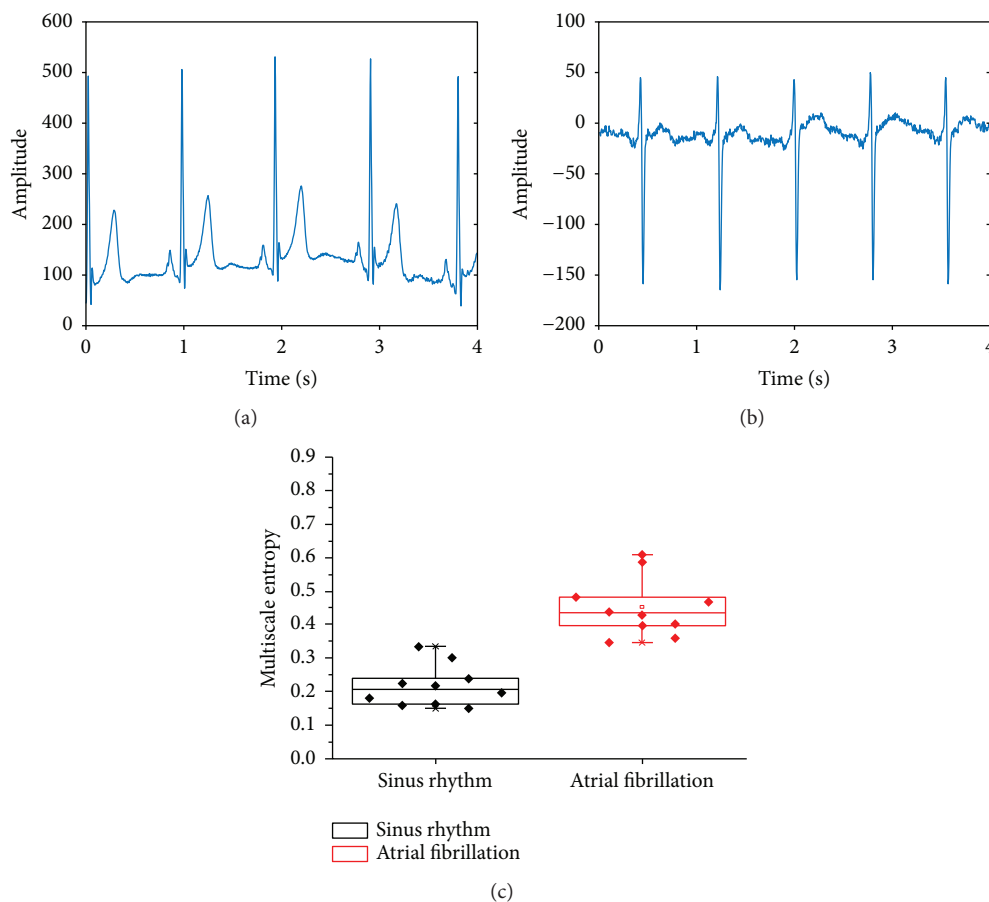


FIGURE 6: (a) Representative example of an ECG trace with normal sinus rhythm; (b) representative example of an ECG trace with AF; (c) box plot showing MSE values for sinus rhythm and AF ECG datasets. The NSR and AF were significantly different ( $p < 0.01$ ) on MSE.

demonstrated that MSE robustly estimated the complexity of short time series ECG data even in the presence of noise.

**5.3. Discrimination between NSR and AF.** AF is the most common sustained cardiac arrhythmia that is associated with increased risk of stroke, heart failure, and death affecting more than 2.3 million people in the United States and over 30 million people worldwide [31]. Although the persistent form of AF can be detected relatively easy, detecting paroxysmal AF is often a challenge since continuous monitoring is required, which in turn requires methods to discriminate NSR from AF through large quantities of data [32].

Although there are several methods available for NSR and AF discrimination, they face limitations in successfully detecting AF with high sensitivity and specificity using short-time ECG data [32–34]. The major issues with these approaches are that they often distort the ECG by several preprocessing steps with filters, they do not provide reliable discrimination using short ECG time series data, and many of them lack real-time capability that makes it difficult to trust the data for diagnosis and treatment. Here, we demonstrated that the improved MSE technique can robustly discriminate AF from NSR using a single-lead ECG. The

results motivate the application and use of this MSE technique for many hand-held and remote ECG monitors to autodetect AF.

**5.4. Identification of Pivot Points of Rotors.** Catheter ablation to treat paroxysmal AF has been shown to be up to 87% successful using pulmonary vein (PV) isolation [35–40]. However, in patients with persistent AF ablation, it is challenging since the location of the triggers is unclear, and it has been shown that triggers commonly arise outside the PVs. Recent research suggests that AF ablation has a success rate of 28% with 51% after multiple repeat procedures in persistent AF [41].

It is believed that rotors are caused by reentrant mechanisms which might be responsible for maintaining persistent AF. Identification of the rotor pivot point as a suitable ablation target has been the research focus for many investigators. However, these investigations are challenged with short time series data in the clinical setting. Here, we used optical mapping data in which rotors can be clearly visualized, and we demonstrated that the improved MSE technique can precisely identify pivot points in both single rotor and figure-of-8 reentry, thus offering a robust mapping tool to guide identification of

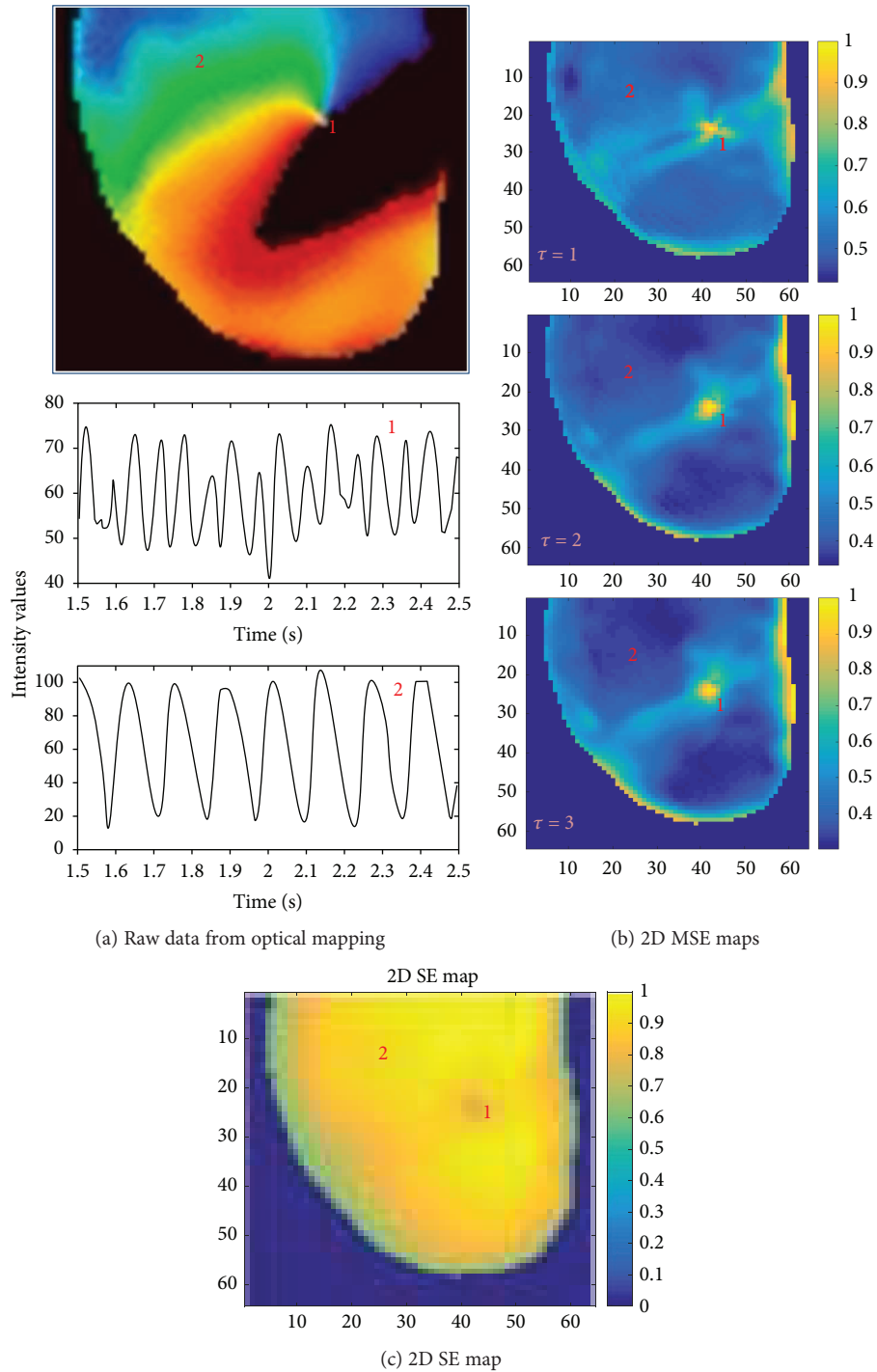


FIGURE 7: (a) Top panel shows a representative example of a single rotor. Pixel locations “1” represent rotor core region and “2” represent rotor periphery; bottom panel shows corresponding voltage traces at those pixel locations. (b) Normalized 2D MSE maps; top panel with scale factor  $\tau = 1$ ; middle panel with  $\tau = 2$ ; bottom panel with  $\tau = 3$ , correctly identifying rotor core regions; (c) normalized 2D SE map with lower SE values at the rotor core.

AF ablation targets. In the clinical setting, electrogram recordings are frequently limited to 2.5–5-second segments due to the need for frequent catheter repositioning during the procedure, challenging conventional mapping approaches to precisely identifying substrates in AF and other arrhythmias.

**5.5. Limitations.** A limitation of the improved MSE technique is the need to select a correct choice of the time scale factor “ $\tau$ .” Since the nearest-neighbor moving averaging is employed, large time scales will cause excessive smoothing of the data which may lead to loss of some complexity information. Therefore, caution should be used in the appropriate

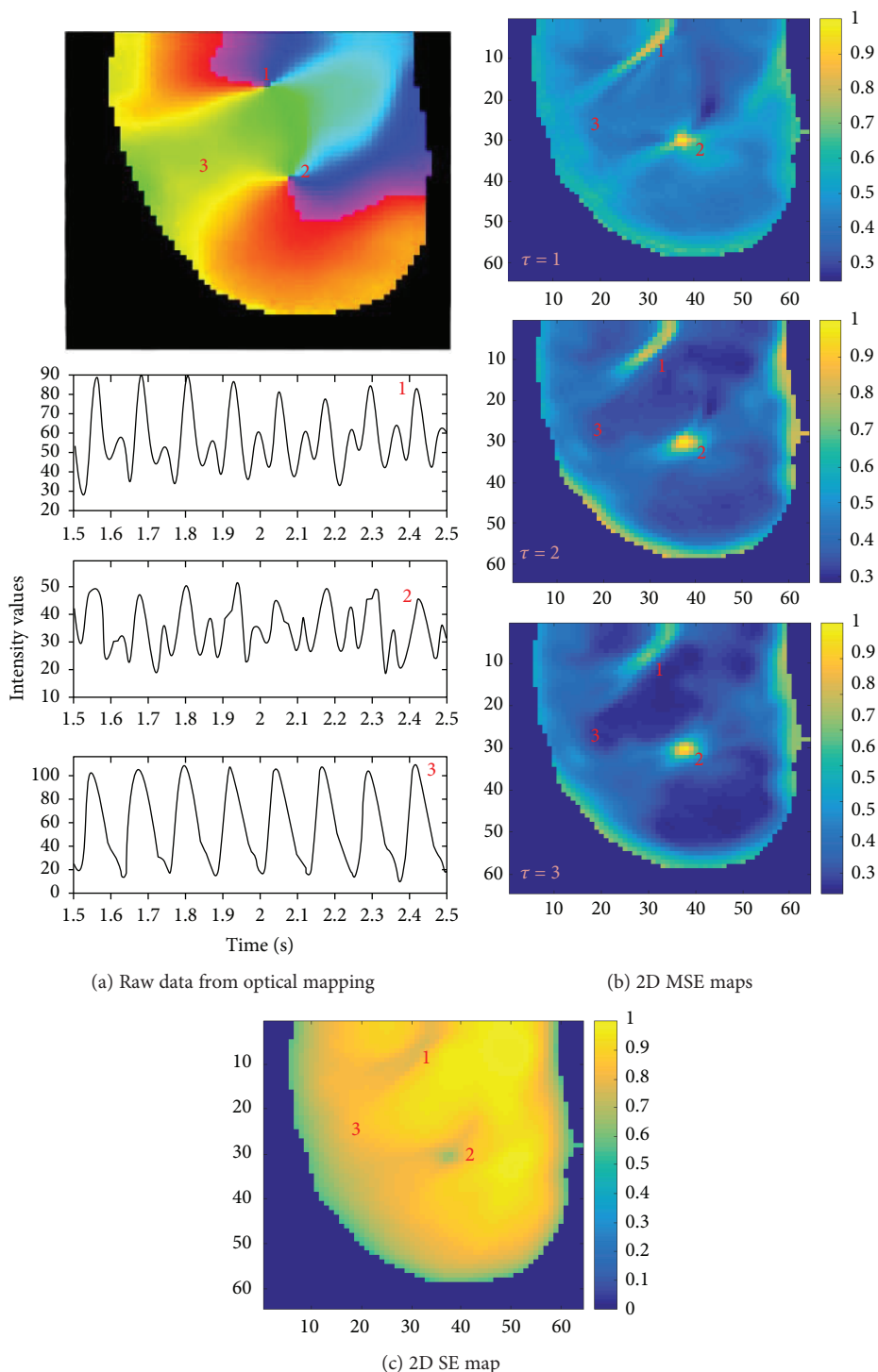


FIGURE 8: (a) Top panel shows a representative example of a figure-of-8 reentry. Pixel locations “1” and “2” represent rotor core region and “3” represent rotor periphery; bottom panel shows corresponding voltage traces at those pixel locations. (b) Normalized 2D MSE maps; top panel with scale factor  $\tau=1$ ; middle panel with  $\tau=2$ ; bottom panel with  $\tau=3$ , correctly identifying rotor core regions; (c) normalized 2D SE map with lower SE values at the rotor core.

choice of scaling factor. The results from this study suggest that a scale factor of  $\tau=3$  may be a reasonable starting point for many applications, but clinical validation is needed.

In addition, our analysis was limited to relatively small number of datasets. More rigorous evaluation using a larger

number of datasets is critical in order to validate these findings for ECG discrimination as well as for rotor identification. Finally, we did not specifically evaluate ex vivo examples of AF but only of more organized cardiac arrhythmias to determine critical rotor elements. Given the higher-order

complexity associated with AF, further study is needed in experimental models of AF to validate the use of MSE for characterization of rotors in these arrhythmia examples.

## 6. Conclusions

An improved MSE technique with nearest-neighbor moving-average kernel was developed to eliminate the systematic bias from one-sided averaging. The results demonstrate that MSE technique can be successfully used for the analysis of nonlinear and nonstationary short time series physiological data. Compared to the commonly used SE approach, MSE robustly estimated complexity with short time series data with various noises such as white, pink, and brown noises. The MSE discriminated NSR and AF on single-lead ECG of 10 s recordings without any preprocessing steps and precisely identified the pivot point of the rotors with 3 s optical mapping data from isolated rabbit hearts by providing better contrast between the rotor core and the periphery region when compared to the SE approach. Wide-range application of this technique on a variety of time series data can open new avenues for analysis and interpretation.

## 7. Future Work

Future work will focus on further validating the efficacy of NSR and AF discrimination on a larger dataset. Also, the MSE algorithm will be validated with a variety of rotor data for accurate identification of ablation targets using both optical mapping and intracardiac electrograms that can guide patient-specific mapping and ablation.

## Ethical Approval

In this study no animal studies were performed. Data from previous animal studies were used for which all applicable international, national, and/or institutional guidelines for the care and use of animals were followed. This article does not contain any studies with human participants performed by any of the authors.

## Conflicts of Interest

S. P. Arunachalam declares that he has no conflict of interest. S. Kapa declares that he has no conflict of interest. S. K. Mulpuru declares that he has no conflict of interest. P. A. Friedman declares that he has no conflict of interest. E. G. Tolkacheva declares that she has no conflict of interest.

## Acknowledgments

This study was funded by the National Science Foundation Grants CAREER PHY-125541 and DCSD 1662250; and the National Institute of Health (NIH) Grant R21HL128790.

## Supplementary Materials

*Supplementary 1. SV1:* phase movie of the single rotor from optical mapping of isolated rabbit heart.

*Supplementary 2. SV2:* phase movie of the figure-of-8 reentry from optical mapping of isolated rabbit heart.

## References

- [1] N. P. Reddy, "Book review: biomedical signal analysis: a case-study approach, by Rangaraja M. Rangayyan," *Annals of Biomedical Engineering*, vol. 30, no. 7, pp. 983–983, 2002.
- [2] M. Kutz, *Standard Handbook of Biomedical Engineering and Design*, McGraw-Hill, New York, NY, USA, 2003.
- [3] M. Baumert, A. Porta, and A. Cichocki, "Biomedical signal processing: from a conceptual framework to clinical applications [scanning the issue]," *Proceedings of the IEEE*, vol. 104, no. 2, pp. 220–222, 2016.
- [4] P. F. Lin, M. T. Lo, J. Tsao, Y. C. Chang, C. Lin, and Y. L. Ho, "Correlations between the signal complexity of cerebral and cardiac electrical activity: a multiscale entropy analysis," *PLoS One*, vol. 9, no. 2, article e87798, 2014.
- [5] C. E. Shannon, "A mathematical theory of communication," *Bell System Technical Journal*, vol. 27, no. 3, pp. 379–423, 1948.
- [6] A. N. Kolmogorov, "Entropy per unit time as a metric invariant of automorphism," *Academy of Sciences*, vol. 124, pp. 754–755, 1959.
- [7] G. E. Powell and I. C. Percival, "A spectral entropy method for distinguishing regular and irregular motion of Hamiltonian systems," *Journal of Physics A: Mathematical and General*, vol. 12, no. 11, pp. 2053–2071, 1979.
- [8] S. J. Roberts, W. Penny, and I. Rezek, "Temporal and spatial complexity measures for electroencephalogram based brain-computer interfacing," *Medical & Biological Engineering & Computing*, vol. 37, no. 1, pp. 93–98, 1999.
- [9] O. A. Rosso, S. Blanco, J. Yordanova et al., "Wavelet entropy: a new tool for analysis of short duration brain electrical signals," *Journal of Neuroscience Methods*, vol. 105, no. 1, pp. 65–75, 2001.
- [10] C. Bandt and B. Pompe, "Permutation entropy: a natural complexity measure for time series," *Physical Review Letters*, vol. 88, no. 17, 2002.
- [11] S. Pincus, "Approximate entropy (ApEn) as a complexity measure," *Chaos*, vol. 5, no. 1, pp. 110–117, 1995.
- [12] J. S. Richman and J. R. Moorman, "Physiological time-series analysis using approximate entropy and sample entropy," *American Journal of Physiology-Heart and Circulatory Physiology*, vol. 278, no. 6, pp. H2039–H2049, 2000.
- [13] H. C. Fogedby, "On the phase-space approach to complexity," *Journal of Statistical Physics*, vol. 69, no. 1-2, pp. 411–425, 1992.
- [14] M. Costa, A. L. Goldberger, and C. K. Peng, "Multiscale entropy analysis of complex physiologic time series," *Physical Review Letters*, vol. 89, no. 6, article 068102, 2002.
- [15] S. D. Wu, C. W. Wu, K. Y. Lee, and S. G. Lin, "Modified multiscale entropy for short-term time series analysis," *Physica A: Statistical Mechanics and its Applications*, vol. 392, no. 23, pp. 5865–5873, 2013.
- [16] A. Humeau-Heurtier, "The multiscale entropy algorithm and its variants: a review," *Entropy*, vol. 17, no. 5, pp. 3110–3123, 2015.
- [17] J. Gao, J. Hu, F. Liu, and Y. Cao, "Multiscale entropy analysis of biological signals: a fundamental bi-scaling law," *Frontiers in Computational Neuroscience*, vol. 9, 2015.

- [18] H. Azami and J. Escudero, "Improved multiscale permutation entropy for biomedical signal analysis: interpretation and application to electroencephalogram recordings," *Biomedical Signal Processing and Control*, vol. 23, pp. 28–41, 2016.
- [19] Y. Zhang, S. Wei, Y. Long, and C. Liu, "Performance analysis of multiscale entropy for the assessment of ECG signal quality," *Journal of Electrical and Computer Engineering*, vol. 2015, Article ID 563915, 9 pages, 2015.
- [20] W. Y. Pan, M. C. Su, H. T. Wu, M. C. Lin, I. Tsai, and C. K. Sun, "Multiscale entropy analysis of heart rate variability for assessing the severity of sleep disordered breathing," *Entropy*, vol. 17, no. 1, pp. 231–243, 2015.
- [21] C. C. Wang, C. D. Chang, and B. C. Jiang, "Pattern recognition of multiscale entropy curve for ECG signal analysis," *Applied Mechanics and Materials*, vol. 195–196, pp. 603–607, 2012.
- [22] J. Wang, X. Ning, J. Li, Q. Ma, Y. Xu, and C. Bian, "Multiscale entropy analysis of electrocardiogram," *Sheng wu yi xue gong cheng xue za zhi= Journal of biomedical engineering= Shengwu yixue gongchengxue zazhi*, vol. 24, no. 5, pp. 978–980, 2007.
- [23] M. Costa, A. L. Goldberger, and C. K. Peng, "Multiscale entropy analysis of biological signals," *Physical Review E*, vol. 71, no. 2, article 021906, 2005.
- [24] R. Parasnis, A. Pawar, and M. Manivannan, "Multiscale entropy and poincare plot-based analysis of pulse rate variability and heart rate variability of ICU patients," in *2015 International Conference on Intelligent Informatics and Biomedical Sciences (ICIIBMS)*, pp. 290–295, Okinawa, Japan, November 2015.
- [25] H. C. Chiu, Y. H. Lin, M. T. Lo et al., "Complexity of cardiac signals for predicting changes in alpha-waves after stress in patients undergoing cardiac catheterization," *Scientific Reports*, vol. 5, no. 1, article 13315, 2015.
- [26] G. D. Clifford, F. Azuaje, and P. Mcsharry, "ECG statistics, noise, artifacts, and missing data," *Advanced Methods and Tools for ECG Data Analysis*, vol. 6, p. 18, 2006.
- [27] O. El B'charri, R. Latif, K. Elmansouri, A. Abenaou, and W. Jenkal, "ECG signal performance de-noising assessment based on threshold tuning of dual-tree wavelet transform," *Biomedical Engineering Online*, vol. 16, no. 1, p. 26, 2017.
- [28] A. L. Goldberger, L. A. N. Amaral, L. Glass et al., "PhysioBank, PhysioToolkit, and PhysioNet: components of a new research resource for complex physiologic signals," *Circulation*, vol. 101, no. 23, pp. e215–e220, 2000.
- [29] S. P. Arunachalam, S. K. Mulpuru, P. A. Friedman, and E. G. Tolkacheva, "Feasibility of visualizing higher regions of Shannon entropy in atrial fibrillation patients," in *2015 37th Annual International Conference of the IEEE Engineering in Medicine and Biology Society (EMBC)*, pp. 4499–4502, Milan, Italy, August 2015.
- [30] A. Matiukas, A. M. Pertsov, P. Kothari, A. Cram, and E. G. Tolkacheva, "Optical mapping of electrical heterogeneities in the heart during global ischemia," in *2009 Annual International Conference of the IEEE Engineering in Medicine and Biology Society*, vol. 1, pp. 6321–6324, Minneapolis, MN, USA, September 2009.
- [31] S. S. Chugh, R. Havmoeller, K. Narayanan et al., "Worldwide epidemiology of atrial fibrillation: a global burden of disease 2010 study," *Circulation*, vol. 129, no. 8, pp. 837–847, 2014.
- [32] D. D. McManus, J. Lee, O. Maitas et al., "A novel application for the detection of an irregular pulse using an iPhone 4S in patients with atrial fibrillation," *Heart Rhythm*, vol. 10, no. 3, pp. 315–319, 2013.
- [33] E. J. Benjamin, P. S. Chen, D. E. Bild et al., "Prevention of atrial fibrillation: report from a National Heart, Lung, and Blood Institute workshop," *Circulation*, vol. 119, no. 4, pp. 606–618, 2009.
- [34] M. J. Patil, B. K. Khadse, and S. R. Suralkar, "Discrimination between atrial fibrillation (AF) & normal sinus rhythm (NSR) using linear parameters," *Pratibha: International Journal of Science, Spirituality, Business and Technology (IJSSBT)*, vol. 1, p. 108, 2012.
- [35] H. Calkins, K. H. Kuck, R. Cappato et al., "2012 HRS/EHRA/ECAS expert consensus statement on catheter and surgical ablation of atrial fibrillation: recommendations for patient selection, procedural techniques, patient management and follow-up, definitions, endpoints, and research trial design," *Heart Rhythm*, vol. 9, no. 4, pp. 632–696.e21, 2012.
- [36] R. Weerasooriya, P. Khairy, J. Litalien et al., "Catheter ablation for atrial fibrillation: are results maintained at 5 years of follow-up?," *Journal of the American College of Cardiology*, vol. 57, no. 2, pp. 160–166, 2011.
- [37] C. Medi, P. B. Sparks, J. B. Morton et al., "Pulmonary vein antral isolation for paroxysmal atrial fibrillation: results from long-term follow-up," *Journal of Cardiovascular Electrophysiology*, vol. 22, no. 2, pp. 137–141, 2010.
- [38] W. S. Tzou, F. E. Marchlinski, E. S. Zado et al., "Long-term outcome after successful catheter ablation of atrial fibrillation," *Circulation. Arrhythmia and Electrophysiology*, vol. 3, no. 3, pp. 237–242, 2010.
- [39] C. Pappone, G. Vicedomini, G. Augello et al., "Radiofrequency catheter ablation and antiarrhythmic drug therapy: a prospective, randomized, 4-year follow-up trial: the APAF study," *Circulation Arrhythmia and Electrophysiology*, vol. 4, no. 6, pp. 808–814, 2011.
- [40] S. M. Narayan and J. A. Zaman, "Mechanistically based mapping of human cardiac fibrillation," *The Journal of Physiology*, vol. 594, no. 9, pp. 2399–2415, 2016.
- [41] T. F. Chao, H. M. Tsao, Y. J. Lin et al., "Clinical outcome of catheter ablation in patients with nonparoxysmal atrial fibrillation: results of 3-year follow-up," *Circulation Arrhythmia and Electrophysiology*, vol. 5, no. 3, pp. 514–520, 2012.

## Research Article

# Dynamic Analysis of the Abnormal Isometric Strength Movement Pattern between Shoulder and Elbow Joint in Patients with Hemiplegia

Yali Liu <sup>1</sup>, Yuezhen Hong <sup>2</sup>, and Linhong Ji <sup>1</sup>

<sup>1</sup>Division of Intelligent and Biomechanical System, State Key Laboratory of Tribology, Tsinghua University, Haidian, Beijing, China

<sup>2</sup>National Key Laboratory of Human Factors Engineering, China Astronaut Research and Training Center, Haidian, Beijing, China

Correspondence should be addressed to Linhong Ji; [jilh@tsinghua.edu.cn](mailto:jilh@tsinghua.edu.cn)

Received 10 August 2017; Revised 14 November 2017; Accepted 12 December 2017; Published 11 February 2018

Academic Editor: Kunal Pal

Copyright © 2018 Yali Liu et al. This is an open access article distributed under the Creative Commons Attribution License, which permits unrestricted use, distribution, and reproduction in any medium, provided the original work is properly cited.

Patients with hemiplegia usually have weak muscle selectivity and usually perform strength at a secondary joint (secondary strength) during performing a strength at one joint (primary strength). The abnormal strength pattern between shoulder and elbow joint has been analyzed by the maximum value while the performing process with strength changing from 0 to maximum then to 0 was a dynamic process. The objective of this study was to develop a method to dynamically analyze the strength changing process. Ten patients were asked to perform four group asks (maximum and 50% maximum voluntary strength in shoulder abduction, shoulder adduction, elbow flexion, and elbow extension). Strength and activities from seven muscles were measured. The changes of secondary strength had significant correlation with those of primary strength in all tasks ( $R > 0.76$ ,  $p < 0.01$ ). The antagonistic muscles were moderately influenced by the primary strength ( $R > 0.4$ ,  $p < 0.01$ ). Deltoid muscles, biceps brachii, triceps brachii, and brachioradialis had significant influences on the abnormal strength pattern (all  $p < 0.01$ ). The dynamic method was proved to be efficient to analyze the different influences of muscles on the abnormal strength pattern. The muscles, deltoid muscles, biceps brachii, triceps brachii, and brachioradialis, much influenced the stereotyped movement pattern between shoulder and elbow joint.

## 1. Introduction

Hemiplegia, including the characteristics such as weakness and decreased selective motor control, is a common clinical sequelae following a stroke [1]. Hemiplegia is associated with a reduced number of functional corticospinal and corticobulbar fibers to the spinal and brainstem because of lesions in the cerebral cortex.

Deficits in the control of independent joint movements have been reported, especially the abnormal torque pattern and the abnormal muscle coordination patterns [2–5]. Researchers analyzed the abnormal joint torque pattern to explore the characteristics of the symptom and what caused the symptom [3, 6–8]. Dewald and Beer studied the abnormal joint torque patterns using a six-freedom load cell [9]. They pointed out that the strong abnormal implicated torque pattern existed in the conjunct movement of shoulder

abduction during elbow flexion and shoulder adduction during elbow extension. Bohannon and Smith tested the muscle strength by a manual hand-held dynamometer and found that there were muscle strength imbalances in hemiplegic patients [10]. These studies focused on the mean or the peak of the torque and strength at shoulder and elbow joint by considering the torque and strength as a static value, and the muscle activation and torque pattern were separately analyzed [11]. The static analysis method for the strength and few analyses of relationship between strength and muscle activation limit our knowledge on the characteristics of the abnormal patterns. The dynamic analysis between the kinematic or dynamic parameters and the muscle activation has been reported to be beneficial to understand patients' movement relationship between the extrinsic characteristics and the inherent nature [12]. Therefore, a dynamic analysis on the performing process is needed to explore the

relationship between the strength and muscle activation and investigate the elements influencing the abnormal strength patterns.

The main purpose of this study is to explore the strength patterns between shoulder and elbow joint and develop the relationship between strength patterns and muscle activation. Our hypothesis is that the strength performing is a dynamic process with the strength changing from 0 to maximum and then to 0. The strength patterns could be generated by some specific muscles during primary strength actions and the primary strength could have different influences on different muscles at the secondary joint.

## 2. Methods

**2.1. Subjects.** Ten stroke patients with unilateral hemiplegia in the upper extremity were recruited. Most patients (7/10) had lesions at the basal ganglia on the right hemisphere and were evaluated by Fugl-Meyer Assessment scores for upper limb (Table 1). The criteria for recruitment in this experiment were (1) the first onset of stroke, diagnosed with definite lesions on hemisphere by CT or MRI; (2) able to understand experimenter's request; (3) age between 30 and 80 years; (4) no lesions on cerebellum and brainstem; (5) no severe inflammation, pathological injury, and malformation in the paretic arm; (6) no severe visual impairment; and (7) no acute conditions.

All subjects were provided the informed consent form for the experiment, which was approved by the medical ethics committee.

**2.2. Isometric Strength Measurement Instrument Description.** Isometric strength measurement instrument (ISMI) was used to measure the shoulder and elbow strength. The mechanical apparatus comprises of two main parts (i.e., supporting part and the measuring part) including two three-freedom force sensors (Figure 1). The supporting part, which is made of aluminum alloy, consists of a U frame, two inclined beams, and a weight support part. The U frame is used to fix the position of the force sensors and the inclined beams are used to enhance the structure when users perform tasks. The weight support part is used to keep the apparatus' balance when users perform actions. The measuring part is used to measure the strength at the segment's center of mass. The positions of centers of mass (COM) of segments are decided according to the human anatomy (Table 2) [13].

**2.3. Experiment Protocol.** Each subject performed four group strength tasks including maximum and 50% maximum voluntary strength in shoulder abduction (MVS-ABD and 50% MVS-ABD), shoulder adduction (MVS-ADD and 50% MVS-ADD), elbow flexion (MVS-FLEX and 50% MVS-FLEX), and elbow extension (MVS-EXT and 50% MVS-EXT). Each subject was asked to sit in the chair (Figure 1) with his/her trunk fixed to restrict trunk movement and maintain his/her shoulder 75° abduction and 40° flexion as well as elbow neutral flexion at 90° (Figure 2). The strength

TABLE 1: The clinical data of hemiplegic stroke patients.

| Item                                   | Patients with hemiplegia (N = 10) |
|--|-----------------------------------|
| Age (years)                            | 53.80 ± 13.32                     |
| Gender, male/female                    | 8/2                               |
| Lesion location, left/right hemisphere | 1/9                               |
| Days since stroke                      | 76.0 ± 43.9                       |
| FMA score for UL                       | 21.1 ± 9.4                        |

FMA score for UL, Fugl-Meyer Assessment scores for upper limb (maximum score = 66).

was defined by the force detected by the force sensor at the segment's center of mass in Table 2.

The strength at shoulder and elbow joint and electromyographic (EMG) signals from pectoralis major (PM), anterior, intermediate, and posterior deltoid (AD, MD, and PD), biceps brachii (BB), triceps brachii (TB), and brachioradialis (BR) were recorded during each task (Figure 3). The strength was measured at 10 Hz by two force sensors (Baisen, China). Real-time visual feedback of the strength value was shown to the subject in the display instrument (XSR90 color paperless recorder, Baisen, China). EMG signals were measured by active differential electrodes (Delsys, 16-channel Bagnolis EMG System, Boston, MA, USA) attached on muscle bellies with 1 cm interelectrode distance after cleaning the skin. EMG signals were sampled at 2000 Hz.

First, each subject performed maximum voluntary strength in each group. Then the maximum strength value was used to calculate the target strength in fifty percent voluntary strength task. Each strength task lasted 1-2 s and the subject can adjust the performing strength according to the displayer mentioned earlier. Each task was repeated three times. EMG signals and strength signals were measured simultaneously by a synchronous trigger using a continuous high-level signal from the same control computer.

### 2.4. Data Processing

**2.4.1. Dynamic Analysis of Strength Patterns.** The primary strength was defined as the strength which subjects intended to make maximum and the secondary strength was defined as the strength at the adjacent joint during performing the primary strength.

The strengths of each task were calculated using MATLAB (Matlabworks R2014a). In each trail, subjects performed the primary strength from 0 to the target and then to 0. The overall effort of the performing task lasted 1-2 s, which was a dynamic process. The changing strength was the extrinsic characteristic of different muscle contraction. The dynamic process can make it clear to understand the relationship between the strength and the muscle contraction in patients with hemiplegia.

For each task, strength magnitude was calculated by averaging values with a moving 250 ms window. The maximum voluntary strength (MVS) was determined by the maximum strength value in MVS task. All strength values in the 50% MVS task were normalized by the corresponding MVS



FIGURE 1: The main parts of ISMI.

TABLE 2: The ratio of COM position of segments.

| Segments   | Gender | Lcs  | Lcx  |
|------------|--------|------|------|
| Upper limb | M      | 47.8 | 52.2 |
|            | F      | 46.7 | 53.3 |
| Forearm    | M      | 42.4 | 57.6 |
|            | F      | 45.3 | 54.7 |

COM: center of mass; M: male; F: female; Lcs: the ratio of the length from COM position to the proximal point on the total length of the segment; Lcx: the ratio of the length from COM position to the distal point on the total length of the segment.

according to equation (1). The process of strength performing task in the 50% MVS task was normalized to 101 points by the entire duration of the task in order to compare the subjects' performance.

$$F_{\text{normalized}} = \frac{F_{50\% \text{task}}}{MVS_{\text{task}}} \quad (1)$$

$F_{\text{normalized}}$  meant the normalized strength value in the 50% MVS task;  $F_{50\% \text{task}}$  meant the strength values in the 50% MVS tasks; and  $MVS_{\text{task}}$  meant the maximum strength value in the corresponding MVS task.

**2.4.2. Analysis of EMG Signals.** The raw EMG signals were removed baseline drift and rectified. Then, a fourth-order Butterworth band-pass filter with cutoff values between 10 Hz and 500 Hz was applied [14–16]. The root mean square was calculated with a moving 100 ms window to smooth the signals [12, 17]. All rectification, filtering, and smoothing were processed in the software (EMGworks 4.1.7, Analysis). Afterwards, MATLAB (Matlabworks R2014a) was used to

extract the EMG signals of each muscle in the corresponding strength performing duration. The EMG signals in the 50% MVS task were normalized by the maximum value in the corresponding MVS task according to equation (2). The EMG signals in the 50% MVS task were normalized to 101 points by the entire duration of the task.

$$R_{\text{muscle}(i)} = \frac{A_{50\% \text{muscle}(i)}}{A_{\text{max}}(A_{\text{maxmuscle}(i)})} \quad (2)$$

Muscle( $i$ ) ( $i=1,2,3\dots7$ ) meant the seven different muscles: pectoralis major, anterior, intermediate, and posterior deltoid, biceps brachii, triceps brachii, and brachioraialis.  $A_{50\% \text{muscle}(i)}$  meant the EMG amplitudes of muscle( $i$ ) in the 50% MVS task and  $A_{\text{max}}(A_{\text{maxmuscle}(i)})$  meant the EMG maximum amplitude of muscle( $i$ ) in the MVS task.

**2.4.3. Influence of Muscles on Strength Patterns.** The process of subjects' performing strength tasks was considered as a dynamic process. The changes of primary strength and secondary strength were the extrinsic characteristics of muscle contraction. A regression analysis was conducted to analyze the relationship between secondary strength in primary strength tasks and muscle activation.

**2.5. Statistical Analysis.** Statistical analysis of the strengths and EMG signals was processed in the software IBM SPSS Statistics 22. General linear regression and ridge regression were used to analyze the different influences of muscle activation on secondary strength patterns. The coefficients of muscles described the degree of the muscle influences on the strength patterns.

We used correlation analysis to explore the correlation between the primary strength and secondary strength as

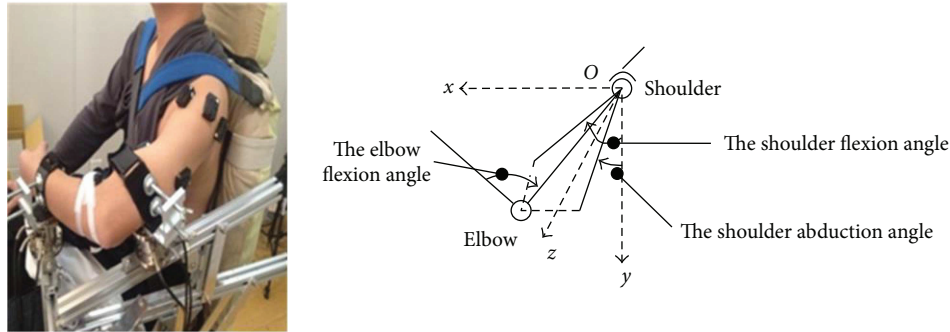


FIGURE 2: The subject's posture during experiment. The  $x,O,y$  coordinate plane represented the sagittal plane, the  $y,O,z$  coordinate plane represented the coronal plane, and the  $x,O,z$  coordinate plane represented the transection plane. The shoulder flexion angle was defined by the angle between the projection of upper limb on the sagittal plane (the  $x,O,y$  coordinate plane) and the coordinate axes (the  $y$ -axes). The shoulder abduction angle was defined by the angle between the projection of upper limb on the coronal plane (the  $y,O,z$  coordinate plane) and the coordinate axes (the  $y$ -axes). The elbow flexion angle was defined by the angle between the forearm and upper limb on the plane determined by the forearm and upper limb.

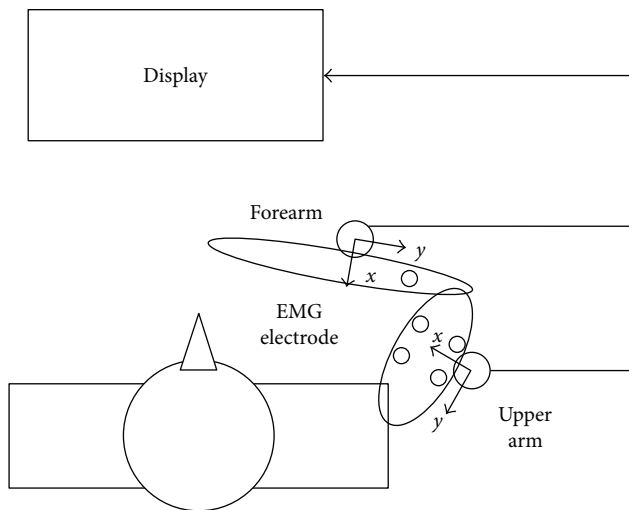


FIGURE 3: The schematic design for forces and EMG measured. The force in the X positive direction at the forearm meant the force in elbow flexion direction and the force in the X positive direction at the upper arm meant the force in shoulder adduction direction.

well as activation of muscles at secondary joints. Bivariate Pearson correlation with two-tailed test was carried out to analyze (i) the dynamic relationship between the primary strength and the secondary strength and (ii) the relationship between primary strength and muscles at secondary joints. Statistical significance in all of the statistical analysis was set at  $p < 0.05$ .

### 3. Results

**3.1. Dynamic Analysis of Strength Patterns.** Primary strength at shoulder or elbow joint changed from 0 to 50% MVS and then to 0 during 50% MVS tasks. The variation of secondary strength was in high correlation to the variation of primary strength with all correlation coefficients above 50%, especially elbow flexion during shoulder abduction and shoulder

adduction during elbow extension with the correlation coefficients above 85% (Figure 4).

In 50% MVS-ABD, 50% MVS-ADD, 50% MVS-FLEX, and 50% MVS-EXT task, all variations of secondary strength were in high correlations to the variations of primary strength ( $R^2 > 50\%$ ). It should be highlighted that the correlation coefficients of elbow flexion during shoulder abduction and shoulder adduction during elbow extension were above 85% (Figure 4).

**3.2. Relationship between the Strength Patterns and Muscle Activation.** Table 3 illustrated the results of the linear regression analysis for the relationship between the strength patterns and muscle activation during the dynamic strength changing process. There existed a significant linear relationship ( $R^2 > 0.70$ ) between primary strength and the activation of muscles at secondary joint in each task, which indicated that muscles at secondary joint can be activated in primary strength task, especially TB, BR activation in shoulder abduction, BB, TB, BR activation in shoulder adduction, AD, MD, PD activation in elbow extension, and PM, AD, MD, PD activation in elbow flexion.

The correlation coefficients by the multilinear regression analysis reflected the influence degree of the independent variable on the dependent variable. Muscle activation influenced the strength, and the degree of the influence can be described by the correlation coefficients. There was a significant linear relationship between secondary strength and muscles at primary joint via ridge regression analysis in each task (50% MVS-ABD  $R^2 = 0.70$ , 50% MVS-ADD  $R^2 = 0.72$ , 50% MVS-FLEX  $R^2 = 0.94$  and 50% MVS-EXT  $R^2 = 0.65$ , Table 4).

### 4. Discussion

Most of the previous quantitative studies of upper limb strength and muscle activation were analyzed separately [1, 9, 10], and the strength pattern was just analyzed by an averaged value. However, the strength pattern was a dynamic process. The process of the strength changes during

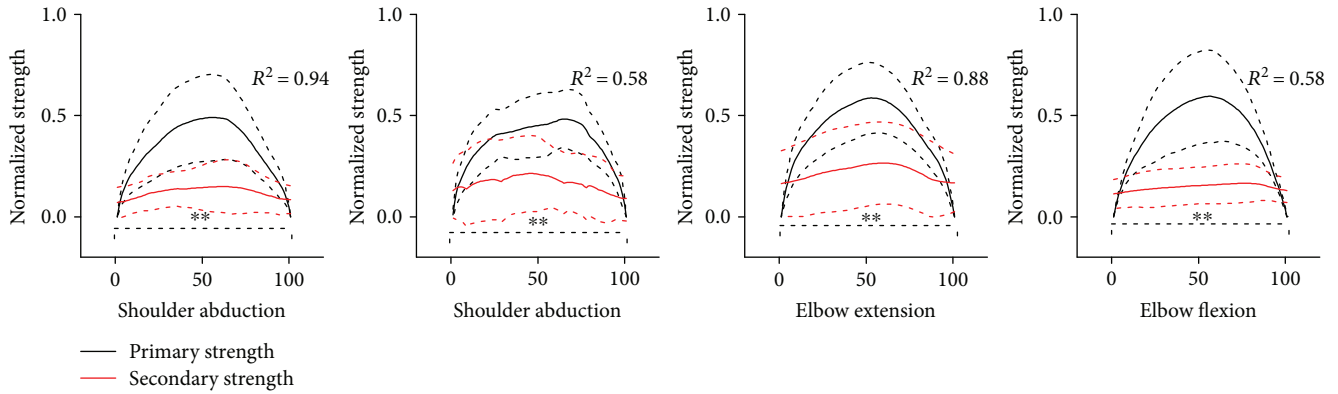


FIGURE 4: The variation of secondary and primary strength during primary strength actions. The horizontal axis in Figure 4 represented the total effort of the primary strength and the vertical axis represented the normalized strength of secondary and primary strength in 50% MVC tasks. The black curves represented the normalized primary strength and the red ones represented the normalized secondary strength. The solid curves represented the average values among different subjects and the dashed curves represented one standard deviation among different subjects.  $**p < 0.01$ .

TABLE 3: Pearson correlation coefficients between the activation of muscles at secondary joint and primary strength.

| Primary strength | Secondary strength | Pearson correlation coefficients of variables |          |          |          |          |          |          |
|------------------|--------------------|---|----------|----------|----------|----------|----------|----------|
|                  |                    | $R_{PM}$                                      | $R_{AD}$ | $R_{MD}$ | $R_{PD}$ | $R_{BB}$ | $R_{TB}$ | $R_{BR}$ |
| ABD              | FLEX               | —   | —        | —        | —        | -0.07    | -0.42**  | -0.59**  |
| ADD              | EXT                | —   | —        | —        | —        | 0.61**   | 0.30**   | 0.83**   |
| EXT              | ADD                | -0.08   | 0.94**   | 0.95**   | 0.45**   | —        | —        | —        |
| FLEX             | ABD                | 0.67**  | 0.77**   | 0.54**   | 0.75**   | —        | —        | —        |

ABD: strength at shoulder abduction; ADD: strength at shoulder adduction; EXT: strength at elbow extension; FLEX: strength at elbow flexion.  $R_{muscles}$  (muscles = PM, AD, MD, PD), the standardized coefficients between the strength at elbow and the activation of muscles (pectoralis major(PM), anterior deltoid (AD), intermediate deltoid (MD), posterior deltoid (PD));  $R_{muscles}$  (muscles = BB, TB, BR), the standardized coefficients between the strength at shoulder and the activation of muscles (biceps brachii (BB), triceps brachii (TB), brachioradialis (BR)).  $**p < 0.01$ .

TABLE 4: Multiple regression analysis of normalized secondary strength and muscles at primary joint.

| Normalized second strength | Primary strength direction | Standardized coefficients of independent variables |          |          |          |          |          |          | $R^2$  |
|----------------------------|----------------------------|--|----------|----------|----------|----------|----------|----------|--------|
|                            |                            | $R_{PM}$   | $R_{AD}$ | $R_{MD}$ | $R_{PD}$ | $R_{BB}$ | $R_{TB}$ | $R_{BR}$ |        |
| FLEX                       | ABD                        | 0.13**   | 0.14**   | 0.29**   | 0.32**   | —        | —        | —        | 0.70** |
| EXT                        | ADD                        | 0.33**   | 0.33**   | 0.04     | 0.28**   | —        | —        | —        | 0.72** |
| ADD                        | EXT                        | —  | —        | —        | —        | -0.07*   | 1.12**   | 0.19**   | 0.94** |
| ABD                        | FLEX                       | —  | —        | —        | —        | -0.30**  | 0.49**   | 0.45**   | 0.65** |

ABD: strength at shoulder abduction; ADD: strength at shoulder adduction; EXT: strength at elbow extension; FLEX: strength at elbow flexion.  $R_{muscles}$  (muscles = PM, AD, MD, PD), the standardized coefficients between the strength at elbow and the activation of muscles (pectoralis major(PM), anterior deltoid (AD), intermediate deltoid (MD), posterior deltoid (PD));  $R_{muscles}$  (muscles = BB, TB, BR), the standardized coefficients between the strength at shoulder and the activation of muscles (biceps brachii (BB), triceps brachii (TB), brachioradialis (BR)).  $*0.01 < p < 0.05$ ;  $**p < 0.01$ .

actions cannot be described by a certain average value and the muscles which have more influence on the secondary strength pattern cannot also be determined by a single value. In this study, participants were asked to perform the dynamic process through the strength changing from 0 to target values and then to 0 again. A multiple linear regression method was used to analyze the relationship between the strength and muscle activation and explore which muscle activation primarily influencing the abnormal pattern.

**4.1. The Dynamic Process of Strength Patterns.** For subjects with hemiplegia, secondary strengths were in significant correlations with primary strengths in the conjunct movement of shoulder abduction during elbow flexion and elbow extension during shoulder adduction, which was compatible with the abnormal joint torque patterns found in 2000 by Dewald and Beer [9]. Furthermore, it can be found that the secondary strength was in a higher correlation to the primary strength in shoulder abduction and elbow extension with both of the

correlation coefficients above 0.95. The phenomenon may be demonstrated by the common stereotyped flexor synergies in upper limb, which was consistent with the Roh et al. study [5]. The higher correlation coefficients reflected that patients can perform a stronger secondary strength during performing primary strength in shoulder abduction and elbow extension. The remarkably increasing elbow flexion strength along with shoulder abduction could be explained by patients generating a large strength at the distal joint to compensate for the weakness of shoulder [18, 19]. The increasing elbow flexion may decrease the mechanical inertial torque of upper limb and make it easier for subjects with weak shoulder strength to perform shoulder abduction.

The increasing shoulder adduction along with elbow extension demonstrated the rationale of the motor learning method in Bobath concept [20, 21]. Patients could generate a large strength at the proximal joint in order to guarantee the stabilization of the shoulder during performance at distal joint. Besides, patients generated an opposite torque at the upper arm by increasing shoulder adduction during elbow extension, thus decreasing the total torque.

**4.2. Relationship between Muscle Activation and Secondary Strength.** Patients with hemiplegia usually have lesions in their cerebral cortex. They generally have reduced corticospinal input to shoulder and distal arm muscles. The reduction from corticospinal control signals results in an increased dependence on residual brainstem descending pathways (such as vestibulospinal, reticulospinal, and rectospinal pathways) [22], which may activate extensive branching and innervate more neurons over spinal segments. Accordingly, the increased dependence on brainstem pathways may induce coactivation of more muscles, thus altering the strength pattern in patients with hemiplegia [23]. Muscles at secondary joint were influenced by the activation of muscles at primary joint because of the decreased control of muscle selectivity [24].

However, all of the muscles at secondary joint were influenced at different degrees. The antagonistic muscles at the elbow joint were much influenced during the primary strength at shoulder joint. For example, TB, the antagonistic muscle for elbow flexion, was much influenced during shoulder abduction; BB and BR, the antagonistic muscles for elbow extension were much influenced during shoulder adduction. Besides, the antagonistic muscles at shoulder joint were also much influenced by primary strength at elbow joint. Primary strength in elbow extension had much influence on PD and MD (the antagonistic muscles for shoulder adduction) and primary strength in elbow flexion had much influence on AD (the antagonistic muscles for shoulder abduction). These results may also reflect the declined inhibition on the antagonistic muscles for patients with hemiplegia [25–27].

The dynamic analysis of muscle activation and secondary strength demonstrates the different degrees of different muscles' influence on the secondary strength. The significant level of each muscle's influence on the normalized secondary strength illustrates how the secondary strength patterns depend on the muscle activation. Secondary strength pattern of shoulder abduction during elbow flexion

is much influenced by shoulder abduction agonist and antagonist (MD and PD). Secondary strength pattern of shoulder adduction during elbow extension is significantly influenced by shoulder adduction muscles (PM, AD, and PD). Elbow extension muscles (TB and BR) have significant effects on secondary strength pattern of elbow extension during shoulder adduction. Elbow flexion muscles (BB, TB, and BR) have significant effects on secondary strength pattern of elbow flexion during shoulder abduction.

An important limitation of this study is that it only explored the secondary strength patterns between shoulder abduction/adduction and elbow flexion/extension, while shoulder flexion/extension and shoulder internal/rotation may also influence elbow flexion/extension in subjects with hemiplegia. The designed isometric strength measurement instrument for the upper limb may have influence on the activation of muscles at proximal and distal segments. Finally, the sample size of investigated subjects was small and the patients were not in the same rehabilitation state: some were in subacute stroke and others were in chronic stroke. In the future, we should recruit more numbers of patients in the same rehabilitation state and design more test postures in the experiment.

## 5. Conclusions

The process of strength performing is a dynamic process with strength changing from 0 to target values and then to 0 again, even in an isometric strength task. This study conducted a dynamic analysis of the abnormal secondary strength pattern in patients with hemiplegia by using multiple linear analysis. It can be concluded that secondary strength in elbow flexion during shoulder abduction and shoulder adduction during elbow extension was in high correlation with the primary strength. It also suggests that patients may intend to decrease the total torque by generating an opposite torque at shoulder or elbow joint during elbow or shoulder strength tasks. Deltoid, biceps brachii, triceps brachii, and brachioradialis have more influences on the abnormal movement pattern.

## Conflicts of Interest

No financial conflict exists.

## Acknowledgments

The study was supported by the National Natural Science Foundation of China (Grant no. U1613207). The authors are grateful to the subjects who participated in the investigation and the Chinese PLA General Hospital for recruiting patients. Special thanks are for Dr. Xinyu Guan who provided a lot of advice to revise this manuscript.

## References

- [1] N. Neckel, M. Pelliccio, D. Nichols, and J. Hidler, "Quantification of functional weakness and abnormal synergy patterns in the lower limb of individuals with chronic stroke," *Journal of Neuroengineering and Rehabilitation.*, vol. 3, no. 1, pp. 17–28, 2006.

- [2] C. Bosecker, L. Dipietro, B. Volpe, and H. I. Krebs, "Kinematic robot-based evaluation scales and clinical counterparts to measure upper limb motor performance in patients with chronic stroke," *Neurorehabilitation and Neural Repair*, vol. 24, no. 1, pp. 62–69, 2010.
- [3] J. Metrot, D. Mottet, I. Relave et al., "Bimanual coordination in stroke recovery: kinematic analysis provides open leads to individualize upper limb rehabilitation," *Annals of Physical and Rehabilitation Medicine*, vol. 54, article e235, 2011.
- [4] J. M. Wagner, C. E. Lang, S. A. Sahrmann, D. F. Edwards, and A. W. Dromerick, "Sensorimotor impairments and reaching performance in subjects with poststroke hemiparesis during the first few months of recovery," *Physical Therapy*, vol. 87, no. 6, pp. 751–765, 2007.
- [5] J. Roh, W. Z. Rymer, E. J. Perreault, S. B. Yoo, and R. F. Beer, "Alterations in upper limb muscle synergy structure in chronic stroke survivors," *Journal of Neurophysiology*, vol. 109, no. 3, pp. 768–781, 2013.
- [6] G. J. C. Ettema, E. Taylor, J. D. North, and V. Kippers, "Muscle synergies at the elbow in static and oscillating isometric torque tasks with dual degrees of freedom," *Motor Control*, vol. 9, no. 1, pp. 59–74, 2005.
- [7] L. Ada, N. O'Dwyer, and E. O'Neill, "Relation between spasticity, weakness and contracture of the elbow flexors and upper limb activity after stroke: an observational study," *Disability and Rehabilitation*, vol. 28, no. 13–14, pp. 891–897, 2006.
- [8] P. S. Lum, C. G. Burgar, and P. C. Shor, "Evidence for improved muscle activation patterns after retraining of reaching movements with the MIME robotic system in subjects with post-stroke hemiparesis," *IEEE Transactions on Neural Systems and Rehabilitation Engineering*, vol. 12, no. 2, pp. 186–194, 2004.
- [9] J. P. A. Dewald and R. F. Beer, "Abnormal joint torque patterns in the paretic upper limb of subjects with hemiparesis," *Muscle & Nerve*, vol. 24, no. 2, pp. 273–283, 2001.
- [10] R. W. Bohannon and M. B. Smith, "Assessment of strength deficits in eight paretic upper extremity muscle groups of stroke patients with hemiplegia," *Physical Therapy*, vol. 67, no. 4, pp. 522–525, 1987.
- [11] Y.-z. Hong, J.-f. Sui, L.-h. Ji, L. Xi, and B. Sheng, "Force characteristics of synergistic movement between shoulder and elbow joints," *Chinese Journal of Rehabilitation Theory and Practice*, vol. 21, no. 14, pp. 1319–1324, 2015.
- [12] X. Guan, Y. Liu, L. Gao et al., "Trunk muscle activity patterns in a person with spinal cord injury walking with different unpowered exoskeletons: a case study," *Journal of Rehabilitation Medicine*, vol. 48, no. 4, pp. 390–395, 2016.
- [13] China Standards Press, *Inertial Parameters of Adult Human Body*, The state standard of the People's Republic of China: Standards Press of China, Beijing, China, 1998.
- [14] S.-K. Chen, M.-T. Wu, C.-H. Huang, J.-H. Wu, L.-Y. Guo, and W.-L. Wu, "The analysis of upper limb movement and EMG activation during the snatch under various loading conditions," *Journal of Mechanics in Medicine and Biology*, vol. 13, no. 1, pp. 1350–1360, 2013.
- [15] I. Rogowski, D. Rouffet, F. Lambalot, O. Brosseau, and C. Hautier, "Trunk and upper limb muscle activation during flat and topspin forehand drives in young tennis players," *Journal of Applied Biomechanics*, vol. 27, no. 1, pp. 15–21, 2011.
- [16] K. Nagai, M. Yamada, K. Uemura, Y. Yamada, N. Ichihashi, and T. Tsuboyama, "Differences in muscle coactivation during postural control between healthy older and young adults," *Archives of Gerontology and Geriatrics*, vol. 53, no. 3, pp. 338–343, 2011.
- [17] P. Konrad, *The ABC of EMG: a practical introduction to kinesiological electromyography*, Noraxon INC, Scottsdale, USA, 1 edition, 2005.
- [18] C. Mercierand and D. Bourbonnais, "Relative shoulder flexor and handgrip strength is related to upper limb function after stroke," *Clinical Rehabilitation*, vol. 18, no. 2, pp. 215–221, 2004.
- [19] M. Smith, "Neurological rehabilitation: optimizing motor performance," *Physiotherapy Canada*, vol. 67, no. 2, pp. 215–220, 2015.
- [20] S. Raine, L. Meadows, and M. Lynch-Ellerington, *Bobath Concept: Theory and Clinical Practice in Neurological Rehabilitation*, John Wiley & Sons, Hoboken, NJ, USA, 2013.
- [21] B. J. Kollen, S. Lennon, B. Lyons et al., "The effectiveness of the Bobath concept in stroke rehabilitation: what is the evidence?," *Stroke*, vol. 40, no. 4, pp. e89–e97, 2009.
- [22] R. N. Lemon, "Descending pathways in motor control," *Annual Review of Neuroscience*, vol. 31, no. 1, pp. 195–218, 2008.
- [23] H. G. J. M. Kuypers, "The descending pathways to the spinal cord, their anatomy and function," *Progress in Brain Research*, vol. 11, pp. 178–202, 1964.
- [24] M. Staudt, W. Grodd, C. Gerloff, M. Erb, J. Stitz, and I. Krägeloh-Mann, "Two types of ipsilateral reorganization in congenital hemiparesis: a TMS and fMRI study," *Brain*, vol. 125, no. 10, pp. 2222–2237, 2002.
- [25] C. Gowland, H. deBruin, J. V. Basmajian, N. Plews, and I. Burcea, "Agonist and antagonist activity during voluntary upper-limb movement in patients with stroke," *Physical Therapy*, vol. 72, no. 9, pp. 624–633, 1992.
- [26] M. F. Levin, R. W. Selles, M. H. G. Verheul, and O. G. Meijer, "Deficits in the coordination of agonist and antagonist muscles in stroke patients: implications for normal motor control," *Brain Research*, vol. 853, no. 2, pp. 352–369, 2000.
- [27] A. Silva, A. S. P. Sousa, J. M. R. S. Tavares, A. Tinoco, R. Santos, and F. Sousa, "Ankle dynamic in stroke patients: agonist vs. antagonist muscle relations," *Somatosensory & Motor Research*, vol. 29, no. 4, pp. 111–116, 2012.

## Research Article

# Enhancement of the Comb Filtering Selectivity Using Iterative Moving Average for Periodic Waveform and Harmonic Elimination

José L. Ferreira <sup>1</sup>, Yan Wu,<sup>1</sup> and Ronald M. Aarts<sup>1,2</sup>

<sup>1</sup>Department of Electrical Engineering, Eindhoven University of Technology, P.O. Box 513, 5600 MB Eindhoven, Netherlands

<sup>2</sup>Philips Research Laboratories, Eindhoven, Prof. Holstlaan 4, 5656 AE Eindhoven, Netherlands

Correspondence should be addressed to José L. Ferreira; [j.l.ferreira@tue.nl](mailto:j.l.ferreira@tue.nl)

Received 10 August 2017; Accepted 28 November 2017; Published 1 February 2018

Academic Editor: Saugat Bhattacharyya

Copyright © 2018 José L. Ferreira et al. This is an open access article distributed under the Creative Commons Attribution License, which permits unrestricted use, distribution, and reproduction in any medium, provided the original work is properly cited.

A recurring problem regarding the use of conventional comb filter approaches for elimination of periodic waveforms is the degree of selectivity achieved by the filtering process. Some applications, such as the gradient artefact correction in EEG recordings during coregistered EEG-fMRI, require a highly selective comb filtering that provides effective attenuation in the stopbands and gain close to unity in the pass-bands. In this paper, we present a novel comb filtering implementation whereby the iterative filtering application of FIR moving average-based approaches is exploited in order to enhance the comb filtering selectivity. Our results indicate that the proposed approach can be used to effectively approximate the FIR moving average filter characteristics to those of an ideal filter. A cascaded implementation using the proposed approach shows to further increase the attenuation in the filter stopbands. Moreover, broadening of the bandwidth of the comb filtering stopbands around  $-3$  dB according to the fundamental frequency of the stopband can be achieved by the novel method, which constitutes an important characteristic to account for broadening of the harmonic gradient artefact spectral lines. In parallel, the proposed filtering implementation can also be used to design a novel notch filtering approach with enhanced selectivity as well.

## 1. Introduction

In biomedical signal processing and signal processing in general, comb filtering approaches represent an important class of filters that play a relevant role in different fields, such as extraction or elimination of periodic signal and harmonic components, speech and audio signal processing, decimation processes, prediction and estimation of geophysical signals, and power line rejection [1–5]. In its simplest form, a comb filter can be viewed as a combination of notch filters in which the null frequencies occur periodically across the filter bandwidth. Another very popular comb filtering approach is the conventional FIR moving average filter indicated in

$$y_n = \frac{1}{M} \sum_{k=0}^{M-1} x_{n-k}, \quad (1)$$

whose representation in  $z$ -domain and discrete time realisation is shown, respectively, in (2) and Figure 1.

$$\frac{Y(z)}{X(z)} = \frac{1}{M} \frac{(1 - z^{-M})}{(1 - z^{-1})} = H_{\text{MAF}}(z), \quad (2)$$

with  $M = f_s/f_M$ , where  $f_s$  is the sampling frequency and  $f_M$  is the fundamental of the periodic null frequencies.

The comb filter realisation indicated in (2) is widely employed because of its computational efficiency. As limitations, however, (2) provides a magnitude response with low attenuation in the filter stopbands as well as nonuniform gain and high attenuation in the pass-bands, as depicted in Figure 2(a). In addition, despite the piecewise linearity of the phase characteristic (Figure 2(b)), it can provoke increased phase delay for higher values of  $M$  [1, 4].

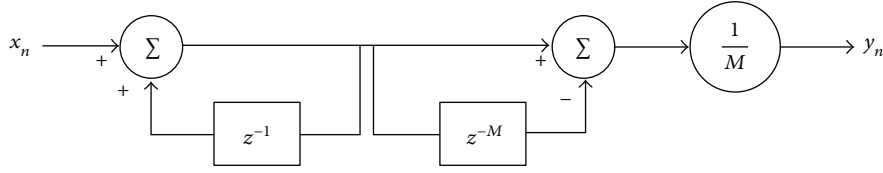
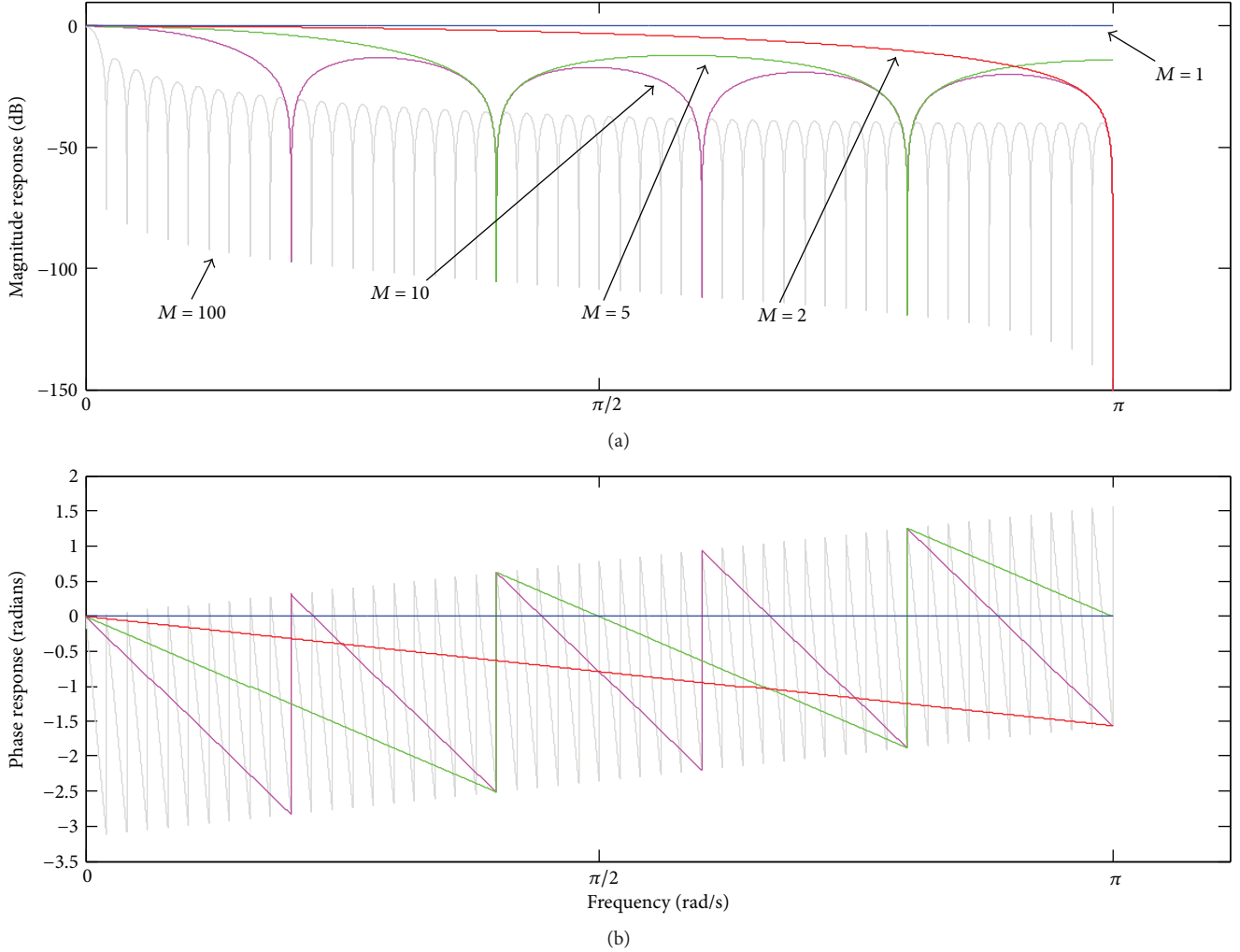


FIGURE 1: Discrete time realisation of the moving average filter described in (2).

FIGURE 2: Frequency response of  $H_{\text{MAF}}(\omega)$  for some values of  $M$ : (a) magnitude response; (b) phase response.

Such characteristics are undesirable in some applications and are far from those of an ideal comb filter: zero gain at notch frequencies, uniform and unity gain in the pass-bands, and no effects on the signal phase. To make the comb filter realisation of (2) more selective or closer to the ideal behaviour, some strategies have been suggested in the literature. For instance, it can be achieved by the introduction of poles in the transfer function of (2), as indicated in [4, 6, 7]

$$H_{\text{MOD}}(z) = \frac{1 - z^{-M}}{1 - z^{-1}} \frac{1 - r \cdot z^{-1}}{1 - (r \cdot z^{-1})^M}, \quad (3)$$

where the value of the parameter  $r$  is contained in the interval  $0 \leq r < 1$ . As mentioned by Proakis and Manolakis [4], the insertion of poles in (2) has the effect of introducing a resonance in the vicinity of the null, thus provoking reduction of the bandwidth of the stopbands. Thereby, the zeros  $z = e^{j2\pi k/M}$  placed at the unit circle in the  $z$ -plane will have in their vicinity the poles  $z = r \cdot e^{j2\pi k/M}$ . The comb filter described in (3) has been successfully used in several applications, such as in harmonic compensators and rectifiers in power systems [6, 7]. However, one of the limitations of this approach is the decreased attenuation in the stopbands, as the value of  $r$  increases towards 1. Furthermore, there is a

trade-off between the values of  $M$  and  $r$ , which is contingent to the performance requirement of the filter: on one hand, the use of higher values of  $M$  makes this method computationally expensive regarding memory usage. On the other hand, the exponential decrease of the power  $r^M$  makes the filter to be implemented by using lower resolution computer unit. Thus, there exists a compromise between the value of  $M$  and the computer unit resolution [6].

Another proposed strategy to improve the selectivity of the comb filtering provided by (2) is the time-domain averaging approach. Time-domain averaging consists of a kind of comb filtering approach based on a coherent detection process whereby estimation and elimination of the periodic activity are carried out by averaging repetitive sequences of a periodic signal,  $p(t)$ , observed in the input signal,  $x(t)$ .

$$x(t) = p(t) + e(t). \quad (4)$$

In (4),  $e(t)$  represents the nonperiodic component of  $x(t)$ , which could be a noise signal or some stochastic process. Under the assumption that  $p(t)$  and  $e(t)$  are uncorrelated, summing up  $N$  subsequent segments  $x(t_i)$  corresponding to the periodic signal results in coherent summation of  $p(t)$  [8]. Thus, the estimate of  $p(t)$  obtained by time-domain averaging can be calculated by the following discrete representation:

$$\hat{p}_n = \frac{1}{N} \sum_{i=0}^{N-1} x_{n-iM}. \quad (5)$$

Or in  $z$ -domain,

$$H_p(z) = \frac{1}{N} \frac{(1 - z^{-NM})}{(1 - z^{-M})}. \quad (6)$$

The frequency response associated with the nonperiodic component is derived from the subtraction between the discrete representation of  $x(t)$  and (5).

$$e(t) = x(t) - p(t) \Rightarrow \hat{e}_n = x_n - \frac{1}{N} \sum_{i=0}^{N-1} x_{n-iM} = y_n. \quad (7)$$

$$\Rightarrow \frac{Y(z)}{X(z)} = 1 - H_p(z) \Rightarrow H_{\text{TDA}}(z) = 1 - |H_p(z)|, \quad (8)$$

where  $H_{\text{TDA}}(z)$  is the magnitude response of the comb filtering for elimination of the periodic component.

Time-domain averaging is a well-established comb filtering approach which has been widely used to estimate and extract periodic signals encountered in phenomena involving some rotating machinery [2, 8, 9]. Time-domain averaging-based approaches have been also proposed to estimate and eliminate the gradient artefact from the EEG signal, such as the average artefact subtraction method [10, 11]. The gradient artefact consists of a periodic waveform voltage interference which is induced in the electrical potential recorded in the human scalp (scalp potential) by the rapidly varying magnetic field gradients and radiofrequency pulses used in MRI sequences during simultaneous acquisition of EEG and fMRI data [12, 13]. One limitation of time-domain averaging, however, is its high dependency on accurate sampling of the

periodic waveform  $p(t)$ . The occurrence of jitter errors may result in imprecise sampling of the averaging waveforms, which can impair the effectiveness of the method. Thus, the period of the repetitive waveform must be an exact multiple of the sampling interval. In parallel, the period of  $p(t)$  must be precisely known, which requires an external trigger or reference signal provided by an additional hardware [8, 14]. In case of the suppression of the gradient artefact from the EEG signal, subject movements or small drifts may also compromise the performance of the algorithm, since they change the morphology and shape of the artefact, in such a way that it is not possible to obtain an accurate estimate of  $\hat{p}(t)$ . Subject movements or small drifts also provoke broadening of the harmonic artefact spectral lines [15], whose attenuation may not be effectively accounted for by the time-domain averaging comb filter. As a consequence, residual artefacts are left behind in the corrected EEG after subtraction of the estimated periodic waveform  $\hat{p}_n$ .

In this paper, we present a novel comb filtering implementation to improve the selectivity of the comb filtering provided by the FIR moving average filter of (2). As described in Section 2, implementation of such a comb filter has been based upon an iterative filtering decomposition process [16], whereby an estimation of the filtered signal can be obtained by the iterative application of a FIR moving average filter-based approach named double average filter. Comparison between the novel comb filtering implementation and those existing methodologies to enhance the selectivity of (2) described above shows that the novel method could be used in scenarios in which those approaches are not effective, such as during broadening of the harmonic gradient artefact spectral lines. In addition, the iterative application of time-domain averaging is revealed to enable the use of a smaller number of averages during application of such a method, as shown in Sections 3 and 4.

## 2. Methods

In recent research [16, 17], iterative filtering decomposition has been proposed as an alternative implementation for empirical mode decomposition [18]. According to this methodology, a series  $\mathbf{L}_1$  of low-pass filters (or moving average filters) is used to decompose a signal in intrawave frequency modes or intrinsic mode functions (IMFs). Here, we have further exploited the estimation of the first IMF,  $\mathbf{F}_1$ , by application of the filter  $(1 - \mathbf{L}_1)$  in the input signal  $\mathbf{x}$ :

$$\mathbf{F}_1 = \lim_{j \rightarrow \infty} (1 - \mathbf{L}_1)^{j-1} \mathbf{x}, \quad (9)$$

where  $\mathbf{L}_1$  corresponds to a FIR moving average-based filter. The convergence of the iterative filtering decomposition is ensured by the coefficients (masks) of the filter  $\mathbf{L}_1$  having a value between 0 and 1, which has been demonstrated by Lin et al. [16].

*2.1. Design of a Novel Comb Filtering Approach for Elimination of Periodic Waveforms.* As  $\mathbf{L}_1$ , initially, we investigated the forward-backward application of the moving average filter indicated in (1) in the input signal,  $x_n$  [19,

20]. This procedure allows obtaining a filtered signal with zero-phase distortion, which is a characteristic of an ideal comb filter. The forward-backward application of (1) in  $x_n$  can be expressed as

$$y_n = \frac{1}{M} \sum_{k=-M-1}^0 \left[ \frac{1}{M} \sum_{k=0}^{M-1} x_{n-k} \right]_{n+k} = \frac{1}{M} \sum_{k=-M+1}^{M-1} \left( \frac{M-|k|}{M} \right) x_{n+k}. \quad (10)$$

Equation (10) is also referred to as double average filter [16, 17], where the coefficients of  $x_{n+k}$  correspond to a triangular window of length  $2 \times M$ . By applying the  $z$ -transformation in (10), it results in the following transfer function:

$$H_D(z) = \frac{1}{(M)^2} \frac{(1-z^{-M})(1-z^M)}{(1-z^{-1})(1-z)}, \quad (11)$$

whose discrete time realisation is depicted in Figure 3.

The frequency response of  $H_D(z)$  is derived from (11) by setting  $z = e^{j\omega}$ . Hence,

$$H_D(\omega) = \frac{1}{(M)^2} \frac{\sin^2(\omega M/2)}{\sin^2(\omega/2)}. \quad (12)$$

Figure 4 depicts the magnitude response of  $H_D(\omega)$ , calculated according to (12), for some values of  $M$ . It also shows the presence of spaced zeros at the frequency  $2\pi/M$ . For a hypothetical value  $M = 1$ ,  $H_D(\omega)$  becomes an all-pass band filter.

The phase response of  $H_D(\omega)$  possesses a zero-phase characteristic, as a result of the forward-backward application of the moving average filter of (1).

$$\theta_D(\omega) = \tan^{-1} \left\{ \frac{\text{Im}[H_D(\omega)]}{\text{Re}[H_D(\omega)]} \right\} = 0. \quad (13)$$

Therefore, (11) describes a kind of FIR moving average-based filter that provides no distortion effects in the phase of the signal in the whole filter pass-band. Replacing (11) by  $\mathbf{L}_1$  in (9) and taking into account a number  $J$  of iterations, it can be rewritten as [19]

$$F_1(z) = (1 - H_D(z))^J X(z) \Rightarrow \frac{F_1(z)}{X(z)} = (1 - H_D(z))^J = H_1(z). \quad (14)$$

Equation (14) corresponds to the transfer function that relates the extracted periodic waveform,  $p(t)$ , and the input signal,  $x(t)$ , as likewise indicated in (4). Therefore, after elimination of  $p(t)$ , the output  $y(t)$  of the proposed comb filter has been related to  $x(t)$  as [20]

$$Y(z) = (1 - H_1(z))X(z) \Rightarrow \frac{Y(z)}{X(z)} = 1 - H_1(z) = H_C(z). \quad (15)$$

In order to improve the attenuation in the stopbands, we investigated the application of  $H_C(z)$  within the cascade implementation indicated in

$$H_L(z) = [H_C(z)]^L, \quad (16)$$

where  $L$  is the number of cascades. Since (15) and (16) have been derived from (11), which has zero-phase distortion characteristic, they do not cause any distortion effects on the filtered signal phase either.

**2.2. Iterative Application of Time-Domain Averaging.** As an alternative for the filter  $\mathbf{L}_1$  in (9), we have also investigated the use of the time-domain averaging filter described in (8). To this end, we have taken into account a number  $J$  of iterations of (9), which has been rewritten as

$$\begin{aligned} F_2(z) &= (1 - H_{\text{TDA}}(z))^J X(z) \Rightarrow \frac{F_2(z)}{X(z)} \\ &= (1 - H_{\text{TDA}}(z))^J = (H_p(z))^J = H_2(z). \end{aligned} \quad (17)$$

Thereby, by eliminating the estimated periodic signal, the output has been related to the input as

$$\frac{Y(z)}{X(z)} = 1 - H_2(z) = H_{\text{RTDA}}(z). \quad (18)$$

**2.3. Using the Proposed Method to Design a Novel Notch Filtering Approach.** As remarked by Braun [2], the frequency response provided by (7) and (8) corresponds to the convolution between the frequency response depicted in Figure 2 and a train of unit pulses separated by the period  $M$ . Making use of this idea, we also investigated the convolution of a single pulse,  $\delta$ , and the magnitude response indicated in Figure 2(a) to design a novel notch filtering approach approximated to the ideal case.

$$H_3(\omega) = \delta(\omega) * |H_{\text{MAF}}(\omega)|. \quad (19)$$

Figure 5 shows this convolution, where the unit pulse has been located at the frequency  $\omega_0$ , and  $|H_{\text{MAF}}(\omega)|$  was calculated for  $M = 2$ .

As can be noticed in Figure 5(b), (19) corresponds to a pass-band filter with unit amplitude and central frequency at  $\omega_0$ . Replacing  $\mathbf{L}_1$  in (9) by  $(1 - H_3(z))$  and taking into account a certain number  $J$  of iterations, it results in the notch filter  $H_{\text{NTC}}(z)$  of

$$\begin{aligned} F_3(z) &= [1 - (1 - H_3(z))]^J X(z) \Rightarrow \frac{F_3(z)}{X(z)} \\ &= (H_3(z))^J \Rightarrow H_{\text{NTC}}(z) = 1 - (H_3(z))^J. \end{aligned} \quad (20)$$

Like in (16), we investigated the application of (20) in a cascade implementation to enlarge the attenuation at the notch frequency, as indicated in

$$H_{\text{NL}}(z) = [H_{\text{NTC}}(z)]^L, \quad (21)$$

where  $L$  represents the number of cascades as well.

### 3. Results

**3.1. Frequency Characteristics of the Novel Comb Filtering Approach.** All frequency responses depicted below have been calculated using a number of samples  $N_s = 300000$

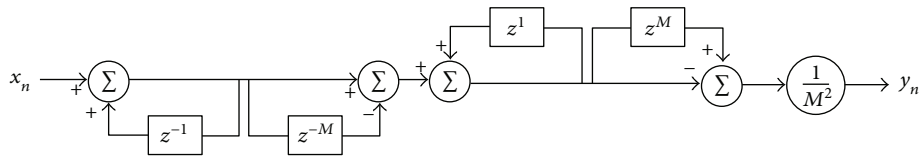


FIGURE 3: Discrete time realisation of (11).

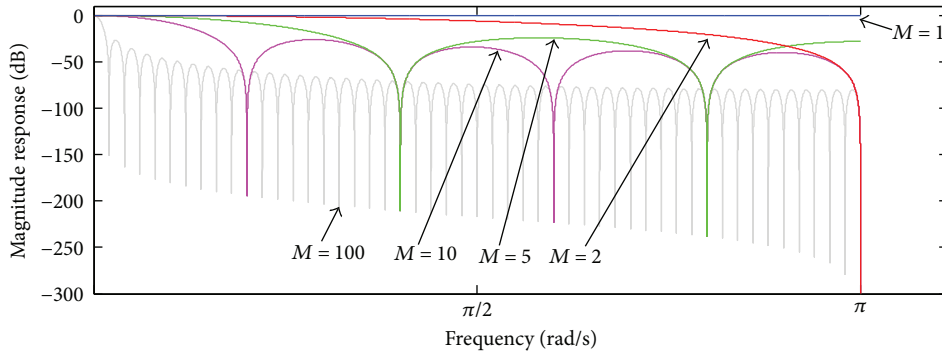


FIGURE 4: Magnitude response of  $H_D(\omega)$  for some values of  $M$ .

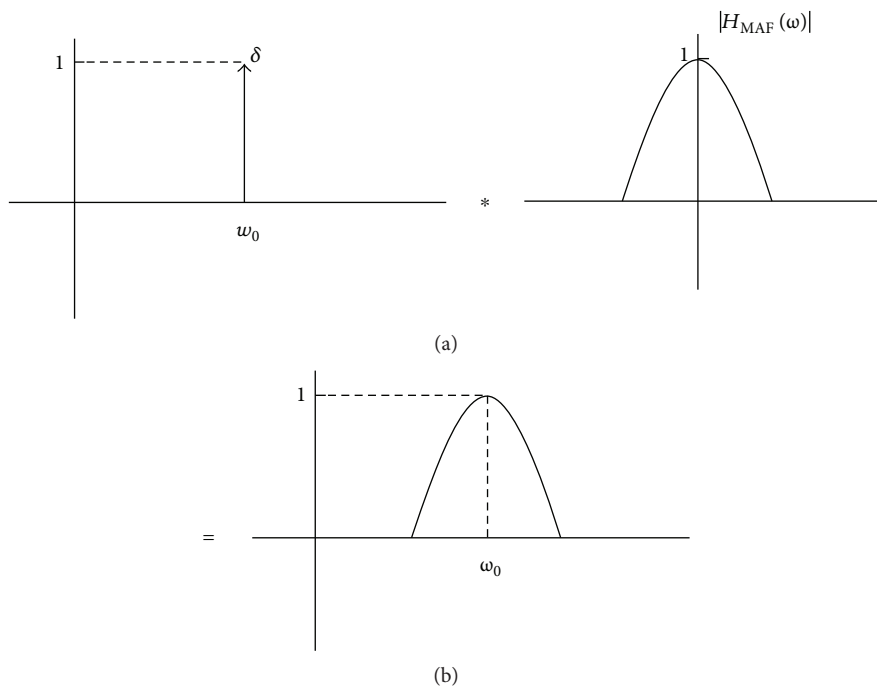


FIGURE 5: Convolution between the unit pulse  $\delta$  (located at the frequency  $\omega_0$ ) and  $|H_{MAF}(\omega)|$  ( $M = 2$ ). It results in a pass-band filter with a central frequency at  $\omega_0$ .

samples, so that  $\omega$  was set as  $\omega = [-\pi, \pi]$ , with a frequency interval at  $2\pi \times (1/N_s)$ . In these figures, only the frequencies ranging from 0 to  $\pi$  are shown. The simulations were performed in MATLAB environment (The MathWorks Inc., Natick, USA).

In Figure 6, the magnitude response of  $H_C(z)$  (15) is depicted, taking into account  $M = 10$  and  $M = 100$  and some

values of  $J$ . It can be observed that increasing of  $J$  is followed by substantial increasing of the filter gain, which attained 0 dB as well as became more uniform in the different passbands. On the other hand, increasing of  $J$  is also followed by a reduction in the attenuation in the filter stopbands. On the extreme case, when  $J \rightarrow \infty$ , (15) tends to become an all-pass band filter, as shown in Figure 7(a). By fixing

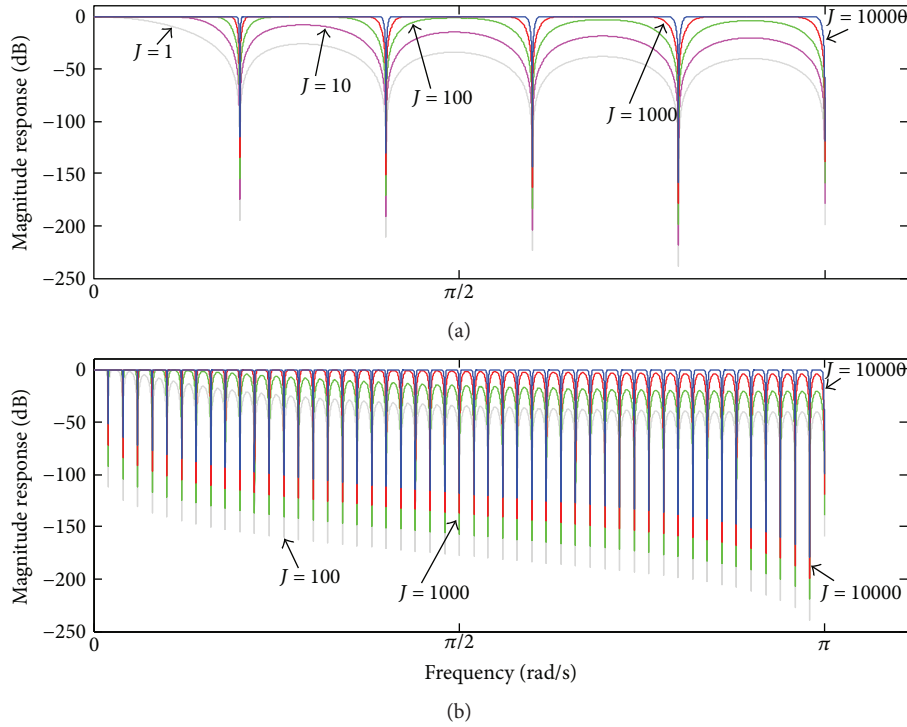


FIGURE 6: Magnitude response of  $H_C(\omega)$ , taking into account (a)  $M = 10$  and (b)  $M = 100$  and some values of  $J$ .

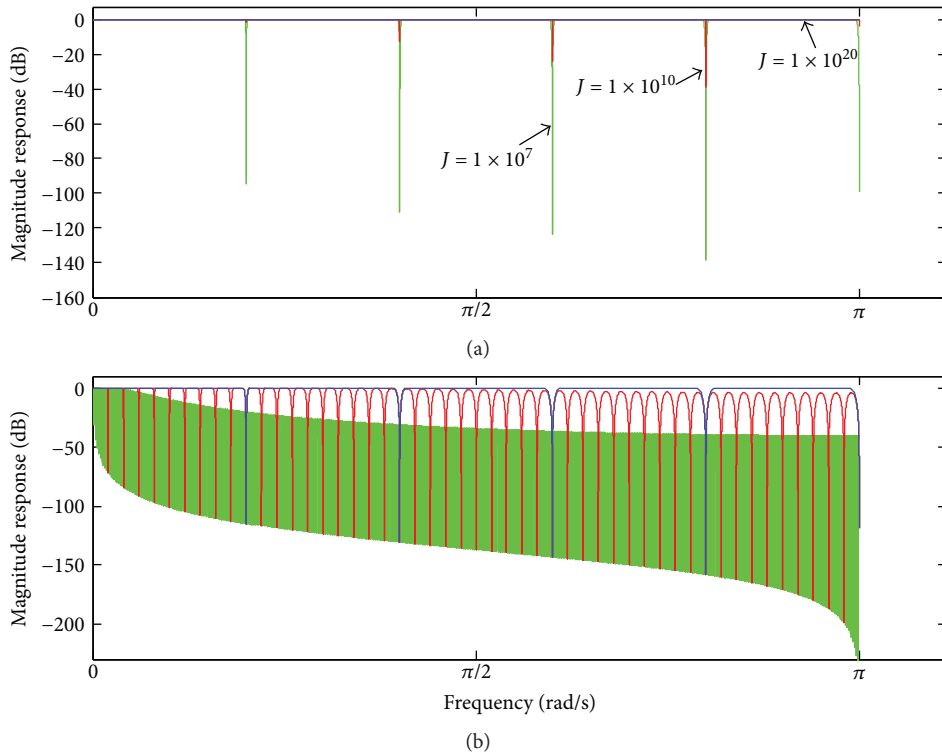


FIGURE 7: (a) Magnitude response of  $H_C(\omega)$  for  $M = 10$  and some values of  $J$  ( $J \rightarrow \infty$ ); (b) magnitude response of  $H_C$  for  $J = 10000$  and some values of  $M$ :  $M = 10$  (blue trace),  $M = 100$  (red trace), and  $M = 1000$  (green trace).

the value of  $J$  and varying  $M$ , (15) shows to provide more uniform gain in the pass-bands for smaller values of  $M$ , as observed in Figure 7(b).

To demonstrate the enhancement of attenuation in the stopbands using (16), its magnitude response has been calculated taking into consideration different values of  $L$ . Figure 8

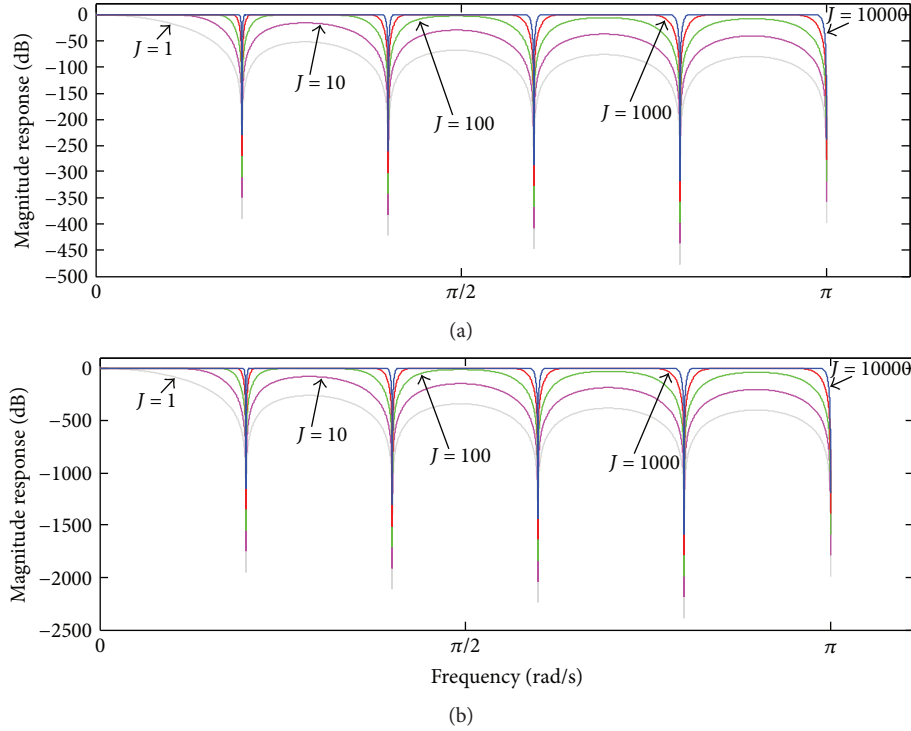


FIGURE 8: Magnitude response of  $H_L(\omega)$  (16) for (a)  $L = 2$  and (b)  $L = 10$ , taking into account  $M = 10$  and some values of  $J$ .

depicts the magnitude response of  $H_L(z)$ , for  $L = 2$  and  $L = 10$ , and taking into account  $M = 10$ , and some values of  $J$ . As can be noticed, (16) provides higher attenuation in the stopbands by increasing the value of  $L$ .

**3.2. Iterative Application of Time-Domain Averaging.** By setting  $z = e^{j\omega}$  in (6), the magnitude and phase response of the periodic component  $\hat{p}(t)$  obtained by time-domain averaging can be, respectively, derived as

$$|H_p(\omega)| = \frac{1}{N} \left| \frac{\sin(\omega NM/2)}{\sin(\omega M/2)} \right| \quad (22)$$

and

$$\theta_p(\omega) = \tan^{-1} \left\{ \frac{\text{Im}[H_p(\omega)]}{\text{Re}[H_p(\omega)]} \right\}. \quad (23)$$

Figure 9 depicts the magnitude and phase response of (22) and (23), taking into account  $M = 10$ , for  $N = 4$  (dark trace),  $N = 8$  (green trace), and  $N = 16$  (gray trace).

The main lobes of the magnitude response  $|H_p(\omega)|$  lie spaced at the frequency  $2\pi/M$  and have unit amplitude. By increasing  $N$ , the amplitude of the side lobes is reduced as well as the main lobes are narrowed. Regarding the phase response, it is not linear, but has approximated piecewise linearity in between the null frequencies of the lobes [4, 8, 9]. In turn, Figure 10 shows the frequency response associated with the nonperiodic component  $e(t)$ , as indicated in (8).

Figure 11 depicts the frequency response provided by (17), taking into account  $M = 10$  and  $N = 4$ , for  $J = 1$  (dark trace),  $J = 3$  (green trace), and  $J = 8$  (gray trace).

It can be noticed that increasing  $J$  in (17) has a similar effect to increasing  $N$  in (22), by reducing the amplitude of the side lobes and narrowing the main lobes. Regarding the phase response, it remains piecewise linear after increasing  $J$ . In Figure 12, the frequency response corresponding to (18) is depicted, for  $M = 10$ ,  $N = 8$ , and some values of  $J$ . It can be observed that as  $J$  increases, the filter gain is approximated to unity along the pass-bands as well as the stopbands become narrower. Therefore, an increase of  $J$  in (18) attests a similar effect to that provided by increasing  $N$  in (8) alike.

### 3.3. Notch Filter Characteristics Obtained by Iterative Filtering.

The magnitude response corresponding to  $H_{\text{NTC}}(z)$  is depicted in Figure 13, taking into account  $M = 2$ , some values of  $J$ , and  $N_s = 300000$  samples for  $|H_{\text{MAF}}(\omega)|$  as well. The notch filter stopband was located at  $\omega_0 = \pi/2$ . It can be observed that the bandwidth of the notch filter stopband is narrowed by increasing the value of  $J$ , as well as (20) tends to become an all-pass band filter when  $J \rightarrow \infty$ . This notch filter does not cause any effects on the phase of the signal.

In Figure 14, we show the use of (20) within the cascade implementation indicated in (21). The variation of the bandwidth of the notch filter stopband around  $-3$  dB provided by (21) is indicated, taking into account  $M = 2$ , some values of  $J$  and  $L$ ,  $f = (\omega/2\pi) \times f_s$ , and  $f_s = 5$  kHz. As can be seen, combination of proper values of  $J$  and  $L$  allows obtaining stopband bandwidths ranging from 0 (when  $J \rightarrow \infty$ ) up to

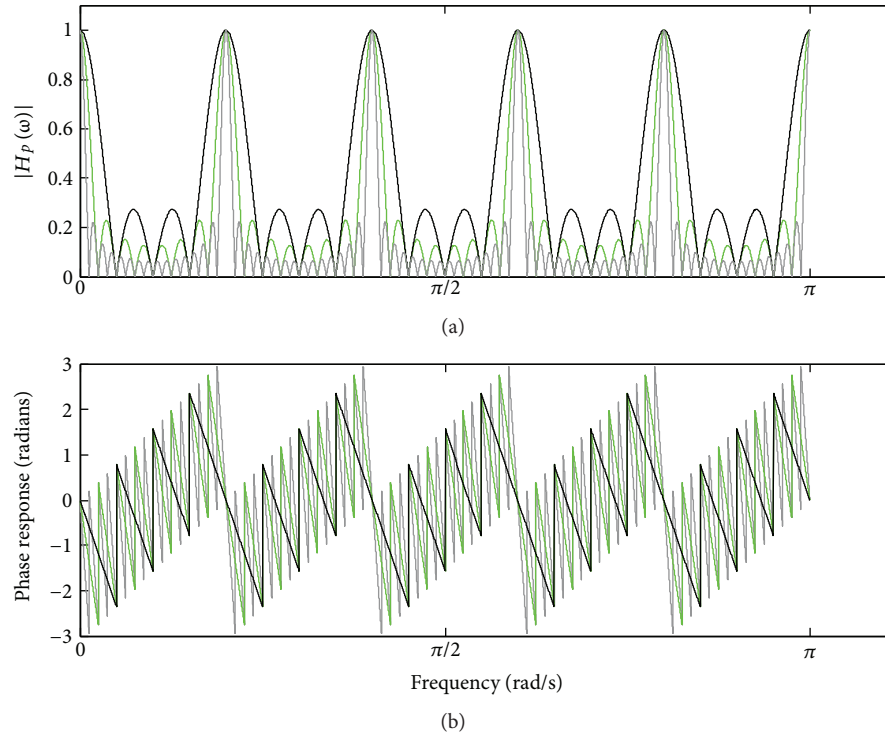


FIGURE 9: Frequency response of  $H_p(\omega)$  for  $M = 10$ , taking into account  $N = 4$  (dark trace),  $N = 8$  (green trace), and  $N = 16$  (gray trace): (a) magnitude response; (b) phase response.

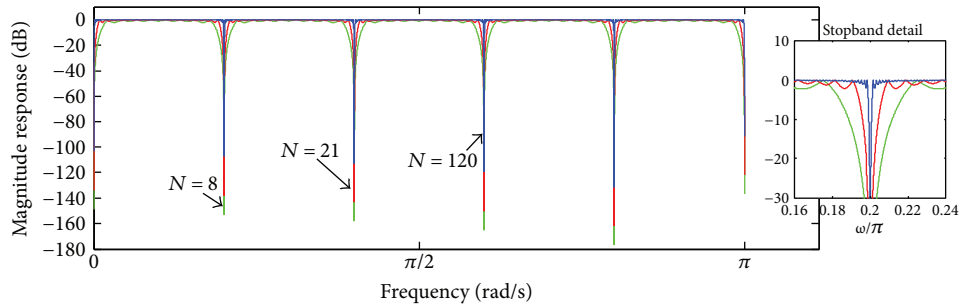


FIGURE 10: Magnitude response of  $H_{TDA}(\omega)$  ((8)) for  $M = 10$  and some values of  $N$ .

4500 Hz (for  $L = 20$ ). Therefore, (21) can produce a notch filter with a large range of values for the stopband bandwidth around  $-3$  dB.

#### 4. Further Comparative Analyses and Discussion

Figure 15 shows the frequency response of (3), for some values of  $r$  and  $M = 10$ .

It can be noticed that as the value of  $r$  increases towards 1, the gain of the filter approximates to unity and becomes more uniform along the different pass-bands, as well as the phase response approaches to a zero-phase distortion. On the extreme scenario of  $r \rightarrow 1$ , the filter becomes an all-pass band filter. On the other extreme, when  $r = 0$ , (3) equals (2) [6].

As indicated in Figures 6 and 10, by increasing the parameters  $J$  ((15)) and  $N$  ((8)), the gain in the filter pass-bands provided, respectively, by  $H_C$  and  $H_{TDA}$  increases and attains unity (0 dB). Simultaneously, a reduction of attenuation in the stopbands is also observed. Nevertheless, rather than the response of  $H_{MOD}$  shown in Figure 15, there is no effect on the phase response corresponding to  $H_C$  and  $H_{TDA}$ , which remains zero radians for any values of frequency. On the other hand,  $H_{TDA}$  ((8)) cannot be applied in a cascade implementation because of the ripple that occurs below and around 0 dB in the pass-bands (see stopband detail in Figure 10), which can compromise the gain uniformity along the pass-bands. As  $H_C$  shows no ripple along the pass-bands and no phase distortion, these characteristics allow the application of  $H_C$  in a cascade implementation ((15)) to improve the attenuation in the

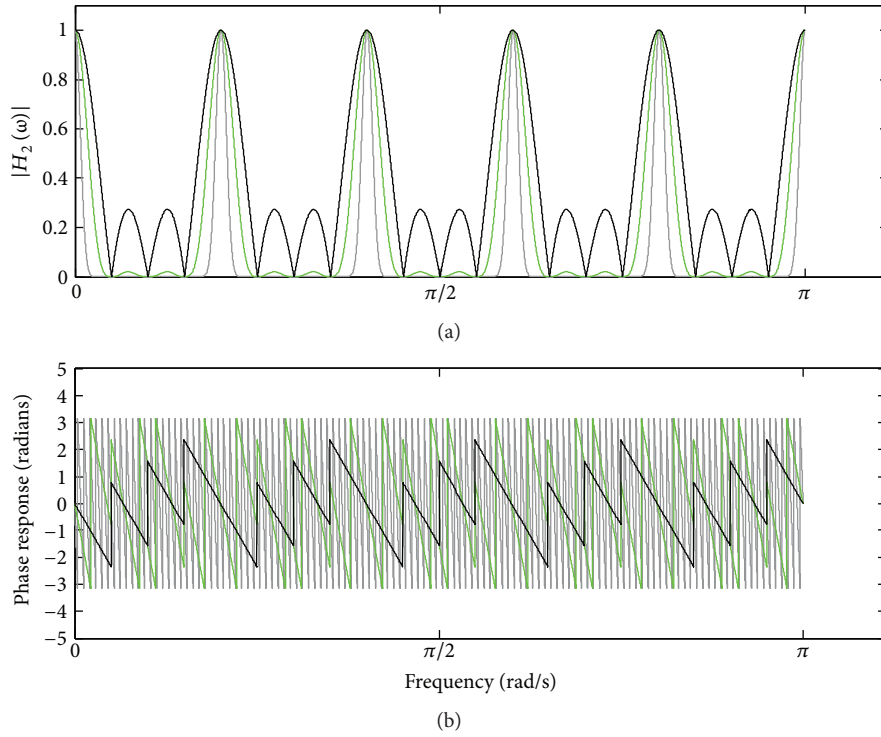


FIGURE 11: Frequency response of (17), taking into account  $M = 10$  and  $N = 4$ , for  $J = 1$  (dark trace),  $J = 3$  (green trace), and  $J = 8$  (gray trace): (a) magnitude response; (b) phase response.

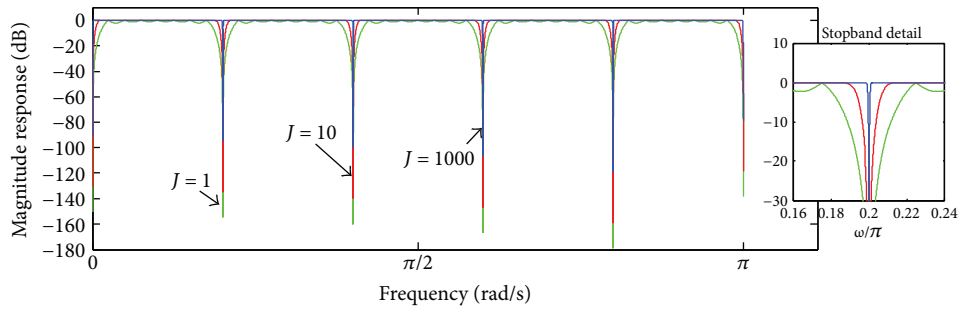


FIGURE 12: Magnitude response of  $H_{RTDA}(\omega)$  ((18), taking into account  $M = 10$  and  $N = 8$  and some values of  $J$ .

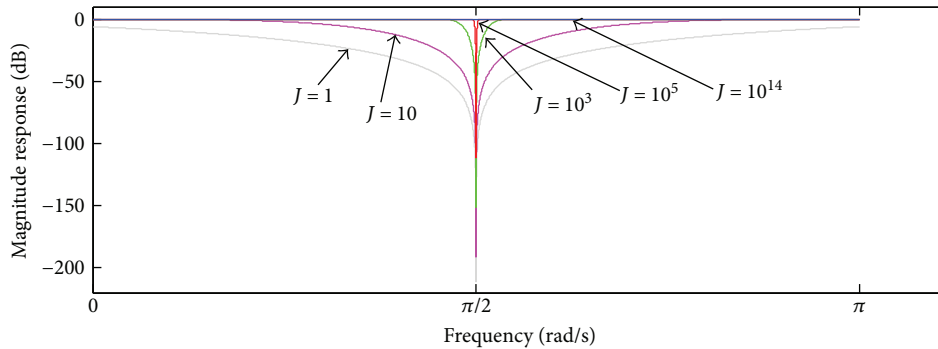


FIGURE 13: Magnitude response of  $H_{NTC}(\omega)$  ((20), taking into account some values of  $J$  and cutoff frequency at  $\omega_0 = \pi/2$ .

stopbands.  $H_{MOD}$ , in turn, cannot be applied within a cascade implementation without causing some distortion in the signal phase alike.

Figures 9–12 reveal that the iterative application of time-domain averaging, according to (18), represents an alternative to using higher values of  $N$ , since it permits to obtain

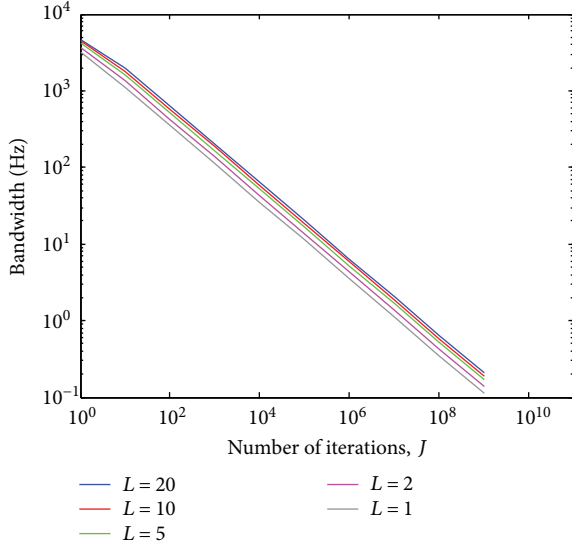


FIGURE 14: Bandwidth of the notch filter stopband around  $-3$  dB ((21), taking into account  $M = 2$  and some values of  $J$  and  $L$ .  $f_s = 5$  kHz.

narrower comb filter stopbands as well as phase distortion approximately zero along the filter pass-bands. Thus, in addition to enhancing the comb filter selectivity, time-domain averaging applied with a  $J$  number of iterations enables to use a smaller number of averaging periods. In Figure 16, we illustrate the variation of the number of averaging epochs according to the number of iterations, which was calculated by taking into consideration a certain bandwidth (18.01 Hz) in the stopbands around  $-3$  dB and  $M = 20$ .

For instance, by using  $J = 1$  and  $N = 21$  averaging epochs, it was possible to produce the same bandwidth in the stopbands around  $-3$  dB by setting  $N = 3$  and  $J = 71.77$  in (18). Therefore, when  $J \neq 1$  in (18), the attenuation of the noise component is carried out by a factor higher than  $\sqrt{N}$  [8].

Figure 17 shows the difference amongst  $H_{\text{MOD}}$ ,  $H_{\text{TDA}}$ ,  $H_C$ , and  $H_L$  regarding the bandwidth in the stopbands around  $-3$  dB.

The analysis depicted in this figure has taken into account  $M = 20$ . In case of  $H_{\text{MOD}}$ , above around  $r = 0.95$ , the bandwidth around  $-3$  dB is equal for all stopbands. In turn, for  $H_{\text{TDA}}$  (and  $H_{\text{RTDA}}$ ), such a bandwidth is approximately similar for all stopbands, irrespective of the value of  $N$  (and  $J$ ). On the other hand, for  $H_C$ , the width of the stopbands around  $-3$  dB depends on the frequency of the stopband as well as the value of  $J$ . The attenuation in the stopbands (as well as the gain in the pass-bands) may lie below  $-3$  dB for smaller values of  $J$  (see Figure 6). As the gain in the pass-bands approximates to 0 dB when  $J$  increases, the bandwidth of the stopbands around  $-3$  dB becomes narrower. However, it is not the same for all stopbands, but it enlarges according to the fundamental frequency ( $f_d$ ) of the stopband (Figure 17(c)). Such a difference is even higher for smaller values of  $J$ . Therefore, as shown in Figure 17(c), the higher the fundamental frequency of the stopband, the broader is its respective bandwidth. This characteristic has been

demonstrated to be useful for obtaining a more effective attenuation in the frequency bins associated with the harmonic gradient artefact spectral lines, with similar preservation of the EEG signal than that provided by the AAS method which is based upon time-domain averaging [20]. Thereby, broadening of the gradient artefact spectral lines provoked by micromovements of the subject head with the fMRI scanner, which are mostly observed in higher frequencies, can be more effectively accounted for by  $H_C$  because of the increasing stopband bandwidths around  $-3$  dB according to  $f_d$ .

In Figure 18, an exemplary setting of parameters  $r$ ,  $N$ ,  $J$ , and  $L$  are used to illustrate the bandwidth of the stopbands according to the fundamental frequency ( $f_d$ ). As predicted by (16), the stopband bandwidth is further enlarged when  $H_C$  is applied within the cascade implementation ( $H_L$ ), especially in stopbands with higher fundamental frequency (Figures 17(d) and 18). As can also be observed in Figure 18,  $H_C$ ,  $H_L$ , and  $H_{\text{MOD}}$  do not provide a stopband around 0 Hz, whereas it is produced by  $H_{\text{TDA}}$  and  $H_{\text{RTDA}}$ .

Figure 19 depicts the impulse response associated with  $H_{\text{MOD}}$ ,  $H_{\text{TDA}}$ ,  $H_C$ , and  $H_L$ , for some values of the parameters  $r$ ,  $N$ ,  $J$ , and  $L$ . After the impulse is applied, an overshoot occurs in each of these responses, followed by decaying peaks spaced at the window length  $M$ . The peak overshoot as well as the duration of the decaying peaks depend on the value of the parameter: smaller  $r$ ,  $N$ , and  $J$  produce an increase in the overshoot and decreased settling time. Rather, a higher value of  $L$  provides an increase in the overshoot and increased settling time.

Regarding the computational effort, we verified that  $H_C$  and  $H_L$  are less computationally demanding than  $H_{\text{MOD}}$ ,  $H_{\text{TDA}}$ , and  $H_{\text{RTDA}}$ . This can be ascribed to the computational efficiency of (11), which precisely requires the double of the computations of (2), as indicated in Figures 1 and 3. The worst case of computational effort was for  $H_{\text{MOD}}$ , whose application was seriously compromised because of expensive computational memory demand by higher values of  $M$  [6, 7].

Since a comb filter can be also implemented as a combination of notch filters, the selectivity provided by (21) could be used to design a highly selective comb filtering approach with a variable bandwidth for the different filter stopbands. Regarding the use of values of  $M > 2$  in (20), we observed that some ripple around and below 0 dB may appear in the frequency response of  $H_{\text{NTC}}$  for smaller values of  $J$ , which can cause nonuniform gain along the pass-bands within the cascade implementation indicated in (21). Case higher values of  $J$  are used in this scenario, the filter gain becomes uniform, but the notch filter stopband would have narrower bandwidth than  $M = 2$  in (21).

In future work, (20) should have its performance compared with other notch filter approaches [21], as well as (21) should be used and evaluated in applications where notch or comb filtering is required, such as power line rejection in biomedical signals [1]. Additionally, other filters  $L_1$  in (9) should be investigated and evaluated for the iterative comb filtering implementation proposed here. Equations (15) and (16) should also be used and have their performance

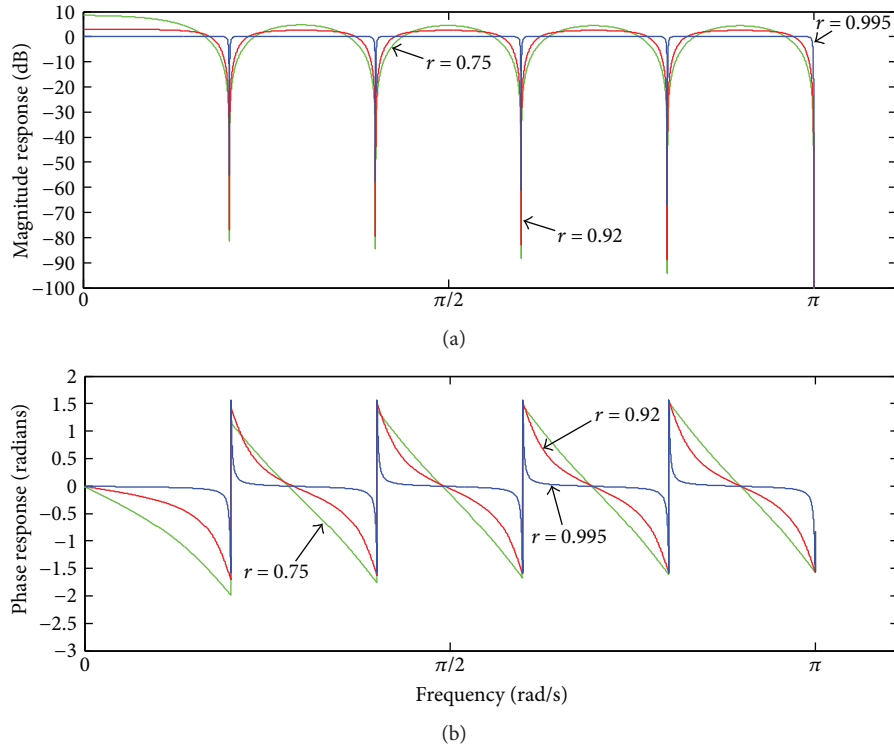


FIGURE 15: Frequency response of  $H_{MOD}(\omega)$  for some values of  $r$ : (a) magnitude response; (b) phase response.

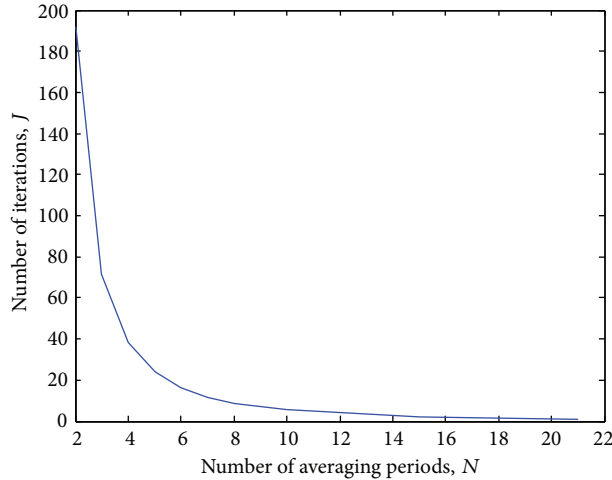


FIGURE 16: Variation of the number of averaging epochs ( $N$ ) according to the number of iterations ( $J$ ) in (18), taking into account a certain bandwidth (18.01 Hz) in the pass-bands around  $-3$  dB.  $f_s = 5$  kHz.

evaluated in signal processing applications other than the suppression of the gradient artefact from the EEG recordings [19, 20], where broadening of harmonic spectral lines is observed. As a further suggestion for future work, the iterative application of time-domain averaging should be assessed by using other kinds of moving-averaging filters, such as the exponential averaging and running averaging [2]. Last, the novel comb and notch filtering implementation described in this work shall be used and evaluated in other biomedical signal processing applications, such as speech

signal processing and during estimation of evoked potentials (EPs) and event-related potential (ERPs) responses [1, 22].

## 5. Conclusions

A number of biomedical and other signal processing applications require the use of comb filtering approaches that perform elimination or extraction of periodic waveforms with a high degree of selectivity. As regards the elimination of periodic waveforms, the comb filter should be able

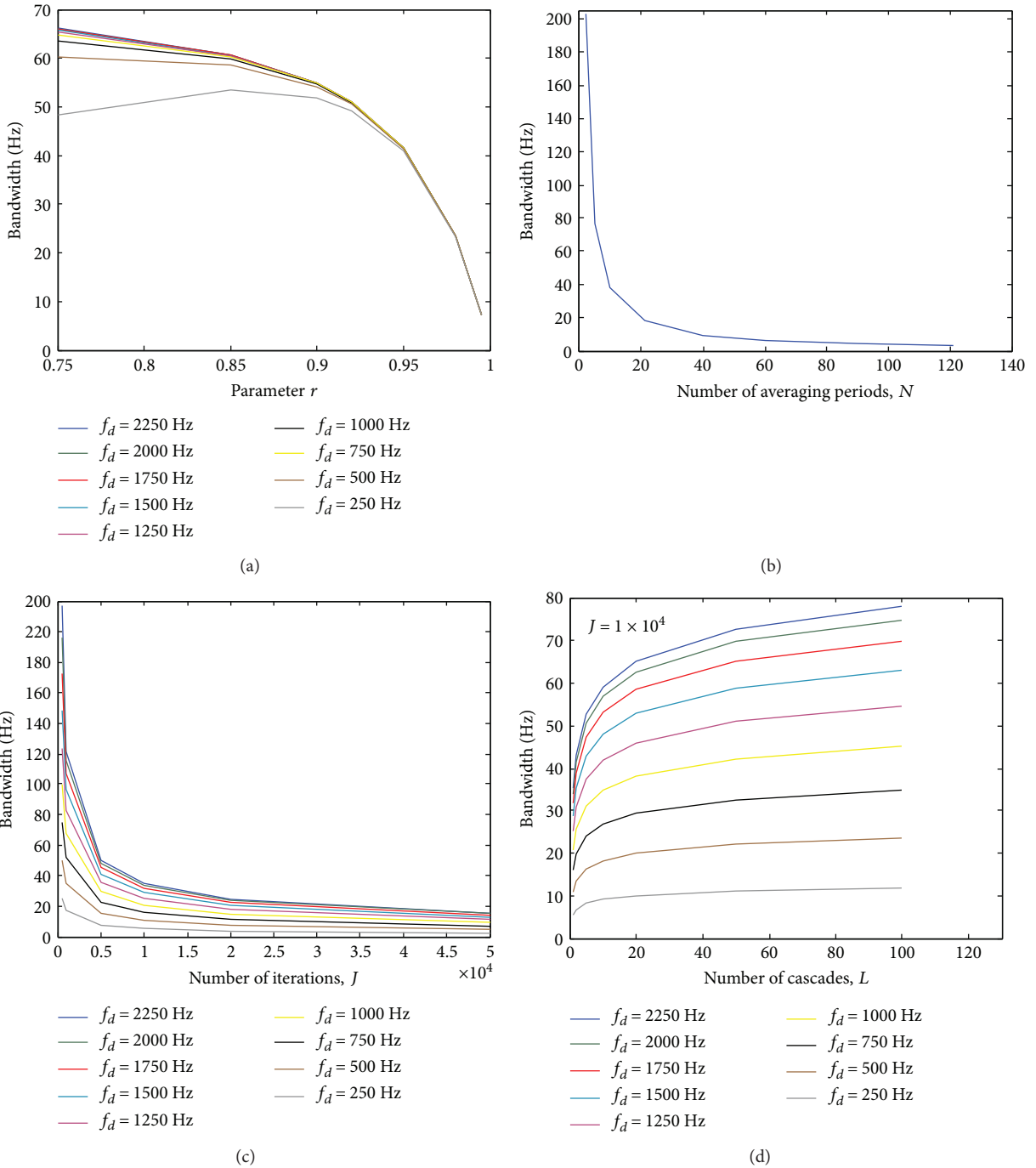


FIGURE 17: Bandwidth of the stopbands around  $-3$  dB ( $M = 20$ ), for (a)  $H_{MOD}$ , (b)  $H_{TDA}$ , (c)  $H_C$ , and (d)  $H_L$  ( $J = 1 \times 10^4$ ).  $f_s = 5$  kHz.

to suppress the harmonics associated with the periodic signal and, simultaneously, to preserve the stochastic component or noisy signal according to the level of quality required by the application. Thus, it is important to make sure that the performance of the comb filtering approach meets the selectivity requirements of the application. Since such requirements are not always met by the existing methods, investigation and proposal of novel approaches to improve the comb filtering selectivity have been often described in the literature.

In this work, we have demonstrated how iterative filtering can be used to improve the selectivity of comb filtering approaches as well as to design a novel notch filter, which are based on the conventional FIR moving average filter. The novel comb filtering approach implementation is revealed to provide unity gain in the pass-bands, no effects on the signal phase, and broadening of the stopband bandwidth around  $-3$  dB according to the fundamental frequency of the stopband. This characteristic has been proven to be useful within a scenario of broadening of spectral lines, such

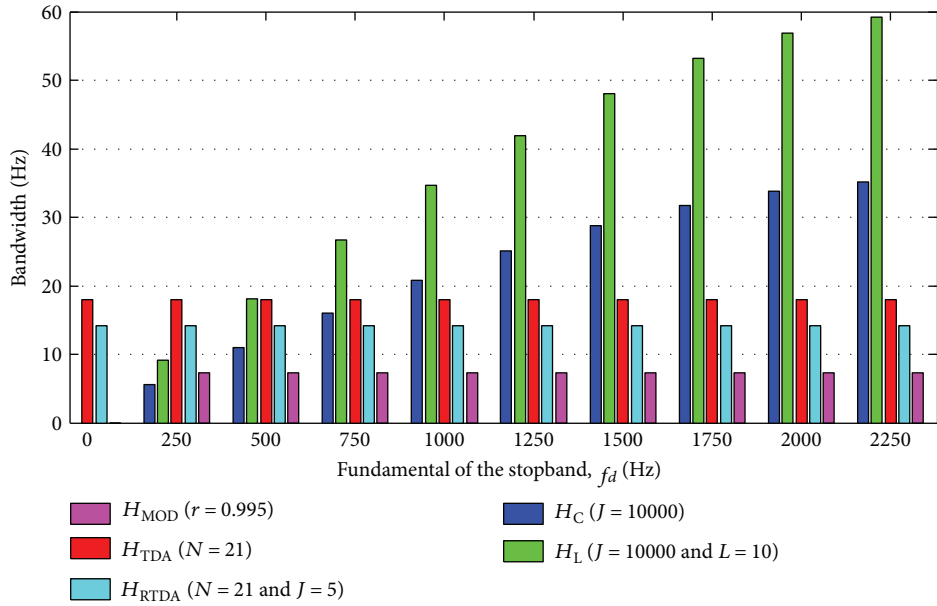


FIGURE 18: Bandwidth of the stopbands around  $-3$  dB ( $M = 20$ ) for an exemplary setting of parameters  $r$ ,  $N$ ,  $J$ , and  $L$ .  $f_s = 5$  kHz.

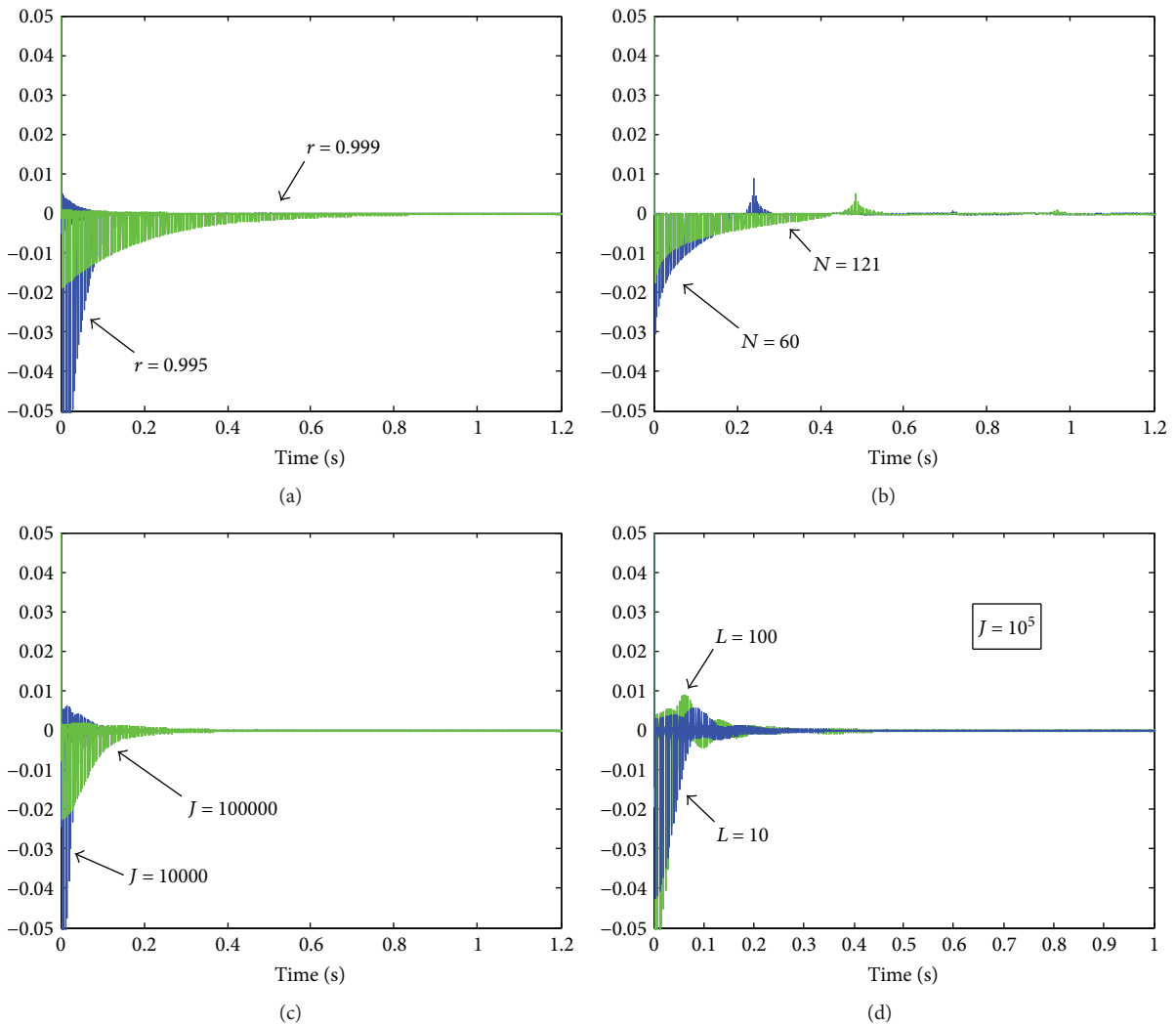


FIGURE 19: Impulse response ( $M = 20$ ), for (a)  $H_{MOD}$ , (b)  $H_{TDA}$ , (c)  $H_C$ , and (d)  $H_L$  ( $J = 10^5$ ).

as that observed during the occurrence of the gradient artefact in the EEG signal recorded simultaneously with fMRI data. Moreover, a cascade implementation of the proposed approach permits to further increase the attenuation provided in the stopbands. In parallel, the iterative application of time-domain averaging allows using a smaller number of averaging epochs in order to estimate the periodic signal component. Hence, when a number of iterations are taken into consideration, the noise component can be attenuated with a factor higher than the square roots of the number of averaging epochs. Last, the novel notch filter implementation by iterative decomposition shows to provide a selective filtering with a large range of values for the stopband bandwidth around  $-3$  dB.

### Conflicts of Interest

The authors declare that there is no conflict of interest regarding the publication of this article and regarding the funding that they have received.

### Acknowledgments

The authors are grateful to René M. H. Besseling for kindly providing review support. This work has been made possible by a grant from the European Union and Erasmus Mundus – EBW II Project and by a grant from CNPq – Science without Borders Program.

### References

- [1] R. M. Rangayyan, *Biomedical Signal Analysis: A Case-Study Approach*, Wiley, New York, 2002.
- [2] S. Braun, “The synchronous (time domain) average revisited,” *Mechanical Systems and Signal Processing*, vol. 25, no. 4, pp. 1087–1102, 2011.
- [3] J. Meher, P. Meher, and G. Dash, “Improved comb filter based approach for effective prediction of protein coding regions in DNA sequences,” *Journal of Signal and Information Processing*, vol. 2, no. 02, pp. 88–99, 2011.
- [4] J. G. Proakis and D. G. Manolakis, *Digital Signal Processing: Principles, Algorithms, and Applications*, Prentice-Hall, Upper Saddle River, 3rd edition, 1996.
- [5] Z. Zeng, Y. Xie, Y. Wang, Y. Guan, L. Li, and X. Zhang, “An improved harmonic current detection method based on parallel active power filter,” in *Proceedings of the 2nd Asia Conference on Power and Electrical Engineering, ACPEE 2017*, pp. 1–6, IOP Publishing, Shanghai, China, March 2017.
- [6] M. Tahir and S. K. Mazumder, “Improving dynamic response of active harmonic compensator using digital comb filter,” *IEEE Journal of Emerging and Selected Topics in Power Electronics*, vol. 2, no. 4, pp. 994–1002, 2014.
- [7] A. Prodić, J. Chen, D. Maksimović, and R. W. Erickson, “Self-tuning digitally controlled low-harmonic rectifier having fast dynamic response,” *IEEE Transactions on Power Electronics*, vol. 18, no. 1, pp. 420–428, 2003.
- [8] S. Braun, “The extraction of periodic waveforms by time domain averaging,” *Acustica*, vol. 32, no. 2, pp. 69–77, 1975.
- [9] P. D. McFadden, “A revised model for the extraction of periodic waveforms by time domain averaging,” *Mechanical Systems and Signal Processing*, vol. 1, no. 1, pp. 83–95, 1987.
- [10] P. J. Allen, O. Josephs, and R. Turner, “A method for removing imaging artifact from continuous EEG recorded during functional MRI,” *NeuroImage*, vol. 12, no. 2, pp. 230–239, 2000.
- [11] R. Becker, P. Ritter, M. Moosmann, and A. Villringer, “Visual evoked potentials recovered from fMRI scan periods,” *Human Brain Mapping*, vol. 26, no. 3, pp. 221–230, 2005.
- [12] K. Anami, T. Mori, F. Tanaka et al., “Stepping stone sampling for retrieving artifact-free electroencephalogram during functional magnetic resonance imaging,” *NeuroImage*, vol. 19, no. 2, pp. 281–295, 2003.
- [13] W. X. Yan, K. J. Mullinger, M. J. Brookes, and R. Bowtell, “Understanding gradient artefacts in simultaneous EEG/fMRI,” *NeuroImage*, vol. 46, no. 2, pp. 459–471, 2009.
- [14] H. Mandelkow, P. Halder, P. Boesiger, and D. Brandeis, “Synchronisation facilitates removal of MRI artefacts from concurrent EEG recordings and increases usable bandwidth,” *NeuroImage*, vol. 32, no. 3, pp. 1120–1126, 2006.
- [15] G. S. Spencer, *EEG-fMRI: Novel Methods for Gradient Artefact Correction [Ph.D. Thesis]*, University of Nottingham, Nottingham, UK, 2015.
- [16] L. Lin, Y. Wang, and H. Zhou, “Iterative filtering as an alternative algorithm for empirical mode decomposition,” *Advances in Adaptive Data Analysis*, vol. 1, no. 4, pp. 543–560, 2009.
- [17] Y. Wang, G.-W. Wei, and S. Yang, “Iterative filtering decomposition based on local spectral evolution kernel,” *Journal of Scientific Computing*, vol. 50, no. 3, pp. 629–664, 2012.
- [18] N. E. Huang, Z. Shen, S. R. Long et al., “The empirical mode decomposition and the Hilbert spectrum for nonlinear and non-stationary time series analysis,” *Proceedings of the Royal Society A: Mathematical, Physical and Engineering Sciences*, vol. 454, no. 1971, pp. 903–995, 1998.
- [19] J. L. Ferreira, R. M. Aarts, and P. J. M. Cluitmans, “Optimized moving-average filtering for gradient artefact correction during simultaneous EEG-fMRI,” in *Proceedings of the 5th ISSNIP-IEEE Biosignals and Biorobotics Conference (2014): Biosignals and Robotics for Better and Safer Living (BRC)*, pp. 1–6, IEEE, Salvador, Brazil, May 2014.
- [20] J. L. Ferreira, Y. Wu, R. M. H. Besseling, R. Lamerichs, and R. M. Aarts, “Gradient artefact correction and evaluation of the EEG recorded simultaneously with fMRI data using optimised moving-average,” *Journal of Medical Engineering*, vol. 2016, Article ID 9614323, 17 pages, 2016.
- [21] M. Vlček and P. Zahradník, “Fast analytical design algorithms for FIR notch filters,” *IEEE Transactions on Circuits and Systems I: Regular Papers*, vol. 51, no. 3, pp. 608–623, 2004.
- [22] S. Sanei and J. A. Chambers, *EEG Signal Processing*, Wiley, Hoboken, 2007.

## Research Article

# A Predictive Model to Classify Undifferentiated Fever Cases Based on Twenty-Four-Hour Continuous Tympanic Temperature Recording

Pradeepa H. Dakappa,<sup>1</sup> Keerthana Prasad,<sup>2</sup> Sathish B. Rao,<sup>1</sup> Ganaraja Bolumbu,<sup>3</sup>  
Gopalkrishna K. Bhat,<sup>4</sup> and Chakrapani Mahabala<sup>1</sup>

<sup>1</sup>Department of Internal Medicine, Kasturba Medical College, Manipal University, Mangaluru, Karnataka, India

<sup>2</sup>School of Information Sciences, Manipal Institute of Technology, Manipal University, Manipal, Karnataka, India

<sup>3</sup>Department of Physiology, Kasturba Medical College, Manipal University, Mangaluru, Karnataka, India

<sup>4</sup>Department of Microbiology, Kasturba Medical College, Manipal University, Mangaluru, Karnataka, India

Correspondence should be addressed to Chakrapani Mahabala; [chakrapani.m@manipal.edu](mailto:chakrapani.m@manipal.edu)

Received 15 May 2017; Accepted 31 October 2017; Published 22 November 2017

Academic Editor: Saugat Bhattacharyya

Copyright © 2017 Pradeepa H. Dakappa et al. This is an open access article distributed under the Creative Commons Attribution License, which permits unrestricted use, distribution, and reproduction in any medium, provided the original work is properly cited.

Diagnosis of undifferentiated fever is a major challenging task to the physician which often remains undiagnosed and delays the treatment. The aim of the study was to record and analyze a 24-hour continuous tympanic temperature and evaluate its utility in the diagnosis of undifferentiated fevers. This was an observational study conducted in the Kasturba Medical College and Hospitals, Mangaluru, India. A total of ninety-six ( $n = 96$ ) patients were presented with undifferentiated fever. Their tympanic temperature was recorded continuously for 24 hours. Temperature data were preprocessed and various signal characteristic features were extracted and trained in classification machine learning algorithms using MATLAB software. The quadratic support vector machine algorithm yielded an overall accuracy of 71.9% in differentiating the fevers into four major categories, namely, tuberculosis, intracellular bacterial infections, dengue fever, and noninfectious diseases. The area under ROC curve for tuberculosis, intracellular bacterial infections, dengue fever, and noninfectious diseases was found to be 0.961, 0.801, 0.815, and 0.818, respectively. Good agreement was observed [ $\kappa = 0.618$  ( $p < 0.001$ , 95% CI (0.498–0.737))] between the actual diagnosis of cases and the quadratic support vector machine learning algorithm. The 24-hour continuous tympanic temperature recording with supervised machine learning algorithm appears to be a promising noninvasive and reliable diagnostic tool.

## 1. Introduction

Undifferentiated fever is a commonly encountered febrile illness without any localized signs or symptoms [1]. According to a systematic review, the percentage of undiagnosed cases of undifferentiated fever in Asia is about 8% to 80% [2]. In resource-limited countries, the decision regarding clinical investigations at an early stage is a challenging task for the physicians [3]. The nonspecificity of symptoms and lack of availability of accurate diagnosis not only has a significant impact on clinical decision-making but often leads to the irrational use of antibiotics [3, 4]. In most of the undifferentiated fever cases, empirical treatment either does not work

or may be harmful and might delay hospitalization of the patient, with subsequent increase in medical expenses.

Monitoring of the fever can provide valuable information for diagnosis and prognosis of the disease. Many scientific studies reported on the utility of temperature monitoring as a predictive tool for certain clinical diseases [5–15]. One century earlier, Woodhead et al. studied the 24–48 hours of quasicontinuous temperature recordings in patients for the diagnosis and prognosis of tuberculosis. In cases of tuberculosis, they observed a few characteristic features of temperature curve like sudden rise of afternoon and evening temperature, rapid fall, continuous high temperature above 99°C for 8 to 9 hours, and mountain peaks on plateau

phase [11]. However, not enough studies were done to explore the utility of temperature, probably because of limited hardware capabilities, with cumbersome recording methods and software issues, which were not well developed at that time. Two decades earlier, interest in 24-hour temperature recording system re-emerged after Varela et al. showed continuous recording of body temperature using tympanic and axillary probes and analysis of temperature data [4, 12]. The quantitative measurement of body temperature has shown promising results in the management of hypovolemia, mortality in critically ill patients, diagnosis of lactic acidosis, the prognosis of organ hypoperfusion and shock, besides acting as a marker of cardiovascular status, dyspnea, and tissue perfusion [5–10]. Another study reported that the abnormal body temperature could act as a predictor of the diagnosis of sepsis in febrile, critically ill patients [16]. However, these studies did not address the underlying issue of diagnostic utility of temperature recordings in undifferentiated fevers.

Body temperature is a physiological signal which has essential features and trends associated with it. However, some of this information like minute variations, trends, and patterns in time series domain may not be apparent with conventional methods and may require complex mathematical models for their analysis. Unlike other vital signals like ECG, EEG, and EMG, there are only a limited number of studies on the temperature signal for predicting certain diseases by using mathematical models [12, 13, 15]. Researchers observed the body temperature variations in patients either visually or by using specific mathematical models. Papaioannou et al. studied the temperature patterns using linear discriminant analysis and cluster analysis by extracting wavelet features for the differentiation of patients with systemic inflammatory response syndrome, sepsis, and septic shock. Researchers extracted different wavelet features from the temperature pattern among the three groups (systemic inflammatory response syndrome, sepsis, and septic shock) and found statistically significant outcome [15]. Varela et al. applied approximate entropy and detrended fluctuation analysis (DFA) methods for determining the loss of complexity of the temperature curve associated with the diseased state. They compared results with conventional Sequential Organ Failure Assessment (SOFA) score and found that the temperature curve complexity is inversely related to the severity of patient's status. The approximate values were significantly low in nonsurvivors than in survival patients [13, 17]. In another study, Varela et al. used approximate entropy as a feature and found 72% accuracy in classifying two groups: death and survival patients with multiple organ failure [18]. Two more scientific studies reported the predictive model for differentiating dengue fever cases with other febrile illness, early phase of illness using multivariate logistic regression model and decision tree algorithm [19, 20]. Although these studies were done either in critical care settings for prognostication or for studying the extent of complications, they have not been studied in formal settings of diagnostic utility in undifferentiated tropical fevers.

Machine learning provides techniques, tools, and models that can aid in solving diagnostic and prognostic problems in

a variety of clinical conditions. Machine learning algorithms are widely applied in classification of diseases based on ECG, EEG, and EMG signals [21]. Automated detection and classification of fever patterns using machine learning techniques with the specific algorithm-based classifier for specific diseases might have potential benefits such as increasing efficiency, reproducibility, and cost-effectiveness by providing early diagnosis of the disease and treatment, especially in undifferentiated fever cases.

It is through this study that we intend to record, analyze, and classify the tympanic temperature recordings of patients presenting with undifferentiated fever and using body temperature as a predictive variable for differentiating undifferentiated fevers.

## 2. Materials and Methods

*2.1. Data Collection.* This was an observational study conducted in a tertiary care hospital. A total of ninety-six ( $n = 96$ ) patients presenting with prolonged fever symptom were recruited in the study. Patients who were on antipyretics, steroids, and with a history of hyperthermia and central nervous system disorder were excluded from the study. Malaria-infected fever patients were excluded in this study, because it is evident that malarial fever cycle occurs at every 48 hours [22] and we recorded the temperatures only for 24 hours. The patients were informed not to take a bath during temperature monitoring. Complete procedure of the study was explained to subjects before taking the informed consent and conducting the study. The study was approved by the institutional ethics committee. Anthropometric parameters like age, blood pressure, pulse rate, and BMI of each subject were noted. The continuous 24-hour tympanic temperature was recorded by using TherCom® temperature monitoring device [23, 24]. The final diagnosis of each patient was noted.

*2.2. Preprocessing of Data.* The temperature recordings were plotted and visually inspected for any missing data and filtered by using the Savitzky–Golay filter for smoothing the tracings without greatly distorting the signal. Each temperature recordings have 1440 data points, which were plotted at 9:00 AM to 9:00 AM timeframe.

*2.3. Feature Extraction.* Characteristic features of signal such as fast Fourier transform, entropy, energy, power, principal component analysis coefficients, autoregressive coefficients, wavelet transform coefficients, mean, and variance were extracted using MATLAB software (version R2013b), and visual observations of each temperature recordings such as presence of late night rise and presence of more than or equal to three peaks features were extracted. Extracted features were standardized using the normalization method. Further, 90% of extracted features were used for training and 10% for the test, using the classical 5-fold cross-validation setup.

To identify the accuracy of classification of the disease type, the four target diseases (tuberculosis, intracellular bacterial infections, dengue fever, and noninfectious (inflammatory and neoplastic) diseases) were assigned as responses

TABLE 1: Demographic details of subjects.

| Sl number | Cases<br>( <i>N</i> = 96)                                 | Age, mean (SD),<br>years | BMI, mean (SD),<br>kg/M <sup>2</sup> | Blood pressure          |                         | Pulse rate, mean (SD),<br>per min |
|-----------|---|--------------------------|--------------------------------------|-------------------------|-------------------------|-----------------------------------|
|           |   |                          |                                      | SBP, mean (SD),<br>mmHg | DBP, mean (SD),<br>mmHg |                                   |
| 1         | Tuberculosis ( <i>N</i> = 28)                             | 44.14 (14.39)            | 20.07 (3.61)                         | 121.07 (11.0)           | 79.71 (7.45)            | 83.25 (10.24)                     |
| 2         | Intracellular<br>bacterial infections<br>( <i>N</i> = 27) | 32.18 (13.77)            | 23.10 (3.53)                         | 124.11 (9.33)           | 80.0 (3.92)             | 82.51 (5.36)                      |
| 3         | Dengue fever ( <i>N</i> = 15)                             | 41.13 (12.50)            | 24.10 (5.52)                         | 122.00 (9.41)           | 78.93 (5.49)            | 81.33 (7.15)                      |
| 4         | Noninfectious diseases<br>( <i>N</i> = 26)                | 44.03 (15.05)            | 22.03 (3.46)                         | 123.00 (10.52)          | 78.65 (7.42)            | 83.38 (8.46)                      |

BMI: body mass index; SBP: systolic blood pressure; DBP: diastolic blood pressure.

TABLE 2: Confusion matrix of quadratic support vector machine algorithm of undifferentiated fever cases.

| Cases                              | Tuberculosis | Intracellular bacterial infections | Dengue fever | Noninfectious diseases |
|------------------------------------|--------------|------------------------------------|--------------|------------------------|
| Tuberculosis                       | 27           | 01                                 | 0            | 0                      |
| Intracellular bacterial infections | 06           | 15                                 | 01           | 05                     |
| Dengue fever                       | 0            | 01                                 | 08           | 06                     |
| Noninfectious diseases             | 0            | 03                                 | 04           | 19                     |

and extracted features were assigned as predictors. Responses were assigned based on the final clinical diagnosis of each case corresponding to temperature recordings.

**2.4. Evaluation of Algorithm.** Evaluation of classification algorithm was done by using classification application in MATLAB, which has a set of algorithms, where we can train extracted feature datasets. The algorithm which gives the highest accuracy was selected. In our study, we found the highest classification accuracy in quadratic support vector machine (SVM) algorithm.

**2.5. Statistical Analysis.** Data were expressed as mean  $\pm$  SD. Descriptive data analysis was done and an agreement between the classification of fever patterns by quadratic support vector machine learning algorithm and final diagnosis of the cases was performed by Kappa statistics by using Statistical Package for Social Sciences (SPSS) version 16, Chicago, IL. Feature extraction and area under receiver operating characteristic (ROC) curve of each categorized data were performed using the MATLAB software (version R2013b, the Mathworks, USA).

### 3. Results

A total of ninety-six ( $n = 96$ ) patients presenting with undifferentiated fever were recruited in the study. As per the physician's diagnosis and based on laboratory diagnostic tests, subjects were categorized into tuberculosis ( $n = 28$ ), intracellular bacterial infections ( $n = 27$ ), dengue fever ( $n = 15$ ), and noninfectious diseases ( $n = 26$ ). Table 1 summarizes the demographic details of each disease category. Demographic measures such as mean age, body mass index (BMI), blood pressure, and pulse rate did not differ between different disease groups.

We analyzed a quadratic support vector machine algorithm model for the differentiation of cases of the fever with 24-hour continuous tympanic temperature data and found an overall 71.9% accuracy in the algorithm. The algorithm performance for classifying the undifferentiated fever cases is summarized in Table 2. The overall area under ROC curve of each categorized data set is described in Table 3. The positive and negative predictive values and likelihood ratios of each categorized data set are described in Table 4. In summary, the quadratic support vector machine algorithm shows clinically significant accuracy in classifying assigned diseases.

We performed kappa agreement test between the classification of temperature patterns by quadratic support vector machine learning algorithm and with an actual diagnosis of cases.

We found a statistically significant good kappa agreement of 0.618 [ $p < 0.001$ , 95% CI (0.498–0.737)] between the quadratic support vector machine (SVM) learning algorithm and final diagnosis of cases.

### 4. Discussion

In this study, we found a very high yield in the quadratic support vector machine (SVM) learning algorithm in classifying undifferentiated fevers using data obtained from 24-hour continuous noninvasive temperature monitoring. We found that classification of undifferentiated fevers into four major categories is possible and is likely to optimize the evaluation of undifferentiated tropical fevers.

Undifferentiated tropical fevers are very perplexing issues for the internist or general physicians in resource-limited settings, because undirected investigations add to the cause and lead to inappropriate clinical decisions. The classification model confirmed the utility of body temperature signal as a primary variable for classifying the undifferentiated fevers.

TABLE 3: Area under ROC curve of quadratic support vector machine algorithm.

| Cases                              | AUROC <sup>#</sup> | False-positive rate | True-positive rate | Sensitivity (%)     | Specificity (%)     |
|------------------------------------|--------------------|---------------------|--------------------|---------------------|---------------------|
| Tuberculosis                       | 0.961              | 0.088               | 0.964              | 96.43 (81.65–99.91) | 91.18 (81.78–96.6)  |
| Intracellular bacterial infections | 0.801              | 0.072               | 0.555              | 55.56 (35.33–74.52) | 92.75 (83.89–97.61) |
| Dengue fever                       | 0.815              | 0.061               | 0.533              | 53.33 (26.59–78.73) | 93.83 (86.18–97.97) |
| Noninfectious diseases             | 0.818              | 0.157               | 0.730              | 73.08 (52.21–88.43) | 84.29 (73.62–91.89) |

<sup>#</sup>Area under ROC curve was automatically calculated and given by MATLAB software.

TABLE 4: Positive and negative predictive values of quadratic support vector machine algorithm.

| Cases                              | Positive predictive value (%) | Negative predictive value (%) | Positive likelihood ratio | Negative likelihood ratio |
|------------------------------------|-------------------------------|-------------------------------|---------------------------|---------------------------|
| Tuberculosis                       | 81.82 (67.63–90.65)           | 98.41 (90.03–99.77)           | 10.93 (5.07–23.54)        | 0.04 (0.01–0.27)          |
| Intracellular bacterial infections | 75.00 (54.72–88.16)           | 84.21 (77.68–89.10)           | 7.67 (3.09–19.03)         | 0.48 (0.31–0.73)          |
| Dengue fever                       | 61.54 (37.70–80.88)           | 91.57 (86.31–94.92)           | 8.64 (3.27–22.84)         | 0.50 (0.29–0.86)          |
| Noninfectious diseases             | 63.33 (48.90–75.72)           | 89.39 (81.61–94.12)           | 4.65 (2.58–8.39)          | 0.32 (0.17–0.61)          |

In particular, diagnostic yield for tuberculosis was extremely high and sensitivity and specificity of tuberculosis group were found to be 96.43% (81.65%–99.9%) and 91.18% (81.78%–96.6%), respectively (Table 3). This could help in limiting unnecessary investigations focusing on a group of diseases and will allow a targeted investigative approach in undifferentiated fevers.

We found that the SVM learning algorithm showed higher sensitivity of 96.43% (95%CI, 81.65–99.91) and specificity of 91.18% (81.78–96.6) in detecting tuberculosis in comparison to acid-fast bacilli smear test with a sensitivity of 67.5% (95%CI, 60.6–73.9) and specificity of 97.5% (95%CI, 97.0–97.9) among 5336 samples reported by Mathew et al. [25]. The SVM learning algorithm showed low sensitivity [53.33% (95%CI, 26.59–78.73)] and specificity [93.83% (95%CI, 86.18–97.97)] in predicting the cases of dengue in comparison to the sensitivity [77.3% (95%CI, 69.8–83.6)] and specificity [100% (95%CI, 98.5)] of the NS1 Ag rapid strip test for the diagnosis of dengue fever in 154 patients [26]. In case of intracellular bacterial infections, SVM learning algorithm presented sensitivity [55.56% (95% CI, 35.33–74.52)] and specificity [92.75% (95%CI, 83.89–97.61)] in predicting the bacterial infections from undifferentiated fever cases using features of temperature tracings which were comparable with findings of procalcitonin as a biomarker for bacterial infection with 64.5% sensitivity and 84.0% specificity in differentiating the bacterial infections from febrile patients as reported by Qu et al. [27]. The advantage of SVM learning algorithm is that one test is sufficient to differentiate four major clinical conditions, whereas culture or serology tests are to be performed separately for each clinical condition and these tests are invasive and expensive.

The procedure is simple, noninvasive, inexpensive, and reliable. The algorithm can easily be exported to any conventional computational devices, thereby allowing this to be implemented as a point of care diagnostic test. In addition, the 24-hour continuous temperature recording also helps us

in identifying the undetected fever spikes in conventional monitoring method. Two scientific studies were reported on the significance of continuous temperature monitoring over conventional temperature monitoring method [4, 24]. Varela et al. studied in 62 patients presenting with fever and found that continuous temperature recording method detected mean of 0.7 (95% CI, 0.27–1.33) peaks of fever unnoticed by conventional care [4]. In our previous study, we found that intermittent nature of fever patterns was clearly detected by continuous recordings, whereas conventional method failed to capture 29.9% of intermittent nature of fever patterns. Hence, capturing complete variations of body temperature was an added benefit of 24-hour continuous temperature monitoring method.

In the previous study, some of the mathematical models were utilized for prediction and prognostication of certain clinical conditions. In two different studies, Varela et al. applied approximate entropy alone, and along with detrended fluctuation analysis (DFA) to measure the complexity of temperature curve in correlating with SOFA values for predicting survival in critically ill patients [17, 18]. Papaioannou et al. assessed the temperature complexity in a cohort of critically ill patients who developed sepsis and septic shock during their stay in ICU and found an early prediction of mortality in them by extracting Tsallis entropy (TsEn) and Shannon entropy (Sh) as features [28]. Varela et al. also tried the classification of diagnostic groups using complexity variable (approximate entropy) [4]. However, researchers did not yield fruitful results probably because of single or either of the two mathematical parameters such as approximate entropy and DFA, TsEn, and Shannon entropy were looked for in the signal, and the other features which we believe are important were not evaluated. Moreover, the previous studies addressed the complexity of temperature signal in critical care patients and not in formal settings. Wavelet analysis and multiscale entropy were used in one study by Papaioannou et al. [15]; however, in our study, we included wavelet coefficients as a feature of one-dimensional signal

and applied it in the machine learning processes. In addition to this, we observed some of the important features visually. We combined both visually important and other extracted features in the machine learning algorithm, which appears to yield a very high success rate in appropriate classification.

While the concept of continuous fever recording began way back a century ago, [11], somehow it was not taken forward because of hardware and software impediments. Now, there is a need to revisit this interesting concept with manifold better hardware and software technologies and their issues have been largely dealt with.

Limitation of the study includes relatively very small sample size, but case mixes were similar those in other reported study [29]. Some technical difficulties while monitoring temperature were mainly the falling off of the tympanic probe from the ear canal which interrupts the continuous recording. Secondly, the loose connection of probe to the data logger interrupted continuous data storage. This was also mentioned in a previously conducted study by Varela et al. [4]. We applied the Savitzky–Golay filter for noise reduction and smoothing of the temperature signal without distorting the signal. There are other filtering methods that can be applied to filter the data which may increase the yield in classification algorithm.

The interesting observations found in this small group of samples need to be studied in a bigger sample size. Once the large data sets are obtained, artificial neural network analysis may offer a higher yield. Extensive use of this promising algorithm may yield significant output with a larger dataset in the future, which will further allow us to apply artificial neuronal network at that point in time. We have done the analysis in undifferentiated fever settings, but it is very likely that it may also be useful in pyrexia of unknown origin settings. We have four classifying groups of samples, but with the expanding samples, further groups may be apparently evident and might improve the accuracy of the model. Another important possibility would be to record two or three days of temperature and to look for patterns and extract features in a bigger recording time frame.

## 5. Conclusion

Use of supervised automated classifying algorithm can provide a significant clue for the discrimination of undifferentiated fevers at an early stage. An accurate diagnostic test aids the process of quick decision-making by the physician, in addition to minimizing the cost of unnecessary diagnostic tests. As a noninvasive tool, temperature pattern classifier algorithm may become an essential, additional diagnostic tool which can be used as inpatient and outpatient clinical settings in the future for the evaluation of fever of various clinical conditions.

## Conflicts of Interest

The authors declare that they have no conflict of interest.

## Acknowledgments

This research was supported by the Kasturba Medical College and Hospitals, Manipal University, Mangaluru, Karnataka, India.

## References

- [1] R. Joshi, *The Epidemiologic Features of Acute Encephalitis Syndrome in Central India*, 2009, [http://digitalassets.lib.berkeley.edu/etd/ucb/text/Joshi\\_berkeley\\_0028E\\_10123.pdf](http://digitalassets.lib.berkeley.edu/etd/ucb/text/Joshi_berkeley_0028E_10123.pdf).
- [2] T. N. Susilawati and W. J. McBride, “Acute undifferentiated fever in Asia: a review of the literature,” *Southeast Asian Journal of Tropical Medicine and Public Health*, vol. 45, no. 3, pp. 719–726, 2014.
- [3] R. Joshi and S. P. Kalantri, “Acute undifferentiated fever: management algorithm,” in *Update on Tropical Fever*, pp. 1–14, Association of Physicians of India, Indian College of Physicians, New Delhi, 2015.
- [4] M. Varela, R. Ruiz-Esteban, A. Martinez-Nicolas, J. A. Cuervo-Arango, C. Barros, and E. G. Delgado, ““Catching the spike and tracking the flow”: Holter-temperature monitoring in patients admitted in a general internal medicine ward,” *International Journal of Clinical Practice*, vol. 65, no. 12, pp. 1283–1288, 2011.
- [5] J.-L. Vincent and M. H. Weil, “Fluid challenge revisited,” *Critical Care Medicine*, vol. 34, no. 5, pp. 1333–1337, 2006.
- [6] S. Clarke, R. Parris, and K. Reynard, “Core–peripheral temperature gradient as a diagnostic test in dyspnoea,” *Emergency Medicine Journal*, vol. 22, no. 9, pp. 633–635, 2005.
- [7] P. Kiekkas, D. Velissaris, M. Karanikolas et al., “Peak body temperature predicts mortality in critically ill patients without cerebral damage,” *Heart & Lung: The Journal of Acute and Critical Care*, vol. 39, no. 3, pp. 208–216, 2010.
- [8] L. J. Kaplan and S. Frangos, “Clinical review: acid–base abnormalities in the intensive care unit–part II,” *Critical Care*, vol. 9, no. 2, pp. 198–203, 2005.
- [9] V. Menon, J. N. Slater, H. D. White, L. A. Sleeper, T. Cocke, and J. S. Hochman, “Acute myocardial infarction complicated by systemic hypoperfusion without hypotension: report of the SHOCK trial registry,” *The American Journal of Medicine*, vol. 108, no. 5, pp. 374–380, 2000.
- [10] H. R. Joly and M. H. Weil, “Temperature of the great toe as an indication of the severity of shock,” *Circulation*, vol. 39, no. 1, pp. 131–138, 1969.
- [11] G. Woodhead and P. Varrier-Jones, “The value of the quasi-continuous temperature record in the early diagnosis and prognosis of tuberculosis,” *The Lancet*, vol. 197, no. 5090, pp. 573–582, 1921.
- [12] M. Varela, L. Jimenez, and R. Farina, “Complexity analysis of the temperature curve: new information from body temperature,” *European Journal of Applied Physiology*, vol. 89, no. 3, pp. 230–237, 2003.
- [13] M. Varela, J. Churrua, A. Gonzalez, A. Martin, J. Ode, and P. Galdos, “Temperature curve complexity predicts survival in critically ill patients,” *American Journal of Respiratory and Critical Care Medicine*, vol. 174, no. 3, pp. 290–298, 2006.
- [14] S. M. Pikkujamsa, T. H. Makikallio, L. B. Sourander et al., “Cardiac interbeat interval dynamics from childhood to senescence: comparison of conventional and new measures

- based on fractals and chaos theory,” *Circulation*, vol. 100, no. 4, pp. 393–399, 1999.
- [15] V. E. Papaioannou, I. G. Chouvarda, N. K. Maglaveras, and I. A. Pneumatikos, “Temperature variability analysis using wavelets and multiscale entropy in patients with systemic inflammatory response syndrome, sepsis, and septic shock,” *Critical Care*, vol. 16, no. 2, article R51, 2012.
- [16] A. M. Drewry, B. M. Fuller, T. C. Bailey, and R. S. Hotchkiss, “Body temperature patterns as a predictor of hospital-acquired sepsis in afebrile adult intensive care unit patients: a case-control study,” *Critical Care*, vol. 17, no. 5, article R200, 2013.
- [17] M. Varela, M. Calvo, M. Chana, I. Gomez-Mestre, R. Asensio, and P. Galdos, “Clinical implications of temperature curve complexity in critically ill patients,” *Critical Care Medicine*, vol. 33, no. 12, pp. 2764–2771, 2005.
- [18] D. Cuesta, M. Varela, P. Miro et al., “Predicting survival in critical patients by use of body temperature regularity measurement based on approximate entropy,” *Medical & Biological Engineering & Computing*, vol. 45, no. 7, pp. 671–678, 2007.
- [19] E. Fernandez, M. Smieja, S. D. Walter, and M. Loeb, “A predictive model to differentiate dengue from other febrile illness,” *BMC Infectious Diseases*, vol. 16, no. 1, p. 694, 2016.
- [20] L. Tanner, M. Schreiber, J. G. Low et al., “Decision tree algorithms predict the diagnosis and outcome of dengue fever in the early phase of illness,” *PLoS Neglected Tropical Diseases*, vol. 2, no. 3, article e196, 2008.
- [21] A. H. Shoeb and J. V. Guttag, “Application of machine learning to epileptic seizure detection,” in *Proceedings of the 27th International Conference on Machine Learning (ICML-10)*, Haifa, Israel, 2010.
- [22] D. Ogoina, “Fever, fever patterns and diseases called “fever”—a review,” *Journal of Infection and Public Health*, vol. 4, no. 3, pp. 108–124, 2011.
- [23] D. Cuesta-Frau, M. Varela, M. Aboy, and P. Miro-Martinez, “Description of a portable wireless device for high-frequency body temperature acquisition and analysis,” *Sensors*, vol. 9, no. 10, pp. 7648–7663, 2009.
- [24] P. H. Dakappa, G. K. Bhat, G. Bolumbu, S. B. Rao, S. Adappa, and C. Mahabala, “Comparison of conventional mercury thermometer and continuous TherCom® temperature recording in hospitalized patients,” *Journal of Clinical and Diagnostic Research*, vol. 10, no. 9, pp. OC43–OC46, 2016.
- [25] P. Mathew, Y. H. Kuo, B. Vazirani, R. H. Eng, and M. P. Weinstein, “Are three sputum acid-fast bacillus smears necessary for discontinuing tuberculosis isolation?,” *Journal of Clinical Microbiology*, vol. 40, no. 9, pp. 3416–3420, 2002.
- [26] S. Chaterji, J. C. Allen Jr., A. Chow, Y. S. Leo, and E. E. Ooi, “Evaluation of the NS1 rapid test and the WHO dengue classification schemes for use as bedside diagnosis of acute dengue fever in adults,” *The American Journal of Tropical Medicine and Hygiene*, vol. 84, no. 2, pp. 224–228, 2011.
- [27] J. Qu, X. Lü, Y. Liu, and X. Wang, “Evaluation of procalcitonin, C-reactive protein, interleukin-6 & serum amyloid A as diagnostic biomarkers of bacterial infection in febrile patients,” *Indian Journal of Medical Research*, vol. 141, no. 3, pp. 315–321, 2015.
- [28] V. E. Papaioannou, I. G. Chouvarda, N. K. Maglaveras, G. I. Baltopoulos, and I. A. Pneumatikos, “Temperature multiscale entropy analysis: a promising marker for early prediction of mortality in septic patients,” *Physiological Measurement*, vol. 34, no. 11, pp. 1449–1466, 2013.
- [29] S. K. Abrahamsen, C. N. Haugen, P. Rupali et al., “Fever in the tropics: aetiology and case-fatality—a prospective observational study in a tertiary care hospital in South India,” *BMC Infectious Diseases*, vol. 13, no. 1, p. 355, 2013.

## Research Article

# Combination of Deep Recurrent Neural Networks and Conditional Random Fields for Extracting Adverse Drug Reactions from User Reviews

Elena Tutubalina<sup>1</sup> and Sergey Nikolenko<sup>1,2</sup>

<sup>1</sup>Kazan (Volga Region) Federal University, Kazan, Russia

<sup>2</sup>Steklov Institute of Mathematics, St. Petersburg, Russia

Correspondence should be addressed to Elena Tutubalina; [tutubalinaev@gmail.com](mailto:tutubalinaev@gmail.com)

Received 14 April 2017; Accepted 27 July 2017; Published 5 September 2017

Academic Editor: Arindam Bit

Copyright © 2017 Elena Tutubalina and Sergey Nikolenko. This is an open access article distributed under the Creative Commons Attribution License, which permits unrestricted use, distribution, and reproduction in any medium, provided the original work is properly cited.

Adverse drug reactions (ADRs) are an essential part of the analysis of drug use, measuring drug use benefits, and making policy decisions. Traditional channels for identifying ADRs are reliable but very slow and only produce a small amount of data. Text reviews, either on specialized web sites or in general-purpose social networks, may lead to a data source of unprecedented size, but identifying ADRs in free-form text is a challenging natural language processing problem. In this work, we propose a novel model for this problem, uniting recurrent neural architectures and conditional random fields. We evaluate our model with a comprehensive experimental study, showing improvements over state-of-the-art methods of ADR extraction.

## 1. Introduction

Recent studies on text mining applications increasingly employ nonstandard sources of information to obtain new data related to health conditions, the efficiency of treatment, drug reactions, and interactions between different drugs. Users provide information about themselves through social media posts and free-text forum comments. This rich source of information has been successfully used, for instance, to monitor adverse drug reactions, making it possible to detect rare and underestimated reactions through the users complaining about their health [1].

In this work, we focus on the identification of adverse drug reactions (ADRs). ADRs are an essential part of drug postmarketing surveillance. Traditionally, reports about ADRs have been identified using (i) FDA's Adverse Event Reporting System (AERS) complaints from individual patients and their physicians and (ii) scientific literature and reports on clinical trials [2, 3]. Nowadays, drug reactions can be extracted from user reviews provided on the Web, and processing this information in an automated way represents a novel and exciting approach to personalized medicine and

wide-scale drug tests. Our goal is to extract phrases about ADRs in the context of a user's post. For example, a sentence "1st pill taken with food, a few hours after I experienced shortness of breath, a sense of depression, cramping, upset stomach" contains four ADRs, namely, *shortness of breath*, *depression*, *cramping*, and *upset stomach*. Formally, this challenging task is divided into the two subtasks: identification of ADRs and normalization of ADRs. In this paper, we focus on the first subtask.

Bidirectional recurrent neural networks (RNN) and conditional random fields (CRF) are considered to be among the most powerful models for sequence modeling [4–13], each one having its own advantages and disadvantages. In a direct RNN application, especially with LSTM or GRU cells, one can get a better model for long sequences of inputs, but the RNN output (a softmax layer) will classify every tag independently. CRF can solve this problem but is less expressive than RNN in modeling the sequence itself; therefore, it is natural to try to unite the two.

In this work, we apply a combination of RNN and CRF using the following strategy. We feed word-level representations into a bidirectional RNN to encode the context vectors

for each word. On top of this RNN, we use a sequential CRF to jointly decode the words' labels for the entire sentence. A similar strategy has been successfully proposed in the past for two sequence labeling tasks: part-of-speech (POS) tagging and named entity recognition (NER) [14–16]. We evaluate our model for ADR extraction on an annotated corpus CADEC. The CADEC corpus consists of 1250 medical forum posts taken from AskaPatient.com [17], where each post has been manually annotated with mentions of ADRs. Our results show that the joint model of RNN and CRF improves the performance of state-of-the-art CRF and RNN models trained separately. Hence, we can summarize the contributions of this work as follows: (i) we have introduced a joint model that combines CRF and RNN to model the sequence of labels for ADR extraction; (ii) we have conducted empirical evaluation of this model on benchmark datasets; and (iii) experimental results have shown that the proposed model improves over state-of-the-art performance.

The paper is organized as follows: in Section 2, we survey related work; Section 3 introduces the combined RNN + CRF model, and Section 4 considers in detail our experimental evaluation. We conclude in Section 5.

## 2. Related Work

Our work represents a new look at the recently popular studies on biomedical text mining and pharmacovigilance from social media.

**2.1. Biomedical Text Mining.** Recent studies in various fields of biomedical research have applied text mining, including such problems as named entity recognition [10, 11], relation extraction [18, 19], text classification [9, 20], hypothesis generation [21, 22], and the creation of knowledge sources and linguistic resources. A comprehensive review of important areas of biomedical text mining can be found in [23, 24]. Huang and Lu [23] reported a series of evaluations of natural language processing (NLP) systems for various biomedical tasks, including both knowledge-based methods and machine learning approaches to NLP.

In general, biomedical named entities include genes/proteins, chemicals, drugs, and diseases. As for relations, most research studies have focused on the entities' functions (e.g., gene functions), relational events, and interactions (e.g., drug-drug or protein-protein interactions). Many studies have employed simple classifiers to extract information from texts. For example, Ngo et al. [25] employed a classification method on a set of features based on distributed representations to predict drug-disease relations in cancer treatment. Rastegar-Mojarad et al. [26] used machine learning methods to identify disease names from user reviews for about top 180 most frequently searched medications on the *WebMD* forum. In order to identify candidates for drug repurposing, the authors removed indications of known drugs and did a manual review of the comments without using FDA reports. The main limitation of this work is the lack of an annotated corpus to evaluate the proposed system. Zhang et al. [20] proposed a weighted average ensemble of four classifiers, based respectively on a handmade lexicon,

*n*-grams, and word representation vectors (also called word embeddings). Avillach et al. [3] developed a method to find previously established relationships between drugs and adverse events using the MEDLINE corpus and medical subject headings and subheadings such as “chemically induced” and “adverse effects.” Well-recognized limitations of these resources include the need of volunteers to report events and lack of sufficiently large result sets to draw the statistical conclusion. These drawbacks have led to the rise of pharmacovigilance from social media.

**2.2. Pharmacovigilance from Social Media.** Social media has been increasingly used for medical and pharmacological research since the early 2010s; the term “pharmacovigilance” was coined for automated monitoring of social media for potentially adverse drug effects and interactions.

NLP techniques have been applied in five main domain of texts: (i) biomedical literature, clinical trial records, and electronic medical/health records (e.g., medical correspondence and letters) [3, 5, 10, 27–30]; (ii) short messages from Twitter [9, 31, 32]; (iii) user reviews from health-related and e-commerce websites [4, 26, 33, 34]; (iv) web search logs [22]; and (v) forum discussions and message boards about medications, health conditions, treatment modality, and so on [35–37]. Most of these works focused on creating linguistic methods based on keywords for extracting major adverse effects, classifiers to detect whether a text contains ADRs or is relevant to drug reactions, and sequence labeling algorithms to extract mentions of ADRs. A review of techniques applied to drug reaction detection has been given in [38, 39].

In opinion mining, one of the major tasks is the identification of opinion targets (also called aspects) or opinion expressions. This task has been studied by many researchers using frequency-based methods and unsupervised and supervised methods. In [40], authors described linguistic resources for event extraction: linguistics databases and vocabularies such as thesauri. Currently, most of the state-of-the-art methods are based on CRF with a set of hand-crafted features and bidirectional RNNs [7, 8, 10]. Irsoy and Cardie [7] applied deep RNNs to extract direct or expressive subjective expressions; in their experiments, 3-layer RNN outperformed CRF, semi-CRF, and 1-layer (i.e., shallow) RNN. Liu et al. [8] applied RNNs for aspect extraction from data sets about laptops and restaurants, and RNNs based on pretrained word embeddings outperformed feature-rich CRF-based models.

In recent years, there has been a growing interest in the area of detecting ADRs from social media. It started in 2010 with a pioneering study of Leaman et al. [41], who analyzed user posts regarding six drugs from the health-related social network *DailyStrength*. FDA alerts were used as a gold standard to evaluate discovered associations between drugs and ADRs. Yang et al. [42] conducted an experiment for ten drugs and five ADRs to examine associations between them on texts from online healthcare communities using association mining techniques. Rastegar-Mojarad et al. [26] developed a rule-based system to extract drug effects. Feldman et al. [37] identified ADRs on texts from health-related online forums. They employed dictionary-based drug

detection, and symptoms were extracted with a combination of dictionary-based and pattern-based methods. Pointwise mutual information (PMI) was computed to evaluate the likelihood of a drug-ADR relation. The authors analyzed several case studies of drugs to show that some ADRs were reported prior to the FDA communication. One limitation of this work is the amount of annotated data; the test set contained less than 500 samples. See [39] for a comprehensive review of ADR extraction from social media data with NLP-based approaches.

Supervised machine learning techniques have been successfully applied to detect ADRs. Bian et al. [31] utilized an SVM classifier to identify tweets describing ADRs. Yom-Tov and Gabrilovich [22] analyzed web search query logs to extract information related to drugs and adverse reactions. ADR extraction has been regarded in many studies as a sequence labeling problem using conditional random fields (CRF). CRFs with a rich set of contextual, lexicon-based, grammatical, and semantic features were used in [6, 9, 33]. In [6], the semantic features were based on word clusters using  $k$ -means clustering on pretrained word embeddings. A set of experiments showed that contextual and semantic features are the most effective to classify ADRs in tweets. We also note a Social Media Mining Shared Task Workshop (organized as part of the Pacific Symposium on Biocomputing 2016) devoted to mining pharmacological and medical information from Twitter, with a competition based on a published dataset [32].

Supervised models tend to work well when trained on fully labeled data. Although there is a large amount of unlabeled data from social media, labeled data are time-consuming to obtain. Gupta et al. [35, 43] used semisupervised learning of patterns to identify drugs, symptoms, and conditions. Lexico-syntactic patterns have been learned with a seed dictionary of terms, and a bootstrapped rule-based method extracted specific entities that were missing from the seed dictionaries. One limitation of this approach is that it does not identify long descriptive phrases. Stanovsky et al. [44] employed an active learning technique to create a bootstrap lexicon of ADRs. The main advantage of this approach is that it can identify entities with a small number of hand-written rules or hand-labeled examples. We mark these works as possibilities for future improvements of this area.

The most relevant studies to the present paper are the works by Metke-Jimenez and Karimi [33], Miftahutdinov et al. [4], and Stanovsky et al. [44]; all of them used the CADEC corpus for training and testing. Metke-Jimenez and Karimi [33] applied dictionary-based methods and CRFs to identify ADRs from the CADEC corpus. They used baseline features, including a bag of words, letter  $n$ -grams, and word shapes (e.g., if the token composed of uppercase letters). For evaluation, they applied strict and relaxed versions of the evaluation for each matching span. The authors divided the corpus into training and testing sets, using a 70/30 split. CRF outperformed knowledge-based methods on the sentence level and achieved strict and relaxed  $F_1$ -measures of 60.2% and 84.9%, respectively. Miftahutdinov et al. [4] applied CRF with a rich set of features to extract

all disease-related entities including drug indications, ADRs, and patient history. For CRF features, they used hand-crafted features including contextual features, dictionaries, and cluster-based and distributed word representations. CRF outperformed bidirectional 2-layer and 3-layer RNNs on review level based on 5-fold cross evaluation and achieved  $F_1$ -measures of 69.1% and 79.4% on recognition of disease-related expressions in the exact and partial matching exercises, respectively. They used word embeddings trained on social media and on scientific literature separately. Stanovsky et al. [44] employed RNN and word embeddings trained on a Blekko medical corpus in conjunction with embeddings trained on DBpedia. If a word was a lexical match with one of the DBpedia entities, then the DBpedia embedding was used as the input of RNN. Otherwise, Blekko embedding was used. The authors used a 75/25 split and computed evaluation metrics for every word in a sentence instead of extracted spans of ADRs. The knowledge-infused RNN achieved  $F_1$ -measures of 93% in the evaluation of each word. The authors did not evaluate RNN in comparison with CRF and LSTM in comparison with GRU. We also note that those papers did not analyze the number of epochs for training RNNs and did not apply the joint model of RNN and CRF.

Our work differs from the mentioned works in several important aspects.

- (1) We experiment with a joint model of CRF and RNN as well as both models separately.
- (2) In addition, we employ CNN to extract character-level features instead of engineering of hand-crafted features.
- (3) We use word embeddings trained on social media and on scientific literature.
- (4) We present quantitative analysis as well as qualitative analysis of extracted ADRs to demonstrate variation in ADRs across different patient groups.

### 3. Model

This section illustrates our supervised model combining recurrent neural network (RNN) and conditional random fields (CRF) to the extraction of ADRs. We formulate the disease-related entity extraction as a sequence labeling problem. In the following subsections, we describe the architecture of the model.

**3.1. Recurrent Neural Networks.** RNNs are naturally used for sequence learning, where both input and output are word and label sequences. RNN has recurrent hidden states, which aim to simulate memory, that is, the activation of a hidden state at every time step depends on the previous hidden state [45]. The recurrent unit computes a weighted sum of the input signal.

Training RNNs to capture long-term dependencies is difficult due to the effect of vanishing gradients [46], so the most widely used modification of RNN units is the long short-term memory (LSTM) [47] that provides the “constant error

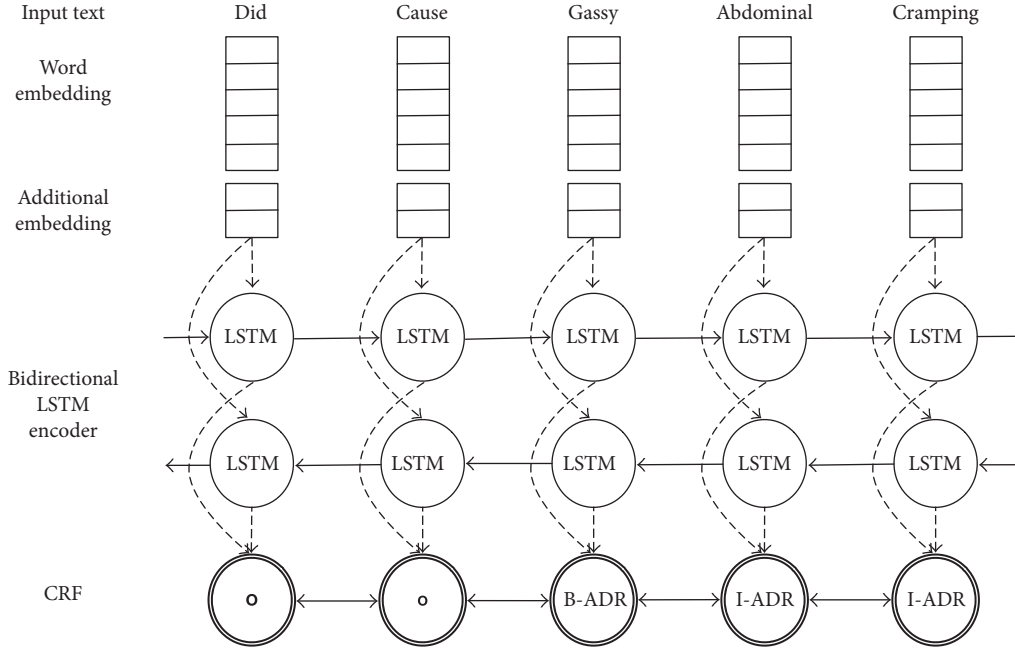


FIGURE 1: The main architecture of our model. Word embeddings are given as input to the bidirectional LSTM network. Dashed arrows represent the input and output vectors of the network with dropout. The labels follow the BIO (Beginning Inside Outside) tagging scheme.

carousel” and does not preclude free gradient flow. The most common LSTM architecture contains three gates: input gate, forget gate, and output gate, together with a recurrent cell. LSTM cells are usually organized in a chain, with outputs of previous LSTMs connected to the inputs of subsequent LSTMs. A recent simplification of the LSTM architecture is given by gated recurrent units (GRU) introduced by Cho et al. [48]. GRU is very similar to an LSTM cell; GRU has a single “update gate” instead of separate forget and input gates, does not distinguish cell state and hidden state, and always exposes the entire hidden state, without a special gate for it.

An important modification of the basic RNN architecture is bidirectional RNNs, where the past and the future context is available on every time step [49]. Bidirectional LSTMs, developed by Graves and Schmidhuber [50, 51], contain two chains of LSTM cells flowing in both forward and backward direction, and the final representation is either a linear combination or simply concatenation of their states.

**3.2. Conditional Random Fields.** CRF [52] is one of the state-of-the-art methods that takes a sequence of tokens as input, estimates the probabilities of labels (from a predefined set), and returns the best scoring label sequence. We denote by  $x_1, \dots, x_n, x_i \in R^m$  corresponding to the input sequence and by  $Y$  to the labels. The CRF is defined by a graph whose vertices are indexes of  $Y$  and edge weights correspond to the effects that  $X$  and  $Y$  have on each other, given that the Markov property holds. A linear-chain CRF is a CRF with a simple chain as the graph, where each edge has the form of  $(j-1, j)$ .

As shown in [52], the conditional probability of a label sequence is computed as follows:

$$P_{\lambda, \mu}(y|x) = \frac{1}{Z(x)} \cdot \prod_{t=1}^n \exp\left(\lambda_{y_{t-1}y_t} + \langle \mu_{y_t}, x_t \rangle\right), \quad (1)$$

where  $Z(x)$  is the normalization,  $x$  is the feature vector,  $\mu$  is the matrix of size  $|Y| \times m$ ,  $\lambda$  is the matrix of  $|Y| \times |Y|$ , and  $\mu_{y_t}$  is the  $y_t$  row in the matrix  $\mu$ . In the equation, the augend represents the score of a transition from the tag  $y_{t-1}$  to the tag  $y_t$ . In our case, the addend represents the score of the tag  $y_t$  of the  $t$ th word. We define the addend to be the matrix of scores output by the recurrent network. Maximum likelihood learning involves maximizing

$$y = \arg \max_{y \in Y} \frac{1}{Z(x)} \cdot \prod_{t=1}^n \exp\left(\lambda_{y_t y_{t-1}} + \langle \mu_{y_t}, x_t \rangle\right). \quad (2)$$

We use an implementation of the linear-chain CRF that minimizes the loss function and trains the weights for computing the global tag sequence scores. During testing, the model applies the Viterbi algorithm to predict the best scoring tag sequence.

**3.3. Joint Model.** The main idea of our proposed model is to combine CRF with a neural network, using nonlinear potentials modeled by a neural network instead of linear potential functions based on sparse features. Figure 1 illustrates the proposed architecture for ADR extraction.

First, word embeddings are fed into the bidirectional RNN (e.g., LSTM). Circles represent LSTM cells. The network returns a representation of the forward and backward context for each word. Then, these output vectors go through a dropout layer for regularization [53]. The result feeds into a dense layer with linear activation, whose output size equals the number of tags. The difference with standard RNN

architecture is that we do not use the softmax output from this layer directly but rather utilize the output of the dense layer for an additional CRF layer to jointly decode the sequence of context tags.

Another important part of the model is the extra vector marked as “additional embedding” on Figure 1. In the experiments shown below, we augmented the basic word embeddings with an additional vector trained with a character-level CNN [16], simply concatenating the two vectors as input for the bidirectional LSTM; we will see that this additional model also improves the final results.

## 4. Experiments and Discussion

**4.1. Quality Metrics and Datasets.** In this section, we evaluate our model and compare it with baseline approaches. Since the boundaries of expressions are hard to define even for human annotators [54], we follow [55, 56] and conduct the experimental evaluation as follows:

- (1) Exact matching following CoNLL evaluation [57]
- (2) Partial matching as described in [56].

We computed several model accuracy metrics such as macroaveraged precision ( $P$ ), recall ( $R$ ), and  $F_1$ -measure ( $F$ ) as follows:

$$\begin{aligned} P &= \frac{TP}{TP + FP}, \\ R &= \frac{TP}{TP + FN}, \\ F &= \frac{2 \cdot P \cdot R}{P + R}, \end{aligned} \quad (3)$$

where TP is the number of correctly predicted annotations and FP and FN are the numbers of false positives and false negatives, respectively. Following [56], we used the following formulas for partial matching:

$$\begin{aligned} P &= \frac{|t \cap t_s|}{|t_s|}, \\ R &= \frac{|t \cap t_s|}{|t|}, \end{aligned} \quad (4)$$

where  $t_s$  is an extracted term which intersects with the term  $t$ ,  $t_s \cap t$  is the intersection between  $t$  and  $t_s$ , and  $|t|$  is the length of this term in tokens. For partial matching, we calculated metrics for every sentence and averaged the resulting values.

We used the Keras library (<https://keras.io/>) to implement neural networks and the BIO (Beginning Inside Outside) tagging scheme on the sentence level. The batch size was 128; we used the Adam optimizer with default parameters [58]. We evaluated our network using the high-quality annotations from the CADEC corpus. Similar to [33], we excluded overlaps between spans of ADRs in the CADEC corpus, selecting the longest continuous span and combining these ADRs into a single annotation.

The corpus was split into two different datasets, leaving 70% for training (with a total of 875 reviews, 5264 sentences,

and 3933 ADRs) and 30% (375 reviews, 2356 sentences, and 1837 ADRs) for testing.

**4.2. Experimental Results.** We evaluate our model by comparing with the following methods:

- (1) CRF with the following baseline features: each word itself with a part-of-speech tag, the suffixes and prefixes to 6 characters in length, and a window of two words in both directions (backward and forward) from the current word
- (2) Feature-rich CRF-based approach with parameters as proposed in [4]; this method utilizes the following features: baseline contextual features, dictionaries, and cluster-based and distributed word representation. The authors used the following dictionaries: the Unified Medical Language System (UMLS), ADR lexicons, and a dictionary of multiword expressions such as “feel tired,” and “feel sleepy.” The Brown hierarchical algorithm was used for cluster-based word representations (vector size of 150). The authors trained Continuous Bag of Words model on a corpus of health-related reviews with the following parameters: vector size of 200, the length of local context of 10, negative sampling of 5, and vocabulary cutoff of 10. We used publicly available implementation of this feature-rich approach (<https://github.com/dartrevan/ChemTextMining/>)
- (3) Deep bidirectional RNNs with a softmax layer, in particular, LSTM and GRU, where the combination of the network’s outputs is fed into a fully connected layer with softmax activation.

We used a maximum of 100 epochs to train each network. For fair comparison, all networks used the same word embeddings trained on 2.5 million of health-related reviews [4]. We found 97% of words in the vocabulary, and for 3% of words, the representations were uniformly sampled from the range of embedding weights [59]. The results of different methods are shown in Table 1.

Table 1 shows that the proposed model consistently outperforms other approaches in terms of both precision and  $F$ -measure, while staying roughly on par with the best recurrent models in terms of recall. Therefore, we conclude that a combination of RNN and CRF indeed leads to quality improvements for ADR extraction from free-text reviews. The second conclusion is that concatenating input word embeddings with an extra embedding vector based on a character-level CNN also significantly improves the results. Another interesting conclusion from Table 1 is that GRU-based recurrent architectures consistently outperform LSTM-based architectures in the exact matching exercise. Finally, another interesting conclusion is that  $F_1$ -scores of 3-layer GRU+CNN+CRF increased from 70.65% to 79.78% in the partial matching as compared to the exact exercise due to boundary problems. Qualitative analysis of results indicates errors associated with boundaries of entities due to the presence of negations (e.g., “I have *no pain*”),

TABLE 1: Results of the proposed models and baseline methods.

| Method                   | $P$           | Exact<br>$R$  | $F$           | $P$           | Partial<br>$R$ | $F$           |
|--------------------------|---------------|---------------|---------------|---------------|----------------|---------------|
| Baseline CRF             | 0.6254        | 0.5972        | 0.6110        | 0.8145        | 0.7539         | 0.7521        |
| Feature-rich CRF         | 0.6726        | 0.6532        | 0.6628        | <b>0.8303</b> | 0.7646         | 0.7622        |
| 1-layer LSTM             | 0.5798        | 0.6587        | 0.6167        | 0.8121        | 0.8065         | 0.7809        |
| 2-layer LSTM             | 0.6362        | 0.7044        | 0.6686        | 0.8090        | 0.8495         | 0.8005        |
| 3-layer LSTM             | 0.6588        | 0.7022        | 0.6798        | 0.8247        | 0.8323         | 0.7997        |
| 4-layer LSTM             | 0.6689        | 0.7093        | 0.6885        | 0.8255        | 0.8280         | 0.8000        |
| 1-layer GRU              | 0.5862        | 0.6772        | 0.6284        | 0.7995        | 0.8368         | 0.7900        |
| 2-layer GRU              | 0.6384        | 0.7093        | 0.6720        | 0.8165        | 0.8338         | 0.8002        |
| 3-layer GRU              | 0.6675        | 0.7191        | 0.6923        | 0.8151        | 0.8373         | 0.8009        |
| 4-layer GRU              | 0.6565        | <b>0.7262</b> | 0.6896        | 0.8006        | <b>0.8665</b>  | 0.8033        |
| 2-layer LSTM + CRF       | 0.6947        | 0.6973        | 0.6960        | 0.8191        | 0.8161         | 0.7872        |
| 2-layer LSTM + CNN + CRF | 0.6809        | 0.7039        | 0.6922        | 0.8083        | 0.8488         | 0.7978        |
| 3-layer LSTM + CNN + CRF | 0.6868        | 0.7066        | 0.6965        | 0.8270        | 0.8488         | <b>0.8115</b> |
| 3-layer GRU + CNN + CRF  | <b>0.7048</b> | 0.7082        | <b>0.7065</b> | 0.8219        | 0.8311         | 0.7978        |

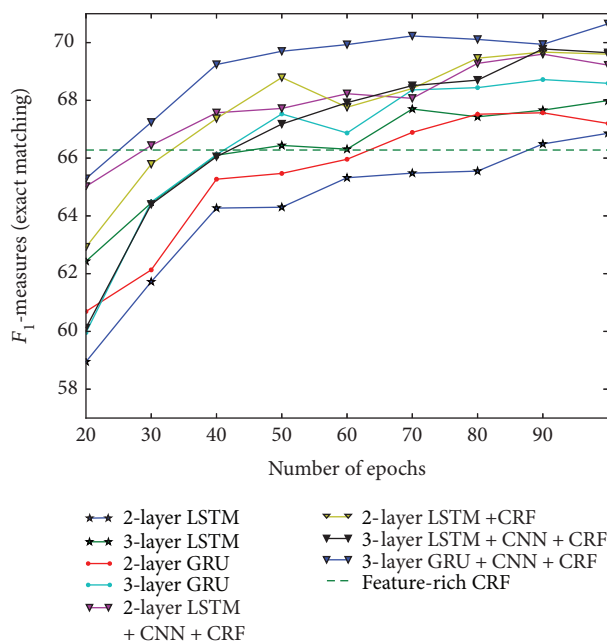


FIGURE 2: Performance on the testing data set or different number of training epochs.

conjunctions, verbs, adjectives, or adverbs (e.g., “lowered total cholesterol dramatically”).

We initially set the number of epochs for training models to be 100 and explored the quality metrics for the number of training epochs ranging from 20 to 100. Figure 2 presents the results. It shows that training of deep LSTM and GRU can be effectively achieved at around 60–80 epochs before the performance becomes stable. The joint model of 2-layer LSTM + CNN + CRF and 3-layer GRU + CNN + CRF outperformed CRF starting at 30–40 epochs, and from here on, performance improved slowly.

4.3. *Qualitative Analysis of Extracted ADR Mentions.* Adverse drug reactions can differ significantly depending on the patient. To investigate the difference between adverse effects for various drugs, we collected reviews from a health information service webmd.com. Each review contains the following fields:

- (1) *Brand name* of a drug used to treat this disease
- (2) *Condition/reason* for taking treatment
- (3) *The free-text review* given for the effects caused by the use of the drug
- (4) *Demographic information* about the author of this review (age and gender).

We also note that such demographic information is not commonly provided in discussion groups and websites. In a recent study [60], several approaches to automated mining of demographic information from texts about drugs were evaluated including neural networks, supervised machine learning, and topic modeling.

We selected reviews about the following health conditions for analysis:

- (1) 4,563 reviews about depressive disorder (drugs: Cymbalta, Lexapro, Xanax, Zoloft, or Prozac)
- (2) 5,422 reviews about high blood pressure (drugs: lisinopril, atenolol, Bystolic, Diovan, and hydrochlorothiazide)
- (3) 10,914 reviews about fibromyalgia (drugs: Cymbalta, Lyrica, tramadol, Prozac, amitriptyline, Savella, Paxil CR, Ultram, Paxil, cyclobenzaprine).

In order to detect ADRs related to a particular demographic group, we extracted all ADRs that appeared in

TABLE 2: ADRs extracted from reviews for the drugs that treat depression.

| Group                 | Adverse drug reactions  |
|-----------------------|---|
| All authors           | Anxiety, depression, panic attacks, depressed, pain, weight gain, nausea, headaches, dizziness, insomnia, dizzy, mood swings, tired, dry mouth, sweating  |
| Gender group “female” | Rash, gained weight, could not sleep, heartburn, severe nausea, lost weight, restless, very irritable, heart racing, disconnected, stiffness, upset, severe migraines, cramping, neck pain, twitching, fever, skin problems |
| Gender group “male”   | Erectile dysfunction, pins and needles, burning sensations, loose bowels, urination, uneasiness, trouble with dizziness, severe drowsiness, night sweat, chest pressure, blisters, clammy hands                             |
| Age group “19–34”     | Couldn’t sleep, anger issues, loss of sex drive, cramps, unmotivated, jaw pain, frequent headaches, fever, stomach pains, crying for no reason, severe dizziness, intrusive thoughts  |
| Age group “45–64”     | Nervous breakdown, aches and pains, swelling, muscle aches, delayed ejaculation, profuse sweating, indigestion, ringing in my ears, spasms, trouble urinating, palpitations   |

TABLE 3: ADRs extracted from reviews for the drugs that treat high blood pressure.

| Group                 | Adverse drug reactions   |
|-----------------------|--|
| All authors           | Cough, coughing, dizziness, dizzy, headaches, dry cough, fatigue, tired, headache, weight gain, hair loss, nausea, anxiety, shortness of breath, tiredness, diarrhea, chest pain, depression, joint pain, rash, swelling, very tired, light headed, blurred vision |
| Gender group “female” | Heart palpitations, hives, gagging, hot flashes, extremely tired, nightmares, chronic cough, cold hands and feet, panic attacks, exhausted, weight loss, blurry vision, heartburn, sleepy, persistent cough, severe headaches, stomach pain, numbness              |
| Age group “45–64”     | Bloating, muscle aches, persistent cough, indigestion, stomach pain, post nasal drip, sick, lack of sleep, ringing in my ears, stomach pains, foot cramps, tightness in chest, falling out, severe coughing, faint, nagging cough, no energy                       |
| Age group “25–44”     | Short-term memory loss, slight weight gain, fast heartbeat, lost sex drive, cramp, unusual tiredness, bad dreams, numbness in my toes, pain in my side, dazed feeling, intense salt cravings, lip to swell, chronic headaches, throat and neck swelled             |

TABLE 4: ADRs extracted from reviews for the drugs that treat fibromyalgia.

| Group                 | Adverse drug reactions   |
|-----------------------|--|
| All authors           | Pain, depression, anxiety, weight gain, nausea, headaches, depressed, dizziness, dizzy, panic attacks, nerve pain, insomnia, dry mouth, constipation, sweating, tired, headache, fatigue, back pain, mood swings, hot flashes, nightmares, suicidal thoughts, severe pain, blurred vision, muscle pain, vomiting, chronic pain, suicidal, neuropathic pain, drowsiness, trouble sleeping, sex drive, diarrhea, seizures, crying, anxious, nauseous, numbness, swelling, leg pain, night sweats, vertigo, tremors, joint pain, itching, burning, panic attack, sleepiness, drowsy |
| Gender group “female” | Severe migraines, water retention, severe panic attacks, suicidal ideation, exhaustion, stiff, inability to sleep, rapid heartbeat, crazy dreams, sweaty, nervous breakdown, extreme sweating, fogginess, flushing, major weight gain, increased my appetite   |
| Gender group “male”   | Blisters, premature ejaculation, foot neuropathy, burning discomfort, can barely walk, pain in my toes, anger problems, loss of libido, pancreatitis, pain in lower back, hiccups, shock sensations, couldn’t walk, can’t walk, panic problems, “shock” sensations, hangover, short-term memory, severe trouble urinating  |

reviews more than four times and then excluded ADRs if the exact match appears in reviews of authors with a different demographic tag (e.g., “male”/“female” or “age 19–34” over other ages). Tables 2, 3, and 4 present the results. The tables indicate that key adverse reactions change with age or gender, reflecting quite natural progressions that match well with medical and commonsense intuition. Hence, our method can also be used to mine qualitative information from a dataset of medical reviews, perhaps uncovering new ADRs in a certain user group.

## 5. Conclusion

In this work, we have proposed a novel approach to extracting adverse drug reactions from user reviews: a combination of a bidirectional LSTM-based recurrent neural network and a CRF that operates on the scores extracted by this neural network. We have evaluated our approach against state-of-the-art neural models on a representative ADR extraction dataset and have found that the results have improved significantly. Moreover, further improvements were obtained by

extending input embeddings with a character-level model. Thus, our final model successfully combines three different approaches to statistical modeling in NLP. In further work, we plan to experiment with other neural models in similar general architectures and further improve the state of the art in ADR extraction from free-text reviews.

## Conflicts of Interest

The authors declare that they have no conflicts of interest.

## Acknowledgments

The work was supported by the Russian Science Foundation Grant no. 15-11-10019.

## References

- [1] I. Segura-Bedmar, P. Martínez, R. Revert, and J. Moreno-Schneider, "Exploring Spanish health social media for detecting drug effects," *BMC Medical*, vol. 15, Supplement 2, p. S6, 2015.
- [2] M. S. Boguski, K. D. Mandl, and V. P. Sukhatme, "Repurposing with a difference," *Science*, vol. 324, no. 5933, pp. 1394-1395, 2009.
- [3] P. Avillach, J.-C. Dufour, G. Diallo et al., "Design and validation of an automated method to detect known adverse drug reactions in MEDLINE: a contribution from the EU-ADR project," *Journal of the American Medical Informatics Association*, vol. 20, no. 3, pp. 446-452, 2013.
- [4] Z. S. Miiftahutdinov, E. V. Tutubalina, and A. E. Tropsha, *Identifying Disease-Related Expressions in Reviews Using Conditional Random Fields*, Komp'yuternaja Lingvistika i Intellektual'nye Tehnologii, 2017.
- [5] A. N. Jagannatha and H. Yu, "Bidirectional RNN for medical event detection in electronic health records," *Proceedings of the Conference Association for Computational Linguistics*, vol. 2016, pp. 473-482, 2016.
- [6] A. Nikfarjam, A. Sarker, K. O'Connor, R. Ginn, and G. Gonzalez, "Pharmacovigilance from social media: mining adverse drug reaction mentions using sequence labeling with word embedding cluster features," *Journal of the American Medical Informatics Association*, vol. 22, no. 3, pp. 671-681, 2015.
- [7] O. Irsoy and C. Cardie, "Opinion mining with deep recurrent neural networks," in *Proceedings of the 2014 Conference on Empirical Methods in Natural Language Processing (EMNLP 2014): A meeting of SIGDAT, a Special Interest Group of the ACL*, pp. 720-728, Doha, Qatar, October 2014.
- [8] P. Liu, S. R. Joty, and H. M. Meng, "Fine-grained Opinion Mining with Recurrent Neural Networks and Word Embeddings," in *Proceedings of the 2015 Conference on Empirical Methods in Natural Language Processing (EMNLP 2015)*, pp. 1433-1443, Lisbon, Portugal, September 2015.
- [9] W. Wang, "Mining adverse drug reaction mentions in twitter with word embeddings," in *Proceedings of the Social Media Mining Shared Task Workshop at the Pacific Symposium on Biocomputing*, 2016.
- [10] H.-C. Lee, Y.-Y. Hsu, and H.-Y. Kao, "An enhanced CRF-based system for disease name entity recognition and normalization on BioCreative V DNER task," in *Proceedings of the Fifth BioCreative Challenge Evaluation Workshop*, pp. 226-233, 2015, <http://www.biocreative.org>.
- [11] Q. Wei, T. Chen, R. Xu, Y. He, and L. Gui, "Disease named entity recognition by combining conditional random fields and bidirectional recurrent neural networks," *Database*, vol. 2016, 2016.
- [12] R. Gareev, M. Tkachenko, and V. Solovyev, *Introducing Baselines for Russian Named Entity Recognition*, 2013.
- [13] V. A. Mozharova and N. V. Loukachevitch, "Combining knowledge and CRF-based approach to named entity recognition in Russian," in *Analysis of Images, Social Networks and Texts*, pp. 185-195, Springer, Cham, 2016.
- [14] Z. Huang, W. Xu, and K. Yu, *Bidirectional LSTM-CRF Models for Sequence Tagging*, 2015, arXiv preprint arXiv:1508.01991.
- [15] J. Chiu and E. Nichols, *Named Entity Recognition with Bidirectional LSTM-CNNs*, 2015, arXiv preprint arXiv:1511.08308.
- [16] X. Ma and E. Hovy, *End-to-End Sequence Labeling via Bi-Directional LSTM-CNNs-CRF*, 2016, arXiv [cs.LG].
- [17] S. Karimi, A. Metke-Jimenez, M. Kemp, and C. Wang, "Cadec: a corpus of adverse drug event annotations," *Journal of Biomedical Informatics*, vol. 55, pp. 73-81, 2015.
- [18] C.-H. Wei, Y. Peng, R. Leaman et al., "Overview of the BioCreative V chemical disease relation (CDR) task," *Proceedings of the Fifth BioCreative Challenge Evaluation Workshop*, pp. 154-166, 2015, <http://www.biocreative.org>.
- [19] J. Gu, L. Qian, and G. Zhou, "Chemical-induced disease relation extraction with various linguistic features," *Database*, vol. 2016, 2016.
- [20] Z. Zhang, J.-Y. Nie, and X. Zhang, "An ensemble method for binary classification of adverse drug reactions from social media," *Proceedings of the Social Media Mining Shared Task Workshop at the Pacific Symposium on Biocomputing*.
- [21] S. Spangler, A. D. Wilkins, B. J. Bachman et al., "Automated hypothesis generation based on mining scientific literature," *Proceedings of the 20th ACM SIGKDD International Conference on Knowledge Discovery and Data Mining*, pp. 1877-1886, ACM, New York, NY, USA, 2014.
- [22] E. Yom-Tov and E. Gabrilovich, "Postmarket drug surveillance without trial costs: discovery of adverse drug reactions through large-scale analysis of web search queries," *Journal of Medical Internet Research*, vol. 15, no. 6, article e124, 2013.
- [23] C.-C. Huang and Z. Lu, "Community challenges in biomedical text mining over 10 years: success, failure and the future," *Briefings in Bioinformatics*, vol. 17, no. 1, pp. 132-144, 2016.
- [24] A. M. Cohen and W. R. Hersh, "A survey of current work in biomedical text mining," *Briefings in Bioinformatics*, vol. 6, no. 1, pp. 57-71, 2005.
- [25] D. L. Ngo, N. Yamamoto, V. A. Tran et al., "Application of word embedding to drug repositioning," *Journal of Biomedical Science and Engineering*, vol. 9, p. 7, 2016.
- [26] M. Rastegar-Mojarad, H. Liu, and P. Nambisan, "Using social media data to identify potential candidates for drug repurposing: a feasibility study," *JMIR Research Protocols*, vol. 5, no. 2, article e121, 2016.
- [27] S. N. Deftereos, C. Andronis, E. J. Friedla, A. Persidis, and A. Persidis, "Drug repurposing and adverse event prediction using high-throughput literature analysis," *Wiley Interdisciplinary Reviews: Systems Biology and Medicine*, vol. 3, no. 3, pp. 323-334, 2011.
- [28] T. C. Carter and M. M. He, "Challenges of identifying clinically actionable genetic variants for precision medicine," *Journal of Healthcare Engineering*, vol. 2016, Article ID 3617572, 14 pages, 2016.

- [29] A. Helmer, M. Lipprandt, T. Frenken, M. Eichelberg, and A. Hein, "3DLC: a comprehensive model for personal health records supporting new types of medical applications," *Journal of Healthcare Engineering*, vol. 2, no. 3, pp. 321–336, 2011.
- [30] S. Saboor, A. Hoerbst, and E. Ammenwerth, "Quality of electronic health records-coverage of potential information weaknesses by major EHR quality seals," *Journal of Healthcare Engineering*, vol. 2, no. 3, pp. 365–388, 2011.
- [31] J. Bian, U. Topaloglu, and F. Yu, "Towards large-scale twitter mining for drug-related adverse events," *Proceedings of the 2012 International Workshop on Smart Health and Wellbeing*, pp. 25–32, ACM, New York, NY, USA, 2012.
- [32] A. Sarker, A. Nikfarjam, and G. Gonzalez, "Social media mining shared task workshop," *Pacific Symposium Biocomputing*, vol. 21, pp. 581–592, 2016.
- [33] A. Metke-Jimenez and S. Karimi, *Concept Extraction to Identify Adverse Drug Reactions in Medical Forums: A Comparison of Algorithms*, 2015, arXiv [cs.AI].
- [34] C. K. Reddy and C. C. Aggarwal, *Healthcare Data Analytics*, CRC Press, 2015.
- [35] S. Gupta, D. L. MacLean, J. Heer, and C. D. Manning, "Induced lexico-syntactic patterns improve information extraction from online medical forums," *Journal of the American Medical Informatics Association*, vol. 21, pp. 902–909, 2014.
- [36] A. Benton, L. Ungar, S. Hill et al., "Identifying potential adverse effects using the web: a new approach to medical hypothesis generation," *Journal of Biomedical Informatics*, vol. 44, pp. 989–996, 2011.
- [37] R. Feldman, O. Netzer, A. Peretz, and B. Rosenfeld, "Utilizing text mining on online medical forums to predict label change due to adverse drug reactions," *Proceedings of the 21th ACM SIGKDD International Conference on Knowledge Discovery and Data Mining*, pp. 1779–1788, ACM, New York, NY, USA, 2015.
- [38] S. Karimi, C. Wang, A. Metke-Jimenez, R. Gaire, and C. Paris, "Text and data mining techniques in adverse drug reaction detection," *ACM Computing Surveys*, vol. 47, pp. 56:1–56:39, 2015.
- [39] A. Sarker, R. Ginn, A. Nikfarjam et al., "Utilizing social media data for pharmacovigilance: a review," *Journal of Biomedical Informatics*, vol. 54, pp. 202–212, 2015.
- [40] V. Solovyev and V. Ivanov, "Knowledge-driven event extraction in Russian: corpus-based linguistic resources," *Computational intelligence and neuroscience*, vol. 2016, Article ID 4183760, 11 pages, 2016.
- [41] R. Leaman, L. Wojtulewicz, R. Sullivan, A. Skariah, J. Yang, and G. Gonzalez, "Towards internet-age pharmacovigilance: extracting adverse drug reactions from user posts to health-related social networks," *Proceedings of the 2010 Workshop on Biomedical Natural Language Processing*, pp. 117–125, Association for Computational Linguistics, Stroudsburg, PA, USA, 2010.
- [42] C. C. Yang, H. Yang, L. Jiang, and M. Zhang, "Social media mining for drug safety signal detection," *Proceedings of the 2012 International Workshop on Smart Health and Wellbeing*, pp. 33–40, ACM, New York, NY, USA, 2012.
- [43] S. Gupta and C. D. Manning, *Improved Pattern Learning for Bootstrapped Entity Extraction*, 2014, CoNLL.
- [44] G. Stanovsky, D. Gruhl, and P. N. Mendes, *Recognizing Mentions of Adverse Drug Reaction in Social Media Using Knowledge-Infused Recurrent Models*, 2017, EAACL.
- [45] J. L. Elman, "Finding structure in time," *Cognitive Science*, vol. 14, pp. 179–211, 1990.
- [46] Y. Bengio, P. Simard, and P. Frasconi, "Learning long-term dependencies with gradient descent is difficult," *IEEE Transactions on Neural Network*, vol. 5, no. 2, pp. 157–166, 1994.
- [47] K. Greff, R. K. Srivastava, J. Koutnik, B. R. Steunebrink, and J. Schmidhuber, "LSTM: a search space odyssey," *IEEE Transactions on Neural Networks and Learning Systems*, 2016.
- [48] K. Cho, B. van Merriënboer, C. Gulcehre et al., "Learning phrase representations using RNN encoder-decoder for statistical machine translation," *Proceedings of the 2014 Conference on Empirical Methods in Natural Language Processing (EMNLP)*, pp. 1724–1734, Association for Computational Linguistics, Stroudsburg, PA, USA, 2014.
- [49] M. Schuster and K. K. Paliwal, "Bidirectional recurrent neural networks," *IEEE Transactions on Signal Processing*, vol. 45, pp. 2673–2681, 1997.
- [50] A. Graves, S. Fernández, and J. Schmidhuber, "Bidirectional LSTM networks for improved phoneme classification and recognition," *Artificial Neural Networks: Formal Models and Their Applications – ICANN 2005*, pp. 799–804, Springer, Berlin, Heidelberg, 2005.
- [51] A. Graves and J. Schmidhuber, "Framewise phoneme classification with bidirectional LSTM networks," *Proceedings 2005 IEEE International Joint Conference on Neural Networks*, vol. 4, pp. 2047–2052, 2005.
- [52] J. Lafferty, A. McCallum, and F. Pereira, "Conditional random fields: probabilistic models for segmenting and labeling sequence data," *Proceedings of the Eighteenth*.
- [53] N. Srivastava, G. E. Hinton, A. Krizhevsky, I. Sutskever, and R. Salakhutdinov, "Dropout: a simple way to prevent neural networks from overfitting," *Journal of Machine Learning Research*, vol. 15, pp. 1929–1958, 2014.
- [54] J. Wiebe, T. Wilson, and C. Cardie, "Annotating expressions of opinions and emotions in language," *Language Resources and Evaluation*, vol. 39, pp. 165–210, 2006.
- [55] O. Irsoy and C. Cardie, "Opinion mining with deep recurrent neural networks," *Proceedings of the 2014 Conference on Empirical Methods in Natural Language Processing (EMNLP)*, pp. 720–728, Association for Computational Linguistics, Stroudsburg, PA, USA, 2014.
- [56] N. Loukachevitch, P. Blinov, E. Kotelnikov, Y. Rubtsova, V. Ivanov, and E. Tutubalina, "SentiRuEval: testing object-oriented sentiment analysis systems in Russian," *Proceedings of International Conference Dialog*, pp. 3–13, 2015.
- [57] E. F. Tjong Kim Sang and F. De Meulder, "Introduction to the CoNLL-2003 shared task: language-independent named entity recognition," *Proceedings of the Seventh Conference on Natural Language Learning at HLT-NAACL 2003 - Volume 4*, pp. 142–147, Association for Computational Linguistics, Stroudsburg, PA, USA, 2003.
- [58] D. Kinga and J. B. Adam, "A method for stochastic optimization," *International Conference on Learning Representations (ICLR)*.
- [59] K. He, X. Zhang, S. Ren, and J. Sun, "Delving deep into rectifiers: surpassing human-level performance on imagenet classification," in *Proceedings of the IEEE International Conference on Computer Vision*, pp. 1026–1034, Santiago, Chile, 2015.
- [60] E. Tutubalina and S. Nikolenko, "Automated prediction of demographic information from medical user reviews," *International Conference on Mining Intelligence and Knowledge Exploration*, pp. 1–11, Springer, 2016.

## Research Article

# A Method for Assessing the Retention of Trace Elements in Human Body Using Neural Network Technology

**Yulia Tunakova,<sup>1</sup> Svetlana Novikova,<sup>1</sup> Aligejdar Ragimov,<sup>2</sup> Rashat Faizullin,<sup>3</sup> and Vsevolod Valiev<sup>4</sup>**

<sup>1</sup>*Kazan National Research Technical University named after A. N. Tupolev (KAI), Kazan, Russia*

<sup>2</sup>*The I.M. Sechenov First Moscow State Medical University, Moscow, Russia*

<sup>3</sup>*Institute of Fundamental Medicine and Biology, Kazan Federal University, Kazan, Russia*

<sup>4</sup>*Institute of Problems of Ecology and Subsoil Resources of the Academy of Sciences of Tatarstan, Kazan, Russia*

Correspondence should be addressed to Yulia Tunakova; [juliaprof@mail.ru](mailto:juliaprof@mail.ru)

Received 2 April 2017; Accepted 1 June 2017; Published 16 July 2017

Academic Editor: Kunal Pal

Copyright © 2017 Yulia Tunakova et al. This is an open access article distributed under the Creative Commons Attribution License, which permits unrestricted use, distribution, and reproduction in any medium, provided the original work is properly cited.

Models that describe the trace element status formation in the human organism are essential for a correction of micromineral (trace elements) deficiency. A direct trace element retention assessment in the body is difficult due to the many internal mechanisms. The trace element retention is determined by the amount and the ratio of incoming and excreted substance. So, the concentration of trace elements in drinking water characterizes the intake, whereas the element concentration in urine characterizes the excretion. This system can be interpreted as three interrelated elements that are in equilibrium. Since many relationships in the system are not known, the use of standard mathematical models is difficult. The artificial neural network use is suitable for constructing a model in the best way because it can take into account all dependencies in the system implicitly and process inaccurate and incomplete data. We created several neural network models to describe the retentions of trace elements in the human body. On the model basis, we can calculate the microelement levels in the body, knowing the trace element levels in drinking water and urine. These results can be used in health care to provide the population with safe drinking water.

## 1. Introduction

It is known that there is a complex dependence between water and food intake and trace element retention with the formation of their individual statuses, and this dependence has generally a nonlinear nature. Therefore, linear modelling methods in multivariate regression tasks are not able to describe with sufficient precision the whole range of relations among significant factors appearing in the models developed for the human body [1–8].

A number of studies [9–18] assert that trace elements enter the body primarily through water and food intake, then they are carried by the blood by binding them to specific proteins; however, a certain portion of them (which is different for different elements) is present in the blood in an ionized form. The kidneys regulate the trace elements balance by

excreting them in the urine. At the same time, the proportion of trace element forms not bound to proteins drastically increases in the setting of an excessive admission from the outside due to homeostatic limits to the possible presence of transport proteins and, as a consequence, lack of reserves for binding. Under these conditions, the excretory function of the kidneys grows and the concentration of elements in urine increases.

The modelling of the dynamics of trace elements concentration in the serum as well as the process of excretion of minerals in the urine are an important stage that characterizes the processes associated with trace element retention. Thus, this research is aimed at creating models that adequately reflect the balance of the essential elements, as well as the processes of their intake, excretion, and, especially, retention in the body.

The possibilities of neural network methods, which automatically take into account both explicit and implicit dependencies, exist among initial data [19–21]. In addition, neural networks, in contrast to traditional modelling methods, allow for using incomplete and inaccurate input data and are able to reflect nonlinear dependencies and choose the right correction coefficients [22]. However, the use of neural networks is restricted to simple networks of direct distribution. Moreover, scientific publications in the recent years do not contain information regarding the use of neural networks for the assessment and correction of the balance of trace elements in the body. The use of neural networks of “multilayer perceptron” type, self-organizing maps (Kohonen maps or Kohonen networks) and probabilistic neural networks, as well as hybrid and cascade networks (multilayer neural network experts, neural network cascades, etc.), allows for reducing calculation errors from tens to a few percent and even to tenths of percent.

## 2. Materials and Methods

In order to model the processes of retention of trace elements in the body, we analyzed more than 2000 samples of dynamic internal media of children and adolescents living in the city of Kazan (Russia) and more than 750 samples of drinking water consumed by them to assess the concentration of the most common trace elements (Zn, Cu, Fe, Pb, Cr, and Sr).

The blood samples tested in the research were centrifuged for 15 minutes at 3000 rev/min. The calibration solutions (stock and working) were prepared based on the State Standard Samples by the standard method. To measure the metal concentrations in the blood, we previously diluted the serum with bidistilled water at 1:2 ratio (to detect Zn, Cu, and Fe) or in a TCA filtrate (in the case of Pb, Cr, and Sr). To obtain the TCA filtrate, we hydrolyzed whey proteins in hydrochloric acid (reagent grade), adding 0,75 ml of 1,5% HCl solution to 1,5 ml of serum and incubating for 1 hour at 37°C. After hydrolysis, the proteins were precipitated by 0,75 ml of 20% TCA (trichloroacetic acid), with a final dilution at 1:2 ratio, and after 1 h were centrifuged for 10 minutes at 1500 rev/min. The supernatant fluid (TCA filtrate) was collected for analysis.

In those cases when the concentration of a certain trace element was below the detection level and could not be detected directly in the TCA filtrate, we used the concentration/extraction method: added 0,5 ml of 2% sodium diethyldithiocarbamate solution and 2 drops of TRITON-X-100 detergent to 2,5 ml of serum and vigorously shook the mixture for 10 seconds. Then, we let the mixture settle for 10 minutes, added 1,5 ml of butyl acetate, shook it for 1 minute, centrifuged it, and analyzed the extract. This way, we managed to reduce the detection level by a factor of 1,5 for chrome and by a factor of 2,5 for strontium and lead.

In order to determine the trace elements in urine, we collected daily urine samples and examined the concentrations of metals in them by direct analysis.

It is known that the ionized forms of trace elements entering the body with consumed water are effectively assimilated. Trace element salts dissociated in water are characterized by a high biological activity; the adsorption of these salts in the gastrointestinal tract is very quick and complete. Therefore, the fraction of trace elements entering the body in a dissolved form must manifest itself in some way in the change of their concentrations in the serum [5].

During preparation of drinking water samples, we evaporated 1 litre of water in a water bath and then dissolved the solid residue in 50 ml of 1 N nitric acid (reagent grade). The obtained aliquot part was analyzed by the AAS method.

As the analytical method for determining trace elements in the examined media, we chose the AAS method, since it is known as one of the most selective and reproducible methods and is recognized for its high selectivity and speed of execution, which becomes a very important factor when performing a research at a population level. This method is especially adequate for the analysis of solutions, since in this case the dissociation of the analyzed substance into atoms can be achieved by heating in a Bunsen burner. The detection of trace elements in a highly oxygenated air-acetylene flame is highly selective and characterizes itself by an insignificant influence of the sample composition on the analysis result. The primary statistical processing of the results was performed using the software package “STATISTICA 6.” We evaluated the confidence intervals, variances, quartiles, the normality of distributions, and the statistical significance (*t*-test). The significance of the results was determined using a 95% confidence interval ( $p < 0,05$ ).

MLP-type neural networks were chosen as the paradigm of the regression model [23]. The structure of this type of neural networks is defined empirically and is determined by the complexity of the information contained in the data. For training the neural networks, we used a network reduction method based on multiobjective optimization [24].

## 3. Results

A wide concentration gradient was detected for all trace elements in the tested media. Results from previous experiments show that knowing the content of trace elements in drinking water is not enough to build adequate models describing how these elements enter the blood and subsequently are excreted in the urine. For this reason, we decided to supplement the model with information on some physiological characteristics of the human organism. The height and weight of the tested individual were taken as anthropometric factors affecting directly the processes of accumulation of metals in the organism and their excretion from it. These factors define a key morphometric parameter widely used in toxicology and human physiology, and known as the body surface area (1), which characterizes indirectly the length of the circulatory system:

TABLE 1: Correlation between linguistic and quantitative values of the input parameters.

| Input parameter                                | Trace element | Linguistic value | Centre value of the membership function |
|--|---------------|------------------|---|
| Trace elements concentration in drinking water | Zinc          | Low level        | 0,016                                   |
|  |               | High level       | 0,022                                   |
|  | Chrome        | Low level        | 0,0012                                  |
|  |               | High level       | 0,0045                                  |
|  | Iron          | Low level        | 0,0735                                  |
|  |               | High level       | 0,1                                     |
|  | Strontium     | Low level        | 0,107                                   |
|  |               | High level       | 0,17775                                 |
|  | Copper        | Low level        | 0,0012                                  |
|  |               | High level       | 0,0018                                  |
|  | Lead          | Low level        | 0,012                                   |
|  |               | High level       | 0,0165                                  |
| Trace elements concentration in serum          | Zinc          | Low level        | 0,6355                                  |
|  |               | High level       | 0,8275                                  |
|  | Chrome        | Low level        | 0,04                                    |
|  |               | High level       | 0,08525                                 |
|  | Iron          | Low level        | 1,1375                                  |
|  |               | High level       | 1,9635                                  |
|  | Strontium     | Low level        | 0,08925                                 |
|  |               | High level       | 0,156                                   |
|  | Copper        | Low level        | 0,715                                   |
|  |               | High level       | 0,99275                                 |
|  | Lead          | Low level        | 0,0475                                  |
|  |               | High level       | 0,079                                   |
| Trace elements concentration in urine          | Zinc          | Low level        | 0,239                                   |
|  |               | High level       | 0,4895                                  |
|  | Chrome        | Low level        | 0,012                                   |
|  |               | High level       | 0,028                                   |
|  | Iron          | Low level        | 0,0745                                  |
|  |               | High level       | 0,2195                                  |
|  | Strontium     | Low level        | 0,087                                   |
|  |               | High level       | 0,222                                   |
|  | Copper        | Low level        | 0,022                                   |
|  |               | High level       | 0,084                                   |
|  | Lead          | Low level        | 0,028                                   |
|  |               | High level       | 0,055                                   |

$$S_{\text{body}} = \sqrt{\frac{P \times B}{3600}}, \quad (1)$$

where  $S_{\text{body}}$  is the body surface area, measured in  $\text{m}^2$ ,  $P$  is the height, measured in cm, and  $B$  is the weight, measured in kg.

In order to increase the accuracy of the calculation of the concentration of ionized trace elements in the urine, we introduced a characteristic determined by the excretory function of the kidneys, namely, the “daily diuresis,” which is the total volume of urine (in ml) produced by the human organism per day.

Thus, to calculate the retention level, we used data tuples of the following form: “[Concentration of trace elements in drinking water] & [Concentration of trace elements in serum] & [Concentration of trace elements in urine] – [Retention level in the body]”. The input parameter, “Concentration of trace elements in drinking water” was determined by direct measurement, whereas the parameters “Concentration of trace elements in serum” and “Concentration of trace elements in urine” were computed in a cascade-like manner, on the basis of separated neural network models.

The model for assessing the retention level is based on a fuzzy inference system [25], since the models of this kind take into account the blurred boundaries of the notions of “low” (coded with 0) and “high” (coded with 1) for the trace element levels in water, blood, and urine, and also reflects the nonlinear nature of the dependence of the factors that determine the retention. The linguistic values are correlated with the quantitative values of the concentration of trace elements in drinking water, blood and urine (mg/l) by means of Gaussian membership functions with centres computed as the boundary between the first (lower) and the third (upper) quartiles on the basis of a series of outdoor measurements (see Table 1).

#### 4. Discussion

The following reasoning allows to determine the character and values of the output parameter “Retention level.” After analyzing the regression coefficients of the obtained linear models describing the correlation between the concentrations of trace elements in drinking water, serum, and urine, it may be noted that they are in the ratios (“Water” : “Blood” : “Urine”) 5 : 2 : 3. In particular, if we consider the regression of the ratios of the indices of excess rate, which are the values, reduced with respect to the median of the series, of each element of the sample ( $R_{\text{retention}}$ ,  $R_{\text{water}}$ ,  $R_{\text{blood}}$ ,  $R_{\text{urine}}$ ), then it has the form

$$R_{\text{retention}} = 0,327 + 0,52 \times R_{\text{water}} + 0,19 \times R_{\text{blood}} - 0,33 \times R_{\text{urine}}. \quad (2)$$

If we take a conventional unit as maximum intensity of the retention, then the weighting coefficients of the factors of the sequence “Water” => “Blood” => “Urine” are distributed as follows:

- (i) a high level of trace elements in blood (coded with 1) corresponds to a weight of 0,2, whereas a low level of trace elements in blood (coded with 0) corresponds to a weight of  $-0,2$ ;
- (ii) a high level of trace elements in drinking water (coded with 1) corresponds to a weight of 0,5, whereas a low level of trace elements in drinking water (coded with 0) corresponds to a weight of  $-0,5$ ;
- (iii) a high level of trace elements in urine (coded with 1) corresponds to a weight of 0,3, whereas a low level of trace elements in urine (coded with 0) corresponds to a weight of  $-0,3$ .

TABLE 2: Table of rules of inference.

| Trace elements concentration<br>in drinking water | Trace elements concentration<br>in serum | Trace elements concentration<br>in urine | Retention level |                   |
|---|--|--|-----------------|-------------------|
|   |  |  | Value           | Linguistic value  |
| 0   | 0  | 0  | -0,4            | Moderately low    |
| 0   | 0  | 1  | -1              | Minimal           |
| 0   | 1  | 0  | 0               | Equilibrium state |
| 0   | 1  | 1  | -0,6            | Low               |
| 1   | 0  | 0  | 0,6             | High              |
| 1   | 0  | 1  | 0               | Equilibrium state |
| 1   | 1  | 0  | 1               | Maximal           |
| 1   | 1  | 1  | 0,4             | Moderately high   |

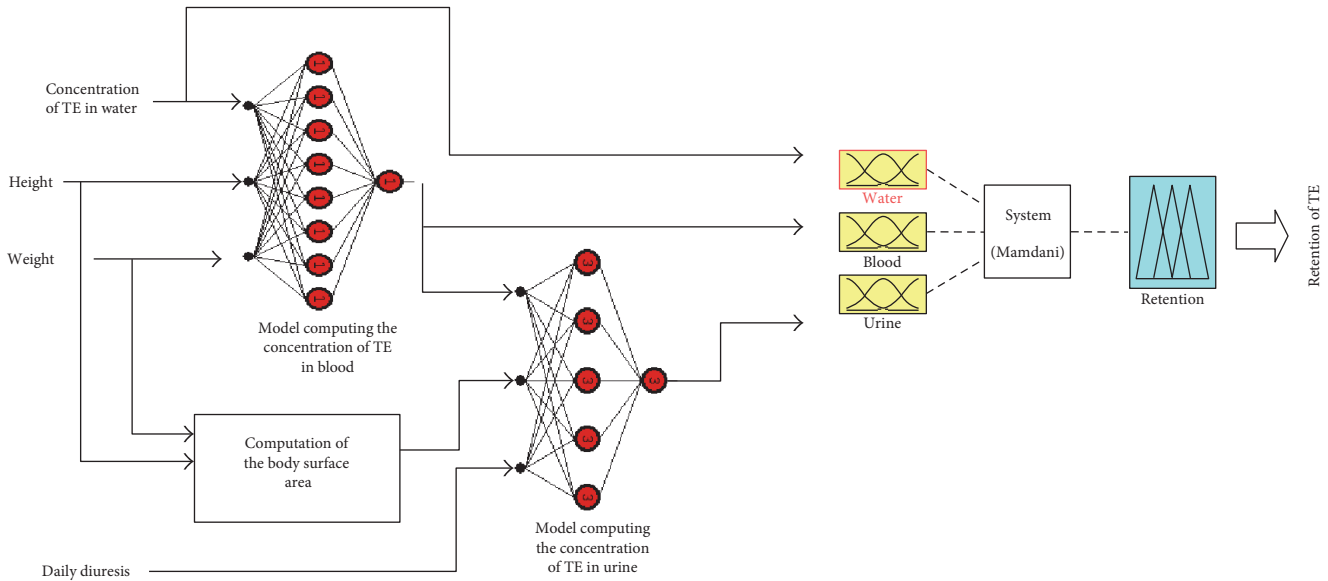


FIGURE 1: Structure of the model assessing the retention of trace elements.

As we see, the intensity of retention varies from  $-1$ , in cases of excessive excretion, to  $+1$ , when the retention level is maximal. When the retention level equals to  $0$ , no concentration changes occur in the body, and the system stays in a state of equilibrium.

Thus, the rules of inference take the following meaning and describe the intensity and direction of the retention processes (“Water” : “Blood” : “Urine”):

- (1) **IF** (Concentration of trace elements in drinking water = “low”) **AND** (Concentration of trace elements in serum = “low”) **AND** (Concentration of trace elements in urine = “low”) **THEN** Retention level =  $-0,5 - 0,2 + 0,3 = -0,4$ , so it is “moderately reduced”.
- (2) **IF** (Concentration of trace elements in drinking water = “low”) **AND** (Concentration of trace elements in serum = “low”) **AND** (Concentration of trace elements in urine = “high”) **THEN** Retention level =  $-0,5 - 0,2 - 0,3 = -1,0$ , so it is “minimal”.
- (3) ... , and so on.

Considering the adopted codes, the basic set of rules can be represented as seen in Table 2.

This distribution gives a dynamic characteristic of the retention levels of trace elements in the body, with an emphasis on the state balance.

There are two fuzzy inference systems that can be reasonably considered as suitable for solving this problem: a Mamdani system with a fuzzy and/or defuzzification of the output and a Takagi-Sugeno system with defuzzification of the linear output. In the case of the Mamdani inference system, the quantitative expressions of the linguistic values of the output variable “Retention level” are either the centre points of the output Gaussian membership functions or singletons. In the case of the Takagi-Sugeno fuzzy system, the quantitative values obtained are the constant terms ( $y$ -intercepts) of the linear combinations of the inputs having zero coefficients [26].

We constructed a hybrid intelligent model consisting of two cascade-coupled neural networks [27] as a practical realization of the proposed approach to determining concentrations of metals in serum and urine, respectively, based on data on the concentrations of trace elements in drinking

TABLE 3

| Weight (kg) | Height (cm) | Body surface area (m <sup>2</sup> ) | Daily diuresis (ml) | Zinc concentration in drinking water (mg/l) |
|-------------|-------------|-------------------------------------|---------------------|---|
| 40,15       | 164         | 1,352                               | 750                 | 0,04  |

TABLE 4

| Weight (kg) | Height (cm) | Body surface area (m <sup>2</sup> ) | Daily diuresis (ml) | Zinc concentration in drinking water (mg/l) |
|-------------|-------------|-------------------------------------|---------------------|---|
| 41,8        | 170         | 1,450                               | 1300                | 0,04  |

TABLE 5

| Weight (kg) | Height (cm) | Body surface area (m <sup>2</sup> ) | Daily diuresis (ml) | Zinc concentration in drinking water (mg/l) |
|-------------|-------------|-------------------------------------|---------------------|---|
| 57          | 159         | 1,587                               | 720                 | 0,017                                       |

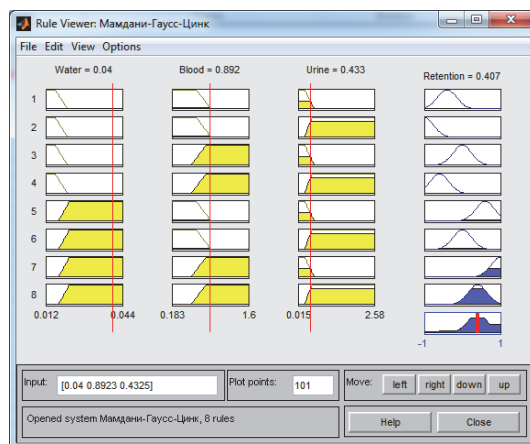


FIGURE 2: Results of the data processing for Table 3 using the Mamdani system.

water and on the physical anthropological characteristics of the tested individuals. The third element of the model is a Mamdani inference system with a definition of the Gaussian membership functions for the output parameter (retention level) based on fuzzy initial data on the concentrations of trace elements in drinking water, serum, and urine obtained in the previous stages. The model assessing the retention of any of the tested trace elements (TE) features the structure shown in Figure 1.

The practical approval of the trace elements retention model was carried out in a test group of children and adolescents. Tables 3–5 provides some results of experiments in the case of zinc.

As a result of cascade modelling, we obtained the following values for zinc concentrations in serum and urine: 0,892 mg/l and 0,433 mg/l, respectively (Table 3). These values were input to the Mamdani system. The results of the data processing are shown in Figure 2.

As a result, the value of zinc retention was found to be 0,407 mg/l, which corresponds to a moderately high level.

As a result of cascade modelling, the following values were obtained for zinc concentrations in serum and urine:

0,867 mg/l and 0 mg/l, respectively (Table 4). The results of the data processing are shown in Figure 3.

The value obtained for zinc retention was 0,708 mg/l, corresponding to a high level.

We obtained, as a result of cascade modelling, the following values for zinc concentrations in serum and urine: 0,778 mg/l and 0,527 mg/l, respectively (Table 5). The data processing results are shown in Figure 4.

The negative value obtained for the zinc retention (−0,463 mg/l) is an evidence of excessive excretion of zinc and corresponds to a moderately low level.

## 5. Conclusions

The method we propose here for assessing and expressing quantitatively the retention of trace elements in the human body is based on a cascade hybrid intelligent system that recommends itself by its high degree of accuracy and reliability. This method does not require expensive laboratory studies and allows for assessing the value of the retention in the body using easily accessible information. The simplified structure of the neural network regression model (its reduced number

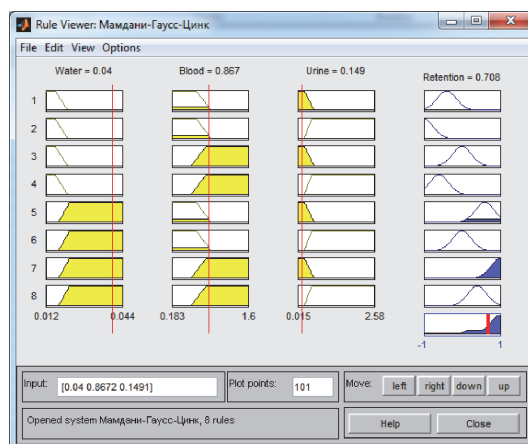


FIGURE 3: Results of the data processing for Table 4 using the Mamdani system.

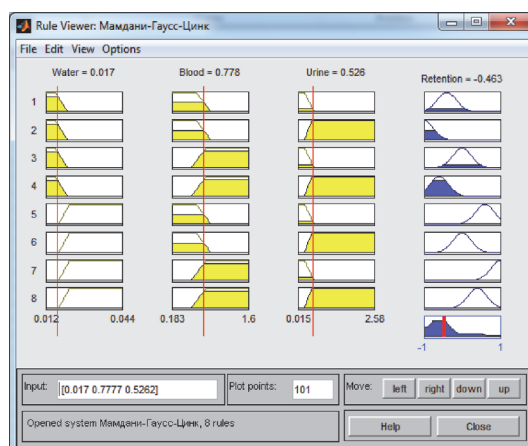


FIGURE 4: Results of the data processing for Table 5 using the Mamdani system.

of inputs) provides sufficient accuracy, and the reduction of the neural networks increases the adequacy of the models.

This method for assessing the retention can be used in the subsequent determination of the balance of trace elements in the human body and the choice of an appropriate method for imbalance correction, both at individual and population levels.

### Conflicts of Interest

The authors declare no conflicts of interest.

### Acknowledgments

This study was supported by the Program of Competitive Growth of Kazan Federal University and subsidy allocated to Kazan Federal University for the state assignment in the sphere of scientific activities.

### References

- [1] P. Coelho, S. Costa, S. Silva, and A. Walter, "Metal(loid) levels in biological matrices from human populations exposed to mining contamination-Panasqueira mine (Portugal)," *Journal of Toxicology and Environmental Health. Part A*, vol. 75, no. 13–15, pp. 893–908, 2012.
- [2] D. Schmidl, S. Hug, W. B. Li, M. B. Greiter, and F. J. Theis, "Bayesian model selection validates a biokinetic model for zirconium processing in humans," *BMC Systems Biology*, vol. 6, p. 95, 2012.
- [3] K. Konzen, S. Miller, and R. Brey, "Proposed modification to the plutonium systemic model," *Health Physics*, vol. 109, no. 4, pp. 307–318, 2015.
- [4] K. M. Unice, B. D. Kerger, D. J. Paustenbach, B. L. Finley, and B. E. Tvermoes, "Refined biokinetic model for humans exposed to cobalt dietary supplements and other sources of systemic cobalt exposure," *Chemico-Biological Interactions*, vol. 216, pp. 53–74, 2014.
- [5] M. Friedrich and M. Kuchlewska, "Assessing the effect, on animal model, of mixture of food additives, on the water balance," *Acta Scientiarum Polonorum. Technologia Alimentaria*, vol. 12, no. 1, pp. 81–90, 2013.
- [6] A. Bitto, A. Horvath, and E. Sarkany, "Monitoring of blood lead levels in Hungary," *Central European Journal of Public Health*, vol. 5, no. 2, pp. 75–78, 1997.

- [7] P. J. Aggett, "Physiology and metabolism of essential trace elements," *Clinics in Endocrinology and Metabolism*, vol. 14, no. 3, pp. 513–543, 1985.
- [8] G. Malinovsky, I. Yarmoshenko, M. Zhukovsky, V. Starichenko, and M. Modorov, "Strontium biokinetic model for mouse-like rodent," *Journal of Environmental Radioactivity*, vol. 118, pp. 57–63, 2013.
- [9] N. Hanson and J. D. Stark, "Comparison of population level and individual level endpoints to evaluate ecological risk of chemicals," *Environmental Science & Technology*, vol. 46, no. 10, pp. 5590–5598, 2012.
- [10] H. Ozmen, S. Akarsu, F. Polat, and A. Cukurovali, "The levels of calcium and magnesium, and of selected trace elements, in whole blood and scalp hair of children with growth retardation," *Iranian Journal of Pediatrics*, vol. 23, no. 2, pp. 125–130, 2013.
- [11] E. Chalvatzaki and M. Lazaridis, "Development and application of a dosimetry model (ExDoM2) for calculating internal dose of specific particle-bound metals in the human body," *Inhalation Toxicology*, vol. 27, no. 6, pp. 308–320, 2015.
- [12] R. W. Leggett, "A biokinetic model for zinc for use in radiation protection," *The Science of the Total Environment*, vol. 420, pp. 1–12, 2012.
- [13] F. Rainone, T. Arcidiacono, A. Terranegra et al., "Calcium sensing receptor and renal mineral ion transport," *Journal of Endocrinological Investigation*, vol. 34, Supplement 7, pp. 8–12, 2011.
- [14] C. D. Klaassen, J. Liu, and B. A. Diwan, "Metallothionein protection of cadmium toxicity," *Toxicology and Applied Pharmacology*, vol. 238, no. 3, pp. 215–220, 2009.
- [15] R. W. Leggett, "The biokinetics of inorganic cobalt in the human body," *The Science of the Total Environment*, vol. 389, no. 2-3, pp. 259–269, 2008.
- [16] S. A. Kiss, T. Forster, and A. Dongó, "Absorption and effect of the magnesium content of a mineral water in the human body," *Journal of the American College of Nutrition*, vol. 23, no. 6, pp. 758S–762S, 2004.
- [17] S. A. Kiss, T. Forster, and A. Dongó, "Absorption and effect of the magnesium content of a mineral water in the human body," *Journal of the American College of Nutrition*, vol. 23, no. 6, pp. 758–762, 2004.
- [18] K. Wesseling-Perry and I. B. Salusky, "Chronic kidney disease: mineral and bone disorder in children," *Seminars in Nephrology*, vol. 33, no. 2, pp. 169–179, 2013.
- [19] S. Lek and J.-F. Guegan, *Artificial Neuronal Networks, Application to Ecology and Evolution*, Springer-Verlag, Heidelberg, 2000.
- [20] X. Zeng, Y. Li, and R. He, "Predictability of the loop current variation and eddy shedding process in the Gulf of Mexico using an artificial neural network approach," *Journal of Atmospheric and Oceanic Technology*, vol. 32, no. 5, pp. 1098–1111, 2015.
- [21] X. Zeng, Y. Li, R. He, and Y. Yin, "Clustering of loop current patterns based on the satellite-observed sea surface height and self-organizing map," *Remote Sensing Letters*, vol. 6, pp. 11–19, 2015.
- [22] L. A. Zadeh, "Fuzzy sets, fuzzy logic, and fuzzy systems fuzzy sets," in *Advances in Fuzzy Systems - Applications and Theory*, vol. 6, World Scientific, River Edge, NJ, 1996.
- [23] K. Hornik, M. Stinchcombe, and H. White, "Multilayer feedforward networks are universal approximators," *Neural Networks*, vol. 2, no. 5, pp. 359–366, 1989.
- [24] J. Schmidhuber, "Deep learning in neural networks: an overview," *Neural Networks*, vol. 61, pp. 85–117, 2015.
- [25] A. Margaret, "Boden creativity and artificial intelligence," *Artificial Intelligence*, vol. 103, no. 1–2, pp. 347–356, 1998.
- [26] B. Li and Y. Zhu, "Uncertain linear systems," *Fuzzy Optimization and Decision Making*, vol. 14, no. 2, pp. 211–226, 2015.
- [27] P. M. Granitto, P. F. Verdes, and H. A. Ceccatto, "Neural network ensembles: evaluation of aggregation algorithms," *Artificial Intelligence*, vol. 163, no. 2, pp. 139–162, 2005.